Perturbations of Electronic Transitions of Organic Molecules in Helium Droplets Generated with a New Pulsed Droplet Source

Dissertation
zur Erlangung des
Doktorgrades der Naturwissenschaften (Dr. rer. nat.)
der Naturwissenschaftlichen Fakultät IV
-Chemie und Pharmazie-
der Universität Regensburg

vorgelegt von
Dominik Pentlehner
aus Marklkofen
2010

Diese Arbeit wurde angeleitet von: Prof. Dr. A. Slenczka
Promotionsgesuch eingereicht am: 19.08.2010
Tag der mündlichen Prüfung: 15.09.2010
Prüfungsausschuss: Prof. Dr. N. Korber , Vorsitzender
Prof. Dr. A. Slenczka
Prof. Dr. B. Dick
Prof. Dr. A. Penzkofer

Table of Contents

1 Introduction

Spectroscopy is a versatile tool of physics and chemistry and is widely used to obtain information about matter on the atomic scale. Thereby, spectroscopic methods are often applied to atoms and molecules isolated in solid matrices or in the gas phase.

Solid matrices can be cooled to temperatures below 1 K, though they are usually held in the range of 4-30 K. They provide a dissipative environment for the embedded species which thus is in thermal equilibrium with its surrounding. Other benefits compared to the gas phase are the rather large density of the isolated species and the ability to study them for long times. [FH84] However, the matrix isolation technique suffers from the interaction of the embedded species with the matrix which leads for example to a shift of electronic transitions and inhomogeneous effects like line broadening or the occurrence of different sites. Further, the mobility of the dopants is usually restricted due to the solid environment which limits experiments involving more than one species, e.g. formation of van der Waals-clusters or chemical reactions. [TV04]

On the other hand, the gas phase provides a unique possibility to study free isolated species without any perturbations from an environment. A common way to obtain isolated cold molecules in the gas phase is the supersonic beam technique. Rotational temperatures below 1 K can be reached, whereas vibrational degrees of freedom are usually less efficiently cooled yielding typically vibrational temperatures above 10 K. Even clusters can be investigated in supersonic beams, though cluster formation and especially their efficient cooling is often difficult to achieve and control due to the lack of a dissipative environment. [Sco88, EJN^{+}00]

In 1992 the isolation of molecules in superfluid helium droplets combining the matrix isolation and the supersonic beam technique was reported for the first time. [GSS92] Since then, helium droplets became a frequently used host system for spectroscopy as reflected by numerous publications and review articles. [TV98, SV01, TV04, CDF^{+}06, ST08]

The helium droplets serve as a dissipative host system cooling the embedded species to an equilibrium temperature of only 0.37 K within picoseconds. At the same time the embedded species are able to rotate and migrate freely inside the droplets which is interpreted to reflect the superfluidity of the droplets. This enables to record rotationally resolved spectra and in particular to generate cold clusters. Further, the perturbations of the embedded species reflected by matrix effects such as solvent shifts were reported to be small compared to solid host systems. [TV98, SV01, TV04, CDF$^+$06, KM07, ST08] This was attributed to an only gentle interaction between the helium environment and the embedded species. Thus, helium droplets were thought to be the 'ultimate matrix' for spectroscopy combining the advantages of the matrix isolation and supersonic beam techniques. [TV04]

However, in particular electronic spectra of organic molecules recorded in helium droplets often reveal significant differences when compared to the corresponding spectra of the isolated molecules in the supersonic jet. These include the occurrence of multiplet splittings, phonon sidebands (phonon wings, PWs) or a broadening of vibronic transitions which cannot be attributed to thermal effects. Consequently, they are caused by the interaction between the helium environment and the embedded molecules.

This interaction is still not fully understood and was the motivation for this work. A deeper understanding of the involved processes is necessary to evaluate experiments and to make full use of the potential of helium droplets for experimental studies on isolated molecules and clusters or (photo)chemical reactions at temperatures below 1 K. Information about the influence of the helium environment is thereby obtained by comparing the electronic spectra of molecules inside helium droplets with the corresponding spectra of the free isolated molecules recorded in the supersonic jet.

The electronic transitions of the molecules under investigation covered the spectral range from the near-UV to the red. For electronic spectroscopy in the blue and UV pulsed dye lasers are advantageous compared to cw dye lasers. However, pulsed lasers probe only a small fraction of a continuous helium droplet beam as commonly used for spectroscopy in helium droplets and reviewed in chapter 2. Thus, a pulsed helium droplet beam providing a higher density of helium droplets within the interrogated time and thus a better S/N-ratio when interrogated with a pulsed laser was used.

Though, the reliability of the pulsed helium droplet sources used by other groups was not satisfying. This was the motivation to take the Even-Lavie valve as a new pulsed helium droplet source. The characterization of this valve is presented in chapter 3 in particular in comparison to continuous and other pulsed helium droplet sources.

The following chapters deal with electronic spectroscopy of organic molecules in the pulsed helium droplet beam. After a more general discussion in chapter 4 the results on various anthracene derivatives (chapter 5), two intramolecular charge transfer systems (chapter 6), and pyrromethene dyes (chapter 7) are presented and discussed.

These chapters include the comparison of the electronic spectra recorded in helium droplets and in the supersonic jet and thus allow for the study of the influence of the helium environment. Thereby, in particular electron-phonon coupling causing the occurrence of PWs and a damping of excited states causing a broadening of electronic transitions are of interest. The thesis ends with a conclusion on these effects in chapter 8 and finally with a summary.

2 Basics of Helium Droplets

In this chapter a few properties of bulk helium and helium droplets produced in continuous droplet beams are reviewed. Further, the doping of droplets with foreign species is discussed. Electronic spectroscopy of organic molecules in helium droplets will be treated in chapter 4.

2.1 From the Bulk to Droplets

The phase diagram of ^{4}He is shown in Fig. 2.1 and displays a few remarkable peculiarities: For pressures below about 25 bar the transition to the solid phase is missing even for temperatures down to absolute zero. Instead, a phase transition to a second liquid phase called HeII is found. This is the superfluid phase which is separated from the liquid phase HeI by the λ-line. In contrast to all other chemical elements no triple point of gaseous, liquid, and solid phase does exist. Quantum effects causing these peculiarities are strongly pronounced for ^{4}He due to its weak interaction and small atomic mass resulting in a high zero-point energy and thus large delocalization of the wavefunction. [TV04] The occurrence of the superfluid phase already below 2.17 K (at atmospheric pressures) is strongly connected to the bosonic nature of ^{4}He (total spin $I = 0$) since for the fermionic isotope ^{3}He (nuclear spin $I = 1/2$) superfluidity is found only at a much lower temperature of about 3×10^{-3} K (at atmospheric pressure). ^{3}He is not relevant for this thesis and thus in the following 'helium' refers only to ^{4}He if not denoted otherwise. Superfluid helium shows unusual phenomena such as the fountain effect, film flow and creep, a very high thermal conductivity, and a vanishing viscosity. [TT90] The latter is reflected in frictionless motion of objects through the superfluid phase for velocities below a critical value called Landau velocity. Below this velocity no elementary excitations of the superfluid can be created due to the conservation laws of energy and momentum and thus no dissipation of energy occurs. The Landau velocity at saturated vapor pressure is about 58 m/s for bulk HeII.

An interesting phenomenon of superfluid ^{4}He is the missing of boiling upon heating. Instead, upon heating He atoms evaporate from the bulk surface. This is ascribed to a unique heat transport mechanism called second sound which enables to transport

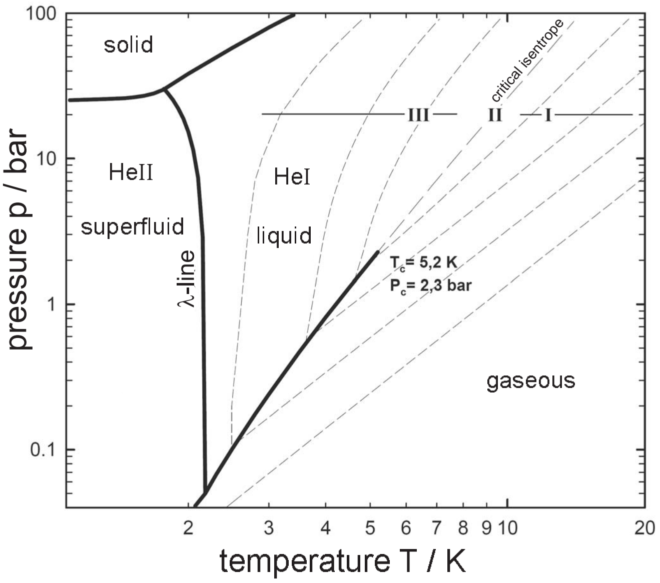

Fig. 2.1: Phase diagram of ^{4}He in double-logarithmic representation. Solid lines are phase boundaries and dashed lines are isentropes starting at different expansion conditions. In the subcritical regime I helium behaves almost like an ideal gas and isentropes follow $pT^{-\gamma/(\gamma-1)}$ = const. For the isentropes in regimes II and III no analytical expression is known. T_c and p_c are the critical temperature and pressure, respectively. (figure according to [BKN+90])

enormous amounts of heat with no temperature gradient. [BKN+90] The relative dielectric constant of liquid Helium for temperatures between 2 and 4 K was determined to $\epsilon = 1.055$ and thus almost equals the vacuum value of $\epsilon = 1.000$. [LST95] This is due to the low polarizability of helium and thus its interaction with any foreign species is extremely weak.

Due to these properties in addition to the inherent low temperature, chemical inertness, and transparency from MW to VUV, superfluid helium was expected to be a suitable host system for spectroscopy.

However, attempts to solve foreign species in the superfluid phase failed due to the extremely low solubility of any impurity. Only a few metal atoms could be successfully immersed using laser induced ablation. [BHT93, TV98, TV04] Instead, the embedded species coagulate with each other or precipitate at the container wall, both which is possible only due to their ability to move almost frictionless through the superfluid phase. These problems are overcome by using free levitating superfluid droplets. In the following, clusters of helium with more than 10^3 He atoms will be referred to as droplets.

The droplets can be varied in size without having a perturbing boundary and fill the gap between single He atoms and small clusters on the one hand and the bulk phase on the other hand. [GSS92] Therefore, droplets provide with the ability to probe superfluidity on a microscopic scale. Experiments on embedded species in the droplets thus can be used to study the properties of the dopants, but in addition also the properties of the droplets themselves. Within this thesis, mainly the interaction between the droplet and the embedded species is of interest. A more detailed understanding of the influence of this host system is mandatory to make full use of the potential provided by the helium droplets.

2.2 Continuous Droplet Beam

Helium droplets are usually generated by a supersonic expansion of helium through a continuous-flow nozzle with a diameter of 2-10 μm into a vacuum chamber. Typical stagnation conditions are a high pressure of 10 to 100 bar and low temperatures between 4 and 30 K. Depending on the stagnation conditions such as stagnation pressure p_0 and nozzle temperature T_0 droplets of different sizes are formed. The size distribution of a droplet beam cannot be measured by means of standard mass selective techniques, because the ionization prerequisite of most mass filters destroys the nascent size distribution of the neutral droplets. [BKN$^+$90] Instead, the size distribution and the scattering cross section were measured by Toennies and coworkers for different expansion conditions by deflecting the droplet beam through the impact of particles from a secondary beam of Ar, Kr or SF_6 and detecting the angular distribution. [LST93, HTD98, TV04] This technique was applied for droplets up to a number of $N = 10^4$ He atoms per droplet. For larger droplets the deflection angle is too small. Thus, their size distribution was obtained by charging the droplets with single electrons and deflecting them in static electric fields. [JN92, KH99, TV04] With this method droplet sizes of $10^5 < N < 10^8$ can be probed. Using a combination of scattering techniques (deflection and attenuation) determining the size and the total scattering cross section, the radial distribution of the particle density in the droplets was determined. [TV04, HTD98] Evaluating the data with density functional calculations revealed a density close to the bulk-liquid value of 0.022 atoms Å^{-3} in the center. In the surface region the density drops from 90 % to 10 % within about 6 Å. [TV04, HTD98] Droplets are expected to be spherical and assuming a uniform density and a sharp outer edge (as in the liquid-drop model) the radius R_0 of a droplet is related to the number of He atoms per droplet N by $R_0 = 2.22N^{1/3}\text{Å}$. [BS90] In Fig. 2.2 the mean droplet size and the diameter of the droplets are plotted versus the nozzle temperature for different stagnation pressures.

Droplets produced via adiabatic expansion of helium can be formed in three different ways, namely by condensation of gas, fragmentation of liquid, and Rayleigh break-up of liquid. [TV04] The thermodynamic equilibrium states occurring in the adiabatic expansion lie on isentropes starting from the initial stagnation conditions (fig.2.1). Droplets are formed whenever an isentrope hits the phase transition between liquid and gaseous phase. Depending on the stagnation conditions, the isentropes are separated into three

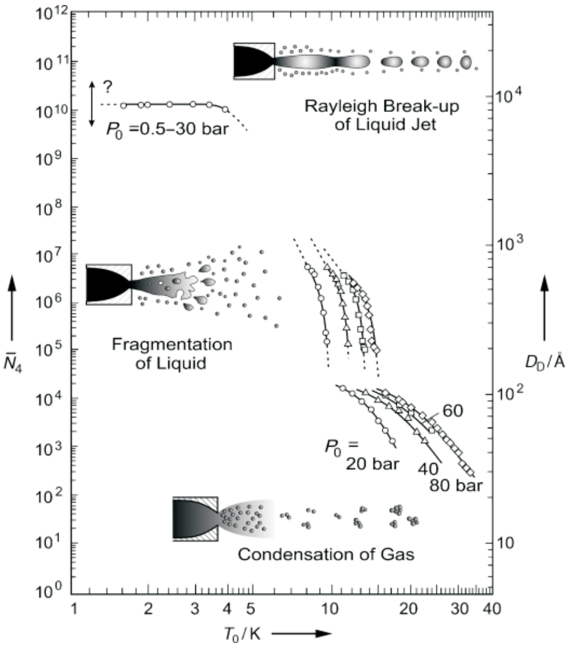

Fig. 2.2: Mean droplet size $\overline{N}_4$ (^{4}He atoms per droplet) and droplet diameters D_0 versus nozzle temperature T_0 for various stagnation pressures p_0. Droplets are formed by different processes. (figure taken from [TV04])

regimes as shown in fig. 2.1.

In regime I (subcritical expansion) the expansion starts from the gas phase. When the isentrope cuts the gas-liquid phase boundary droplets are formed by condensation of the gas. The formation of droplets takes place only if the helium density is high enough to warrant for three-body collisions, i.e. close to the nozzle orifice. Further downstream the droplets stop growing and instead start cooling by evaporation of He atoms (evaporative cooling, see below). The average size of the droplets depends on how far the expansion has progressed before the phase interface is hit. In particular, for a certain stagnation pressure, smaller droplets are formed for higher nozzle temperatures as can be seen from fig. 2.2 (lower part). If an isentrope does not reach the phase transition between gaseous and liquid He, e.g. if the nozzle temperature is too high, the gas only cools down but does not condense. Droplets formed by condensation of helium gas consist of about 10^2-10^4 He atoms per droplet. The obtained droplet size distribution can be fitted with a log-normal distribution [TV98, LST93]

$$f(N) = \frac{1}{N\sigma\sqrt{2\pi}} e^{\frac{-(lnN-\mu)^2}{2\sigma^2}} \tag{2.1}$$

wherein N is the droplet size (number of He atoms per droplet) and μ and σ are parameters. The mean droplet size is given by

$$\overline{N} = e^{\mu + \frac{\sigma^2}{2}} \tag{2.2}$$

and the full width at half maximum of the distribution is

$$s_{\overline{N}} = \overline{N}\sqrt{e^{\sigma^2} - 1} \tag{2.3}$$

which turns out experimentally to be comparable to the most probable size. The droplet size distribution is plotted in fig. 2.3 for different expansion conditions. The droplet size distribution for the supercritical expansion is also reflected in the lineshape of electronic [DS01] and vibrational (IR) [HPS$^+$99] transitions, as will be discussed in more detail in chapter 3.2.3.3. The velocity of the droplets depends on the expansion conditions and covers the range between 200 (smaller droplets) and 400 m/s (larger droplets) with a sharp velocity distribution of Δv/v $\approx$ 0.01-0.03 or a speed ratio of v/Δv $\approx$ 50, respectively. [BKN$^+$90]

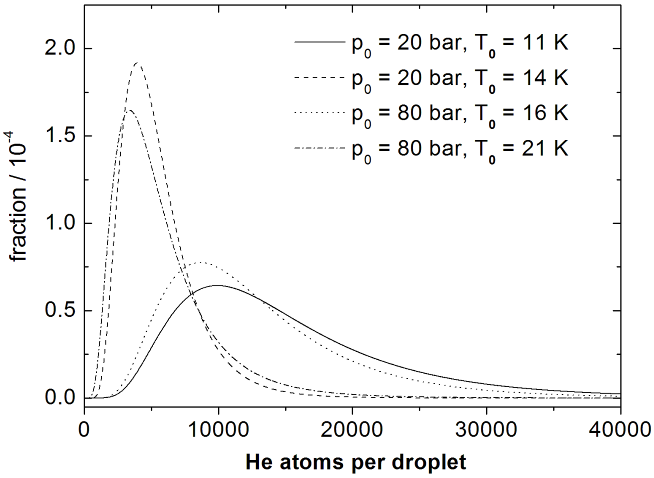

Fig. 2.3: Droplet size distribution for stagnation pressures p_0 and source temperatures T_0 using equ. 2.1. Values for the parameters μ and σ are taken from ref. [Sch93]

In regime III (supercritical expansion) the isentropes approach the gas-liquid phase boundary from the liquid side. (Fig.2.1) Thus, droplets are formed by fragmentation of liquid HeI yielding a bimodal size distribution consisting of large droplets with N $> 10^4$ (fig.2.2) and smaller droplets with N $\approx 10^4$. The smaller droplets are found only for isentropes close to regime II and may be formed by recondensation of helium atoms evaporated from the large droplets. [JN92, BKN$^+$90] For the large droplets an exponentially decreasing size distribution was found. The droplets formed via supercritical expansion have a much lower speed of 50-100 m/s with the larger droplet being slower. [JN92, KH99, BKN$^+$90, HTK97]

The boundary between regimes I and III is defined as regime II (fig.2.1). Isentropes belonging to this regime pass the phase boundary between liquid and gaseous phase near the critical point (T_c = 5.2 K, p_c = 2.3 bar) where the formation process changes. [HTK97]

Even larger droplets with N > 10^{10}-10^{12} can be produced by expanding liquid HeI or superfluid HeII at nozzle temperatures below the boiling point of He through a larger orifice into vacuum. Under these conditions, the droplets are formed via Rayleigh break-up of the liquid. [TV04] (Fig. 2.2)

Once droplets are formed they cool down by evaporative cooling, i.e. by the evaporation of He atoms from the surface. The binding energy per He atom was calculated to be about 1.3×10^{-3} K for the dimer, but reaches the bulk value of 7.2 K for droplets consisting of more than 10^4 He atoms. [TV04] The evaporation rate is initially very high ($\approx 10^{10}$ K s^{-1}) but decreases exponentially with time and is predicted by theory to level out at a final temperature of about 0.4 K within 10^{-4} s. [BS90] This equilibrium temperature agrees well with the experimental value of 0.37 K. Due to the very high initial cooling rate it is not possible to significantly increase the droplet temperature and the droplets can serve as a practically perfect thermostat. [TV04]

The temperature of the helium droplets was determined from the rotational fine structure in the IR-spectra of OCS and SF_6 to 0.37 ± 0.02 K [GHH$^+$00] and 0.38 ± 0.01 K [HHTV97], respectively, assuming thermal equilibrium between the helium and the dopants. Rotationally resolved spectra reveal the ability of the molecules to rotate freely which is interpreted as microscopic indication of the superfluidity of the droplets. [HMTV95, GTV98] The internal pressure of the helium droplets p_i can be estimated from the droplet radius r and the known surface tension γ of bulk liquid helium. It is given by $p_i = 2\gamma/r$ and amounts to about 1.8 bar for a droplet radius of $r = 36$ $\AA$ (2600 atoms). [LST95] Due to their size, the phase diagram of the bulk helium (fig.2.1) is expected to be applicable also to the droplets. Thus, the internal pressure together with the low temperature is a further evidence for the superfluidity of the droplets. [LST95] Finally, the phonon wing of the electronic excitation of glyoxal could be simulated using the dispersion curve that is characteristic for superfluid helium. [HMTV96](cf. chapter 4)

Droplets can also be formed of the fermionic isotope ^{3}He (nuclear spin I = 1/2). The superfluid phase of bulk ^{3}He is found at much lower temperature (3×10^{-3} K at atmospheric pressure) than for the bosonic isotope ^{4}He (total spin I = 0) with the phase transition at 2.17 K at atmospheric pressure. The droplets formed of pure ^{3}He have a lower temperature of 0.15 K due to the lower binding energy per ^{3}He atom of 2.7 K (bulk value) and thus are not superfluid. The lower binding energy is due to the larger zero-point energy of ^{3}He. Due to the non-superfluidity of pure ^{3}He droplets and the high price of ^{3}He, pure ^{3}He droplets are usually not used as a host system for spectroscopy. Experiments with mixed droplets of ^{3}He and ^{4}He revealed that a ^{4}He core is formed inside the ^{3}He droplet and is cooled to 0.15 K. Foreign species doped into these mixed droplets are located in the ^{4}He core which was found to be superfluid if it consists of at least 64 atoms. [HHTV97, GTV98] Thus, spectroscopy in superfluid helium droplets is also possible at 0.15 K.

2.3 Doping of Helium Droplets

Foreign species are doped into the droplets by the pick-up technique. The droplet beam thereby passes through a scattering chamber (pick-up cell) with a well defined and tunable particle density of the sample in the gas phase. The corresponding vapor pressure of the sample is typically in the order of 10^{-6} - 10^{-5} mbar for single particle doping for a flight path of 2 cm through the pick-up cell. [TV04] Thus, the required vapor pressures are by about four orders of magnitude lower than in seeded supersonic beams. This enables to study even low volatile species such as larger biomolecules or thermal labile species. [CLSS01]

Several assumptions are needed to derive an analytical expression for the probability of the pick-up of k particles by crossing through the scattering chamber: (1) The foreign species are embedded individually, i.e. formation of free clusters of the particles in the scattering chamber is neglected. Due to the low vapor pressure of the sample in the pick-up chamber and its high temperature (usually room temperature or higher) the formation of free clusters is indeed very unlikely. (2) The droplets are of uniform size. (3) The cross section for pick-up and coagulation is independent of k, i.e. the number of particles already picked-up. (4) Scattering of droplets out of the beam axis, and thus out of the detection volume, as well as evaporation can be neglected. [LST95]

For a droplet with the coagulation cross section σ_{coa}[1], the probability dW to pick up a foreign particle within the distance dz in the scattering chamber is given by

$$dW = \sigma_{coa} n dz \tag{2.4}$$

with n as the particle density in the chamber. The probability to find k particles inside a droplet depends on its position z along the path through the scattering chamber and is denoted as $P_k(z)$. The variation of this probability at the distance z depends on the one hand on the probability to find droplets at z with (k-1) particles inside which pick-up another one, and on the other hand on the probability to find droplets at z which already have (k) particles inside but also pick-up a further one (the probability to pick-up more than one particle is zero due to assumption (1) and the infinitesimal distance dz).

$$dP_k(z) = P_{k-1}(z)dW - P_k(z)dW \tag{2.5}$$

Inserting equ. 2.4 into equ. 2.5 and integrating along the flight path through the pick-up chamber the Poisson distribution

$$P_k(L) = \frac{(\sigma_{coa} n L)^k}{k!} e^{-\sigma_{coa} n L} \tag{2.6}$$

---

[1] In the nomenclature of ref.[LST95] σ_{coa}=σ_{coag}F$_{a_0}$(∞,x) wherein σ_{coag} is the coagulation cross section and the factor F$_{a_0}$(∞,x) accounts for the relative velocities of droplets and particles in the chamber.

is obtained. P_k(L) is the probability to find k foreign particles inside a droplet after passing through the pick-up unit with the particle density n. In a typical experiment L and σ_{coa} are constant and the particle density n is varied by changing the temperature of a solid sample or the pressure of a gaseous sample. Therefore, equ. 2.6 is better written in the form

$$P_k(n) = \frac{(\sigma_{coa} n L)^k}{k!} e^{-\sigma_{coa} n L} \tag{2.7}$$

with P_k(n) as the probability to find droplets with the cross section σ_{coa} doped with k particles behind the pick-up unit. Fig. 2.4 shows the dependence.

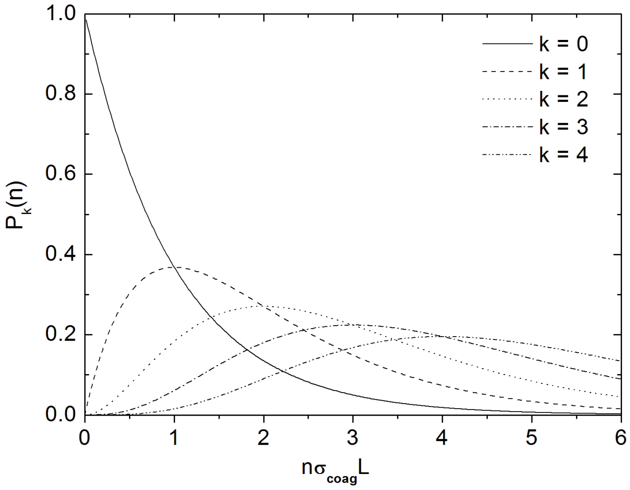

Fig. 2.4: Fraction of a helium droplet beam doped with k foreign particles depending on the particle density in the chamber. The (uniform) coagulation cross section σ_{coa} and the length of the pick-up unit L are constant. nσ_{coa}L is the average number of collisions which lead to capture and remaining of the particles.

Note that the derivation of the Poisson distribution inherently assumes stationary conditions (time independent). For continuous droplet beams this is expected to be fulfilled since both, the droplet and the sample source operate stationary. Otherwise, e.g. if a pulsed droplet beam or a pulsed sample source (laser ablation) are used, stationary conditions are not given. Such conditions may require to consider a time dependency for the sample density which will be discussed in chapter 3.2.3.5.

For k = 0 (undoped droplets), equ. 2.7 decays exponentially (fig. 2.4). For k > 0, P_k(n) starts rising with n^k. In particular, signals corresponding to single doped droplets rise linearly. Further, the maxima are at $n = k/\sigma_{coa}L$ and thus scale linearly with k. For sample densities higher than the corresponding maxima, each of the curves tend to decrease due to the increasing probability of doping with further particles. From fig. 2.4 it can be clearly seen that at maximum probability of single doping an appreciable fraction of the droplets already contain more than one dopant.

Equ. 2.7 was found to describe the experimental dependence of signals stemming from clusters of different sizes k on the pressure in the pick-up unit reasonably well if large enough droplets are used. The necessary droplet size depends on the sample under investigation.

The coagulation cross section σ_{coa} is a measure of the probability that a foreign particle is picked up either by a pure droplet or one already containing k-1 particles and undergoes coagulation with the already embedded particles. This cross section is proportional to the geometric cross section depending on $N^{2/3}$ for a spherical droplet.[LST95] Thus, to account for the droplet size distribution, the probability $P_k(L)$ to find k particles inside a droplet could be obtained by a convolution of the distribution for $N^{2/3}$ (size distribution) with the Poisson-distribution (pick-up probability). [DS01]

Particles which are picked-up by the droplets and remain inside transfer their full momentum and energy into the droplet. From scattering experiments it was shown that the sticking coefficient, i.e. the probability for a captured foreign particle to remain in(on) the droplet was found to be significantly smaller than one. Its value depends on the mass of the particle and the interaction potential between the droplet and the particle. [LST95] Those particles not remaining in the droplets enter them and dissipate only practically all of their momentum and (kinetic and internal) energy but retain just enough of both to leave the droplet again (inelastic scattering). [LST95] The impact and internal energy deposited in the droplet is dissipated through isotropic evaporative cooling and thus leads to a decrease in droplet size and therefore of σ_{coa}. [LST93, LST95] The shrinking in size can be well estimated by the energy intake and the evaporation energy of a He-atom. The latter is usually estimated by the binding energy of a He-atom of 7.2 K (bulk value) and amounts to about 100 - 10000 He atoms depending on the sample and its temperature. Thus, depending on the initial size of the droplets and the number of embedded species, the droplets can significantly decrease in size upon impact. [LST93, LST95] For example, phthalocyanine, which was extensively studied in helium droplets and thereby sublimated at about 600 K, carries about $3N\times\frac{k_BT}{2} \approx 36000\ \text{cm}^{-1}$ into the droplet. Consequently, about 7200 He atoms are released upon pick-up of a single phthalocyanine molecule.

Due to the full momentum transfer upon the purely inelastic processes occuring in the scattering chamber the droplets are also deflected. Though, a deflection of the beam can usually be neglected, in particular for large droplets and a small number of captured particles. [LST93, LST95]

The energy dissipation and thus cooling of the captured particles to the equilibrium temperature of 0.37 K requires some time. An upper limit is estimated by the time of flight required for the dopant to propagate a distance of the droplet diameter. The droplets have a diameter in the range of a few nm and the relative velocity of droplets and particles before their impact amounts to a few hundred m/s. The scattered particles

have to be bound inside the droplet before they pass through the droplets and thus stationary conditions must be reached within picoseconds.
When a second particle enters the droplet it also dissipates its energy on the same time scale. From the velocity of the droplets and the length of the pick-up cell the average time between individual pick-ups can be estimated and is in the order of μs. Thus, clusters are formed of individually cooled reactants. They attract each other by long-range electrostatic or v.d.Waals (R^{-6}) forces. The dielectric constant of liquid He is close to the vacuum value and thus these forces are not significantly shielded by the interspersed helium. [LST95] The particles are able to migrate inside the droplet due to its superfluidity and thus they certainly move to each other and form clusters. Since coagulation of several dopant particles occurs only after cooling of the individual particles long range forces such as dipole-dipole-interaction lead to preferential orientation of the individual particles and thus to preferred formation of certain cluster configurations. This was demonstrated e.g. for clusters of the highly polar HCN molecule forming long chains as long as the droplet diameter. [NMM99, NM99, CDF$^+$06] The binding energy of clusters is again dissipated through evaporative cooling. It is much smaller than the impact and internal energy of the monomers dissipated upon capture and thus its effect on the size of the droplet can be neglected. [LST95]

The assumptions made for the derivation of the Poisson distribution in equ. 2.7 are fulfilled the better the larger the droplets are and the smaller and colder the dopant species is. For droplet sizes used in electronic spectroscopy and low cluster sizes inside, in particular single doping, these requirements are usually fulfilled and experimental data can be fitted well with this model. This enables for the preparation of foreign particle clusters with well-defined cluster size inside helium droplets, but also for the assignment of spectral features to clusters of a particular size.

Particles doped into droplets can be classified either as heliophobic or heliophilic. The former species reside on the surface of the droplets. Among those are ^{3}He as well as alkali-metal atoms and their small clusters. The latter species are located inside the droplets and contain all closed-shell atoms and molecules yet investigated. [TV98, TV04, SV01] All molecules used as dopants in this work are closed shell organic molecules and thus heliophilic.

3 Pulsed Helium Droplet Beam

As part of this work a new apparatus for a pulsed helium droplet beam was put into operation. The most common way to produce a helium droplet beam is a continuous free jet as was discussed in the preceding chapter. Though, experiments are often performed using pulsed lasers in the range from nanoseconds down to femtoseconds thus probing only a small fraction of the continuous beam. The signal to noise ratio in these experiments is expected to increase significantly if a pulsed beam consisting of pulses with high droplet density is used instead of a continuous beam with a lower droplet density. The goal of this work is to establish a pulsed droplet beam in particular for high resolution spectroscopy with pulsed lasers. These are advantageous compared to cw lasers in the frequency tuning rate, if high laser power is required and for spectroscopy in the blue and UV range. The latter aspect is of particular interest for the investigation of small model compounds as in this work and of photoreactions. Another benefit of pulsed lasers is that dynamic processes can be studied directly in the time-domain .

Pulsed molecular beams are not only advantageous compared to continuous beams when pulsed detection schemes (pulsed probe lasers) are applied, but also when pulsed techniques for the sample preparation, such as laser ablation, are used. These techniques are more gentle than heating of the sample and thus are favored in the studies of large biomolecules or thermally labile species. Another important advantage of pulsed beams is the reduced gas flux and thus the required pump capacity. In case of the helium droplets, a lower gas load is of particular interest for experiments with ^{3}He clusters.

To conclude, a pulsed droplet source will open the field for many new experiments in helium droplets.

In this chapter the experimental setup of the vacuum apparatus and the detection scheme is presented, followed by a detailed description and characterization of the Even-Lavie valve as a new pulsed source for helium droplets. The performance of the pulsed droplet beam will be compared to the common continuous beams and to other pulsed beam setups reported earlier in the literature. [GEA02, SKMV02, YBE05, YE08]

3.1 Experimental Setup

Fig. 3.1 (top panel) shows a schematic drawing of the vacuum apparatus which is identical to what is used for continuous droplet beams as described e.g. in ref.s [BKN⁺90, TV98, TV04]. It consists of two differentially pumped vacuum chambers separated by a skimmer. The first chamber (source chamber) is equipped with a 2200 l/s turbo pump (TPH2200,Pfeiffer-Balzer) backed by a roots blower (PMB006CM, ULVAC) and a mechanical pump (DUO 060 A, Pfeiffer-Balzer). The second chamber is pumped by a turbo pump with a pumping rate of 500 l/s (TPH 500, Pfeiffer-Balzer) backed by a mechanical pump (DUO 030 A, Pfeiffer-Balzer). The vacuum is controlled in each chamber with an Active Inverted Magnetron Gauge (Penning Gauge) (AIM-X-NW25, Boc Edwards) connected to the vacuum chamber and an active Pirani gauge (APG-M-NW16, Boc Edwards) mounted to the exit side of the turbo pumps, respectively. All gauges are read with an Active Digital Gauge Controller (Enhanced Version, Boc Edwards). Typical values for the base and operating pressures in both chambers are listed in table 3.1. The high vacuum is mandatory for droplet formation but also to keep the droplets from picking up undesired impurities.

The Helium droplets are formed by expansion of pre-cooled helium with 99.9999 % purity (Helium 6.0, Linde) through the pulsed valve into vacuum. Droplet formation is accomplished by high particle density and low temperatures. Therefore, the valve is mounted to a closed cycle helium refrigerator providing nozzle temperatures down to about 7 K and stagnation pressures up to 100 bar are applied. The droplets formed in the first chamber proceed through a skimmer into the second chamber where they are doped in a pick-up cell and probed with a laser beam.(fig. 3.1) Precooling is achieved by winding the gas inlet tube around the first stage of the cryostat before the connection to the valve. The different regions along the beam path are described in detail in the following.

Tab. 3.1: Typical pressure values (mbar) in both chambers separated by a 6 mm skimmer. The voltage to pressure conversion is calibrated for nitrogen and dry air.

chamber	base pressure	20 Hz, 20 K, 80 bar	50 Hz, 16 K, 80 bar
source chamber	$2{\cdot}10^{-8}$	$5{\cdot}10^{-6}$	$1{\cdot}10^{-5}$
detection chamber	$2{\cdot}10^{-8}$	$8{\cdot}10^{-7}$	$1{\cdot}10^{-6}$

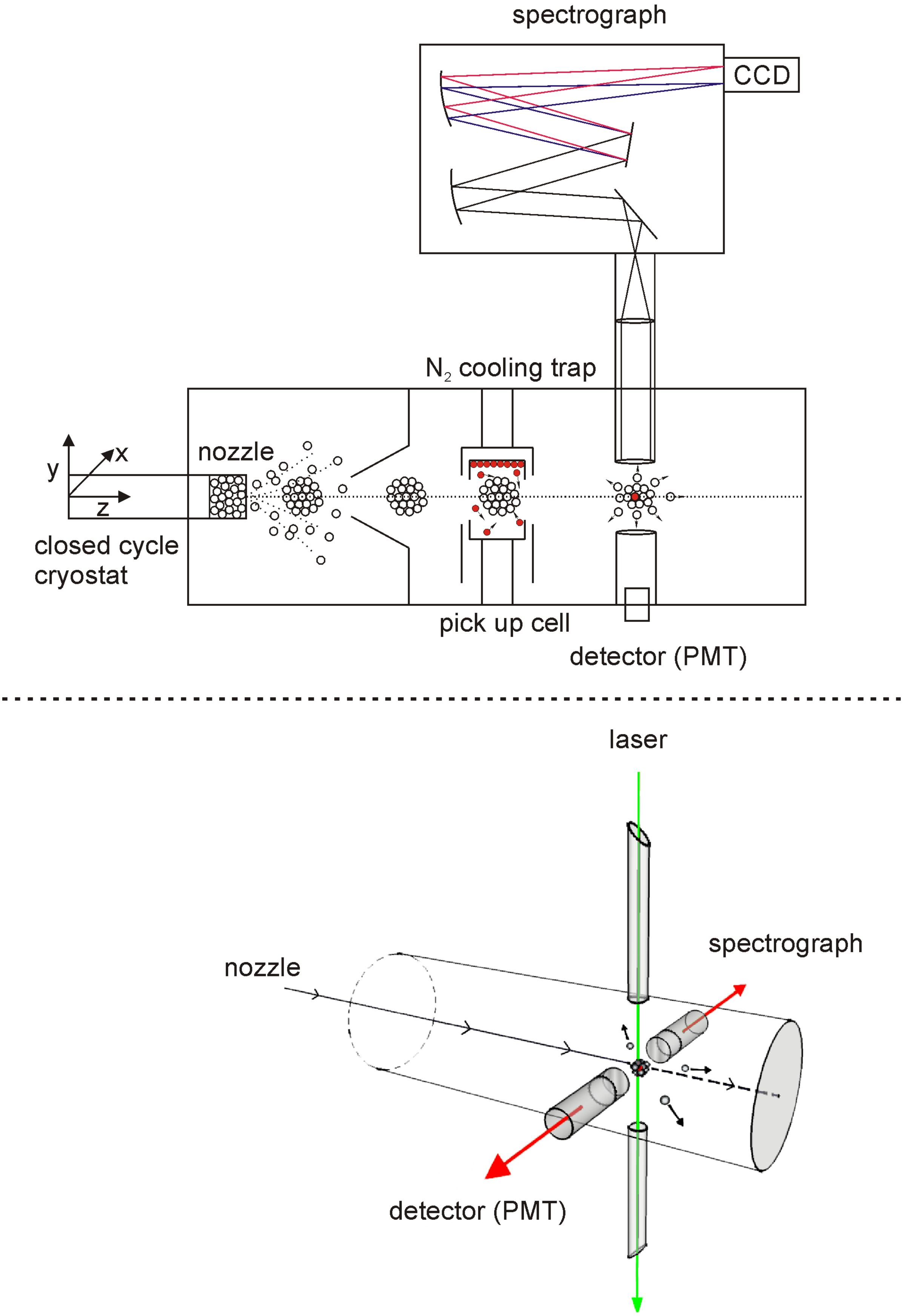

Fig. 3.1: Schematic drawings of the vacuum chamber and the (essential) experimental components. Top panel: Horizontal cross section through the axis of the droplet beam. The laser beam enters from above. Bottom panel: 3D-sketch of the detection region: Light is detected at right angle to both, the droplet and the laser beam.

3.1.1 Nozzle Adapter

The Even-Lavie valve was mounted to the second stage of a two stage closed cycle helium cryostat (4 K cold head RDK-408D2, Sumitomo Heavy Industries supplied by a compressor unit CSW-71, Sumitomo Heavy Industies) with a home built adapter made of copper. As shown in fig. 3.2 the base of the cylindrical adapter is fixed with six screws. The nozzle is kept inside the slotted tube which is squeezed by two screws. The entire unit of valve and cryostat can be moved in all three directions and thus enables to align the axis of the droplet beam. An optimization of the angle of the beam and thus a full alignment of the beam axis to the axis of the vacuum chamber is not possible with this arrangement. Temperature was measured with a calibrated silicon diode (DT-670B-CU, Lake Shore Cryotronics) mounted to the front of the adapter. This temperature is called the nozzle temperature even though it is not exactly the stagnation (source) temperature which will be referred to as the effective nozzle temperature (see below). The lowest nozzle temperature that can be reached is about 7 K. Higher temperatures are obtained by counter heating with a resistor mounted into the base plate of the adapter. (fig. 3.2). This is remote controlled by a commercial temperature controller (Model 331, Lake Shore Cryotronics) and yields nozzle temperatures stabilized to about ± 0.2 K. The stagnation pressure could be varied from about 10 to 100 bar using a conventional pressure reducer and was monitored using a mechanical gauge with an accuracy of ± 1 bar.

The efficiency of cooling the pulsed valve depends critically on the thermal contact between cryostat and adapter and between adapter and valve. The former was best for direct and strong contact between the two plane copper faces. In particular, addition of Apiezon N grease disimproves the thermal contact resulting in higher nozzle temperatures under otherwise identical operation conditions. In contrast, the thermal contact between the nozzle and the holder is optimized if Apiezon N grease is applied. Squeezing the slotted copper tube (adapter) yields a surface different from that of the cylindrical valve and thus only a small contact area. Therefore, the grease increases the thermal conductivity. The thermal contact between the adapter and the nozzle was probed in two ways. Once, the diode was mounted directly to the front plate of the nozzle though this strongly perturbed the beam. Second, nozzle temperatures to obtain certain signals, e.g. optimized fluorescence under otherwise identical conditions, were compared. The thermal contact is also directly reflected by the intensity of the Rayleigh scattering signal (see below) obtained from undoped droplets which increases with decreasing temperature.

The different response of the two contact sites on the application of Apiezon N grease reveals that the thermal contact between adapter and nozzle is not ideal even with the

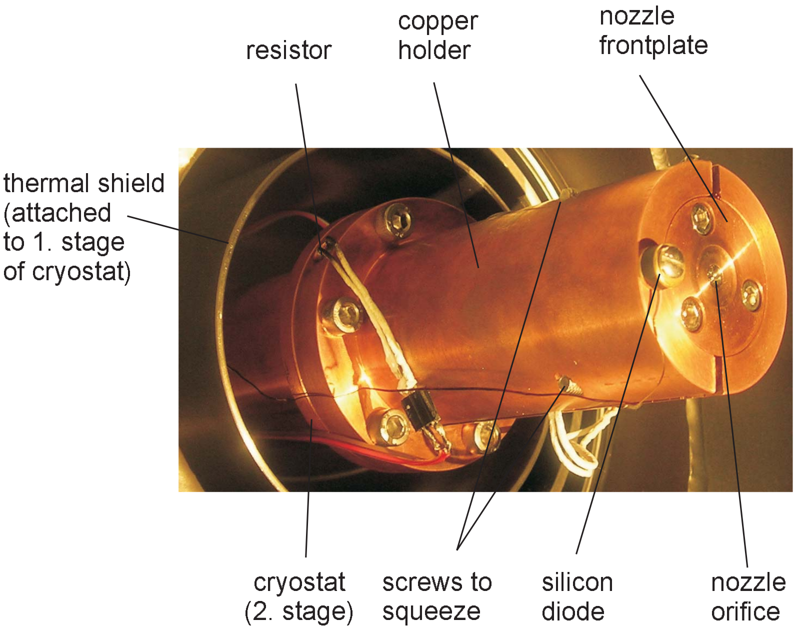

Fig. 3.2: Nozzle holder with the Even-Lavie valve inside. A schematic and sectional drawing of the valve can be found in fig. 3.8 The nozzle temperature is measured at the front of the holder. Mounting the diode onto the front plate of the nozzle itself resulted in a destruction of the droplet beam.

grease. This contact turned out to be a limitation at higher repetition rates due to the operating valve being a source of heat (cf. chapter 3.2.2.3). A better thermal contact might be achieved using indium instead of the Apiezon N grease. Though, according to the manual of the grease [Api] its thermal conductivity is lower compared to indium but heat transfer across pressed metallic joints is significantly better if the grease is applied instead of indium. Another approach would be to manufacture the copper front plate of the nozzle (housing the stainless steel orifice) and the nozzle adapter out of one piece of copper. Note that in any case the real stagnation temperature is given by the temperature of the nozzle orifice made of stainless steel. Thus, the thermal contact between this inlet and the copper front plate instead of the contact between the nozzle (front plate) and the adapter might also limit the cooling.

With the construction used the thermal contact is good enough to cool the nozzle to temperatures optimized for fluorescence with repetition rates up to 400 Hz. (see below) Since pulsed lasers available in our lab can run with repetition rates only up to 50 Hz there was no need to further optimize the thermal contact. Further, nozzle temperatures used in typical LIF-experiments are about 22 K and thus tight counter-heating is necessary already with this setup. With a better thermal contact heating close to the limit of the temperature regulator would be necessary which causes stronger fluctuations of the temperature and thus also of the droplet beam.

The nozzle itself is described in chapter 3.2.

3.1.2 Skimmer and Nozzle to Skimmer Distance

As in many molecular beam experiments the source and detection chambers are separated by a skimmer mounted to the center of a conically shaped separation wall to accomplish free jet conditions in the detection chamber. Helium atoms (and small clusters) otherwise entering the second chamber may interfere with the droplet beam and thus alter its characteristics. If the skimmer aperture is chosen to small, edge effects will occur. These can lead to a scattering of Helium back into the source chamber where it may have a destructive effect on the droplet formation or to a scattering into the beam axis in the second chamber were it also may affect the beam. Obviously, these effects are larger if the aperture is smaller than the beam diameter causing the destruction of a part of the droplet beam and the generation of helium gas (and smaller clusters) interfering with the remaining droplets.
The choice of skimmer in supersonic beam experiments is more crucial the higher the density in the skimmer region. [Cam84, Sco88] For typical high intensity pulsed beams, the skimmer is a less critical component than for continuous beams with high base pressure in the source chamber (Campargue type) but more critical than for those with low base pressures (Fenn type). [Sco88]

Two skimmers were tested within this work under various conditions such as different repetition rates and source conditions. One of them is a commercially available conically shaped skimmer made of nickel with an opening diameter of 2 mm (Model 2, Beam Dynamics) and the other one is a home made trumpet shaped skimmer made of copper with an opening diameter of 6 mm. As described above, the entire source unit can be moved in all three directions under operation. In particular, the nozzle to skimmer distance is a parameter for the optimization.
The signal intensities in all kinds of experiments were practically identical for the two skimmers. The only differences are an increased pressure in the second chamber and a reduced sensitivity for the adjustment of the nozzle plane in the two axis perpendicular to the droplet beam axis (x,y in Fig. 3.1) if the larger skimmer is mounted. Thus, the 6 mm skimmer is used in all of the experiments described if not denoted otherwise.
Fig. 3.3 shows time profiles of the droplet pulse recorded via Rayleigh scattering (see below) for the two skimmers for different nozzle-skimmer distances under otherwise identical conditions. The signal depends only weakly on the distance between the nozzle and the skimmer. For the smallest distance the signal is slightly reduced probably due to self attenuation of the beam in the skimmer. The slight decrease upon increasing the distance above the optimum is presumably due to the droplet beam axis slightly skewed to the axis of the apparatus. The dependence on the distance between skimmer and nozzle is much more sensitive for the 2 mm skimmer than for the 6 mm skimmer. This is presumably also due to the lack of possibility to adjust the angle of the droplet beam.

Qualitatively, the same dependence was found for any kind of experiments (Rayleigh scattering, LIF) and parameter settings, in particular repetition rates and helium fluxes. The optimum signal was found for a distance of about 5 cm from the nozzle to the skimmer opening which is used throughout all experiments if not denoted otherwise. A similar distance was also reported for other experiments using a pulsed droplet beam. [SKMV02]

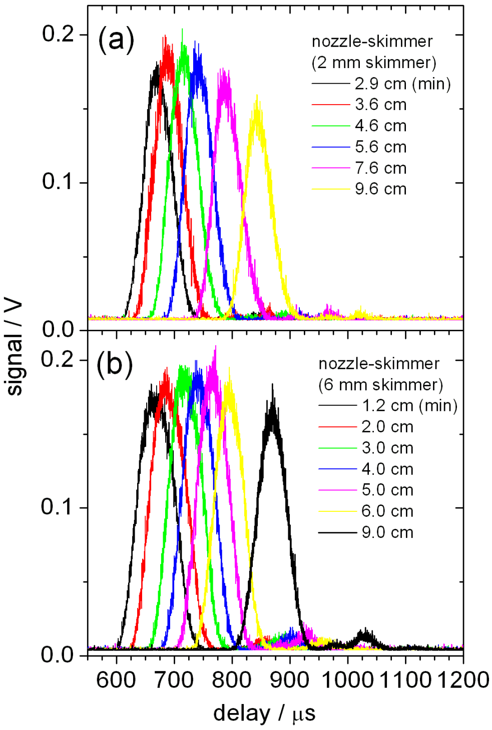

Fig. 3.3: Typical dependence of the time profiles (see below) for Rayleigh scattering on the nozzle to skimmer distance for the 2 mm (a) and 6 mm (b) skimmer. Signals are recorded for a repetition rate of 100 Hz, a stagnation pressure of 80 bar, lowest achievable nozzle temperature of 7.2 K and a capacitor voltage of 19.1 V. The optimum signal is found for a nozzle to skimmer distance of about 5 cm. The skimmers and their holder have different heights and thus the time profiles for the same distances between nozzle and skimmer but different skimmers do not match in time. Signal intensities recorded for the different skimmers can quantitatively be compared and are practically identical at the optimum distance.

Plotting the peak delay time versus the nozzle to skimmer distance a straight line is obtained with the droplet velocity given by the reciprocal gradient. For the data in fig. 3.3 (b) this is shown in fig. 3.4 (a) which yields a mean droplet velocity of 385 m/s. Note that the width of the time profiles mainly reflects the opening time of the valve but not the velocity distribution of the beam.

Time profiles at different nozzle to skimmer distances were also recorded for other experimental conditions to reveal the influence of the nozzle temperature, stagnation pressure and repetition rate on the droplet velocity. Fig. 3.4(b) shows that the velocity of the

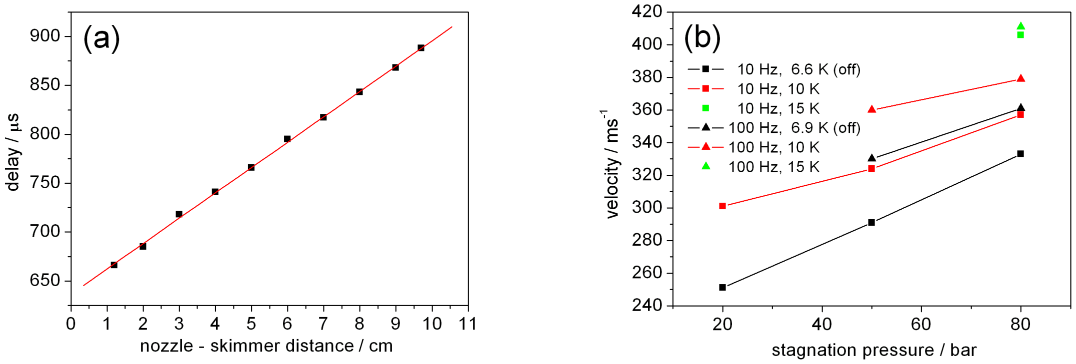

Fig. 3.4: Delay between output sample and maximum of the time profiles in Fig. 3.3(b) versus distance between nozzle and skimmer to determine the velocity of the droplets.(a) Droplet velocities for different stagnation pressures (20, 50, 80 bar) and nozzle temperatures (lowest possible, 10 K, 15 K) recorded via Rayleigh scattering at 10 and 100 Hz, respectively.(b)

droplets probed via Rayleigh scattering ranges from 250 to 410 m/s and increases with stagnation pressure and nozzle temperature. Operating the nozzle with a higher repetition rate causes an additional heating (see below) which is most striking if the nozzle is operated at the lowest possible temperature. At elevated temperatures the heat intake by the solenoid is to a large part compensated by the temperature controller (lower heating current) and thus velocities become independent of the repetition rate. (cf. data for 15 K).

As will be discussed, LIF-signals stem from smaller droplets which have a higher velocity than the larger ones causing the Rayleigh scattering at each stagnation condition. The same velocities as determined from the gradient are also obtained from the distance between the nozzle and the detection area for a flight time given by the recorded delay and an additional delay of about 75 μs due to the mechanical response of the valve to the current pulse. This delay was found to be independent of nozzle temperature, stagnation pressure and driving force within the experimental accuracy.

From time profiles of the doped droplet beam recorded via fluorescence the velocity of the doped droplets can be determined the same way. Fig. 3.5 illustrates time profiles for two different driving forces for distances larger than the optimum distance of around 5 cm. For the lower driving voltage (a) the signal gains in intensity with decreasing distance while the shape of the pulse remains constant. In contrast, the shape changes with the distance if the nozzle is operated with higher driving currents (b). At large distances the profiles reveal two peaks, a sharper leading one and a broader behind. A minor third peak may be spotted at the latest end of the pulse. With decreasing distance the intensity of the former increases whereas the second decreases and merges into the first. At the same time the third contribution becomes clearly separated. Multiple peaks in the time profiles of doped droplets is also found when the nozzle is operated with higher capacitor voltages than for optimum performance. (cf. Fig. 3.13) They are assigned to secondary pulses arising from recoiling of the plunger instead of immediately closing the valve. The two main contributions can be more clearly distinguished at larger distances due to their different velocities. (Fig. 3.5(b)). When operating the nozzle with smaller driving currents no secondary pulses occur and thus have not to be considered. From the data shown in Fig. 3.5(a) a mean velocity of 485 m/s was determined.

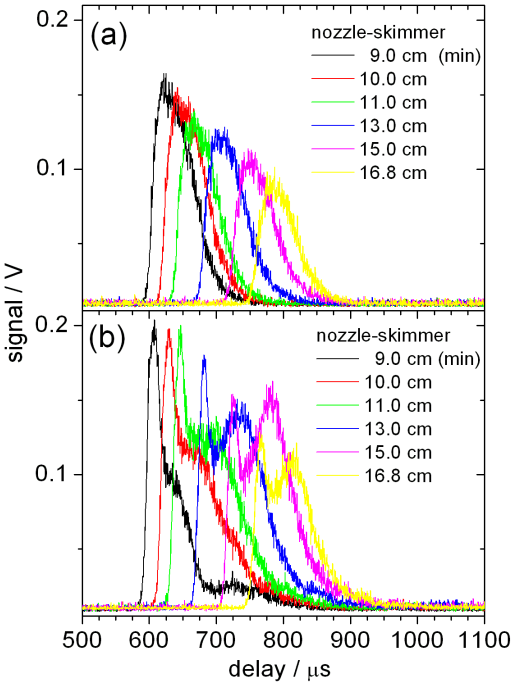

Fig. 3.5: Dependence of LIF-signal on the nozzle to skimmer distance for larger distances than the optimum for the 2 mm skimmer. The nozzle is operating at 20 Hz, p = 80 bar, T = 20 K with different driving forces (fluxes). The capacitor voltage amounts to a typical value of 20.0 V (a) and a larger value of 22.0 V (b), respectively.

In other pulsed droplet beams velocities in the range from 330 to 400 m/s with a velocity spread of 4 m/s for a stagnation pressure of 20 bar and nozzle temperatures in the range from 9 to 14 K were reported. [SKMV02] The droplet velocities in the pulsed beams correspond well with the average velocity of 250-500 m/s (with larger droplets being slower just as in the pulsed beams) found in subcritical continuous expansion. [BKN^{+}90]

It is important to note that all time profiles shown within this work are scaled to the beginning of the output sample from the power supply, but not to the real nozzle opening. However, the delay between the driving pulse and the nozzle opening is almost constant and, thus, shifts in the time position of the profiles can be attributed solely to different droplet velocities.

3.1.3 Pick-up Unit and Liquid Nitrogen Trap

The pick-up unit consists of a resistively heated oven of cylindrical shape with a removable cap holding a pellet of the solid sample to be sublimated. The cylinder has an inner diameter (length of the pick-up cell L) of 26 mm, is wrapped up with a heating wire connected to a tunable DC-voltage supply and has two holes on opposite sides each with a diameter of 5 mm. This pick-up cell is covered by a stainless steel cylinder (with two holes) shielding black-body radiation from the oven. The pick-up cell is mounted onto a tube with a diameter of about 30 mm that can be exchanged through an airlock with a gate valve without breaking the vacuum in the machine. The tube can in situ be shifted perpendicular to the droplet beam axis and rotated around the cylinder axis to align the pick-up cell.

The temperature of the oven is measured with a thermocouple (type k, Thermocoax) fixed in a trough on the bottom of the pick-up cell. The whole pick-up unit is shielded by a copper cylinder connected to a liquid nitrogen reservoir. The copper shield (liquid nitrogen trap) has two holes on the beam axis with diameters of about 7 mm. The spacing between the outer surface of the pick-up unit and the inner surface of the copper shield is about 1.5 cm. This arrangement of the cooling trap surrounding the pick-up cell further reduces the black body radiation detected by the photomultiplier. Moreover, most of the sample effusing from the oven is condensed onto the copper shield and thus contamination of the chamber is reduced. Also other impurities present in the chamber, in particular water, are condensed onto the cooling trap. It turned out that the trap also cools the sample though there is no mechanical contact. This enables to work with sample temperatures below room temperature without an additional cooling device such as a Peltier element. Even lower sample temperatures down to ≈ -25 °C are accessible via the radiative heat transfer but since it takes quite long until thermal equilibrium is reached at these temperatures this is rather impractical. Further, samples that require such a low temperature for single molecule doping use to evaporate before the cooling is completed. Instead, a gas pick-up cell or a separated pick-up chamber should be used for such molecules.

Comparing time profiles of the undoped droplet beam recorded via Rayleigh scattering with and without the copper shield and the pick-up unit mounted on the beam axis their possible interference with the beam can be analyzed. The signal with the copper shield mounted is identical to the signal without any of these parts inside the chamber. Even with the pick-up unit in place identical signal can be obtained. However, careful alignment is required.

Since the droplet beam can pass through the pick-up cell (almost) without any edge effects, the diameter of the beam must be smaller than the 5 mm aperture of the pick-up cell. The exit aperture of the pick-up cell is located about 14.5 cm from the source and thus an upper limit for the full opening angle of the beam can be estimated to about 2°. In continuous droplet beams a noticeably spatial broadening due to collisions with residual background gas was observed which is more important for smaller droplets. [LST93] The above opening angle was estimated for droplets larger than those used for LIF. Though, the latter also consist of about $\approx 10^5$ He atoms per droplet. Consequently, their deflection by inelastic scattering with background gas should be of negligible effect on the beam divergence.

Another way to dope the droplets is to cross the droplet beam by a secondary effusive beam of the dopants. [LST93, LST95] Therefore, the pick-up cell was replaced by a cell containing a slit nozzle with a slit of 10 mm in length and 0.5 mm in width. The effusive beam intersects the droplet beam at right angle with the slit usually aligned parallel to the droplet beam axis. The angle between the slit and the droplet beam axis as well as the distance of the slit to the droplet beam are additional experimental parameters (besides the temperature of the sample reservoir) to vary the particle density of dopants in the scattering region. The advantages of this technique are that high densities of the foreign particles are produced locally and possible interferences of the droplet beam with the apertures of the pick-up unit are avoided. Though, the consumption of sample was much higher, higher sample temperatures were needed and the reproducibility was worse compared to the pick-up cell. Thus, the pick-up cell was used if not denoted otherwise.

3.1.4 Optical Excitation and Detection

The droplet beam is intersected perpendicularly by a laser beam about 21 cm downstream from the skimmer opening (6 mm skimmer). (cf. fig. 3.1) The signal (Rayleigh scattering or laser induced fluorescence(LIF)) is collected at right angle to both, the droplet and the laser beam, by a quartz lens (f=0.5) and imaged with a second lens onto the photocathode of a photomultiplier tube (PMT) or the entrance slit of a spectrograph. The collecting lens is glued to a stainless steel tubing hold at a distance of the focal length from the intersection of laser and droplet beam. It acts also as window of the vacuum apparatus. (Fig. 3.1)

The laser light is coupled into the apparatus from the top through quartz windows mounted at Brewster angle (57°). The laser then proceeds through a black baffle with an opening diameter of 4 mm followed by a black channel (6 mm diameter, 10 cm length) with a coarse thread inside. Both are mounted right behind the Brewster window at the entrance of a 50 cm long blackened tube (4 cm inner diameter). At its end the laser enters the detection chamber through a black aperture with an inner diameter of 7 mm. This last aperture is decisive for the reduction of stray light. It prevents the diffraction of the laser beam arising at the other apertures from entering the detection chamber but has a diameter large enough to not causing diffraction itself. The laser exits the vacuum apparatus through an analogous arrangement however only with the aperture close to the Brewster window. This arrangement helps to drastically reduce the laser stray light and allows to work with cw lasers without using edge filters in front of the respective PMT. The low level of stray light and the obtained S/N-ratio is in particular reflected in fig. 3.6 showing the time trace of a single acquisition cycle (b) with negligible signal outside the averaged pulse profile (c).

Photomultipliers used in this work are two different PMTs (R 943-02, Hamamatsu) cooled to -25°C and -15°C, respectively, to reduce thermal noise. Alternatively, two PMTs operating at room temperature (H5783P and H5783-20, Hamamatsu) were used. Signals from the cooled PMTs were amplified by a factor of 25 (SRS445, Stanford Research Systems(SRS)) or 200 (VT 120A, Ortec) before they were recorded by an oscilloscope (TDS 744A, Tektronix), a photon counter (SR400, SRS) or a gated integrator and boxcar averager (SR250, SRS), respectively. Edge filters can be put in front of the PMTs to reduce stray light of pulsed dye lasers.

Two different Czerny-Turner spectrographs (1870 C, SPEX and MS257, L.O.T.-Oriel) were used for dispersed emission spectra. The former has a focal length of 50 cm (F-number 6.9 - 7.9) and can be operated with a 1200 lines/mm or 2400 lines/mm grating. The latter has a focal length of 22 cm (F-number 3.9) and light can be dispersed with a 400 lines/mm, 1200 lines/mm or 3600 lines/mm grating. The lenses focussing the fluorescence light onto the entrance slit of the spectrographs were chosen to match the F-number of the corresponding spectrograph. Dispersed light was detected with two different CCD (charge coupled device) cameras (DU 401-BV or DU 420A-BU2, Andor iDus) cooled to -80°C to reduce thermal noise. The CCD-chip of both consists of 1024×256 pixels each with a size of $26\times26\,\mu\text{m}^2$. The DU 420A-BU2 model is more sensitive in the UV. However, artificial signals are observed covering about 20-40 pixel columns with a peak intensity of up to 0.4 % of the real signal depending on the angle of incidence. This artefact results from reflection of parts of the signal on the window shielding of the CCD-chip. This effect was absent for the DU 401-BV camera though it carries the same window.

A cw Ar^+-laser (Innova I70C-5, Coherent) was used for Rayleigh scattering. It was operated in multiline-UV mode with an output power of up to 170 mW mostly tuned down to 5 mW. Further, a tunable cw dye laser (899-21 autoscan, Coherent) pumped by an cw Ar^+-laser (Innova Sabre, Coherent) was used for recording LIF. The dye laser runs in single-mode operation with a linewidth $\leq$ 1 MHz and an output power of typically about 300 mW. This laser system is connected to a wavemeter registering the absolute wavelength (vacuum) and remote controlling the frequency tuning with an accuracy of 0.0017 cm^{-1} .

The nanosecond pulsed lasers used were a tunable dye laser (Scanmate 2E, Lambda Physik) with a spectral linewidth of about 0.2 cm^{-1} pumped by a frequency doubled or tripled output (532 nm or 355 nm) of a Nd:YAG-laser (SL803, Spectron Laser Systems) with a repetition rate of 20 Hz and a pulse duration of 10 ns or another tunable dye laser (LPD 3002, Lambda Physik) with a spectral linewidth of about 0.2 cm^{-1} pumped with 308 nm (XeCl*) radiation of an Excimer-laser (LEXtra 100, Lambda Physik) with a repetition rate up to 50 Hz and a pulse duration of 5 to 50 ns. For most of the experiments the pulse energies provided from the dye lasers operated without amplifier cuvettes (typically 400 to 1200 μJ) are fairly enough. Only in case of creating UV-radiation by frequency doubling the dye laser amplifier cuvettes were installed. For frequency doubling BBO I or BBO III crystals connected to compensator crystals (Lambda Physik) were used. After cleaning the UV-light from the fundamental by means of a set of Pellin-Broca prisms pulse energies of up to 1 mJ were achieved.

Frequency calibration of the Scanmate dye laser was accomplished by comparison with the high precision wavemeter of the cw dye laser. As a result the wavenumbers had to be calibrated by applying the function ν_{cal} = 3.76156 + 1.00121ν_{sm} - 1.78078 × E-8 ν_{sm}^2 with ν_{cal} as the calibrated wavenumbers (vacuum values) and ν_{sm} the wavenumbers given by the laser software, respectively, to match the respective wavenumbers of the cw dye laser within ± 1 cm^{-1} . For the LPD 3002 the wavelengths were calibrated using a spectrograph and had to be shifted by a constant value of 0.1 nm to the red and thereby match the calibrated vacuum values of the transitions of NO_2 in the gas phase and anthracene in helium droplets within ± 5 cm^{-1} . Relative wavenumbers can be given for both pulsed dye lasers with an accuracy of ± 1 cm^{-1} .

All numbers given for the laser intensities listed above are measured directly behind the lasers, and thus ignore losses on the long path to the experiment either through a fibre or guided by several prisms. Further, for most of the experiments the lasers were attenuated. The laser and detection system used for the individual experiments are listed in chapters 5-7.

3.1.5 Detection Scheme

The signals of the PMT were recorded either by feeding directly to an oscilloscope to obtain time profiles, or to a photon counter for recording excitation spectra by means of the cw dye laser, or to a Boxcar averager when excitation spectra were recorded using a pulsed dye laser. Dispersed emission spectra were recorded with a CCD camera attached to a spectrograph detecting emission induced upon excitation with either cw or pulsed lasers.

time profiles A cw laser (Ar^+-ion or dye) is used to probe the beam and the signal from the PMT is recorded with the oscilloscope triggered by the signal from the 'output sample' port (O.S.) of the pulse driver for the Even-Lavie valve. This way it is

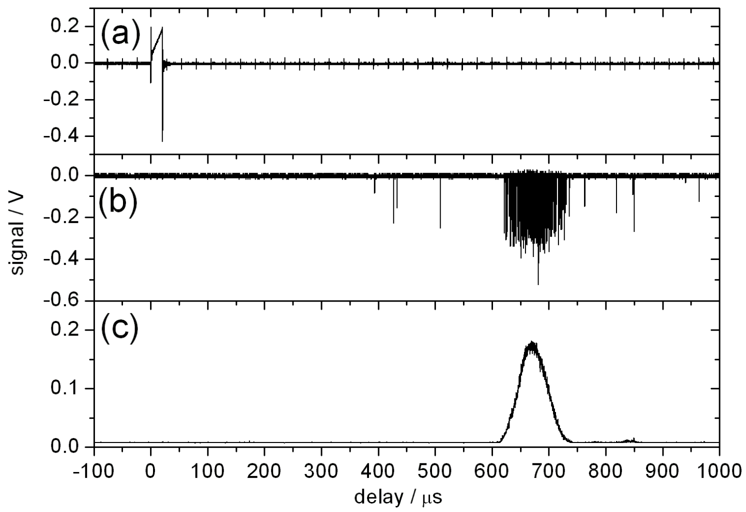

Fig. 3.6: Output sample of the pulse driver for the nozzle (a), PMT-signal for one single beam pulse (b) and its inverted average over 200 beam pulses (c). A 5 mW Ar^+ laser in multiline-UV operation is used to probe undoped droplets stemming from the nozzle running with 100 Hz at a nozzle temperature of 7.2 K and a stagnation pressure of 80 bar. The Rayleigh scattering is collected with the PMT H5783P without an edge filter.

possible to monitor the whole droplet beam to exploit its dependence on various experimental parameters. An example is shown in fig. 3.6 under typical conditions for Rayleigh scattering also demonstrating the signal to noise ratio. The O.S.-signal of the driver is shown in fig. 3.6 (a), the signal from the PMT obtained from a single droplet beam pulse in fig. 3.6 (b) and its inverted averaged trace over 200 beam pulses in fig. 3.6(c) which in the following will be referred to as a time profile. While the time profile shows a smooth envelope the single pulse trace consists of a bunch of distinguishable photons.

excitation spectra taken with a cw laser The cw dye laser is used to excite the doped droplet beam and the signal from the PMT is preamplified and fed into the PC-controlled photon counter. At the beginning of a frequency scan the laser is set to a certain frequency and the photons are accumulated for a chosen time-interval. After this time, the counter sends a trigger to the laser and to the data acquisition program. Upon the trigger the laser is tuned a chosen frequency interval to the next frequency position and the contents of the counter is read by the PC. As soon as the new frequency is set, the laser sends a trigger to the counter starting the next acquisition cycle. The laser frequencies are saved by PC remote controlling the laser frequency tuning. For each laser frequency the corresponding counted events are stored on the experiment's PC. Putting together the two data lists yields an excitation spectrum.

excitation spectra taken with a pulsed laser Pulsed dye lasers are used as excitation sources for most of the electronic excitation spectra discussed in the following chapters. The boxcar averager is used to analyze the signals recorded by the PMT when pulsed dye lasers are used. The boxcar is triggered by a photodiode detecting an out coupled fraction of the laser beam. Typically best S/N-ratio was obtained for 80 ns gates starting synchronously with the stray light of the laser. In principle the signal from the boxcar is converted by an A/D converter (SR245, SRS) and read out by a PC. This readout is limited to a rate of 15 Hz and thus averaging is done exclusively by the boxcar itself. At the beginning of an acquisition cycle the PC sends a software trigger to the laser to tune to a certain wavelength. As this is done the laser sends a software trigger back to the PC. Only after a certain time delay determined by the number of pulses to be averaged and the repetition rate of the laser the PC reads the boxcar signal level via the A/D converter. Afterwards, the next acquisition cycle starts with a software trigger sent to the laser.

Communication with the laser is accomplished via an external server receiving the commands from the experiment's PC and sending commands to and receiving reply signals from the laser. Furthermore, the A/D-converter is not directly read by the experiment's PC but also by the external server which subsequently is read by the PC. A more detailed description of the signal processing can be read in ref. [SF09] The pump lasers and the valve are both triggered externally by a home made trigger generator (constructed by Dr. U. Kensy together with the electronic workshop) to ensure synchronization of the droplet and laser pulses within the detection region.

emission spectra Emission spectra were recorded using different excitation lasers, spectrographs and CCD cameras. In any case the excitation laser was set to a fixed wavelength coincident with a resonance of the system under investigation. In the case of the cw dye laser the precision of the frequency controlling unit was high enough to simply give the correct wavenumber to the controlling PC. In case of the pulsed dye lasers the reproducibility of the frequency settings is limited only to about ± 0.1-0.3 cm^{-1} . This is in the order of the line width of some of the transitions. In order to accomplish perfect coincidence of the laser frequency with the peak of the molecular resonance an excitation spectrum was recorded tuning the laser and stopping the laser at the frequency of interest.

The spectrographs were set to a certain center wavelength by an external controller (SPEX) or by the camera software (MS257). Both cameras were read out with a commercial software package (Andor Solis 4.9.30000.0, Andor). Dispersed emission spectra were recorded in full vertical binning mode of the CCD-chip and background signals were subtracted. The background spectrum was recorded under identical conditions as the signal spectrum except for the valve not in operation (cw laser) or operated with mismatched timing to the laser pulse. For laser wavelengths not covered by the recorded spectral range the background spectrum can also be measured with the laser shut off. In the vertical binning mode the charges of all 256 pixels of one column (corresponding to the same wavelength interval) are integrated on the CCD-Chip by the hardware of the camera before it is read out. Thus, electronic noise created by the readout procedure is minimized. Best signal to noise ratios are obtained by accumulating the signals directly on the chip and, thus, reducing the read out sequences to a minimum. Impact of cosmic radiation registered by the camera were removed by the Andor software which eliminates single pixel events which do not reappear in a second acquisition cycle. For this procedure at least two read out cycles are necessary. Best S/N-ratio was thus found for reading out two times. For experiments with pulsed dye lasers up to 50 Hz typical settings were accumulation times of 2×1200 s or 2×1800 s.

In the vertical binning mode the camera provides a list of intensities recorded in each of the individual 1024 columns of the chip. The corresponding wavelengths are obtained by calibrating the abscissa with the spectrum of an Ar/Ne-lamp whose tansition frequencies are known with high accuracy. [RkR] This procedure was done after each change of the grating position of the spectrographs to account for limitations in the reproducibility of the mechanics moving the grating. This procedure yields the calibrated wavelength for each of the 1024 data points as a function of the number of the pixel-column x, that is $\lambda^{cal} = \lambda(\mathrm{x})$. The calibration of the emission spectra using the Ar/Ne lamp leads to an accuracy of about ± 5 cm^{-1} (1200 lines/mm, SPEX) or about ± 2 cm^{-1} (2400 lines/mm, SPEX), respectively, for $\lambda > 600$ nm as determined by measuring the stray light from the dye lasers. For spectral ranges not covered by the Ar/Ne lamp the calibration was done by recording the stray light of a pulsed dye laser. This results in a larger error in the absolute accuracy of about ± 10 cm^{-1} .

The calibration function is essentially linear with a small quadratic correction, e.g. $\lambda^{cal} = 696.80335\text{-}0.03564\ \mathrm{x}\ \text{-}\ 6.76624 \times 10^{-7}\ \mathrm{x}^2$ for the SPEX-spectrograph with a 1200 lines/mm grating and a central wavelength of 680 nm. The approximately linear relation demonstrates that the spectrographs disperse the light into almost identical wavelength intervals $\Delta\lambda$ on the CCD-chip. Due to the nonlinear relation between wavelength and wavenumber, a Jacobi-transformation has to be applied to convert the spectra from the wavelength into a wavenumber scale. For a constant wavelength interval $\Delta\lambda$ recorded in a pixel column the corresponding wavenumber interval scales quadratic with the wavenumber. Thus, the spectral resolution $\nu/\Delta\nu$ decreases with the inverse of the wavenumber. The resolution depends also on the size of the entrance slit. Increasing the entrance slit to values limiting the resolution does not gain much in peak intensity as is expected for the incident light focussed in the middle of the entrance slit.

The emission spectra are not corrected for a spectral or local sensitivity profile of the CCD-chip. Typically spectral ranges of less than 40 nm are covered by a spectrum and the sensitivity within this ranges is almost constant for the wavelengths recorded within this work. By changing the central wavelength of the detection a possible spatially different sensitivity of the CCD-chip was checked but not observed.

Details about the spectral resolution obtained in the individual experiment are given together with the discussion of the respective emission spectra.

The individual excitation and detection equipment used will be listed for each investigated compound. When continuous detection schemes are applied (time profiles, photon counting, emission spectra), the Penning Gauge in the second chamber was switched off during measurements since it produces a background signal increasing with increasing pressure which is therefore in particular of importance at higher repetition rates.

3.1.6 Helium flux

For some of the experiments characterizing the droplet formation the helium flux was hold constant. To obtain information about the flux the voltages from the Penning Gauges measuring the gas pressure in the source chamber was directly monitored with an oscilloscope. Typical time dependent signals for repetition rates of 10, 20, and 50 Hz are shown in fig. 3.7. For 10 Hz operation the pressure rises upon the opening of the valve and drops to the base pressure before the next gas pulse. For higher repetition rates, e.g. 20 or 50 Hz, the pumping rate does not suffice to remove the gas before the next pulse. Upon further increasing the repetition rate the modulation of the gas pressure vanishes entirely.

The particle flux ϕ_{He} of Helium into a vacuum chamber is related to the pressure p_{He} in this chamber by

$$\phi_{He} = \frac{s}{k_B T} p_{He} \tag{3.1}$$

which follows directly from the ideal gas law. Therein, s is the pumping rate of the vacuum pumps. Thus, by measuring the pressure the flux can be monitored. The voltage of the Penning Gauges has a nonlinear dependence on the pressure. Though, the absolute flux is of minor interest, but the intention is to hold the flux constant in some of the experiments for the characterization of the Even-Lavie nozzle concerning the efficiency of droplet formation.

The pressure gauge is mounted off the beam axis in the source chamber and is thus a measure for the flux of expanded helium not entering the second chamber. Under operation, the pressure in the second chamber rises approximately linear with the pressure rise

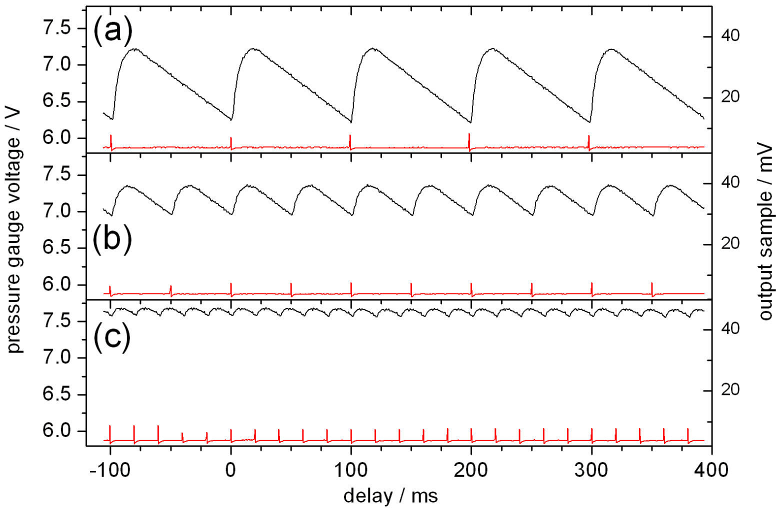

Fig. 3.7: Voltage from the Penning Gauge in the source chamber (left axis) versus time for different repetition rates 10 Hz (a), 20 Hz (b) and 50 Hz (c). The absolute values are a measure for the overall helium flux out of the nozzle. The O.S.-signal from the pulse driver indicating the nozzle openings is also shown (right axis).

in the source chamber by about 10 % of its value despite of the smaller pump capacity. Therefore, the change of the pressure in the source chamber is in a good approximation a measure for the overall flux of helium out of the nozzle.

3.1.7 Chemicals

Most of the samples investigated within this work were purchased from Aldrich with a purity of at least 96 % and were used without further purifications. The laser dyes PM546, PM567 and PM650 were purchased from Radiant Dyes with a purity of at least 99 %. BDP and 8-PhPM were synthesized by Dr. Alexander Schmitt in the group of Prof. jr. Dr. Gregor Jung (Biophysikalische Chemie, Universität des Saarlandes) and had a purity of at least 95 %. FPP was synthesized in our lab according to the literature [YDZ04] and was used after sublimation yielding a white sample.

3.2 Characterization of the Even Lavie Valve as Helium Droplet Source

This chapter gives a comprehensive characterization of the Even-Lavie valve as helium droplet source. The main results can also be found in ref. [PRD$^+$09].

3.2.1 Working Principle

A schematic and sectional drawing of the nozzle are shown in fig. 3.8 illustrating all technical details. At rest, the plunger (7) is pressed against the front gasket (11) by a return spring (5) and the applied gas pressure. A short high current pulse is then sent to the low inductance coil (8) and thus generates a magnetic field pulling back the plunger. After switching off the current the plunger is pushed back to its sealing position by the return spring and the pressure gradient. The current is generated by discharging a capacitor in the power supply (pulse driver). It can be monitored as a voltage pulse at the port 'output sample' (O.S.) of the driver. In the following this pulse will be referred to as the O.S.-signal. This voltage scales to the current sent to the valve and has the same temporal shape, in particular the same pulse duration. The applied current produces heat due to the finite resistance of the wires in the coil as will be discussed in various places.

The nozzle opening (13) is a stainless steel inlet located in the center of the copper front plate (12). (fig. 3.8) Thermal contact is only achieved by the contact of the metal surfaces, but no grease is applied to avoid possible clogging of the orifice or doping the droplets with impurities. The nozzle is located in an adapter made of copper described above and thermal contact between the nozzle and the adapter is achieved by squeezing the adapter and applying Apiezon N grease.
The diameter of the orifice of the front gasket ((11) in fig. 3.8) can be chosen smaller than the orifice of the nozzle inlet (13) itself and thus determines the orifice of the valve. The valve is a modification of a well established pulsed nozzle used for the generation of cold supersonic beams. [EJN$^+$00] Key points in the design of the cryogenic valve are a miniaturization of the moving and static parts, a high precision guidance of the moving plunger, and compensation of thermal contractions. A more detailed description of the technical details can be found in refs. [PRD$^+$09, noz]. This leads to the possibility of providing a highly reliable valve with a low energy dissipation for each pulse and a short opening time of about 20 μs and thus a low gas load. These conditions are prerequisite for using the valve as pulsed source for a helium droplet beam, in particular at high repetition rates.
In the following the performance of the Even-Lavie valve for the production of a pul-

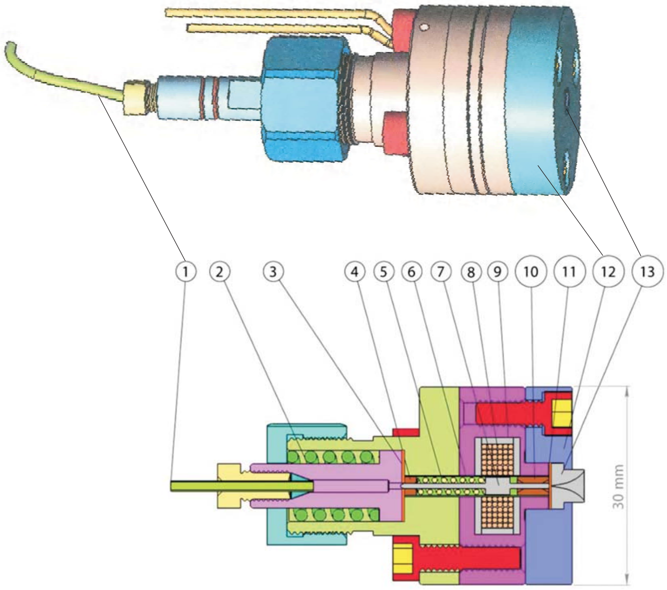

Fig. 3.8: Pulsed valve components. (1)stainless steel gas inlet tube. (2) Tightening spring and pressure relief valve. (3) Kapton foil gasket. (4) Ceramic (Zirconia) guiding ferrule. (5) Return spring. (6) Thin-walled pressure vessel (Zirconia). (7) Reciprocating plunger (magnetic stainless steel alloy). (8) Kapton insulated copper coil. (9) Permendure magnetic shield and field concentrator. (10) Zirconia guiding ferrule. (11) Kapton foil gasket. (12) Front flange and valve body (copper). (13) Conical (or trumpet) shape expansion nozzle (hardened stainless steel). Figure taken from ref. [PRD$^+$09]. A picture of the nozzle assembled inside the apparatus can be found in fig.3.2.

sed helium droplet beam is described. For the characterization mainly time profiles and their dependence on the experimental parameters such as the height and width of the driving current pulse, stagnation conditions, and repetition rate will be discussed for the undoped and doped droplet beam. These parameters are not independent from each other and thus the dependence on each parameter was recorded for various settings of the others. Other experimental parameters important for the overall performance of the pulsed droplet machine, e.g. the skimmer and the distance between the skimmer and the nozzle were discussed already. The data presented in the following are recorded with the latest modifications of the valve carried out on 14.04.2008. In particular, the nozzle opening is conically shaped with an opening angle of 110° and an exit diameter of 100 μm, while the front gasket (fig. 3.8(11)) has a hole of only 60 μm in diameter. The results are discussed and compared with respect to other nozzle configurations, e.g. different shapes of the nozzle opening, a continuous droplet beam and also a General Valve nozzle used as a pulsed helium droplet source in the literature [GEA02, SKMV02, YBE05, YBWE05, YBWE06, YBN$^+$07, YE08] at the end of the chapter.

3.2.2 Undoped Droplets

Undoped droplets were probed by recording the Rayleigh-scattering of the UV-radiation of the cw Ar^+-ion laser. Rayleigh scattering describes the scattering of light by particles much smaller than the wavelength of the incident light. [Cha07] The Rayleigh scattering signal R(λ) obtained upon irradiation of a sphere with electromagnetic radiation of intensity I(λ) is given by [BMB+93]

$$R(\lambda) = \beta I(\lambda) N \sigma \tag{3.2}$$

wherein β is a proportionality constant depending on the individual experimental conditions like the geometry of detection or the detection yield of the PMT, N is the number of scattering particles, i.e. in the present case the helium droplets, and σ is the cross section for the scattering. With

$$\sigma \propto \frac{r^6}{\lambda^4} \tag{3.3}$$

for r $<$ 0.05 λ wherein r is the radius of the scattering sphere and λ the wavelength of the incident radiation one obtains

$$\frac{R(\lambda)}{I(\lambda)} \propto N \frac{r^6}{\lambda^4}. \tag{3.4}$$

Equ. 3.4 gives the relation between the intensity of the Rayleigh scattering signal normalized to the intensity of the incident radiation and the number (N) and size (r^6) of the droplets for a given wavelength. Time profiles used to be recorded for an incident laser power of 5 mW and with the same PMT (H5783P) without an edge filter.

3.2.2.1 Driving Force and Pulse Duration

The current pulse sent to the nozzle can be varied by changing the voltage of the capacitor in the power supply (pulse driver) which can be directly measured. By varying the current the induced magnetic field pulling back the plunger against the recoil spring and the pressure gradient between the applied stagnation pressure and the pressure in the vacuum chamber is altered. Thus, the current determines the force applied to the plunger and hence the distance it is pulled back. As will be discussed below, Rayleigh signal is optimized for lowest nozzle temperature and highest stagnetion pressure. In fig. 3.9 time profiles for various driving forces are illustrated for a repetition rate of 10 Hz (a) and 100 Hz (b). The stagnation pressure is 80 bar and the nozzle is cooled to the lowest temperature achieved under the corresponding operation conditions. Voltages and temperatures are as indicated in fig. 3.9.

For a voltage below 16 V no signal is obtained and the constant pressure in the vacuum

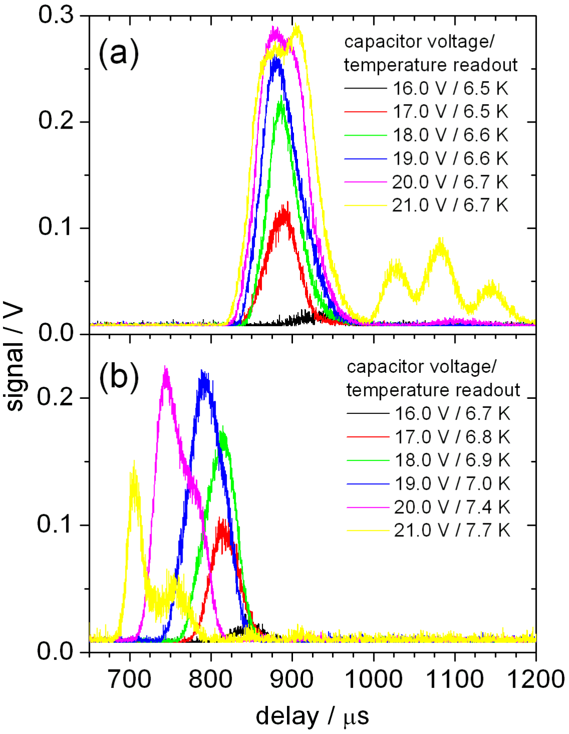

Fig. 3.9: Time profiles of Rayleigh scattering for a stagnation pressure of 80 bar at lowest nozzle temperatures operating the valve at 10 Hz (a) and 100 Hz (b) applying different driving currents.

chambers is given by the base pressures indicating a constantly closed valve. Thus, below 16 V the electromagnetic force does not suffice to open the valve. For a repetition rate of 10 Hz (fig. 3.9 (a)) the peak intensity of the Rayleigh signal rises with increasing voltage up to about 20.0 V due to the larger gas loads. Thereby, the width of the time profile is broadened and the signal is slightly shifted to earlier times. For voltages exceeding 20.0 V secondary pulses appear. Under these conditions the plunger is pulled back so far that it recoils from the gasket when it returns to its sealing position. The recoil causes additional throughput of gas and thus production of helium droplets. The leading peak does not gain in peak intensity if currents causing already secondary pulses are applied. For a repetition rate of 100 Hz (fig. 3.9 (b)) the peak intensity and the width of the time profiles also increase up to a voltage of almost 20.0 V identical as for 10 Hz operation. For voltages between 19 and 20 V the way the plunger is pulled back is optimized to provide a large enough amount of gas required for the formation of droplets but at the same time secondary pulses are avoided. However, at a repetition rate of 100 Hz the droplet pulses appear earlier than at 10 Hz under otherwise identical conditions and the sensitivity of the delay time on the voltage is significantly increased. Moreover, the nozzle temperature rises much more upon increasing the voltage as compared to the 10 Hz conditions. As will discussed below, earlier signals are caused by a higher effective nozzle temperature increasing the kinetic energy of the droplets. Thus, the shift in time can be explained by an increased heat production by the valve operated with higher driving currents. Obviously, the nozzle produces more heat at elevated repetition rates and thus the signal is more sensible on changes in the driving current recorded at 100 Hz than at 10 Hz.

The appearance of secondary pulses is a gradual process: With increasing voltage the peak first gets broader (19.0 V, 100 Hz) then a shoulder grows in (20.0 V, 100 Hz) and finally separate pulses (21.0 V, 100 Hz) appear. In general, secondary pulses appear rather at low nozzle temperatures and low stagnation pressures. The former is presumably due to the increasing stiffness of the sealing gasket upon lowering the temperature rendering the plunger to recoil instead of damping its motion. A higher stagnation pressure damps the recoil.

The width of the current pulse from the power supply to the nozzle was set internally to 20 μs in all experiments described above and could be monitored by the O.S.-signal from the power supply. A different operation mode of the power supply allows for tuning of the width via the width of an external trigger pulse. However, for the power supply used only pulse widths $\leq$ 20 μs can be set. In order to keep a constant flux of helium smaller pulse widths require larger currents to operate the valve. Trigger pulses with widths of 15 and 20 μs (a), resulting O.S.-signals (b) and time profiles (c) are shown in fig. 3.10. The width of the O.S.-signals is not exactly the width of the trigger pulses though it qualitatively decreases when shorter trigger pulses are applied. In contrast, the corresponding droplet pulses (time profiles) show almost identical widths and profiles. Though, the time profile recorded for the 15 μs trigger pulse appears somewhat earlier due to the larger driving force again leading to a slight increase of the effective nozzle temperature. The duration of the current pulse has little effect on the gas pulse duration which is determined by the mechanical constants of the plunger mass, spring constant, and plunger movement amplitude.

The width of the current pulse is set to the maximum value of 20 μs for all experiments described within this work if not denoted otherwise. Longer pulse widths of the current would allow to reduce the driving current and thus to decrease the heat produced by the valve. This is of importance to obtain a pulsed helium droplet beam with high repetition rate.

3.2.2.2 Stagnation Conditions

To obtain information on the dependence of droplet formation on the stagnation conditions, time profiles were recorded for different nozzle temperatures and stagnation pressures. For better comparison of the droplet formation, the signals were recorded for a constant gas flux. Variations of the flux caused by changes in the stagnation conditions

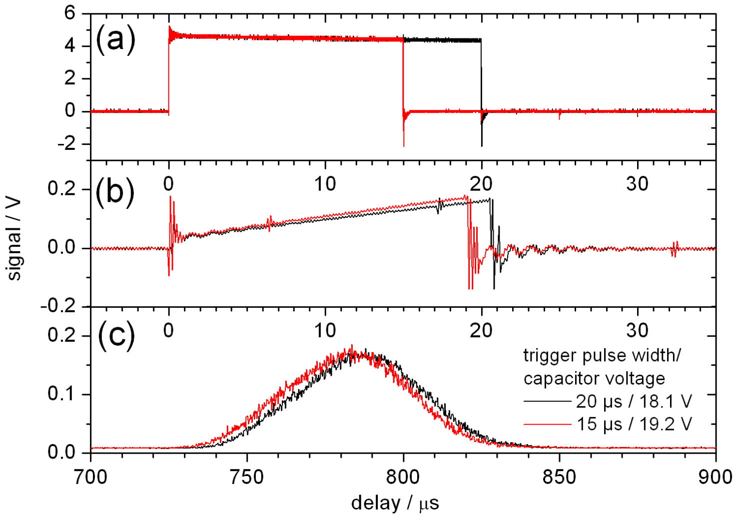

Fig. 3.10: Trigger pulses (a) sent to the power supply, corresponding output samples (b) and time profiles (c) with different time scales of the delay. The nozzle was running at 100 Hz at the lowest temperature possible (6.9 K readout in both cases). The stagnation pressure is 80 bar and the helium flux is equal for both settings achieved by different driving currents.

were compensated by adjusting the driving current. Gas flow was monitored by reading the pressure in the source chamber as described in chapter 3.1.6.

Fig. 3.11 shows time profiles with the nozzle running at 10 Hz (a) and at 100 Hz (b) for stagnation pressures starting with 10 bar up to 100 bar (bottom to top). For each stagnation pressure the time profiles were recorded for different nozzle temperatures as indicated by the different colors. By comparing the time profiles of the same color (but in different lines) the signal dependence on the stagnation pressure for a constant nozzle temperature can readily be seen: With increasing pressure and constant temperature the signal increases and appears earlier in time. The increasing intensity reflects the pressure dependence of the helium condensation in the expansion. It is due to either an increasing number or an increasing size of the droplets. The changes in the arrival time reflect the pressure dependence of the velocity of the droplets in the beam. Comparing the time profiles for a constant pressure but different temperatures (different colors in one line) illustrates the temperature dependence: With increasing temperature and constant pressure the signal decreases and appears earlier. The former supports the expected temperature effect for cluster formation (by condensation or fragmentation). The latter is due to an increase of the droplet velocity which was determined to 250 - 410 m/s. (cf. 3.1.2).

Fig. 3.11 reveals that the Rayleigh signal increases with increasing stagnation pressure and decreasing nozzle temperature. However, depending on the nozzle temperature, the Rayleigh signal reaches its maximum at a stagnation pressure much lower than 100 bar.

Therefore, a higher nozzle temperature can be compensated (at least to some extent) by increasing the stagnation pressure.
Qualitatively, the same dependencies as obtained from the data as shown in fig. 3.11 were obtained for other gas fluxes and repetition rates.

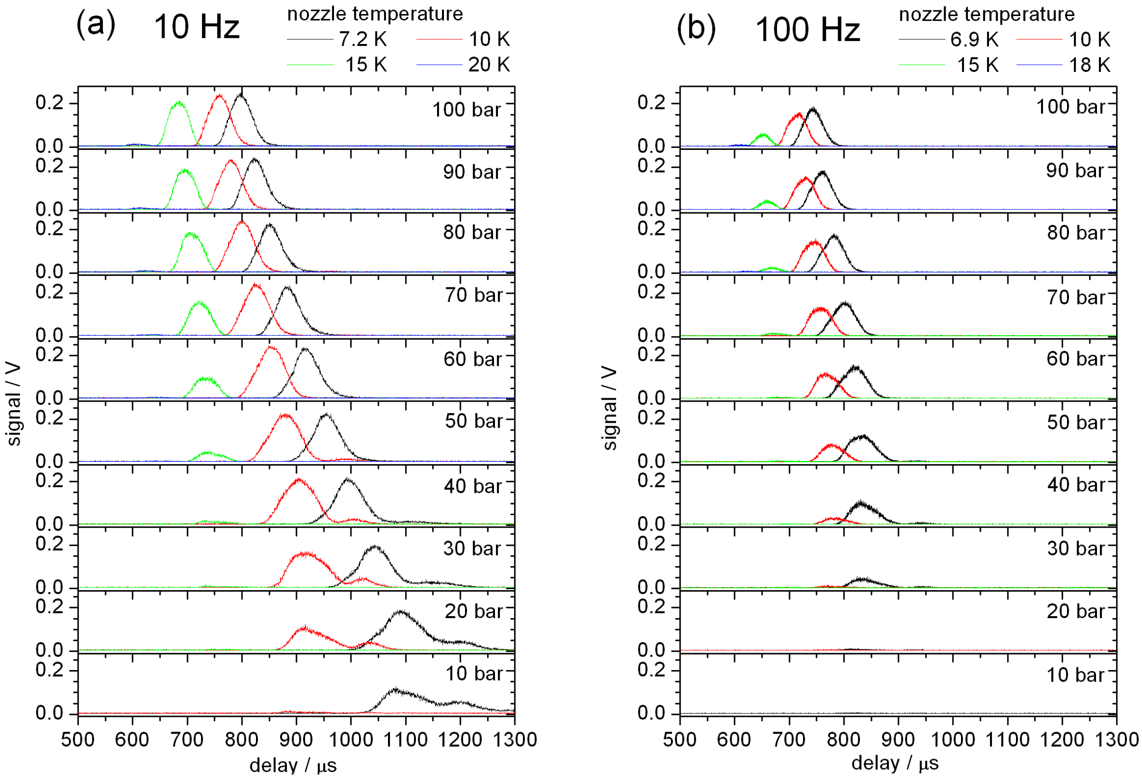

Fig. 3.11: Time profiles of the undoped helium droplet pulse recorded via Rayleigh scattering with the nozzle operating at 10 Hz (a) and 100 Hz (b). Helium stagnation pressure and nozzle temperature were varied as indicated, while the gas flux was kept constant. All signal axis have the same scaling and can be quantitatively be compared. The distance to the 6 mm skimmer was 4.8 cm.

3.2.2.3 Repetition Rate

A comparison of the two data sets (a) and (b) in fig. 3.11 reveals the influence of the repetition rate on the Rayleigh signal. For equal stagnation conditions, the signal decreases and appears earlier in time by increasing the repetition rate. Both observations are consistent with an increase of the effective nozzle temperature reducing the efficiency of droplet formation and increasing the droplet velocity. This interpretation is confirmed by an additional series of time profiles shown in fig. 3.12 recorded for different repetition rates from 10 Hz up to 400 Hz. The top panel contains the profiles for the lowest (effective) nozzle temperature accessible at the respective repetition rate. These time profiles can perfectly be reproduced by operating the nozzle at a repetition rate of only 10 Hz while heating the valve to a temperature as indicated in the lower panels of fig. 3.12. The nozzle temperature measured for the different repetition rates increases from 6.5 K at 10 Hz to almost 7.8 K at 400 Hz. Though, this temperature is the dynamic equilibrium temperature at the position of the thermal sensor (nozzle temperature). The real source temperature (effective nozzle temperature) for the expansion is higher and is expected to be slightly higher than the values set for the respective 10 Hz operation. For example, at 300 Hz the effective nozzle temperature is about 17 K (fig. 3.12). This result proves that the changes in the Rayleigh signal upon increasing the repetition rate is of purely thermal origin and reflects the rising heat intake by the entire system. Most important, the repetition rate is not limited by the pump capacity, though for a repetition rate of 400 Hz the pressure rises up to $9{\times}10^{-5}$ mbar and almost $7{\times}10^{-6}$ mbar in the first and second chamber, respectively. As was discussed in the preceding chapter 3.2.2.2 efficient droplet formation at increased effective nozzle temperatures requires higher stagnation pressures. Therefore, high stagnation pressures are required when the nozzle is operated with high repetition rates.

Additionally, the heating of the nozzle by operating it with high repetition rates can be evidenced as follows: Keeping the nozzle closed for a couple of time by switching off the driver, the system is cooled down to the lowest temperature of about 6.5 K. When starting the nozzle at 400 Hz, for the first few pulses the time profile shows an intense and slow droplet pulse similar as obtained at 10 Hz operation. Within about 5 s (2000 pulses) the signal decreases in intensity, appears earlier and finally merges to the time profile for 400 Hz operation shown at the bottom of fig. 3.12. In between, the signal passes through the different stages shown in the upper panel of fig. 3.12. Simultaneously, the nozzle temperature rises to the equilibrium temperature of 7.8 K corresponding to an effective nozzle temperature of about 19 K.

The thermal load of the system depends not only on the repetition rate but also on the driving current. Therefore, the driving current was varied in order to optimize the Rayleigh signal. For repetition rates less than 200 Hz a capacitor voltage of about 19 V was optimum.(cf. chapter 3.2.2.1) In contrast, a reduced driving current could improve the signal at repetition rates above 200 Hz. However, the reduced driving current not only reduces the heat intake but also the gas flux. Thus, the reduction of the driving current is a compromise and signal intensities obtained at elevated repetition rates with lowered driving current are lower than at repetition rates below 200 Hz with a capacitor voltage of 19 V.

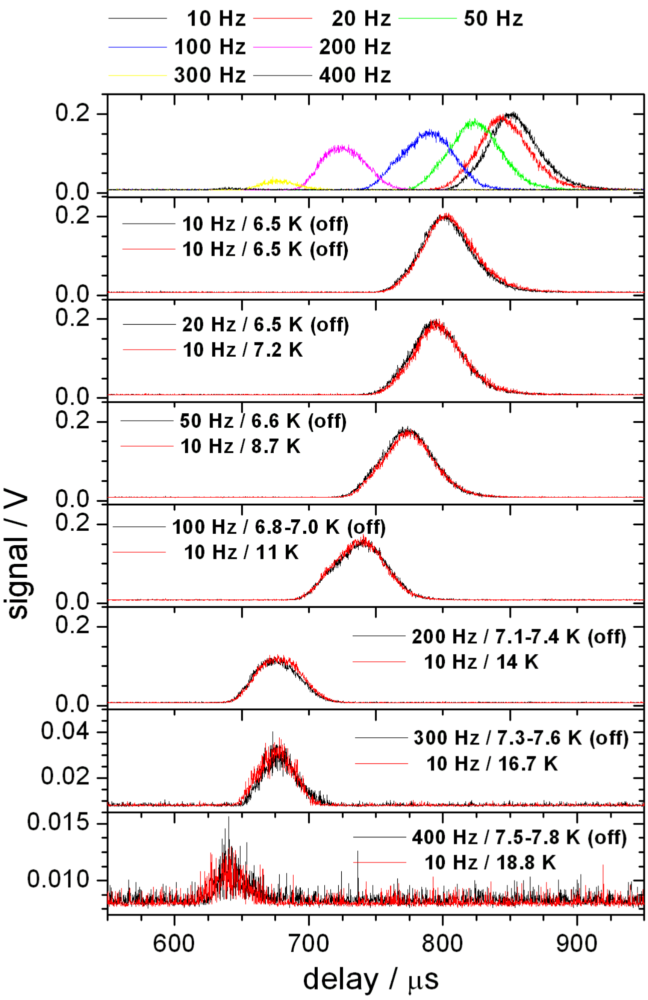

Fig. 3.12: Time profiles of the undoped droplet pulse recorded via Rayleigh scattering for different repetition rates. Top panel: profile series measured for 80 bar at repetition rates of 10, 20, 50, 100, 200, 300, and 400 Hz each recorded at the lowest achievable temperature. Lower panels: same time profiles (black) and the corresponding temperature readouts and in addition the profiles reproduced for 10 Hz operation with additional heating of the system as indicated. The two profiles at 10 Hz illustrates the reproducibility. off designates no additional heating. All panels except the lowest two have the same scaling.

3.2.3 Doped Droplets

The doped droplet pulses were probed by recording the LIF-signal of phthalocyanine (Pc) inside the droplets excited with the cw dye laser. Phthalocyanine is chosen as probe for the droplets since it has a high fluorescence quantum yield and its spectroscopy in helium droplets is well investigated [DS01, SDHT01, HLTV02, LS03, LSK$^+$04, LS04a, LS04b, WHKW05, LSS07]. The resonance frequencies and the peculiar emission behavior of Pc (as well as the spectroscopic features of all other molecules) found in the pulsed beam match with the findings in the continuous droplet beam.

When signals of doped droplets are compared, it has to be considered that they depend not only on the various parameters concerning the droplet formation, but also on the additional doping process. The droplet formation and doping via pick-up are not independent from each other, e.g. larger droplets require a lower particle density in the pick-up cell for single particle doping due to their larger pick-up cross section. Therefore, the efficiency of droplet formation can be determined only by varying the conditions for droplet formation (stagnation conditions and repetition rate) and in addition the pick-up conditions (particle density).

All time profiles and excitation spectra were recorded with the PMTs H5783P, H5783-20 or R 943-02 (all Hamamatsu) without a cut-off filter. Within each series of time profiles the laser power was kept constant.

3.2.3.1 Driving Force and Pulse Duration

As described for probing the undoped droplet pulse via Rayleigh scattering the driving current for the nozzle was also altered probing the doped droplet beam. However, at stagnation conditions optimized for Rayleigh signal LIF-signal is only weak as will be discussed in chapter 3.2.3.2. In fig. 3.13 time profiles for various driving forces are illustrated for typical LIF conditions with a stagnation pressure of 80 bar and a nozzle temperature set to 21 K with the nozzle running at 50 Hz. As for the Rayleigh signal, the signal increases with rising driving currents and reaches its maximum for capacitor voltages in the range between 19 and 20 V. Additionally, the time profiles appear earlier when larger driving currents are applied due to the additional heating caused by the operating valve. A further increase of the capacitor voltage to even 25 V causes a decrease of the peak intensity because of the effective nozzle temperature exceeding the optimum temperature for the signal of singly doped droplets. The same dependence was found for all other repetition rates, though the effect of the heating is obviously less pronounced for lower rates.

Interestingly, no secondary pulses appear in fig. 3.13 even for the largest driving force. For the same capacitor voltages strong secondary pulses were found under the experimental conditions used to probe the undoped droplet beam.(cf. fig. 3.9) Secondary pulses do appear in LIF time profiles for capacitor voltages beyond 20 V for nozzle temperatures below 15 K. Thus, the missing of secondary pulses in fig. 3.13 is attributed to the elevated temperature and is presumably a consequence of the temperature dependence of the stiffness of the front gasket. At lowest temperature it is expected to be more stiff causing the plunger to recoil, whereas at elevated temperatures the plunger motion is damped.

The width of the current pulse from the nozzle driver was also varied as in the experiments probing the undoped droplet beam. (cf. chapter 3.2.2.1) As was described

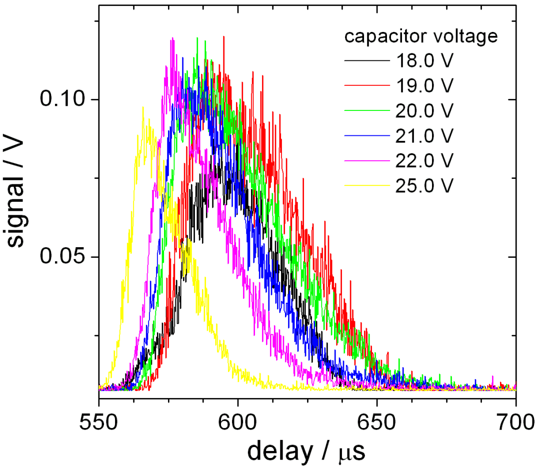

Fig. 3.13: Time profiles of LIF of Pc for a stagnation pressure of 80 bar with a nozzle temperature of 21 K operating the nozzle with 50 Hz with different driving currents. The sample temperature amounts to 618 K.

there, the width could only be reduced and thus a larger capacitor voltage was required to operate the valve. This leads to an increased heat intake reflected by a shift of the droplet signal to earlier times.

3.2.3.2 Stagnation Conditons

Similar as for the characterization of the undoped droplet beam, the doped droplet beam was probed at various stagnation pressures and nozzle temperatures while keeping the helium flux constant.(fig. 3.14) The cw dye laser was tuned to the known frequency of the electronic origin of single Pc in helium droplets. [SDHT01] The cw dye laser induces LIF but also Rayleigh signals. Both signals contribute to the time profiles recorded with a resonant laser whereas exclusively Rayleigh scattering is observed with a non resonant laser. The excitation spectrum of Pc is shown in fig. 3.16 and the respective settings of the dye laser for the time profiles were 15088.92 cm^{-1} (on resonance) and 15088.5 cm^{-1} (off resonance). The Rayleigh scattering recorded with the dye laser is weaker than with the UV-Ar^{+} laser due to its wavelength dependence though the signal shows the identical behavior as the undoped droplet beam.

Fig. 3.14 shows the time profiles with the nozzle running at repetition rates of 20 Hz (a) and 100 Hz (b) for stagnation pressures of 10 bar up to 100 bar (bottom to top). For each stagnation pressure the time profiles were recorded for different temperatures as indicated by the different colors. The LIF signal is represented by the difference of the corresponding time profiles with the laser on and off the resonance. In general, the effect of the expansion parameters on the temporal appearance of the signal is qualitatively identical to the observations for undoped droplets and can be attributed to changes of the droplet velocity. However, conditions favorable for the LIF signal appeared at temperatures much higher than those for the Rayleigh signal. Below a certain temperature (which is significantly higher than the temperature for the optimum Rayleigh signal at the same pressure), the LIF signal is hardly observable. Upon heating of the system the LIF first increases, reaches a maximum, and finally disappears again. Only within a temperature range of about 10 K a reasonable LIF signal was observable, and the temperature for maximum LIF signal increases with increasing pressure.

The dependence of the LIF signal recorded at different repetition rates (fig. 3.14) shows qualitatively the same behavior. Increasing the repetition rate causes an additional heat intake produced by the solenoid (cf. chapter 3.2.3.4) and thus for a respective stagnation pressure optimum LIF-signal is obtained at lower nozzle temperatures though corresponding to the same effective nozzle temperature.

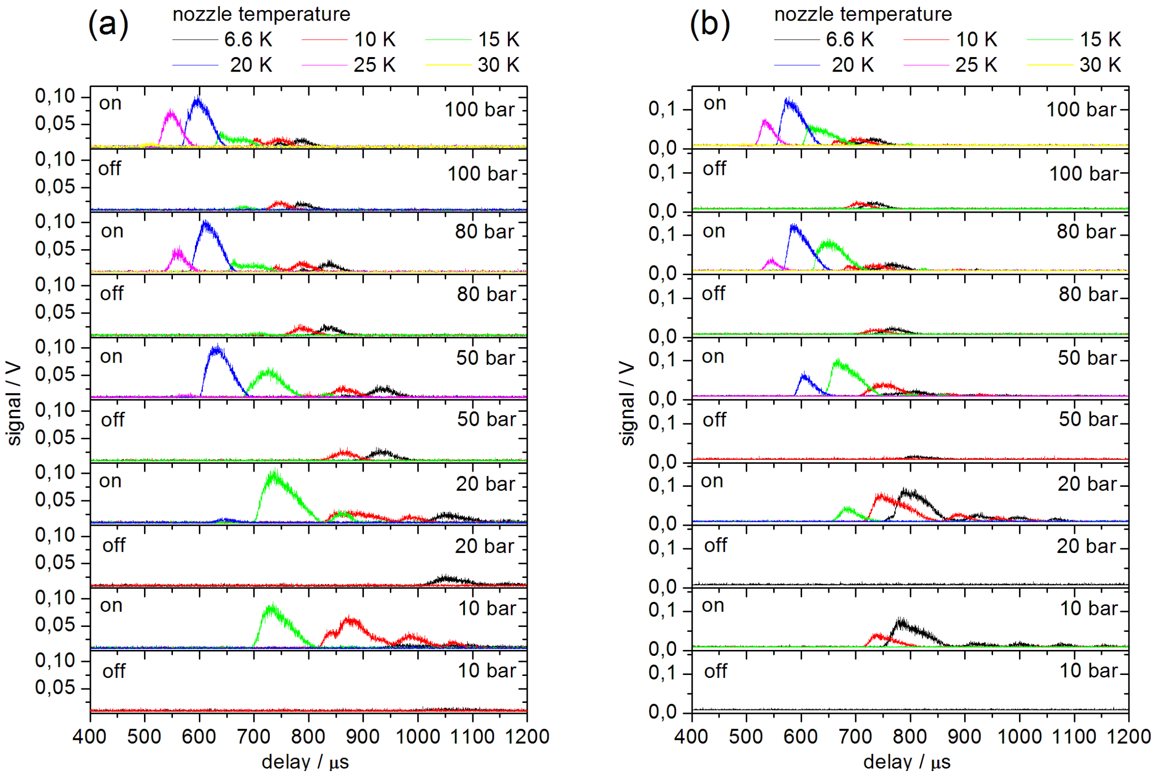

Fig. 3.14: Time profiles of the doped helium droplet pulse recorded with the cw dye laser tuned on and off the resonance (on/off) with single Pc with the nozzle operating at 20 Hz (a) and 100 Hz (b). Helium gas pressure and nozzle temperature were varied as indicated, while the gas flux was kept constant. The signals for each repetition rate can be compared quantitatively though the series of different repetition rates cannot due to different laser intensities. The influence of the repetition rate is quantitatively discussed below. The sample temperature was 598 K in all experiments.

When doped droplets are probed the additional parameters of the pick-up process have to be considered which are entangled with the parameters of the droplet formation such as stagnation conditions and repetition rate. The sample temperature and thus the particle density in the pick-up cell was chosen well below the optimum for the LIF signal for a stagnation pressure of 80 bar and a repetition rate of 100 Hz to ensure that the signal of single doped droplets is not limited by multiple doping. The dependence of the LIF signal on the stagnation conditions were also recorded for different sample temperatures leading to the same qualitative dependence as shown in fig. 3.14. Variation of the particle density also has only a minor effect on the line shape of the electronic origin of Pc.(fig.3.17)

The dependence of the LIF signal on the stagnation conditions was further determined for different fluxes of helium gas. As for the different repetition rates and sample temperatures, the LIF-signals recorded for different fluxes showed qualitatively the same dependence on the stagnation conditions as in fig. 3.14. Thus, the dependence of the LIF-signal on the stagnation conditions reflects the efficiency of the formation of droplets that can be doped. Though, the shape of the time profiles depends on the repetition rate and (in particular at low repetition rates) on the sample pressure.

The discrepancy between the optimum stagnation conditions for the Rayleigh and the LIF signal becomes evident by comparing the time profiles with the laser on and off resonance as shown in fig. 3.15. The time profiles are taken from fig. 3.14(b) for a stagnation pressure of 80 bar and nozzle temperatures as indicated. Thus, stagnation conditions were optimum for the Rayleigh signal. The time profiles with the dye laser off resonance show a single peak which also appears when tuning the laser on resonance. However, in the latter case an additional leading peak appears. With increasing temperature the intensity of this leading peak increases while the slower component disappears gradually. Moreover, only the slow component remains when switching off the doping process. Obviously, the slow component is due to Rayleigh scattering of undoped droplets, and only the leading peak is the LIF signal of Pc doped into helium droplets. The variation of the pick up conditions by any means, in particular lowering the sample pressure, did not lead to additional LIF within the time domain of the Rayleigh signal. In other words, it was not possible to singly dope (a sufficient number of) the droplets responsible for the Rayleigh signal.

Under conditions optimized for LIF the Rayleigh signal is usually negligible. Though, when working in the UV without a cut-off filter it can be significant, especially for intense laser radiation (pulsed laser) and at the same time weak fluorescence signals.

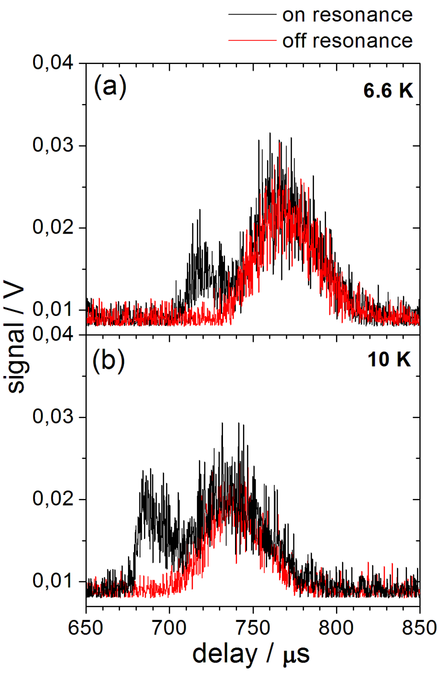

Fig. 3.15: Time profiles of the doped droplet beam while operating under ideal conditions for Rayleigh signal with the dye laser once on (red) and off (black) with the resonance of single Pc. The four time profiles were recorded with the same laser intensity and can quantitatively be compared and are taken from 3.14.

3.2.3.3 Droplet Size and Size Distribution

The quantitative different temperature and time dependence of the Rayleigh and LIF signals discussed in the previous chapter 3.2.3.2 provide evidence for a bimodal size distribution. Helium clusters probed via Rayleigh scattering have a lower velocity, a larger cross section for Rayleigh scattering, and under the stagnation conditions for optimum Rayleigh signal larger clusters are expected to be formed. Therefore, it can be concluded that the Rayleigh signal is generated by larger droplets, while the LIF signal stems from a leading fraction of smaller droplets, which are therefore much less sensitive to Rayleigh scattering. The relative abundance of the two kinds of droplets depends on the stagnation conditions.

The average size and size distribution of the smaller dopable droplets is of special interest for the evaluation of spectroscopic data and to evaluate the applicability of the pulsed droplet beam for different experimental (e.g. spectroscopic) methods. Therefore, the line shape at the electronic origin of single Pc was recorded and compared to data known from the continuous droplet beam. [DS01] The excitation spectra were recorded using the cw dye laser because the line width of the transition is in the order of the line width of the pulsed dye lasers and the observed shift is smaller than the mechanical reproducibility of the wavelength settings of the pulsed dye lasers.

The line shape at the electronic origin in the excitation spectrum of Pc in droplets for-

med in the continuous expansion strongly depends on the stagnation conditions. [DS01, SDHT01, LSK$^+$04] For droplets formed via subcritical expansion of helium gas an inhomogeneous asymmetric line shape with a steep rise at the red side and an extending tail on the blue side is observed. (cf. fig. 3.16(a), dotted line) For stagnation conditions leading to an increased cluster size the asymmetry gradually decreases and the peak position shifts towards the steeply rising edge, i.e. to the red. For a supercritical continuous expansion the line shape is observed to collapse to a very narrow double peak structure which could be fitted with the envelope of the rotational fine structure of Pc. [LSK$^+$04] (fig. 3.16(b), dotted line) Further, the peak position is slightly shifted to the blue by about 0.05 cm^{-1} from the maximum red shift. (fig. 3.16(b) and (c), dotted lines) The change in the line shape reflects the vanishing of the inhomogeneous line broadening due to the droplet size distribution present for subcritical expansions ($< 10^5$ He atoms per droplet) when approaching the bulk limit for droplets larger than $\approx 10^6$ He atoms.
The asymmetric line shape observed for subcritical expansions can be explained by a theoretical model taking into account the known cluster size distribution in the continuous droplet beam, the size dependent capture cross section for the doping, the shrinking of the droplet size upon doping, and a phenomenological description of the size dependent resonance frequency of the molecular transition. [DS01, SDHT01] Therein, the line shape in helium droplets is treated in analogy to the line shape in other environments and is thus described by a convolution of a homogeneous line shape at a center frequency with an inhomogeneous distribution of these center frequencies depending on the size of the doped droplets. The size distribution of the droplets formed in the continuous expansion was experimentally determined in scattering experiments and is given by a log-normal distribution. [LST93] The probability of doping clusters of a given size by the pick-up technique is described by a Poisson distribution [LST95].(cf. chapter 2) The center frequency is determined by short range repulsive and long range attractive interactions between the dopant and the helium surrounding. These interactions are different for the dopant molecule in the ground and excited state. Thus, the frequency shift reflects the differences in the two contributions in the ground and the excited state. The frequency shift of molecular transitions in clusters is described by the excluded-volume model [Jor92] as discussed in the following. The total shift ν given by

$$\nu = \nu_s + \nu_l \tag{3.5}$$

with ν_s and ν_l as the shifts due to the changes in the short and long range interaction upon excitation, respectively. The dopant is assumed to be located at the center of the droplet. Thus, shifts of the center frequency induced by changes in the droplet size are due to changes in the interaction with the helium atoms which are farthest away from the dopant. [DS01] For radial dependencies as described by the Lennard-Jones or Buckingham potential the repulsive interaction becomes constant already at distances of a third helium layer. Thus, for typical droplet sizes used in electronic spectroscopy and assuming radial dependencies as described by these potentials the repulsive interaction can be considered as a constant contribution to the transition frequency and only the long range contribution depends on the droplet size. As discussed in ref. [DS01], for these potentials ν_l can be assumed as

$$\nu_l = \nu_l^{\infty}(1 - \frac{N_a}{N_b}) \tag{3.6}$$

with ν_l^{∞} denoting the shift solely due to the attractive interaction in the bulk limit (infinite cluster size), and N_a and N_b as the number of helium atoms in a sphere with radius r_a and r_b, respectively. N_a is a measure for the size of the cave of the embedded molecule inside the droplet (excluded volume) and N_b is a measure for the size of the doped droplet. Since N_a is constant for a certain molecule, equ. 3.6 describes a monotonic shift of the transition frequency with increasing droplet size.
For droplets formed via subcritical expansion the transition frequency was found to be shifted by up to 43.0 cm^{-1} to the red compared to the unperturbed molecule in the gas phase. [FWL78, FHL80] The shift increases with increasing droplet size and the described model is able to fit the varying line shape. [DS01] However, for Pc doped into droplets formed via supercritical expansion the transition frequency is slightly less shifted to the red. [LSK$^+$04] This can be found in fig. 3.16 (a) and (b) by comparing the dotted spectra. The electronic origin of Pc in the larger droplets formed via supercritical expansion (fig. 3.16(b)) is shifted to the blue compared to the peak position of the origin of Pc doped into droplets formed via subcritical expansion. (fig. 3.16(a)) According to the described model the asymmetric blue tail in the spectrum of Pc in helium droplets formed via subcritical expansion is attributed to smaller droplets than at the peak position. [DS01] The transition frequency of Pc thus reveals a non-monotonic dependence on the droplet size which is not included in the described model and which is not yet understood.

The electronic origin of Pc doped into the pulsed droplet beam was neither of pronounced asymmetric shape nor split into a double peak. (fig. 3.16) Neither the temperature nor the stagnation pressure was of significant influence on the line shape. Only the line position was slightly affected by the nozzle temperature (fig. (a) vs (b) and (c)) and the stagnation pressure (fig. (c) vs (d)). In fig. 3.16 (b) the spectra recorded in the pulsed and in the continuous beam coincide in the spectral position, though the double peak structure is not resolved in the pulsed beam. Therefore, at expansion conditions of 80 bar and 15 K, the solvent shift is not far below the bulk limit ($> 10^6$ atoms [LSK$^+$04]). Increasing the nozzle temperature slightly shifts the excitation spectrum to the red whereas the line width and line shape are hardly affected.(fig. 3.16 (a) vs (b)). In particular, the transitions do not show the asymmetric tail to the blue which is typical for the fraction of small droplets in a log-normal size distribution. The center frequency for stagnation conditions of 25 K, 80 bar in the pulsed expansion coincides with the peak position for conditions of 11 K, 20 bar in the continuous expansion. (fig. 3.16(a)) However, decreasing the nozzle temperature in the pulsed expansion decreases the red shift(fig. 3.16 (a) → (b)) whereas it increases the red shift of the peak position in the continuous expansion [DS01]. This indicates that the smallest droplet sizes formed in the pulsed expansion are larger than the largest droplets formed (and doped) in the subcritical continuous expansion. Therefore, from the peak position only a lower limit of the droplet size in the pulsed beam can be estimated to about 10^4 He atoms per droplet.

For the expansion conditions of 15 K, 80 bar in fig. 3.16(b) in the continuous expansion a similar log-normal size distribution, or even a more broad distribution, respectively, would be expected than for 11 K, 20 bar. (cf. fig.2.3 in chapter 2) Thus, under these conditions a similar asymmetric line shape as observed in the continuous beam (fig. 3.16(a)) would be expected. In the case of 15 K, 20 bar (fig. 3.16(c)) an even more pronounced asymmetric line shape would be expected for a log-normal distribution. The qualitative different frequency shifts upon changing the nozzle temperature and the different line shapes (missing of the asymmetric tail) therefore provide evidence for a different size distribution in the pulsed beam than in the continuous droplet beam formed via subcritical expansion.

From the comparison of the peak positions and the monotonic decrease of the red shift upon lowering the nozzle temperature it can be concluded that the size of the droplets formed in the pulsed expansion can be varied in the range from more than 10^4 to less than 10^6 He atoms per droplet depending on the stagnation conditions. The analysis of the line shape leads to the conclusion that no droplets smaller than about 10^4 He atoms per droplet are doped. Droplets smaller than 10^4 He atoms per droplet do not contribute to the signal independent of the particle density in the pick-up cell (see below) thus indicating that they are not (efficiently) formed in the expansion.

As shown in 3.16(d) the line shapes can be fitted with a Gaussian function with a FWHM of 0.064 cm^{-1} to 0.073 cm^{-1} increasing with temperature. The width is close to the full width of the double peak spectrum observed for Pc doped into droplets formed in supercritical continuous expansion (fig.3.16(b) [LSK$^+$04]. This double peak structure was attributed to the rotational contour of Pc in He droplets thus reflecting the homogeneous line shape in the bulk limit. [LSK$^+$04] Therefore, the fitted Gaussian functions do not only reflect the distribution function of the droplet size.

The line shapes at the electronic origin shown in fig.3.16 are all recorded for the same particle density in the pick-up cell and thus reveal information on the size distribution of the droplets which are doped under these conditions. This is not necessarily equal to the full size distribution of the droplets formed in the expansion.

For the continuous beam the peak position is hardly affected, the line becomes broader

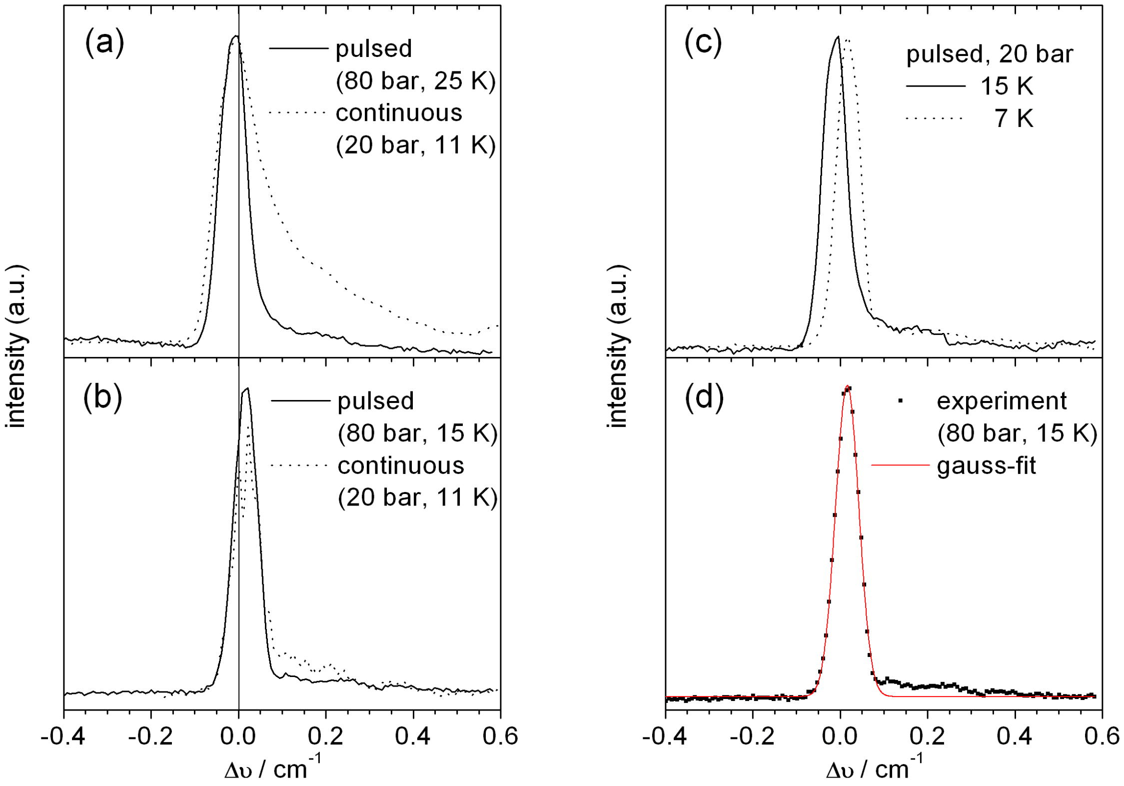

Fig. 3.16: Excitation spectra at the electronic origin of single Pc in helium droplets recorded for different expansion conditions shifted by 15088.92 cm^{-1} . This corresponds to a red shift of 42.9 cm^{-1} with respect to the gas phase. [FWL78, FHL80] Left: Comparison of spectra recorded in the continuous (dotted lines) and pulsed beam (full lines) at stagnation conditions as indicated. Right: Excitation spectra recorded in the pulsed beam for a stagnation pressure of 20 bar (c) and fit of a Gauss function to the excitation spectrum in the pulsed beam with 15 K, 80 bar (d).

and the intensity passes through a maximum for increasing particle density at constant expansion conditions. [DS01] These observations can be explained by the larger cross sections for the pick up of larger droplets: Starting with low particle density only the largest droplets within the size distribution of the generated droplets are doped. Increasing the particle density allows for doping also of smaller droplets wherein Pc exhibits a reduced red shift and thus leads to a broadening of the blue tail of the excitation spectrum at the electronic origin of Pc. At higher sample pressures also multiple doping occurs and thus the larger droplets contribute less to the signal of single doped droplets. The line shape of the electronic origin of Pc doped into the pulsed droplet beam was also measured for different particle densities (oven temperatures) as shown in fig. 3.17 (a) corresponding to particle densities from way below to far exceeding the optimum of single doping. Even within this large range, the line shape is hardly affected by the sample pressure which becomes especially clear by direct comparison of the two normalized spectra in the bottom panel of fig. 3.17. The line shape of the two spectra are

almost identical and a shift is hardly recognizable. This strongly indicates that no droplets smaller than about 10^4 He atoms per droplet can be doped even with high particle densities. This indicates that these droplets are not formed in the pulsed expansion.
Fig.3.17 (b) shows the time profiles of the doped droplet beam for the same particle densities as in fig.3.17(a). The bottom panel is again the direct comparison of the time profiles recorded for particle densities far below and exceeding the optimum of single doping. The time profile is hardly affected by the particle density thus indicating that droplets of the same velocity, i.e. the same size, are doped.
Both series of data reported in fig. 3.17 therefore provide evidence that by probing the line shape of the doped droplets information is obtained not only about the size distribution of the droplets which are doped at the respective particle density but about the size distribution of the droplets formed in the expansion at the respective stagnation conditions. Therefore, the analysis of figures 3.14 and 3.16 yields information on the efficiency and size distribution of the droplet formation at various stagnation conditions.

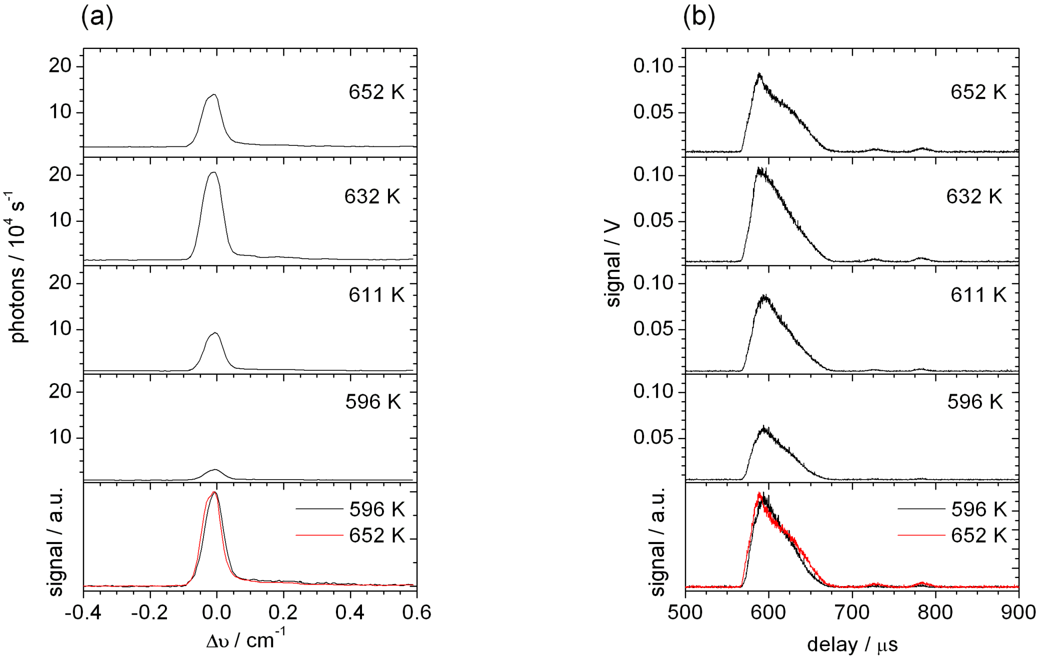

Fig. 3.17: Excitation spectrum of the electronic origin of single Pc in helium droplets (a) and time profiles of the doped droplet beam recorded for different oven temperatures as indicated with a repetition rate of 100 Hz, nozzle temperature of 20 K, stagnation pressure 80 bar.

As already mentioned, no signal of single Pc inside the large droplets causing the Rayleigh scattering could be found. Therefore, neither information about their absolute size, size distribution nor their phase is available. In particular, there is no direct experimental evidence for superfluidity. The dependencies of the Rayleigh signal on the expansion conditions may be due to a change of both size and number of helium droplets. For larger droplets the efficiency of evaporative cooling decreases due to the reduced surface to volume ratio. This might prevent cooling to the superfluid phase within typical flight times in droplet experiments. Assuming that in the expansion a larger droplet with a temperature of 4 K is initially formed and the evaporation energy per He atom amounts to 7 K, the evaporation rate has to be in the order of 10^8 s^{-1} to reach the desired 0.4 K within the flight time between the nozzle and the detection area (500 μs) for droplets of about 10^5 He atoms per droplet. The cooling rate scales linear with the final droplet size and according to ref. [BS90] the evaporative rate can be larger than 10^{13} s^{-1}. Therefore, even droplets up to a size of 10^{10} He atoms per droplet can be cooled to 0.4 K or at least to 2 K (onset of superfluidity) within 500 μs.

To conclude, the data presented in the preceding chapter and the line shape analysis provide evidence for a bimodal size distribution. The variation in the expansion conditions is of minor influence on the size distribution of the smaller dopable droplets but varies mainly the relative abundance of the two fractions in the droplet pulse. In particular, the smaller dopable droplets show no indication for forming size distributions as obtained in the supercritical continuous expansion even at low nozzle temperatures and high stagnation pressures. At the same time, at higher nozzle temperatures droplet formation becomes inefficient but does not gradually level out by forming smaller droplets as in the continuous beam. This sharp onset of droplet formation and almost invariance of droplet size on stagnation conditions without any indication for droplet sizes expected for supercritical continuous expansion was also found for other pulsed droplet sources. [SKMV02] The sharp onset may indicate a threshold for the droplet formation due to the lack of nucleation centers (small He clusters) in the expanding gas at elevated temperatures as suggested in ref. [SKMV02]. Slightly below the threshold temperature, the number of nucleation centers may be insufficient for the formation of many small droplets, and thus the few centers grow into large droplets in the following stages of the expansion. [SKMV02]
According to the phase diagram, expansions found to be optimum for the formation of droplets causing Rayleigh scattering start from the liquid phase, whereas expansions optimum for the formation of droplets that can be probed via LIF start from the gas phase. Interestingly, a bimodal size distribution was found also in the supercritical continuous expansion. [JN92]

The large size of the dopable droplets is well suited for high resolution electronic spectroscopy and for the study of large molecules or extended clusters in the droplets. Though, smaller droplets would be preferred e.g. for depletion methods. A possibility to vary the size would therefore be of special interest and will be discussed in chapter 3.2.5.

3.2.3.4 Repetition Rate

The dependence of the LIF-signal on the stagnation conditions was already discussed for repetition rates of 20 and 100 Hz (fig. 3.14) which show qualitatively the same behavior. The differences in the signal intensity and the delay of the signal can be ascribed to the additional heat intake produced by the operating valve which increases with increasing repetition rate.

Time profiles recorded via LIF for repetition rates from 10 to 500 Hz are shown in fig. 3.18 for a constant stagnation pressure of 80 bar and a constant oven temperature of 601 K. At 10 Hz the time profile is recorded for a nozzle temperature set to 20 K, which was found to create the maximum intensity of the LIF-signal. As discussed, increasing of the repetition rate raises the heat production of the valve. In order to maintain a comparable effective nozzle temperature the increased heat intake was compensated by lowering the nozzle temperature set at the controller so far that the leading edge of the time profile coincided for all repetition rates. (fig. 3.18) This procedure was applicable up to 400 Hz where the heater of the system had to be switched off entirely in order to achieve the coincidence of the rising edge of the time profile with the respective part of the 10 Hz profile. At higher repetition rates the signal appears earlier and with significantly reduced intensity. However, as shown for a repetition rate of 500 Hz (magenta) it is possible to optimize the signal by reducing the driving current for the nozzle. For repetition rates up to 400 Hz a reduced driving current was accompanied by reduced signal intensity due to a lower amount of expanded gas substantial for the droplet formation. (cf. chapter 3.2.3.1) Therefore, lowering the driving current is only a compromise that decreases the heat production by the valve but at the same time decreases the amount of helium for the droplet formation below the optimum.

As discussed already, the stagnation pressure optimized for efficient formation of dopable droplets is higher for higher (effective) nozzle temperatures and thus high stagnation pressures such as 80 bar are required when operating the valve with high repetition rates. A more efficient cooling of the nozzle and a further reduction of the heat intake, e.g. by longer but lower current pulses (cf. chapter 3.2.3.1), may help to run the nozzle with even higher repetition rates up to 1 kHz, which matches the repetition rate of many pulsed laser systems.

The time profiles shown in fig. 3.18 were recorded for a constant particle density in the pick-up cell. This might be an additional limiting factor for the signal recorded at high repetition rates. Therefore, the time profile with the nozzle running at 500 Hz was recorded also for a higher oven temperature. (fig. 3.19) However, the signal increases only slightly as is found within this temperature range also for 100 Hz operation. (cf. fig. 3.17) Thus, the decrease in peak intensity at repetition rates above 400 Hz is not due to a lack of sample or a change in the droplet size.

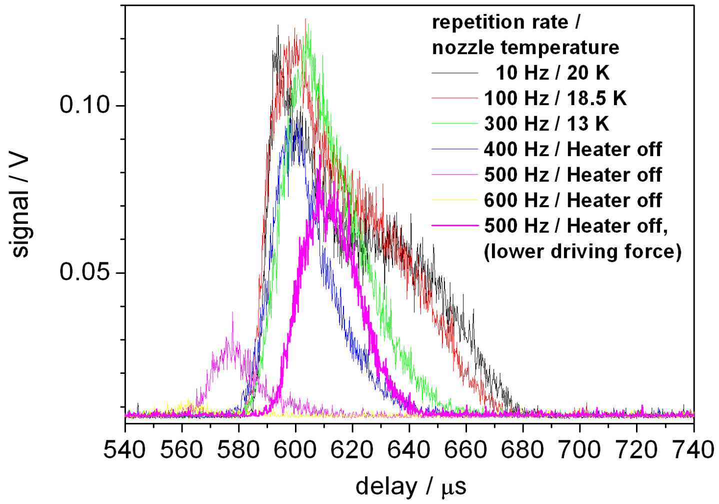

Fig. 3.18: Time profiles recorded via LIF for different repetition rates as indicated with a stagnation pressure of 80 bar. The listed nozzle temperatures are set on the controller, the sample temperature amounts to 601 K.

In contrast to the peak intensity, the shape of the time pofiles in fig. 3.18 changes with the repetition rate already below 400 Hz. At lower repetition rates a bimodal distribution is clearly present. For increasing repetition rate the slower component disappears while the faster component remains almost unaffected. This is also shown in fig. 3.20(b) for repetition rates of 20 Hz and 200 Hz for a sample pressure below the optimum for single doping at a repetition rate of 100 Hz (613 K). Under these conditions the line shape of the electronic origin of single Pc is slightly shifted to the red with increasing repetition rate.(fig. 3.20(a)) Though, the line shape at 20 Hz is recorded for a nozzle temperature of 22 K instead of 20 K as in the corresponding time profile which explains the red shift. From the peak position and the line shape it can be concluded that the size distribution of the doped droplet beam hardly depends on the repetition rate at equal effective nozzle temperatures as given in fig. 3.20. Thus, the droplet size is not distributed over the time profile, i.e. the size of the droplets in the leading part of the pulse doped at both repetition rates equals to the size of droplets in the later fraction doped only at lower repetition rates.

The narrowing of the time profiles recorded via LIF upon increasing the repetition rate as shown in fig. 3.20 can be either due to a lower probability to dope the later component of the droplet pulse or the missing of this component in the pulse.

The former would arise from a drastic variation in size within the time profiles which can be excluded from the line shape analysis (see above) or from a lower particle density in the pick-up cell for the later component. However, the peak intensity at different repetition rates matches if droplets are formed at the same effective stagnation conditions (figs.

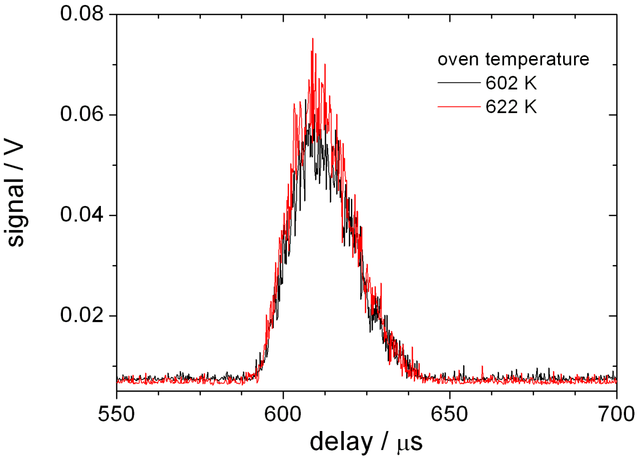

Fig. 3.19: Time profiles recorded for a repetition rate of 500 Hz at the lowest achievable nozzle temperature and a stagnation pressure of 80 bar for different oven temperatures as indicated.

3.18 and 3.20(b)) and thus the particle density in the pick-up cell at the arrival time of the droplet pulse, i.e. for the earlier component, is independent of the repetition rate. Therefore, the sample pressure in the pick-up cell present for the later fraction is also the same for all repetition rates. The missing of LIF-signal within the time domain of the slower fraction thus is not due to their different probability to pick up the sample or to a lack of sample, but due to the absence of this part of the droplet beam. Further evidence for this assignment comes from the invariance of the shape of time profiles recorded at a repetition rate of 100 Hz on the particle density as shown in fig. 3.17.

Note that this argumentation does not assume that the sample pressure in the pick-up cell is constant within the duration of a droplet pulse and thus would even hold if the droplet beam was an appreciable sink for the particle density in the pick-up cell. Though, as will be discussed in the following chapter 3.2.3.5, the droplet beam does not significantly affect the particle density in the pick-up cell.

A missing of the later component of the dopable droplet pulse at elevated repetition rates can be due to a failing of its formation in the expansion or its destruction on the way to the detection region. At elevated repetition rates the pressure in the source chamber increases by almost four orders of magnitude (400 Hz) compared to the base pressure. Therefore, the pressure gradient for the expansion might be only sufficient for the first part of each gas pulse, whereas the later part is not cooled enough by the expansion to form droplets. Further, the droplets might also be deflected by the warmer background gas, e.g. if the beam slightly hits the aperture of the pick-up cell and gas is accumulated there. Though, the scattering should also affect the first part of the pulse which is not the case.

In contrast to the dependence of the shape of the time profiles on the repetition rates at constant effective nozzle temperature as shown in figs. 3.18 and 3.20(b) the time profiles

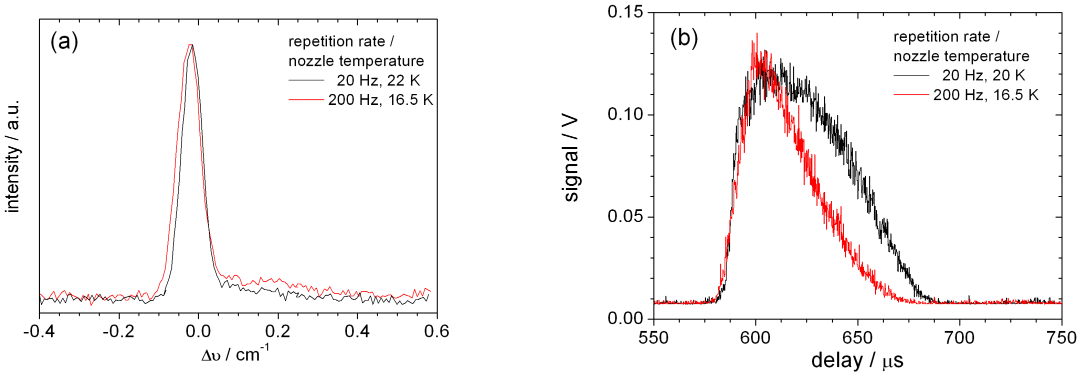

Fig. 3.20: Excitation spectrum of the electronic origin of single Pc in helium droplets (a) and time profiles of the doped droplet beam recorded for different repetition rates of 20 and 200 Hz, each with the heater set to different nozzle temperatures to obtain the same real stagnation temperature. The stagnation pressure is 80 bar and the sample temperature 613 K.

recorded via Rayleigh scattering at different repetition rates and constant effective nozzle temperatures match perfectly. (fig. 3.12) This may indicate that the larger droplets are formed by fragmentation of liquid, for which the pressure gradient is less important, while the smaller dopable droplets are formed by condensation of helium gas. Furthermore, it is not clear if the Rayleigh signal stems from superfluid droplets or non-superfluid large He clusters. The latter might have different temperatures depending on the effective nozzle temperature. Due to their larger mass these droplets/clusters are also less deflected by scattering gas.

To conclude, the variations in the shape of the time profiles recorded via LIF upon variation of the repetition rate at constant effective nozzle temperatures is probably due to a variation in the efficiency of droplet formation within a gas pulse or increased scattering of droplets at elevated repetition rates.

3.2.3.5 Pick up Statistics

At the end of the preceding chapter the question came up if the particle density in the pick-up cell might significantly decrease during the time of the passage of a droplet pulse. However, this could be excluded as the reason for the narrowing of the time profiles of doped droplets with increasing repetition rate, though it is of general interest.

In continuous beams, the probability of the pick-up of k particles is well-described by a Poisson distribution

$$P_k(n) = \frac{(\sigma_{coa} n L)^k}{k!} e^{-\sigma_{coa} n L} \tag{3.7}$$

as discussed in chapter 2.3. For droplet sizes used in electronic spectroscopy the assumptions made for the derivation of equ. 3.7 are fulfilled. The droplet pulses formed in the pulsed expansion consist of quite large ($10^4 < \mathrm{N} < 10^6$) droplets while significant smaller ones are missing and thus requirements concerning the droplet beam are also met in the pulsed expansion.

Time profiles are equal from pulse to pulse and thus (quasi-)stationary conditions are achieved under all investigated conditions. Though, as discussed above, it might be that the amount of sample in the pick-up cell available for droplets in the first part of each pulse is different to that for the later fraction. Thus, in pulsed operation stationary conditions may not be reached within the pulses. A time dependence of the particle density in the pick-up cell during the passage of a droplet pulse might need to be considered. If the change in the sample concentration in the pick-up unit is only little affected by the droplet pulses, the Poisson statistics as applied to continuous beams is valid. To check the validity of the Poisson statistics, the dependence of the LIF-signal of Pc on the particle density was recorded.

Unfortunately, no sharp signals of oligomers of Pc inside helium droplets are known and thus the evaluation of the pick up statistics relies only on the signal of the monomer. The validity of the Poisson distribution thus should better be checked again with another sample with known oligomers or for example with known van der Waals-clusters of Pc such as Pc(Ar)$_n$ clusters (n = 1-4) [LSS07] or other molecules.

The sample pressure in the pick-up cell is determined from the oven temperature T using the Clausius-Clapeyron equation describing the temperature dependence of the vapor pressure p above a solid [Wed97]

$$\frac{dp}{p} = -\frac{\Delta_v H_T dT}{RT^2} \tag{3.8}$$

or

$$ln\frac{p}{p_0} = -\frac{\Delta_v H_T}{RT} + \frac{\Delta_v S_T}{R} \tag{3.9}$$

wherein p_0 is the standard pressure (1 atm), R the gas constant, and $\Delta_v H_T$ and $\Delta_v S_T$ are the heat and entropy of vaporization (sublimation), respectively, known from the literature. [SBGI07] Thus, the dependence of the sample pressure on the oven temperature is given by

$$p \propto exp(-\frac{\Delta_v H_T}{RT}). \tag{3.10}$$

The intensity $I(t)$ of the LIF signal generated by singly doped droplets is proportional to the number of droplets $N(t)$ weighted by the probability for single doping upon passing the pick-up cell $P_1(n)$, i.e.

$$I(t) \propto N(t)P_1(n). \tag{3.11}$$

The intensity depends on the time t since the number of droplets do. Though, as measure for the intensity the peak intensity or the integrated intensity of the electronic origin in the excitation spectrum or the time profile are taken, respectively. Thus, the time dependence of the number of droplets does not have to be considered since it cancels out by comparing these intensities. Equ. 3.7 may be written in the form

$$P_1(n) = (an)e^{-an} \tag{3.12}$$

and thus

$$I_1(n) = b(an)e^{-an} \tag{3.13}$$

with a, b as constants and can be used to describe the dependence of the intensity on the particle density. Assuming that the particles in the pick-up cell behave like an ideal gas the particle density is proportional to the sample pressure p. The dependence of the LIF intensity on the particle density is shown in fig. 3.21 for that range of n were signals of single Pc inside droplets could be observed corresponding to oven temperatures ranging from 533 to 685 K. The particle density is given in units of the density at the peak intensity. Experimentally, the optimum signal with respect to all four kinds of determining the intensity is found at an oven temperature of 632 K corresponding to a vapor pressure of $7{\times}10^{-4}$ mbar. [SBGI07] Note that the accuracy of this value depends strongly on the accuracy of the temperature reading and the literature data of $\Delta_v H_T$. The sample pressure for optimum single doping with different molecules, e.g. Pc, anthracene or tetracene, determined this way was found to vary by more than an order of magnitude. [OS98]

Some of the excitation spectra and time profiles recorded for different oven temperatures at 100 Hz were shown already in fig. 3.17. The background in both experimental series increases with increasing oven temperature due to black body radiation and signal stemming from oligomers. The baseline is subtracted from the signal and thus contribution of LIF of single (excitation spectra) or single and multiple doped droplets (time profiles) are obtained. However, the signal from the oligomers is spectrally very broad and its contribution to the time profiles taken with the narrowband cw laser tuned to the electronic origin of single Pc can thus be neglected, in particular at low sample pressures.

The intensity plots in fig. 3.21 are fitted by the Poisson distribution $\mathrm{I}_1(\mathrm{n})$ (equ. 3.13) for all four data sets. The fitted parameter a for all four data sets varies only by about 3 % around an average value of 2.2. The right panel shows an enlargement of the same signal dependencies for low particle densities. As discussed in chapter 2.3, according to the Poisson distribution a linear increase of the signal is expected in this range. The dependencies of signals extracted from excitation spectra of the electronic origin, (a) and (b), can be fitted well by a straight line going through zero for the lowest five (red) or four (green) data points. For higher particle densities the slope decreases as is expected according to the Poisson distribution. The data points in panel (c) and (d) determined by evaluating the time profiles are only connected to guide the eye and do not reveal a linear dependence within the low density range. The initial slope is much steeper than in panel (a) and (b). For a sample pressure of 0.05 a.u. the signals reach already half of the maximum value whereas they amount to only about 10 % in (a) and (b). In contrast, the maximum signal recorded with the digital (photon counting) or analogue (time profile: photo current) method is found for the same particle density.

The signal dependence was also recorded with a different configuration of the nozzle at 20 Hz. The optimum oven temperature for single doping was lower by 40 K probably due to better thermal contact between the sample pellet and the pick-up cell or a worse contact between the thermocouple and the oven. The same qualitative behaviors as shown in fig. 3.21 were found with the signals recorded via photon counting well described by the Poisson statistics whereas those from the time profiles revealing a stronger deviation but in the same way as shown in panel (c) and (d) of fig. 3.21.

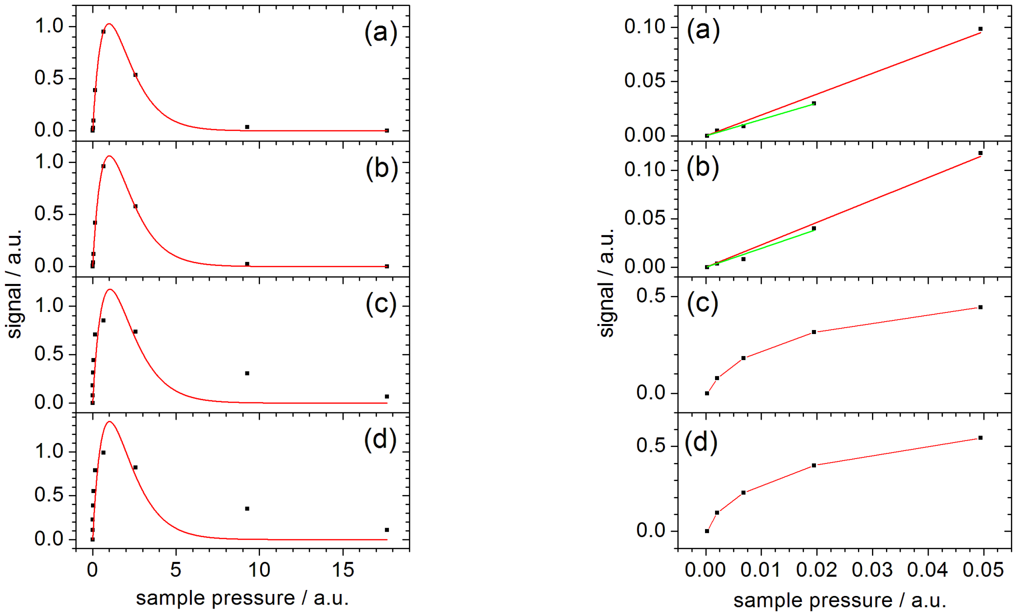

Fig. 3.21: Intensity of LIF signal of single Pc plotted versus particle density determined from the oven temperature. The intensity is given by the integral (a) or the peak intensity (b) at the electronic origin in the excitation spectrum, or as integral (c) or peak intensity (d) of time profiles for the data shown in fig. 3.17. Data are corrected for background signals with the laser off resonance. Left: Dependence of the intensity for the whole recorded range fitted by Poisson distributions. Right: Enlargement of the same dependencies for low particle densities with linear fits (a, b) or points connected to guide the eye (c, d). For details see text.

Unfortunately, the investigation of the pick-up statistic relies on the signal of single Pc since no sharp signals of oligomers of Pc in helium droplets are known and could not be identified in this work. Further, the particle density or sample pressure, respectively, in the pick-up cell could not be measured directly but is determined from the oven temperature by the nonlinear equation 3.10 and assuming ideal gas behavior. Exchanging

the sample pellet different oven temperatures (± 5-20 K depending on the heat of sublimation of the sample) are necessary to obtain the same signal under otherwise identical conditions which reflects the poor control over the thermal contacts.
The intensity distributions shown in fig. 3.21 extracted from the excitation spectra are consistent with a Poisson distribution for the pick-up probability whereas those based on time profiles are not. Thus, at this stage it is not clear if the pick-up process can be described with a time-independent Poisson distribution, i.e. if the droplet beam is not acting as an appreciable sink for the particle density in the pick-up cell. In the continuous beam it is not important for the formal treatment of the pick-up statistics if the beam is an appreciable or negligible sink since in any case stationary conditions are given and thus no time dependence has to be considered.

The data discussed so far do not reveal if constant conditions in the pick-up cell are warranted for the full length of a droplet pulse. Though, estimates of the loss of sample due to the droplet pulses compared to the effusive rate can be made.
From the sample pressure in the pick up cell and its temperature the leak rate of the pick-up cell due to effusion can be estimated to about 5×10^{16} molecules per second. On the other hand, the count rate of photons N_{Ph} is given by

$$N_{Ph} = N_{doped} W_{ex} \phi \alpha \tag{3.14}$$

with N_{doped} the rate of single Pc molecules doped into droplets, W_{ex} the corresponding excitation probability and ϕ the fluorescence quantum yield. Fluorescence is detected with the probability of α. N_{Ph} amounts to 1.2×10^5 s^{-1} for a repetition rate of 20 Hz and a width of the doped pulse of 50 μs.(cf. chapter 3.2.3.6) ϕ is expected to be about 0.7, α is determined by the space angle viewed by the collecting lens (0.0225) and the probability to register a collected photon is assumed to be 0.1. The loss rate of Pc due to doping of the droplet beam is thus given by

$$N_{doped} = 7.6 \times 10^7 / W_{ex}. \tag{3.15}$$

In the pulsed beam, this signal is distributed over only 10^{-3} s (for 20 Hz operation and 50 μs width). For a continuous beam of the same density of doped droplets as for the pulsed beam N_{doped} would be

$$N_{doped} = 7.6 \times 10^{10} / W_{ex}. \tag{3.16}$$

Therefore, even for a very low probability to excite Pc doped into the droplets (W_{ex}) the loss of sample due to the pick up process is negligible compared to effusion into the vacuum chamber.
For this estimate multiple doping is neglected which is a good approximation for oven

temperatures below the optimum of single doping. It should also be noted that for this estimate it is not important which part of the droplet pulse is doped, and thus the possibility of having a very large droplet density in the beginning of the pulse picking up all of the sample is included. Though, the estimate clearly shows that this scenario is very unlikely.

This is also reflected by estimating the number of Pc-molecules on the beam axis, i.e. the number of molecules in a cylinder of the length of the pick-up cell and a diameter as the holes of the cell, which is about 4×10^{12}. Comparing this number of particles that can be picked up with the number of $3.8\times10^{6}/W_{ex}$ particles that are picked by one droplet pulse (cf. equ. 3.15, 20 Hz) it becomes apparent that the particle density is almost not affected by the droplet pulse in agreement with the above estimate.

Furthermore, assuming thermal equilibrium for the Pc molecules they have an average velocity of about 160 m/s. Thus, they need about 30 μs for a distance of 5 mm which is the upper limit for the diameter of the droplet beam (diameter of the holes) inside the pick-up cell. Thus, the sample should be delivered subsequently within the duration of the droplet pulses preventing a significant change of the particle density.

Shape of time profiles

Interestingly, the shape of the time profiles recorded via LIF does depend on the particle density for a lower repetition rate of 20 Hz as shown in fig. 3.22. For low particle densities the signal intensity of single Pc is more even spread over the time profile than at higher temperatures and reflects the number of singly doped droplets. At higher particle densities the leading fraction of the doped droplet pulse contains more single doped droplets than the later. The number of doped droplets depend on the pick-up conditions and the size and number of the droplets. The particle density is not altered within a pulse duration as discussed above. In chapters 3.2.3.3 and 3.2.3.4 it was concluded that the size of the doped droplets is not significantly altered by changing the particle density. Thus, the shape of the time profiles reflect the distribution of the number of dopable droplets. The variation in the shape thus indicates a change of the distribution of the number of droplets within a pulse duration for higher oven temperatures.

This might be due to a perturbation of the droplet beam by the pick up cell which is more significant at higher oven temperatures. At higher temperature the scattering and thus deflection of the droplets in the pick up cell tends to increase. Therefore, a larger amount of warm helium gas might be accumulated in the pick up cell during a droplet pulse leading to a perturbation of the later part of the pulse.

The same change of the shape of the time profile is indicated also at a repetition rate of 100 Hz as can be seen in the bottom panel of fig.3.17(b) by the direct comparison for oven

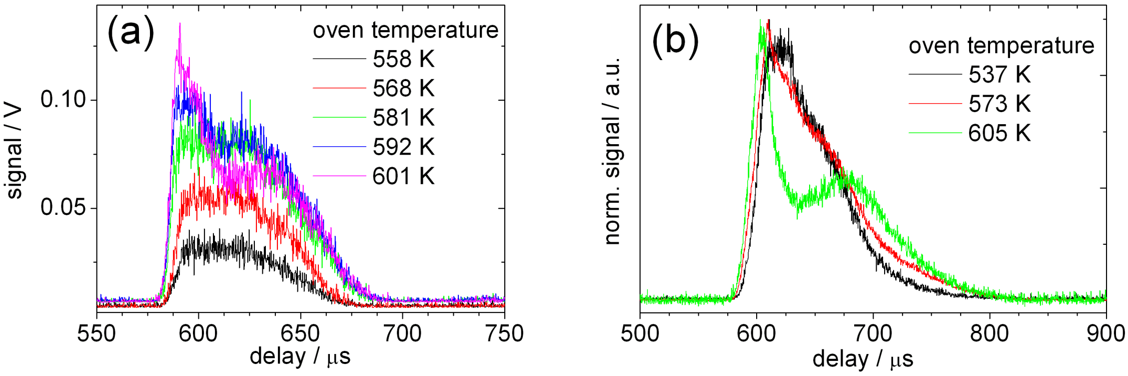

Fig. 3.22: Time profiles recorded via LIF for different oven temperatures up to the optimum with a repetition rate of 20Hz. Left: absolute intensities. Right: normalized time profiles corresponding to oven temperatures below, at, and above the optimum. The two data sets were recorded with different configurations of the Even-Lavie valve and different skimmers.

temperatures less than and far exceeding optimum conditions for singly doping. The less pronounced dependence is due to the fact that the width of the pulses are narrower at higher repetition rates as found in fig.s 3.18 and 3.20. Note that the decreasing width at elevated repetition rates is presumably not due to the perturbation of the beam in the pick up cell but due to the fail of the generation of the corresponding droplets in the expansion as discussed in the preceding chapter.

3.2.3.6 Droplet Density

The motivation to set up a pulsed helium droplet beam was to achieve a higher density of droplets within the pulses as compared to the continuous droplet beam. For a quantitative comparison the excitation spectrum of Pc was recorded in both beams with the same detection unit. Moreover, the detection chambers, the pick-up unit, and therefore the effective detection volume were identical. Conditions were optimized in both experiments individually and LIF-signal was generated using the cw dye laser at an intensity of about 200 mW. The excitation spectra of Pc revealed no saturation effects. The count rate at the peak of the spectrum in the continuous beam was 6.76×10^6 s^{-1} and is proportional to the droplet flux through the detection area. For the pulsed droplet beam operated at 20 Hz the count rate was 3.05×10^4 s^{-1} with the laser attenuated to 26% of its intensity. At 20 Hz the width of the doped pulse amounts to about 50 μs and thus droplets are present only 1 ms within 1 s of data acquisition time. Taking this into account and also the lower laser intensity, a continuous droplet beam with the same density of droplets than the pulsed beam would yield a count rate of 117×10^6 s^{-1}. Thus, the ratio of the corresponding fluxes of the continuous beams would amount to 17. For similar velocities of the pulsed and continuous beam, the ratio of the fluxes reveals the ratio of the droplet densities. Therefore, the density of (dopable) droplets is about a factor of 17 higher in the pulsed beam than in the continuous beam.

A similar estimate can be made from emission spectra recorded in both beams for excitation at the same transition using the cw dye laser and using the same detection unit. This yields a droplet density in the pulsed beam about 30 times higher than in the continuous beam.

The numbers compared are determined for orifices of 60 μm and 5 μm for the pulsed and continuous source, respectively. The ratio of the area of the openings is thus 144 which is by a factor of about 5 to 8 larger than the ratio of the droplet densities. The differences in the two ratios are due to a different efficiency of droplet formation in the expansion. Peak intensities obtained with a 60 μm or 100 μm diameter of the orifice of the pulsed source were found to be almost identical. This reflects that the density of droplets was not altered despite of the larger orifice. Together with the almost invariance of the size of dopable droplets on stagnation conditions, this may indicate that the number or density, respectively, of dopable droplets is limited by the number of nucleation centers required for the droplet formation. (cf. end of chapter 3.2.3.3) In particular, this seems to be the case for large orifices. Possibly, this is due to the change of the pressure gradient of the expansion within a gas pulse.

3.2.4 Different Configurations of the Even-Lavie Valve

The results discussed above were obtained for a nozzle orifice of 100 μm followed by a conically shaped exit channel with an opening angle of 110°. However, the front gasket between plunger and nozzle orifice had an orifice of only 60 μm diameter thus limiting the orifice. The same experimental series were also recorded with a former configuration of the valve differing in the opening diameter of the front gasket (100 μm), the recoil spring and the plunger. The recoil spring had a lower force constant and the plunger was made of a weaker magnetic alloy and had a slightly smaller curvature of its polished sealing surface. Changing from the 100 μm-setup to the 60 μm-setup reduced the gas load by one order of magnitude and lowered the heat intake by the operating valve. Both contributes to the ability to work at higher repetition rates.

The Rayleigh scattering signal showed qualitatively the same dependencies as described above. Though, the signal was more sensitive on changes of stagnation conditions and the repetition rate. The higher sensitivity is presumably due to the somewhat higher optimum driving current corresponding to a capacitor voltage of $\approx$ 23 V compared to $\approx$ 19 V for the 60 μm-setup. This lead to a larger heat intake limiting the repetition rate and thus no reasonable Rayleigh signal was observed already at 30 Hz. Despite of the larger amount of expanded gas, the peak intensities at low repetition rates were found

to be equal for the two setups.
This was also found for the peak intensity of the LIF signal of Pc doped into the droplet beam for repetition rates up to 50 Hz. At higher rates the signal generated with the 100 μm-setup drops faster due to the larger heat intake and gas load and no signal could be detected at 200 Hz. The higher gas load prevents cooling in the expansion efficient enough to form droplets at elevated pressures in the source chamber due to the increased repetition rates. Differences in the performance of the two setups with respect to the LIF signal are the driving current and especially the different dependence of the LIF signal on the stagnation temperature. The optimum driving current for LIF signal corresponded to a capacitor voltage of $\approx$19 V and is thus much lower than for the Rayleigh signal, whereas the same current was optimum for both kinds of signal with the 60 μm-setup. Time profiles for different stagnation conditions recorded via LIF using the 100 μm-setup are shown fig. 3.23 (a). For each stagnation pressure the signal intensity shows no significant dependence on the nozzle temperature up to a certain temperature above which it starts to disappear and thus contrasts the behavior found for the 60 μm-setup. The maximum temperature raises with increasing stagnation pressure as found for the 60 μm-setup.

The line shape studies at the origin of Pc doped into the droplet beam generated with the 100 μm-setup are shown in fig. 3.23 (b) for a wide range of stagnation conditions. As discussed for the other configuration of the valve, changes in the stagnation conditions hardly affect the line shape depending on the droplet size distribution. Changing the conditions in a way that larger droplets are expected to be formed only leads to a slight blue shift of the peak. Fig. 3.23 (c) shows time profiles of the doped beam recorded under conditions optimum for Rayleigh-signal with the dye laser on and off resonance and also a profile recorded with the Ar^+ laser without a pick-up cell inside. As for the 60 μm-setup, the series of data presented reveal a bimodal droplet size distribution. Depending on the stagnation conditions, either large droplets causing Rayleigh scattering or smaller droplets which can be doped are formed more efficiently. The size of the dopable droplets can be varied only within a very small range compared to the continuous beam even upon drastically changing the stagnation conditions, e.g. from 20 bar, 20 K to 80 bar, 7 K. At the same time, the droplet size distribution is hardly affected and does not reveal a log-normal distribution.
To conclude, the droplet beam produced with the two setups showed minor differences. The 60 μm-setup provides with the same peak intensity for Rayleigh and LIF signal at low repetition rates while the heat intake and gas load is decreased and enables to work reasonable with higher repetition rates up to 500 Hz. Next to this two well investigated configurations of the valve preliminary experiments were also made with other configurations. They correspond to the 100 μm-setup described above but with different exit channels. Instead of the conical shaped exit channel a trumpet shaped exit

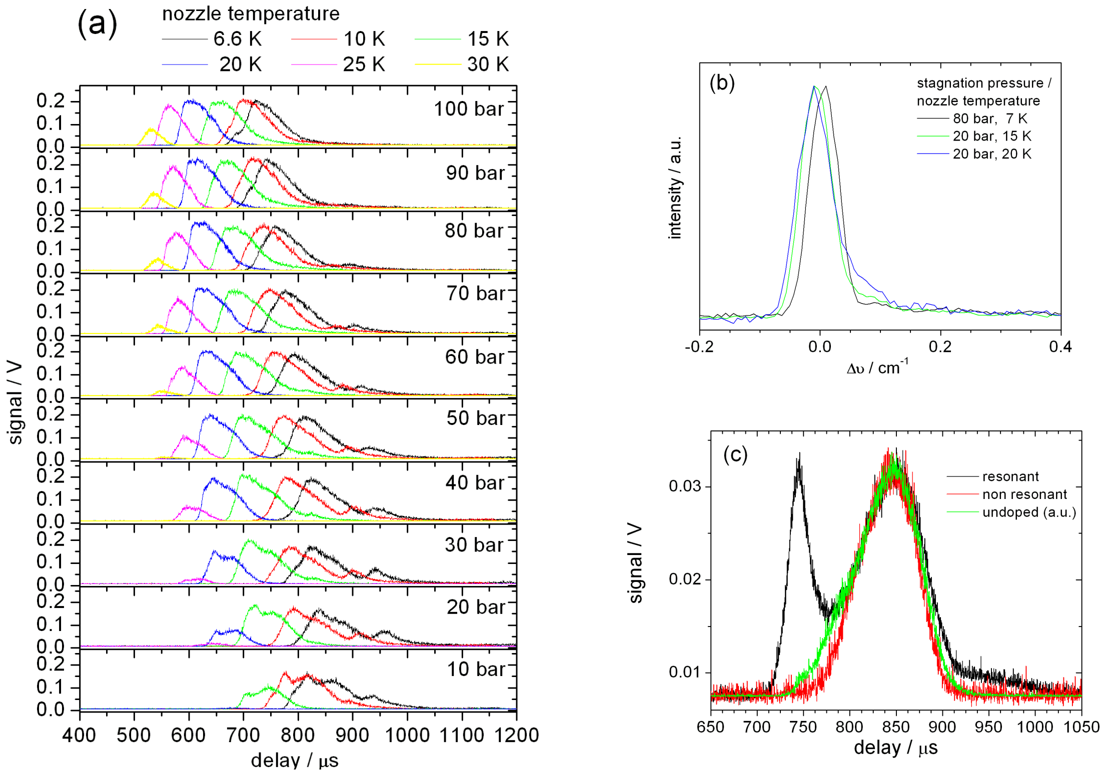

Fig. 3.23: Left: Time profiles of the doped helium droplet pulse operating at 10 Hz with stagnation pressure and nozzle temperature as indicated, while the gas flux was kept constant (a). Right: Excitation spectra at the electronic origin of single Pc in helium droplets recorded for different expansion conditions as indicated shifted by 15088.92 cm^{-1} .(b) Time profiles of the doped droplet beam while operating under ideal conditions for Rayleigh signal with the dye laser once in (red) and off (black) with the resonance of single Pc. Also shown is the scaled time profile recorded with the Ar+-laser under identical conditions without the pick-up oven inside (green).(c) All data were recorded with the setup including the 100 μm gasket.

channel was used, though no significant differences in the performance were observed. Another configuration was a conical shaped channel with a diameter of 250 μm and an opening angle of 40°. Rayleigh and LIF signals could only be observed for repetition rates up to 20 Hz and were not more intense than with the setups discussed above. The larger amount of gas prevents a cooling in the expansion efficient enough to form droplets at higher repetition rates. Further, the smaller opening angle provides a more gradual cooling, i.e. the expanded gas is cooled within longer distances and reaches the temperatures required for droplet formation at distances where the density of gas is already too low to enable cluster formation requiring three body collisions. [Eve]

3.2.5 Even-Lavie vs. General Valve

Pulsed helium droplet beams reported in the literature by other groups are generated with a slightly modified commercially available valve developed for supersonic beams (Series 99 High Speed Solenoid Valve, General Valve Corporation). Before the Even-Lavie valve was installed, preliminary experiments were also made with this pulsed droplet source. Schematic drawings of the different nozzle modifications described in the literature are shown in fig. 3.24 (a-c) in comparison to the Even-Lavie valve (d). The pulses are produced by the movement of a poppet instead of the plunger in the Even-Lavie nozzle. Sealing is achieved by the poppet beating against the stainless steel front plate as indicated in the figure. The most important modification was the shape of the nozzle throat which determines the droplet size and the possibility to vary the size. Without a throat (a) the droplet size is hardly affected by changes of the stagnation conditions and amounts to about 2 - 7 $\times 10^4$ He atoms per droplet. [SKMV02] As for the Even-Lavie valve, the formation sets in sharply and evidence was found neither for smaller droplets nor for larger droplets as formed by supercritical expansion in the continuous beam independent of the stagnation conditions. The droplet density produced was estimated to be about 100 times higher than in the continuous beam from a 5 μm nozzle as found by comparing the peak intensity of the ion signal of He_2^+ and the S/N-ratio in the excitation spectrum of Phthalocyanine recorded with a pulsed dye laser. For a straight channel (throat) drilled through the faceplate of the nozzle (fig. 3.24(b)) droplets larger than about 5×10^4 He atoms per droplet can be produced with their size hardly depending on the expansion conditions. [YBE05] Experimentally, it was found that a compromise between the two configurations as shown in fig. 3.24 (c) with a shorter throat allows for the variation of the size within a large range. This was assigned to be presumably due to the onset of condensation prior to the cooling by expansion. The average size showed a similar dependence on the nozzle temperature as found in the continuous expansion whereas it is less affected by the stagnation pressure. [YBE05] Further, the average size increases monotonic within the droplet pulse, i.e. larger droplets are detected later. [YE08]
The discussion of the nozzle openings in fig. 3.24 (a-c) reveal the influence of the throat on the cluster size. A gradual variation over a wide range is not possible using the Even-Lavie valve. (fig. 3.24 (d)) This might be altered by introducing a throat in the inlet, just as in fig. 3.24 (c).

The General Valve nozzle used in our setup equals the one in fig. 3.24(c) with a poppet made of Kel-F. The observed pulses were rather long and the time profiles showed a double structure with droplets produced only at the beginning and end of each pulse. By lowering the opening time set by the Iota One pulse driver system (General Valve) (driving pulse length) the two droplet signals merged though on the cost of peak intensity. Another disadvantage of the General Valve system next to the longer gas pulse

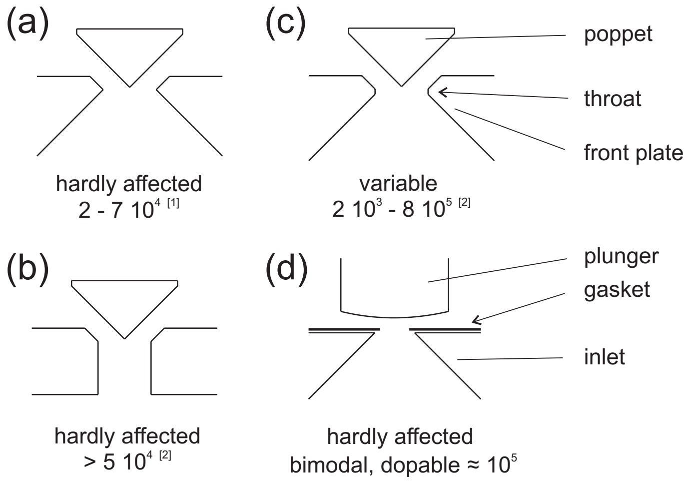

Fig. 3.24: Schematic drawings of nozzle shapes used for generation of pulsed helium droplet beams and possible variation in size (given in He atoms per droplet) by variations of the expansion conditions. The opening diameter is 500 μm (a-c) with a conical opening with an angle of 90° (a,c). The throats have a length of 500 μm (b) or 100 μm (c), respectively. The Even-Lavie nozzle is shown in (d). [1] and [2] denote ref. [SKMV02] and ref. [YBE05], respectively. The high vacuum side is on the bottom.

duration was the reliability of the system limited by the lifetime of the poppet. Further, the pulses showed larger fluctuations from pulse to pulse and the optimum signal level obtained with the Even-Lavie valve was larger by more than one order of magnitude right away. Reasonable signals could only be generated with repetition rates of less than 100 Hz.

3.2.6 Pulsed Beam vs. Continuous Beam

The characteristics of the droplet beam produced in a pulsed expansion using the Even-Lavie valve was already discussed in detail and compared to the continuous expansion. This section only summarizes the valuation of various experimental combinations used within this work.

excitation spectra recorded with a cw laser In the pulsed experiment best S/N-ratio was obtained for defocusing the laser beam to a diameter of about 5 mm in the detection region. The droplet density in the pulsed beam is larger than in the continuous beam by about a factor of 20. Therefore, the same absolute signal as in the continuous beam could only be obtained if the pulse widths would amount to 0.05 / repetition rate. I.e. at a repetition rate of 1 kHz and a pulse width of 50 μs the same signal would be obtained. Though, even in this case the pulse droplet source (as well as any other pulsed experimental tool) fluctuates with time.

Thus, for recording excitation spectra with the cw laser source better S/N-ratio is obtained using also a continuous beam.

excitation spectra recorded with a pulsed laser Best S/N-ratio is obtained for the pulsed dye laser not being focused. It thus has a diameter of about 5 mm in the detection region limited by the apertures. The droplet density within the time interval probed by the laser is about a factor of 20 higher in the pulsed beam compared to the continuous beam and thus the obtained S/N-ratio should be larger by factor of about $\sqrt{20}$.

emission spectra recorded with a cw laser as excitation source Best S/N-ratio is obtained for a large detection volume by defocusing the laser beam to a diameter of about 5 mm in the detection region. The same arguments as for the excitation spectra recorded with a cw laser hold when a CCD-camera is used for the detection.

emission spectra recorded with a pulsed laser as excitation source Optimum S/N-ratio is again found for the laser not focused. Using the pulsed laser the pulsed beam is advantageous compared to the continuous beam due to the higher droplet density within the interrogated time. Though, with the available pulsed dye lasers, only 20 Hz (50 Hz) $\times$ 10 ns are probed resulting in about 20 Hz (50 Hz)$\times$50 ns (duration of the laser pulse and fluorescence decay time) $= 1$ (2.5) μs fluorescence signal within 1 s of detection. This is a factor of about 10^{-6} lower duty cycle compared to the combination cw laser/continuous beam and a factor of 10^{-2} for the combination cw laser/pulsed beam (200 Hz, pulse width 50 μs). These low factors are only partly compensated by the higher droplet density (factor of 20) compared to the continuous beam and by the higher power of the pulsed lasers which is advantageous when weak transitions are probed.

To conclude, the pulsed droplet beam is advantageous compared to the continuous droplet beam only if a pulsed excitation source is used. For excitation spectra recorded with a pulsed laser also a pulsed detection scheme (boxcar integrator) should be applied. When a cw laser is used a better duty cycle is obtained for excitation and emission spectra recorded in the continuous beam. For emission spectra, the same detection technique is used if the droplet beam is probed with pulsed or cw lasers. The combination of a pulsed excitation but continuous detection scheme (CCD-camera) gives the worst duty cycle.

The combination of cw laser and continuous beam yield a better duty cycle in excitation and emission spectra. Further, neither the droplet nor the laser source fluctuate in time and thus also the S/N-ratio is best for this combination. Only when pulsed lasers are used the pulsed droplet source is advantageous. At the same time, the S/N-ratio at least in the emission spectra, is better even in the pulsed droplet beam if the cw laser is used.

3.3 Summary

In this chapter the setup of the new apparatus for the generation of a pulsed helium droplet beam and the signal processing was described. The main focus was the characterization of the Even-Lavie valve as a new source for a pulsed helium droplet beam via Rayleigh scattering from bare droplets and LIF of single Pthalocyanine molecules doped into the droplets. The two kinds of experiments revealed a bimodal size distribution. One fraction of the pulses consists of droplets smaller than 10^6 He atoms per droplet while the other comprises very large droplets of more than 10^6 He atoms per droplet. By variation of the expansion conditions, such as the nozzle temperature and stagnation pressure, the relative abundance of the two fractions can be varied. The larger droplets are preferentially formed at lowest nozzle temperatures and highest stagnation pressures, whereas the smaller ones are formed most efficient at higher temperatures with the optimum temperature depending on the stagnation pressure. Only the fraction of the smaller droplets can be doped with foreign particles. The resonance frequencies and the peculiar emission behavior of Pc (as well as the spectroscopic features of all other molecules) found in the pulsed beam match with the findings in the continuous droplet beam. Variation of the stagnation conditions allows for varying the size of the dopable droplets in the range between about 10^4 and 10^6 He atoms per droplet. In contrast to droplets formed via subcritical continuous expansion with a most probable size in this range (about 10^4 He atoms per droplet), the droplets formed in the pulsed expansion were not accompanied by significantly smaller ones. This is reflected by the different line shape of the excitation spectrum of Pc at the electronic origin and indicates a different size distribution. Unfortunately, the fraction of larger droplets could not be doped and their absolute size could not be determined with the methods applied. Further, it is not clear if these droplets or clusters are superfluid. The size of the dopable droplets make them very well suited for electronic spectroscopy and for the study of large molecules and clusters.

The influence of the repetition rate as an additional parameter of the pulsed beam compared to the continuous beam was also investigated for both kinds of droplets. In case of the large droplets causing the Rayleigh scattering the signal was shifted to earlier times and its intensity decreased with increasing repetition rate. Both could be reduced to the elevated source temperature due to the valve acting as a source of heat which is obviously more pronounced at higher repetition rates. For the fraction of smaller droplets the optimum nozzle temperature is not the lowest possible and thus the additional heat intake could be compensated. Though, for equal real source temperatures, the signals have the same peak intensity but the pulses are narrower at higher repetition rates. The influence of the repetition rate thus cannot be reduced solely to the heating and was assigned to be presumably due to the increased pressure in the source chamber preventing the formation of the later part within the dopable droplet pulses or due to scattering with accumulated background gas, e.g. in the pick up cell.

A lack of sample being the reason for the narrowing of the time profiles could be excluded arguing with the peak intensity and size distribution within the droplet pulse. Further, the droplet beam was estimated to not significantly affect the particle density in the pick-up cell and thus the pick up statistic in the pulsed droplet beam is described by a Poisson distribution as in the continuous beam.

When pulsed lasers are used to probe the droplet beam, only the peak intensity of the time profiles recorded via LIF (or Rayleigh scattering) is of importance. The peak intensity of the LIF signal was shown to be almost constant up to a repetition rate of 500 Hz which is limited by the heat intake of the valve. Within this part of the beam the droplet density was estimated to be larger than in the continuous beam by a factor of about 20. Therefore, the use of the pulsed valve is advantageous compared to the continuous source if pulsed detection (or doping) schemes are applied.

Finally, the performances of different configurations of the Even-Lavie valve were compared among each other and with a General Valve nozzle with respect to the formation of a pulsed droplet beam. A possible variation of the nozzle orifice of the Even-Lavie valve by introducing a throat was discussed which might enable to vary the size of the droplets by changing the expansion conditions. This would be advantageous for experiments calling for smaller droplets, e.g. depletion techniques.

4 Electronic Spectroscopy in the Gas Phase and in Helium Droplets

In this thesis exclusively electronic spectra of various closed shell organic, and thus heliophilic, molecules are discussed. The investigations aim on a better understanding of the molecular properties but also of the helium environment. In particular, the interaction between the helium and the embedded species is of interest. This interaction is reflected by differences in the (electronic) spectra of molecules embedded in helium droplets compared to the corresponding spectra of the free molecules in the gas phase. In the following, the differences that can be observed in electronic spectra of organic molecules changing from the gas phase (supersonic jet) into helium droplets are discussed. The variety of responses to the helium solvation will be merged into a qualitative explanation of the underlying effects.

4.1 Thermal Conditions

Free molecules in the gas phase can be prepared in a supersonic jet. Such a beam is obtained by an adiabatic expansion of gas through a small orifice into vacuum whereby the thermal energy of the gas is converted into translational energy leading to a cooling of the gas. The cooling is thus achieved by collisions during the gas expansion and better cooling is achieved for larger pressure gradients between the gas reservoir and the vacuum chamber. [Lev80, Dem08] The lowest temperatures in a beam can be reached using inert one-atomic gases. [Sco88]. Organic molecules are usually cooled using the seeded beam technique with a small amount of the sample (≤ 1 %) mixed with a seed gas prior to the expansion. During the expansion, the sample molecules are cooled via elastic two-particle collisions with the seed gas. [EJN$^+$00] Due to this cooling mechanism, the cooling efficiency increases with the mass of the seed gas in the row He < Ne < Ar < Kr < Xe. [AEJ80a] Larger rare-gas atoms though have a larger polarizability and therefore tend to form van der Waals complexes with the sample molecules. The tendency to form clusters increases also with the stagnation pressure of the gas. Thus, in experiments on free molecules a compromise between efficient cooling and avoiding cluster formation

has to be found. Both, cooling and complexation, are also strongly influenced by the geometry of the nozzle and the molecular species under investigation. [EJN+00]
The achieved cooling is determined by the number of collisions that took place until the density in the expansion has dropped too far and the cooling is terminated. [Cam84, Sco88, EJN+00] The cooling of internal degrees of freedom usually requires more collisions than the translational cooling. Hence, the different internal degrees of freedom are usually not in thermal equilibrium at distances from the nozzle where binary collisions practically stopped and the internal state distribution 'freezes'. [Cam84, Sco88] The vibrational states are usually less efficiently cooled than the rotational states and thus hot bands can sometimes be observed. Within each of the various degrees of freedom thermal conditions are almost fulfilled and as a rule of thumb

$$T_{trans} < T_{rot} < T_{vib}$$

is usually found for the translational, rotational, and vibrational temperatures (T_{trans}, T_{rot}, and T_{vib}). Within the various vibrational modes the low frequency modes are usually more efficiently cooled than the high energy modes. Typical values are

$$\begin{aligned} T_{trans} &\leq 1K \\ T_{rot} &\leq 5-10K \\ T_{vib} &\leq 10-20K \end{aligned}$$

though much lower temperatures e.g. of $T_{rot} \approx 0.4$ K can be achieved. [EJN+00]

In contrast to the situation in the supersonic jet, in helium droplets thermal equilibrium is achieved via evaporative cooling within picoseconds after the pick-up and thus

$$T_{trans} = T_{rot} = T_{vib} = 0.37\ K$$

is found.
Many of the differences in the spectroscopy of molecules in the gas phase and helium droplets can be attributed to the lower temperature in the quantum liquid. The lower temperature is in favor of the population of lower energetic states and thus leads e.g. to the reduction of hot bands and the width of rotational band contours.

4.2 Solvent Effects

Fig. 4.1 shows simplified Jablonski-diagrams of an organic molecule in the gas phase (left) and in helium droplets (right) to illustrate the differences in the spectroscopic behavior beyond thermal effects. The diagrams show two electronic states, namely the electronic ground state S_0 and the lowest excited singlet state S_1. For each of these states, the fundamental and the first overtone of two different vibrational modes (dashed and full line, respectively) are indicated.

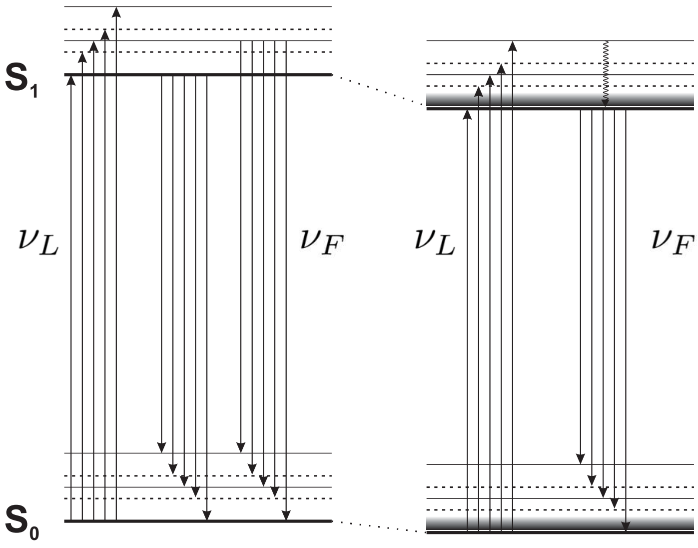

Fig. 4.1: Jablonski diagrams of an organic molecule in the gas phase(left) and in helium droplets(right). For details see text.

If the molecular beam is cold enough, only the lowest vibrational state of S_0 is significantly populated and all photon induced transitions of the free molecules in the gas phase originate from this state. (left) If the laser frequency ν_L is on resonance the excited state gets populated and may emit light of different frequencies ν_F. (Laser induced fluorescence, LIF) Detection of the emission as function of the excitation frequency yields an fluorescence excitation spectrum containing information about the (ro)vibrational structure of the excited state. The intensity pattern depends on the thermal population in the electronic ground state, the transition moments, and the state specific fluorescence quantum yield. The line widths obtained are determined either by experimental conditions such as Doppler and power broadening or the laser line width, or by the life time of the excited state. In case the latter effect is dominant one obtains homogeneous line widths which are of Lorentzian shape. In the supersonic jet rotationally resolved excitation spectra can often be obtained.

Upon excitation the radiative decay competes with different non-radiative decay mechanisms such as internal conversion (IC), internal vibrational redistribution (IVR), and intersystem crossing (ISC) which are known to be state specific. [LFSZ84, AHJ88, KM95] Due to the lack of a dissipative medium, the emission can only stem from levels that are isoenergetic to the level into which the molecule is excited by the laser. Therefore, the dispersed emission spectrum depends on the excitation frequency and thus on the (vibrational) excess energy. This is exemplified in fig. 4.1 (left) for excitation into the vibrational ground state of S_1 and into one specific higher vibronic level. The corresponding dispersed emission spectra recorded for selective excitation of single vibronic levels (SVL-spectra) contain information about the (ro)vibrational frequencies of the electronic ground state. The intensity distribution depends on the corresponding transition moments which are usually separated into an electronic and a nuclear part. The latter determines the vibrational fine structure given by Franck-Condon(FC)-factors which depend on the geometry of the excited and the ground state. [LFSZ84, AHJ88, KM95]

Solvent Shift

Changing from the gas phase into the helium droplet (fig. 4.1(left → right)) is usually accompanied by a solvent shift of the electronic transitions of up to ± 100 cm^{-1} . [SV01, TV04] A solvent shift of electronic transitions is present in all host systems and reflects different interaction energies of the environment with the embedded molecule in its ground and excited state. For heliophilic molecules the ground state is inevitably stabilized by the solvation. Thus, a red shift with respect to the gas phase indicates an even larger stabilization energy for the electronically excited state. [SV01] The solvent shifts observed in helium droplets are smaller by a factor of 10 to 100 compared to solid matrices, e.g. other rare gas matrices, as to be expected due to the lower polarizability of helium. [TV04] In helium droplets, as in any polarizable cluster, the shift depends on the size of the cluster and can be described by the exclude-volume model. [Jor92, DS01](cf. chapter 3.2.3.3) Similar to electronic transition energies also vibrational frequencies are altered by usually not more than about one percent thereby yielding typical shifts of vibrational energies of less than ± 5-10 cm^{-1} as found in electronic and vibrational studies. [SV01, CLSS01, TV04]

As in the gas phase, excitation spectra in helium droplets can be recorded via detection of the laser induced fluorescence and contain information on the (ro)vibrational structure of the excited state. Rotationally resolved spectra can also be observed in the droplets which is interpreted as a microscopic indication of superfluidity. [SV01, CLSS01, TV04] Though, the rotational constants are smaller than in the gas phase scaled by a factor which is close to one for fast rotors and which goes down to 1/3 for slow rotors. [CDF^{+}06] The droplet is also affective on the homogeneous line widths due to additional relaxation

processes (energy dissipation) and in addition leads to an inhomogeneous line broadening due to the cluster size distribution. [CDF⁺06, NM01, SV01, DS01, PPV02]
Instead of detecting laser induced fluorescence leading to LIF-spectra, excitation spectra can also be measured using the depletion method. This technique makes use of the reduction of the droplet size upon dissipation of energy. As a consequence of the reduced droplet size the ionization cross section decreases which is registered by ion-sensitive mass filters such as quadrupol mass spectrometers. Alternatively, the accompanying decrease of the mass flux can be recorded with a bolometer. The depletion technique is not used within this work.
For all molecules yet investigated by dispersed emission spectroscopy in helium droplets, fluorescence was observed exclusively from the vibrational ground level of S_1 and is thus preceded by the dissipation of vibrational excess energy into the helium droplet. (Kasha's rule) [LS03, LS04a, LS04b, LS05] From the line widths of the vibronic transitions in the excitation spectra a lower limit of the decay time due to this energy dissipation of the directly excited states can be deduced and for rigid organic chromophores is typically in the range from 3 to 30 ps. [PGDS10](cf. chapter 5.9.1) Thus, in contrast to the emission spectra in the gas phase, the dispersed emission spectra recorded in helium droplets are usually independent of the excitation frequency, i.e. the excess energy. In rare cases, excess energy can induce also other processes like a relaxation of the helium solvation layer as will be discussed below. The additional relaxation processes in the dissipative medium can also cause a broadening of electronic transitions which will be treated in chapter 5.9.1. [PGDS10]

Phonon Wing (PW)

Another remarkable feature in electronic spectra recorded in helium droplets is the occurrence of phonon sidebands, in helium droplets commonly referred to as phonon wings (PWs). The PWs accompany the zero phonon lines (ZPLs) which are the pure molecular transitions of the embedded species. The spectral shape of the PW depends strongly on the dopant species and can exhibit rather broad asymmetric signals extending over several ten wavenumbers or sharp features of widths of even less than one wavenumber. Typical for the PWs in helium droplets is the so called phonon gap and a steep signal increase a few wavenumbers separated from the ZPL. [SV01, TV04, ST08] PWs are assigned to excitations of the helium environment coupled to the molecular transitions. Thus, they appear on the high energy side in excitation and on the low energy side in emission spectra, respectively. The phonons are indicated as quasi continuum levels (grey stripes) in fig. 4.1 (right) exemplified only for two levels, namely for the vibrational ground state of S_1 and S_0, though they accompany all other levels, too.

The well resolved PW structure in the electronic excitation spectrum of glyoxal could be explained by the characteristic density of states spectrum of bulk HeII which is interpreted as an indication for the superfluidity of the helium droplets. [HMTV96, PPV02] Fig. 4.2(a) shows the experimental excitation spectrum of glyoxal consisting of rotational band contours of the electronic origin (ZPL) and the accompanying PW. Fig. 4.2(b) displays the density of states of superfluid helium modified for finite cluster sized droplets and coupled to the Q-branch of the ZPL. The first maximum of the PW is separated from the ZPL by 5.6 cm^{-1} which corresponds approximately to the roton energy. With increasing excess energy, the PW passes through a second less pronounced maximum at 10.3 cm^{-1} corresponding to the maxon, and then gradually levels out. The gap between the ZPL and the maximum of the PW (phonon gap) is not found for glyoxal embedded in pure ^{3}He droplets but for mixed clusters containing more than about 120 ^{4}He atoms corroborating the assignment of the maximum to an excitation of the roton. [SV01, PÖ1, TV04]

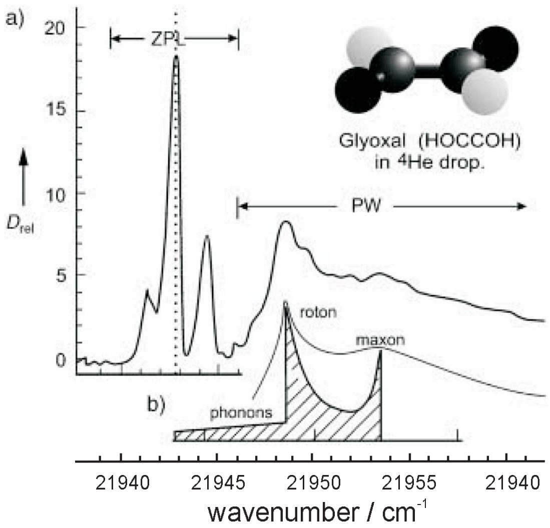

Fig. 4.2: Excitation spectrum of glyoxal (a) recorded with the depletion technique showing the ZPLs and PW. The PW can be simulated from a slightly modified density of states of superfluid helium (b). Figure taken from ref. [TV04].

From fig. 4.2(b) it becomes apparent that rotons cannot be excited below a certain threshold of excess energy, though phonons can be. All excitations shown are volume modes, though also surface modes can be present. [BS90] These so called ripplons are low energy modes that are thermally populated even at the droplet temperature. Their energies have a different dependence on the droplet size as compared to the volume modes. [BS90] Some of the observations in doped helium droplets show a pronounced dependence on the droplet size which is sometimes tentatively attributed to the size dependence of the elementary excitations, in particular of the surface modes. [NM00,

PÖ1, SV01, KMP+02] In the literature on helium droplets, all elementary excitations of the helium environment are usually collectively referred to as phonons. Thus, and in analogy to the language of matrix isolation spectroscopy, the term phonon wing (PW) includes all kinds of excitations of the environment coupled to molecular transitions. This nomenclature is also used within this work.
The PW structures found for different molecules differ from that of glyoxal with respect to the gap between the ZPL and the maximum of the PW and also with respect to the shape. In particular, distinct sharp features with excess energies less than $\approx$ 10 cm^{-1} can often be found. These are attributed to excitations of a non-superfluid solvation layer around the chromophore. [SV01, HLTV02, TV04, ST08] The distinct features of the PWs thus correspond to quasi-localized phonons or excitations of a rigid dopant-He$_n$-cluster in a helium droplet. Further, the PW structure was found to depend on the size of the droplets. (see above) [PÖ1, SV01]

The configuration coordinate model to describe the occurrence of PWs in electronic excitation spectra is shown in fig. 4.3. The well-known potential energy diagram used to explain the intensity pattern of vibronic transitions is depicted on the left side with the arrows indicating different molecular transitions. On the right side an analogue potential energy diagram is shown for one molecular transition (ZPL) and the accompanying phonon wing (PW) resembling elementary excitations of the helium environment coupled to the molecular excitation. One of the differences of the two energy diagrams in fig. 4.3 is that the left one refers to an intramolecular coordinate whereas the right one refers to an intermolecular (environmental) coordinate. The latter is usually called the helium configuration. Molecular vibrations show a discrete pattern, while PWs often have discrete transitions but also a broad quasi-continuous spectrum. The broad spectrum is explained by the quasi-continuous density of states of the superfluid helium whereas the sharp features are attributed to excitations of the non-superfluid solvation layer. [HLTV02] Note that the superfluid part of the droplet has no internal structure and thus the helium configuration-coordinate in fig. 4.3 (right) refers only to the non-superfluid solvation layer. Thus, the configuration coordinate model does not include PW structures due to excitations of the superfluid helium.

Describing the intensity distribution using the potential energy diagram in fig. 4.3 (right) assumes that the total wavefunction Ψ^{total} of the states between transitions are induced can be written as

$$\Psi^{total} = \Psi^{mol}\Psi^{He} \tag{4.1}$$

with Ψ^{mol} as the wavefunction of the molecular states and Ψ^{He} of the states of the environment, i.e. the phonon levels. [WDW09] Within the Born-Oppenheimer approximation Ψ^{mol} can be written as the product of the electronic and nuclear wavefunction

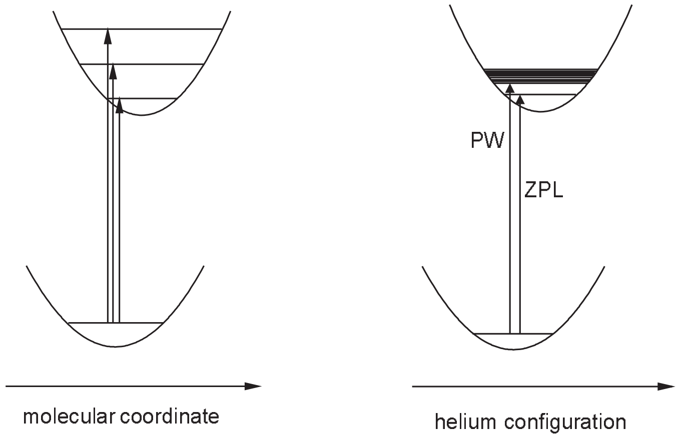

Fig. 4.3: Potential energy diagrams for excitations between levels with respect to a molecular coordinate (left) or the helium configuration (right). The molecular levels correspond to molecular vibrations, the environmental levels to phonons.

Ψ^{el} and Ψ^{k}, respectively:

$$\Psi^{total} = \Psi^{el}\Psi^{k}\Psi^{He}. \tag{4.2}$$

Equ. 4.1 can be interpreted as an 'extended Born-Oppenheimer approximation'. Using Fermi's golden rule the transition probability W for an electronic transition between the total states Ψ_a^{total} and Ψ_b^{total} is thus given by

$$W \propto \left|\langle\Psi_a^{total} \mid \hat{\mu_{el}} \mid \Psi_b^{total}\rangle\right|^2 = {\mu_{ab}^{el}}^2 \cdot \left|\langle\Psi_a^{k} \mid \Psi_b^{k}\rangle\right|^2 \cdot \left|\langle\Psi_a^{He} \mid \Psi_b^{He}\rangle\right|^2 \tag{4.3}$$

wherein μ_{ab}^{el} is the electronic transition dipole moment, $\langle\Psi_a^{k} \mid \Psi_b^{k}\rangle$ the Franck-Condon (FC) factor for the nuclear coordinates (molecular coordinate), and $\langle\Psi_a^{He} \mid \Psi_b^{He}\rangle$ an analogues factor for the solvation coordinates (helium configuration). Therefore, the PW is ascribed to changes in the helium configuration which is considered by extending the Born-Oppenheimer approximation and thus also the FC-factor.

This separation and thus independent treatment of molecular and environmental coordinates (adiabatic approximation) is well established for the description of electron-phonon coupling in solid matrices [OPS73, FH84] and was adapted to the spectroscopy in helium droplets also in ref. [Log08].

According to the configuration coordinate model the displacement of the potential energy curves of S_0 and S_1 along the helium configuration coordinate determines the PW-structure found in the excitation and also emission spectra of molecules embedded in helium droplets. Together with the individual non-superfluid solvation layer depending on the embedded species this might be an explanation for the differences in the shape of the PWs found for different molecules. (cf. chapters 5.9.2 and 6.3 and e.g. refs. [HLTV02, TV04, LS05])

Depending on the displacement of the potential energy curves of the different electronic states with respect to each other the PW can be vanishingly small but can also dominate the spectra as will further be discussed in chapter 6.3.

Since the ZPL and the corresponding PW belong to different transitions they usually have different transition moments. Upon excitation at the ZPL of the electronic origin the fluorescing state with a life time in the order of a few ns is populated. In contrast, excitation at a PW or vibronic transition, i.e. with phonon or vibrational excess energy, is followed (after eventual redistribution) by dissipation of the excess energy which is faster than the competing radiative decay. Thus, the life times of the corresponding excited states is shorter, e.g. in the order of 10 ps. [Leh04] Both a different transition moment and life time of the initially excited state result in a different saturation behavior. Therefore, the saturation behavior probed by recording excitation spectra with different laser intensities can be used to distinguish between ZPLs and sharp features of the corresponding PWs. [SV01, TV04]

In excitation spectra recorded via LIF the intensity of a transition is proportional to the population of the emissive state. Thus, the dependence of the population of the emissive state on the laser intensity reflects the LIF intensity.

Excitation of the ZPL at the electronic origin directly populates the emissive state. In a two level system in equilibrium with the electromagnetic field, the number of embedded molecules (i.e. the pure molecule together with the helium environment) in the excited state N_e depends on the total number of molecules N_0, the cross section for absorption and stimulated emission σ_a, the life time of the excited state τ_e and the photon flux F of the laser and is given by [Dic]

$$N_e = N_0 \frac{\sigma_a F}{2\sigma_a F + \frac{1}{\tau_e}} \tag{4.4}$$

with $\frac{1}{\tau_e} = k_e^r + k_e^{nr}$ as the sum of radiative and non-radiative rate constants of the emissive state. The dependence of the population of the emissive state and thus the intensity of the LIF-signal on the photon flux is shown in fig. 4.4 (a)(solid line) for a typical value of $\tau_e = 10$ ns and σ_a as indicated.

To describe the dependence of the population of the emissive state N_e on the photon flux F upon excitation at PWs or vibronic transitions a three level system in equilibrium with the electromagnetic field needs to be considered. Therein, the number of embedded molecules in the emissive state N_e depends on the total number of molecules N_0, the cross section for absorption and stimulated emission σ_a at the laser frequency, the life time of the initially excited state τ_a, the life time of the emissive state τ_e, the rate constant k_R for the relaxation from the initially excited state into the emissive state and the photon flux F of the laser and is given by

$$N_e = N_0 \frac{\sigma_a F}{2\sigma_a F(\frac{1}{k_R \tau_e} + \frac{1}{2}) + \frac{1}{k_R \tau_a \tau_e}}. \tag{4.5}$$

Assuming $\frac{1}{\tau_a} \approx k_R$, i.e. the life time of the initially excited state is determined by the relaxation process into the emissive state, or in other words all initially excited states relax into the emissive state, equ. 4.5 can be written as

$$N_e = N_0 \frac{\sigma_a F}{2\sigma_a F(\frac{\tau_a}{\tau_e} + \frac{1}{2}) + \frac{1}{\tau_e}}. \tag{4.6}$$

The dependence of the population of the emissive state and hence the LIF-intensity according to equ. 4.6 is shown in fig. 4.4 (a)(dashed and dotted lines) for typical values of $\tau_a = 10$ ps and $\tau_e = 10$ ns and σ_a-values as indicated.
At low laser fluxes, i.e.

$$\frac{1}{\tau_e} \gg 2\sigma_a F \tag{4.7}$$

for the two level system and

$$\frac{1}{\tau_e} \gg 2\sigma_a F(\frac{\tau_a}{\tau_e} + \frac{1}{2}) \tag{4.8}$$

for the three level system, respectively, the population of the emissive state and thus the LIF-intensity rises linearly with the photon flux (laser intensity). At higher photon fluxes saturation effects occur, i.e. the LIF-intensity increases with a smaller slope and finally does not further increase as shown in fig. 4.4(a). Fig. 4.4(b) illustrates the relative population of the emissive states and thus the intensity ratio of the LIF-signals induced upon excitation as indicated corresponding to excitation at the ZPL of the electronic origin (2-level system) and at PWs or vibronic transitions (3-level systems), respectively. It can be seen that the intensity ratio in the fluorescence excitation spectrum reflects the different absorption cross sections (FC-factors) only for low laser fluxes where the LIF-intensity of both signals rises linearly with the photon flux. The condition of equ. 4.8 is usually given for the PWs and vibronic transitions and saturation effects are expected only at photon fluxes orders of magnitude higher than for the ZPL at the electronic origin.

To conclude, a saturation only at higher laser intensities is indicative for a lower transition moment or a shorter life time of the initially excited state. For low laser intensities with none of the transitions saturated the relative intensities reflect the transition moments given by FC-factors. On the other hand, fig. 4.4(b) also shows that if the relative intensity of different transitions is not altered upon changing the laser intensity none or all of the transitions are saturated. A saturation of PWs with life times in the order of 10 ps can be neglected for the laser intensities used in the present work.
At the electronic origin usually a different saturation behavior of different transitions is observed. The transition lowest in energy thereby usually saturates at laser intensities similar as in the gas phase and can be assigned to a ZPL. Transitions to the blue of this ZPL that have no counterpart in the corresponding gas phase spectrum may be due to features of its PW or represent other ZPLs of the molecule in a different helium

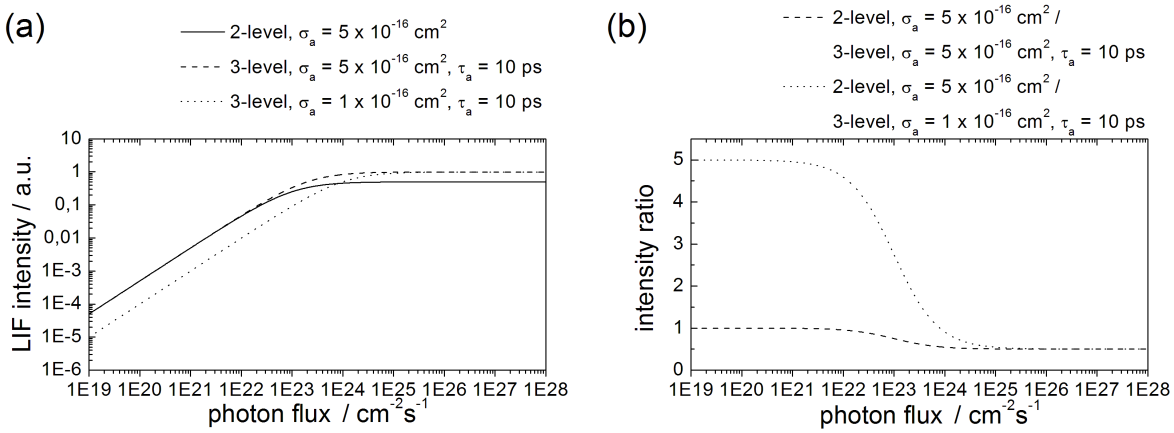

Fig. 4.4: Different saturation behavior of transitions with different absorption cross sections and life times of the excited states depending on the photon flux of the excitation laser (a) and their intensity ratio in the excitation spectrum (b). τ_e=10 ns is assumed as the life time of the emissive state (vibrational ground state of S$_1$), τ_a=10 ps for vibrational excited states of S$_1$ and phonon levels. The photon flux of a typical dye laser pulse (10 ns, 500 nm, 1 mJ) amounts to 2.5 E23 cm^{-1}s^{-1}. For the experiments used in this work typically attenuated pulses in the order of 1E21-1E22 cm^{-1}s^{-1} were used.

environment (multiplet splitting, see below). These latter ZPLs correspond to the same molecular transition as the former ZPL on the red side and thus exhibit (almost) identical saturation behavior. This was found e.g. in the case of tetracene. [HLTV02] Whereas, according to the discussion above, features of the PW are expected to saturate only at higher laser intensities than the ZPL. Thus, signals blue shifted to the ZPL(s) at the electronic origin that have no counterpart in the corresponding gas phase spectrum and saturate only at higher laser intensities than the corresponding ZPL(s) can usually be assigned to features of PWs.

The transition moments for PWs are usually smaller than for the corresponding ZPLs. According to the configuration coordinate model this corresponds to minor displacements of the potential energy curves with respect to the helium configuration. (fig. 4.3(right))

Intensity Pattern of Vibronic Transitions

As mentioned above, emission of free, isolated molecules as present in a supersonic jet stems exclusively from states isoenergetic to the state into which the molecule is excited. In particular, emission from vibrationally excited states within the S$_1$ manifold can be observed. The radiative process competes with non-radiative processes such as IC, IVR and ISC as reflected by the luminescence quantum yield. The intensity of the fluorescence $I_{LIF}^{free}(\nu)$ of a free molecule induced via excitation into a vibronic level $\Psi_{b\beta}$, where b denotes the electronic and β the vibrational state, is proportional to the square of the transition moment for the excitation and the fluorescence quantum yield $\Phi_{Fl}^{b\beta}(\nu)$: (cf. fig. 4.5(left))

$$I_{LIF}^{free}(\nu) \propto \underbrace{|\langle\Psi_{a0}|\,\hat{\mu}\,|\Psi_{b\beta}\rangle|^2}_{absorption}\,\Phi_{Fl}^{b\beta}(\nu) \tag{4.9}$$

The fluorescence quantum yield $\Phi_{Fl}^{b\beta}(\nu)$ describes the probability that excitation into the state $\Psi_{b\beta}$ leads to fluorescence, either directly from this state or after redistribution of the excitation energy. $\Phi_{Fl}^{b\beta}(\nu)$ is known to be state specific which is reflected by its dependence on the excess energy ν. [AHJ88](fig. 4.6(a)) The state specificity is due to state specific radiative and non-radiative rate constants which is also reflected by different homogeneous line widths. [AHJ88]

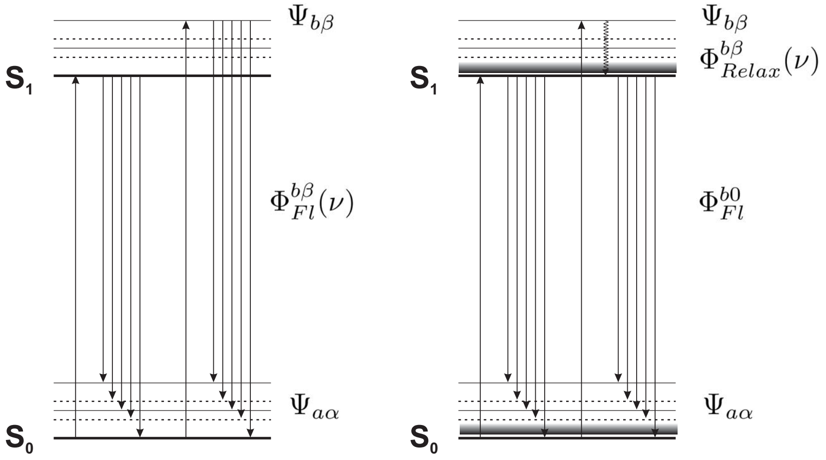

Fig. 4.5: Jablonski diagrams of an organic molecule in the gas phase(left) and in helium droplets(right). For details see text.

In helium droplets, energy dissipation is an additional non-radiative decay process. Further, the solvation may also modify the rates of the other decay channels of the molecules. For example, emission in helium droplets is observed exclusively from the vibrational ground state of S$_1$ (Ψ_{b0}) and is thus independent of the vibrational excess energy of the excitation. This is attributed to the dissipation of vibrational excess energy prior to radiative decay. [LS03, LS04a, LS04b, LS05, ST08] Therefore, the intensity of the fluorescence $I_{LIF}^{droplet}(\nu)$ induced via excitation into a vibronic level $\Psi_{b\beta}$ is proportional to square of the transition moment for the excitation, the quantum yield for the relaxation from $\Psi_{b\beta}$ into the vibrational ground state Ψ_{b0}, $\Phi_{Relax}^{b\beta}(\nu)$, and to the luminescence quantum yield Φ_{Fl}^{b0} of this radiating state: (cf. fig. 4.5(right))

$$I_{LIF}^{droplet}(\nu) \propto \underbrace{|\langle\Psi_{a0}|\,\hat{\mu}\,|\Psi_{b\beta}\rangle|^2}_{absorption}\,\Phi_{Relax}^{b\beta}(\nu)\cdot\Phi_{Fl}^{b0} \tag{4.10}$$

The relaxation into the emissive state competes also with relaxation into other states, in particular the electronic ground state. Thus, the quantum yield for the relaxation into the emissive state, $\Phi^{b\beta}_{Relax}(\nu)$, may be state specific, i.e. depend on the excess energy ν. A comparison of equations 4.9 and 4.10 shows that the intensity pattern of LIF of a certain molecule inside helium droplets is only identical to the pattern found in the gas phase if $\Phi^{b\beta}_{Fl}(\nu)$ in the gas phase and $\Phi^{b\beta}_{Relax}(\nu)$ in helium droplets exhibit identical dependence on the excess energy ν. This is not necessarily the case as is shown in fig. 4.6 for the example of 9,10-dichloroanthracene (9,10-DCA).

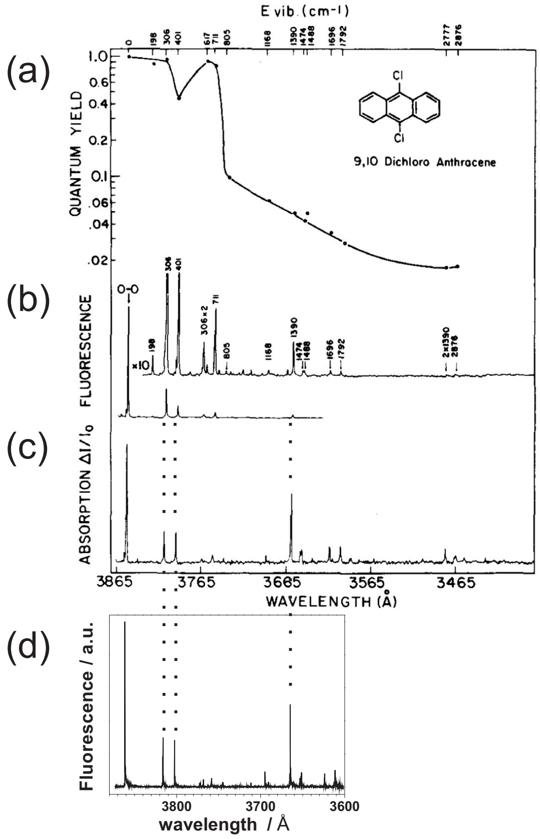

Fig. 4.6: Fluorescence quantum yield (a) of 9,10-DCA in a supersonic jet obtained by simultaneously recording the LIF-spectrum (b) and the absorption spectrum (plotted on a linear scale of the absorbed intensity) (c) compared to the LIF-spectrum recorded in helium droplets (d). The data points in plot (a) are connected only to guide the eye. Gas phase data are taken from ref. [AHJ88], the droplet spectrum is discussed in detail in chapter 5.2.

Fig. 4.6(a) shows the dependence of the fluorescence quantum yield on the excess energy (upper scale) and the excitation wavelength (bottom scale) in the supersonic jet. It was derived from the ratio of the spectrum of LIF-intensities (b) and the absorbed intensity (c) and reflects the state specificity. (cf. equ. 4.9 !) For comparison the LIF-spectrum in helium droplets is shown in fig. 4.6(d) for the same wavelength scale. The intensity pattern is almost identical to the pattern in the absorption (c), but in disagreement with the pattern in the LIF-spectrum (b). This is most striking for vibrational modes with energies of 308 cm^{-1} , 411 cm^{-1} , and 1390 cm^{-1} marked by the vertical dotted lines.

From a comparison of figs. 4.6(c) and (d) it can be concluded that in the case of 9,10-DCA, $\Phi^{b\beta}_{Relax}(\nu) \approx 1$ independent of the excess energy. (cf. equ. 4.10) The drops in the fluorescence quantum yield in fig. 4.6(a) are attributed to be due to a high ISC-rate for the corresponding states. [AHJ88] Hence it can be concluded that for 9,10-DCA in helium droplets the dissipation of vibrational energy is much faster than the competing ISC. Interestingly, for the similar molecule 9,10-dibromoanthracene, the fluorescence quantum yield in the gas phase shows a different dependence on the excess energy than 9,10-DCA demonstrating the state specificity of the fluorescence quantum yield. [AHJ88]

To conclude, the intensity pattern in fluorescence excitation spectra measured in the gas phase and in helium droplets may be different due to a different state specificity of the fluorescence quantum yield in the gas phase and the relaxation quantum yield in helium droplets. It should be noted that fluorescence excitation spectra are usually recorded via detection of the integral emission with a cut-off filter in front of the detector. Since in the gas phase the emission spectrum changes with the excitation wavelength, the detected integral emission may be influenced by the transmission spectrum of the cut-off filter. This does not happen in helium droplets.

Instead of detecting laser induced fluorescence leading to LIF-spectra, excitation spectra can also be measured using the depletion method. Whereas in LIF-spectra the probability that excitation of a certain vibronic state leads to fluorescence is interrogated, in depletion spectra the probability of dissipating the excess energy (weighted with the excess energy) is probed. Since the intensity patterns of both spectra are proportional to the probability for the excitation, a comparison of excitation spectra recorded with the two complementary methods yields information on the state specificity of energy dissipation and fluorescence, respectively.

Emission spectra in helium droplets reveal the emission originating exclusively from the vibrational ground level of S_1 independent of the excess energy. Hence emission spectra in helium droplets usually resemble the emission spectrum in the gas phase recorded via excitation at the electronic origin. However, discrepancies may occur due to a possible fine structure of electronic transitions (PWs) and multiplet structures as discussed in the following section. The intensity pattern in emission spectra reflects the transition probabilities determined by the Franck-Condon factors.

Multiplet Splitting

In few cases a splitting of ZPLs into multiplets has been observed in electronic excitation spectra [HLTV98, LLTV01, BML08, BMLS07, KRH05, TV04, LS03, LS04a, LS04b, LSK+04, LS05]. However, in some cases the criteria for the attribution of sharp features to either ZPLs or PWs remain unclear. [LLTV01] The transitions within a multiplet are assigned to pure molecular transitions with slightly different transition frequencies. The most prominent and detailed studied example is tetracene revealing a splitting of each transition into two ZPLs denoted α and β which are separated by 1.1 cm^{-1} . [HLTV98, HLTV01, PVH01, LTV04, LS05, LTV06] Pump-probe experiments demonstrated that the splitting is a ground state phenomenon but measurements of the fluorescence decay times after selective excitation of the α or β system showed that emission also stems from different excited states. [HLTV01] The splitting was tentatively attributed to different solvation structures that are either static (sites) or interconverted via tunneling. [HLTV01] In agreement with the pump-probe experiments, emission spectra demonstrated that α and β behave like different sites in a solid matrix. [LS05] Thus, the splitting is explained by different solvation structures around the organic molecule between which no relaxation occurs and which lead to the different transition frequencies.

A multiplet splitting of ZPLs was also observed for various phthalocyanine derivatives. [LS03, LS04a, LS04b, LSK+04, LS05] In excitation spectra the ZPLs of Mg-Pc and Zn-Pc reveal a triplet structure, whereas a single ZPL appears for the bare Pc. Though, the emission spectra of the bare Pc consist of two sets of sharp lines, separated by 10.3 cm^{-1} . The intensity of the main spectrum decreases in favor of a red shifted spectrum with increasing excess energy and suggests the presence of a barrier which must be overcome to populate the emissive state for the red shifted spectrum. The two distinct emissive states have been attributed to different solvation configurations around the phthalocyanine chromophore. [LS03] Path-integral Monte Carlo calculations identified the two solvation structures as the totally incommensurate and a mixed incommensurate/commensurate configuration of strongly localized first layers of helium. [WHKW05] A similar behavior was found in the emission spectra of Mg-Pc and van der Waals complexes of Pc with Ar. [Leh04, LS04b]

The spectroscopy of tetracene in helium droplets is discussed in more detail in chapter 5.1 and some more aspects on the behavior of Pc are found in chapter 7.1.

Solvation Structure

The multiplet structures occurring in the electronic spectra of some molecules and the dynamical conversion of the corresponding signals in case of the phthalocyanines provide evidence for multiple sites differing in the non-superfluid solvation layer around the chromophore. [SV01, LS03, LS04a, LS04b, LSK$^+$04, LS05] This interpretation is in line with the observations of distinct features of the PWs that cannot be explained by the dispersion curve of superfluid helium. The existence of a non-superfluid helium layer has previously been deduced from the anomalously large moments of inertia observed in the rotational spectra of large molecules. [CDF$^+$06] This picture of a shell of localized helium atoms is corroborated also by microwave and infrared experiments on helium clusters of small molecules with up to 72 He atoms. [MXJ07] They revealed an oscillation of the rotational constant with increasing cluster size which is interpreted in terms of the formation of distinct solvation shells. [MXJ07]

Further, the same picture of the chromophore surrounded by a non-superfluid helium layer embedded in the superfluid droplet as deduced from the experimental observations is also confirmed by theoretical approaches. [WHKW05, WDW09]

5 Anthracene Derivatives

Within this thesis electronic spectra of a series of anthracene derivatives were recorded. Many anthracene derivatives have a high fluorescence quantum yield and were already investigated in the gas phase experimentally (e.g. refs. [LFSZ84, WBGB87, AHJ88, TYH$^+$89, ZSFH94, SRS$^+$04, MLS$^+$05, NNS$^+$06, BMS$^+$09]) and theoretically (e.g. refs. [ZSFH94, NNS$^+$06, SH03a]). Further, they are available in high purity at low cost and are thus well suited as model compounds. The investigated molecules are shown in fig. 5.1 and differ in the number, nature and position of their substituent(s). They are listed according to their molecular symmetry starting with the unsubstituted Anthracene (AN) and 9,10-Dichloroanthracene (9,10-DCA) (point group D_{2h}). In the series 9-Chloroanthracene (9-CA)(C_{2v}), 9-Cyanoanthracene (9-CNA)(C_{2v}), 9-Phenylanthracene (9-PA)(C_2) and 9-Methylanthracene (9-MA)(C_s) the compounds differ only in the nature of their single substituent. The series starts with a single atom (chloro) as the most simple substituent followed by a diatomic linear rotor (cyano), and rotors with a two-fold (phenyl) and three-fold (methyl) axis, respectively. Finally, the position of the methyl group was varied yielding 1-Methylanthracene (1-MA)(C_s) and 2-Methylanthracene (2-MA)(C_s).

The interaction between the dopant and the helium environment is reflected by differences in the electronic spectra recorded in helium droplets compared to the corresponding gas phase data. The variation of the substituent provides information on its influence on this interaction. Of particular interest is the study of the fine structure of the electronic transitions also in comparison with other aromatic molecules such as benzene, naphthalene, tetracene and pentacene. Further, the vibrational fine structure is of interest which appeared broadened in two cases.

First, the electronic spectroscopy of each of the compounds as listed in fig. 5.1 will be presented and discussed with respect to the corresponding gas phase data. At the end of the chapter, the spectroscopic behavior of the anthracene derivatives in helium droplets will be compared among themselves revealing information about the interaction of the helium with the different molecules.

The helium droplets were generated with a stagnation pressure of 80 bar, nozzle temperatures ranging from 20 K to 23 K and a repetition rate of 20 Hz or 50 Hz. Laser intensities measured at the entrance window of the vacuum apparatus were typically

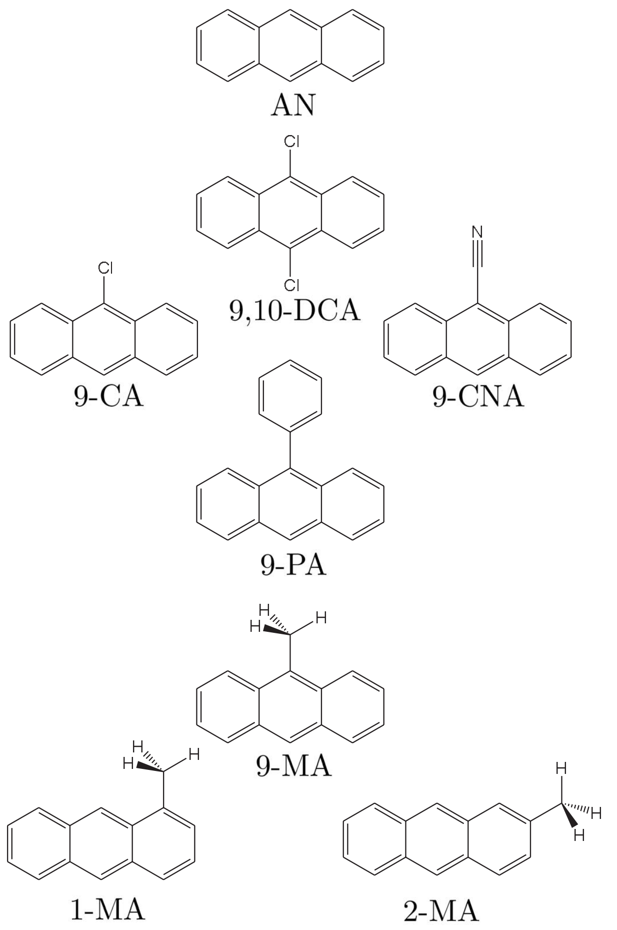

Fig. 5.1: Molecular structures of the investigated anthracene derivatives and their abbreviations: Anthracene (AN), 9,10-Dichloroanthracene (9,10-DCA), 9-Chloroanthracene (9-CA), 9-Cyanoanthracene (9-CNA), 9-Phenylanthracene (9-PA), 9-Methylanthracene (9-MA), 1-Methylanthracene (1-MA) and 2-Methylanthracene (2-MA).

varied from less than 10 μJ up to at most 100 μJ. Below laser intensities of about 10 μJ usually no saturation effects were observed. The displayed gas phase spectra of 1-MA, 2-MA, and 9-MA are taken from ref. [Gre09] and the excitation spectrum of 9-PA from ref. [Str05].

5.1 Anthracene (AN)

Electronic spectra of the series of quasi-one-dimensional fused aromatic rings of benzene [ScD$^+$04, BBC$^+$05, LBD08], naphthalene [Lin99], anthracene [KRH05], tetracene [HLTV98, LTV01, HLTV01, PVH01, HLTV02, LS05, LTV06, WDW09], and pentacene [HLTV98, HLTV02, LS05] in helium droplets have been reported in the literature. Transitions in the excitation spectra of benzene, naphthalene and pentacene consist of a single spectrally sharp ZPL accompanied by a weak PW, whereas in the spectrum of tetracene each transition is split into two ZPLs and accompanied by a PW. In the case of anthracene only the electronic origin was reported to consist of a series of ZPLs and their PWs. [KRH05] In this chapter excitation and emission spectra of AN including the vibrational satellite structure are presented and discussed. These data contribute to the discussion of the solvation of aromatic molecules in helium droplets. Further, the electronic spectra of AN serve as references for the substituted anthracene compounds discussed in the following chapters.

The electronic spectroscopy of AN in the gas phase (e.g. refs. [LFSZ84, KZ85, Ami87, Ami88, AHJ88]) as well as in solid matrices (e.g. refs. [DH81, CG82, ZSFH94]) is well known. AN shows the typical spectroscopic signature of a rigid molecule: The excitation spectrum is dominated by the electronic origin and no intense low frequency modes are observed. Most of the intense observed vibrational modes are total symmetric fundamentals with the lowest energetic prominent mode found at 385 cm^{-1} . From normal coordinate analyses this mode was assigned to a total symmetric bending mode. [Ohn79, ZSFH94, LBH$^+$98] This vibrational mode is characteristic for the anthracene chromophore and appears also in the spectra of all other anthracene derivatives as fundamental, overtones and in combination with other modes. [LFSZ84]
SVL-spectra in the gas phase and solid matrices reveal similar vibrational frequencies in the ground state S$_0$ compared to the electronic excited state S$_1$ for most of the vibrational modes. [LFSZ84, KZ85, AHJ88] For vibrational excess energies below 800 cm^{-1} absorption (excitation) and emission spectra recorded upon excitation at the electronic origin reveal a mirror symmetry as is typical for rigid molecules. [AHJ88] However, at higher excess energies Fermi-resonance effects cause the breakdown of this mirror symmetry. [AHJ88] The electronic and vibrational structure of AN was also investigated in many theoretical works, e.g. in ref.s [Ohn79, ZZ88, ZSFH94, GNB94, ZHS95, JWKJ96, LBH$^+$98, JK97]. These studies corroborate the experimental results and identify AN as a rigid molecule.

All data presented in the following were recorded with the LPD3002 dye laser (dye: DMQ), the PMT R 943-02 (Hamamatsu) with a cut-off filter WG385 in front, and the CCD-camera DU 420A-BU2 (Andor iDus) attached to the SPEX spectrograph. The oven temperature for optimum LIF signal of single AN while avoiding multiple doping of the helium droplets was 20°C.

5.1.1 Excitation Spectrum of AN

The excitation spectrum of anthracene (AN) recorded in helium droplets is shown in fig. 5.2. The intense transition at 27622 cm^{-1} is assigned to the electronic origin corresponding to a red shift of about 65 cm^{-1} compared to the gas phase. [LFSZ84, AHJ88, SRS$^+$04]. The vibrational frequencies in the excitation spectrum are in agreement with those found in the gas phase spectra. (table 5.1) However, the intensity pattern is rather similar to the pattern in the absorption spectrum than in the excitation spectrum in the gas phase. [AHJ88] This is due to the different processes leading to fluorescence in the droplets compared to the gas phase as discussed in chapter 4.2. All of the transitions are accompanied by a broad asymmetric PW to the blue with peak intensities less than about 25 % of the corresponding ZPL, as is typically found for rigid molecules in helium droplets. The PWs are not separated from the ZPLs by a gap as was found for other molecules such as tetracene or pentacene. [HLTV02] The laser intensity for recording the spectrum shown in fig. 5.2 was chosen to avoid saturation effects and was kept constant during the measurement.

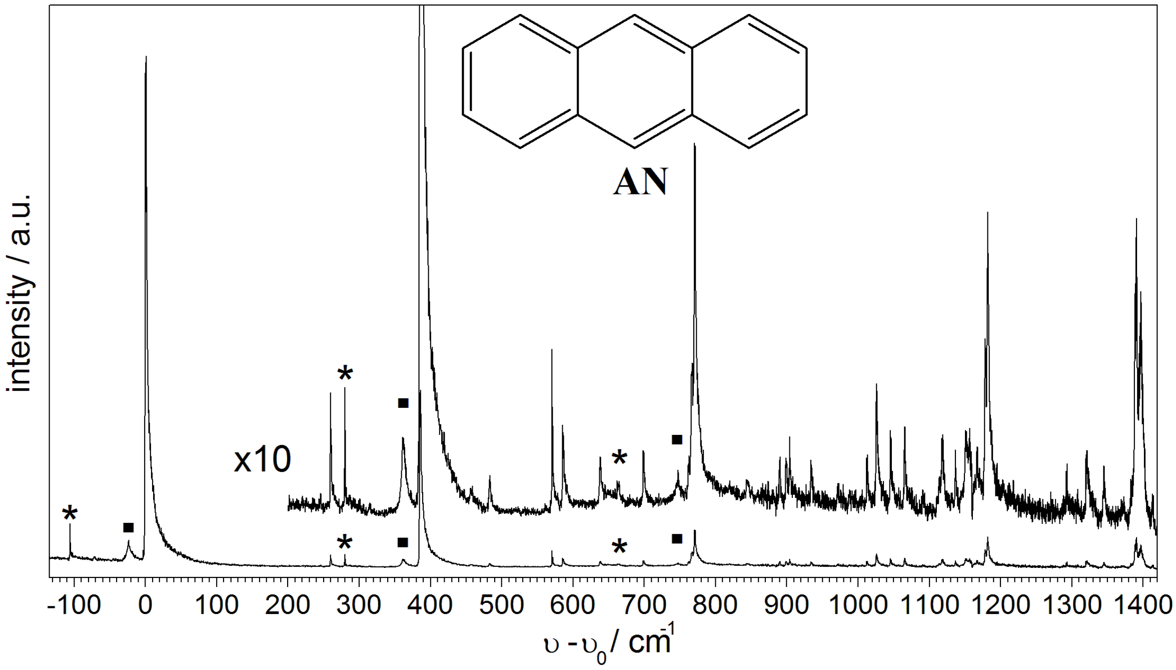

Fig. 5.2: Excitation spectrum of AN in helium droplets with $\nu_0 = 27622\ \mathrm{cm}^{-1}$. Signals marked with asterisks are assigned to complexes with water, signals marked with squares to complexes with other impurities.

Fig. 5.3 shows the electronic origin recorded with different laser intensities and reveals a splitting into at least two transitions α and β separated by 1.0 cm^{-1} .

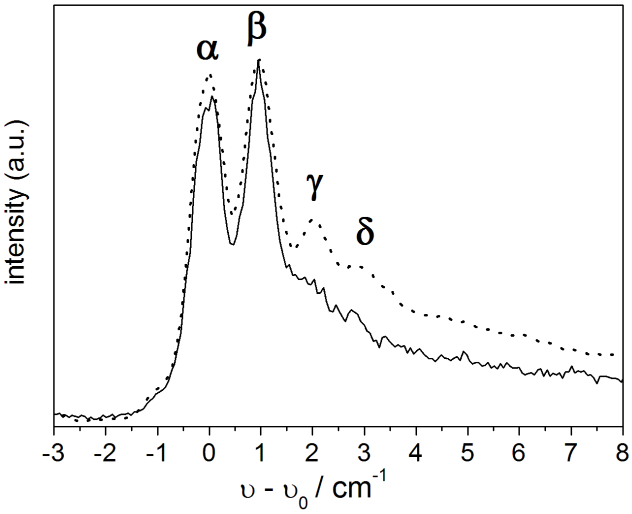

Fig. 5.3: Excitation spectrum of AN in helium droplets at the electronic origin recorded with different laser intensities. $\nu_0 = 27622$ cm^{-1} .(see text)

α and β show identical saturation behavior. At higher laser intensities two additional peaks assigned as γ and δ are resolved shifted by 2 cm^{-1} and 3 cm^{-1} to the blue with respect to the α peak. Both γ and δ saturate only at higher laser power. Therefore, α and β have almost identical transition moments whereas that of γ and δ is much lower. Further increasing the laser intensity causes a broadening of the spectrum with the PW rising in relative intensity as already reported in ref. [KRH05]. A line shape of the electronic origin as shown in fig. 5.3 is only observed in helium droplets but not for the isolated molecule in a supersonic jet and is thus due to the interaction of the helium environment with the embedded AN molecules. [AHJ88, SRS$^+$04] In particular, the splitting into α and β cannot be attributed to rotational contours. [AHJ88, KRH05] A similar splitting of all transitions by about 1.1 cm^{-1} was observed in the electronic excitation spectrum of tetracene doped into helium droplets. [HLTV98, LTV01, HLTV01, PVH01, HLTV02, LS05, LTV06] (see below)

A similar fine structure as compared to the electronic origin was found for all vibronic transitions in fig. 5.2 as shown in fig. 5.4 for selected vibrational satellites. However, with increasing vibrational energy the line widths of the transitions tend to increase and thus the splitting is often not clearly resolved. The relative intensities of α and β is about 1:1 for most of the vibronic transitions whereas it is found to be about 2:1 for transitions with vibrational excess energies of 260 and 571 cm^{-1} , respectively. Most of the vibrational frequencies are shifted by less than ± 10 cm^{-1} with respect to the gas phase. (table 5.1)

The size of the shifts are in the typical range observed for vibrational frequencies of organic molecules doped into helium droplets. [SV01, TV04] In contrast, the vibrations at 260 cm^{-1} and 571 cm^{-1} are shifted by about 30 cm^{-1} compared to the gas phase values of 232 cm^{-1} and 541 cm^{-1} suggesting a stronger perturbation by the helium environment. In solid matrices, these vibronic transitions also show a larger vibrational shift ($\approx$ 100 cm^{-1}) compared to other vibronic transitions with shifts typically below $\pm$ 25 cm^{-1} . [ZSFH94] (cf. table 5.1) Interestingly, the fluorescence decay times recorded in gas phase experiments revealed an essentially constant life time of all vibronic levels except of those populated upon excitation at these two vibronic transitions. [AHJ88] The anomalously long decay times of the corresponding excited states were interpreted as indication for a coupling to another electronic state with a longer life time. [AHJ88] This is corroborated by the low relative intensity, which is interpreted as indication for a non-totally symmetric mode observable only due to vibronic coupling (Herzberg-Teller coupling), and also by normal mode analyses. [LFSZ84, KZ85, GNB94]

A weak vibronic transition separated by 209 cm^{-1} from the electronic origin with an intensity lower by a factor of four than the 232 cm^{-1} mode is found in the gas phase experiments. [KZ85] This vibronic transition is not found in the droplet spectrum.

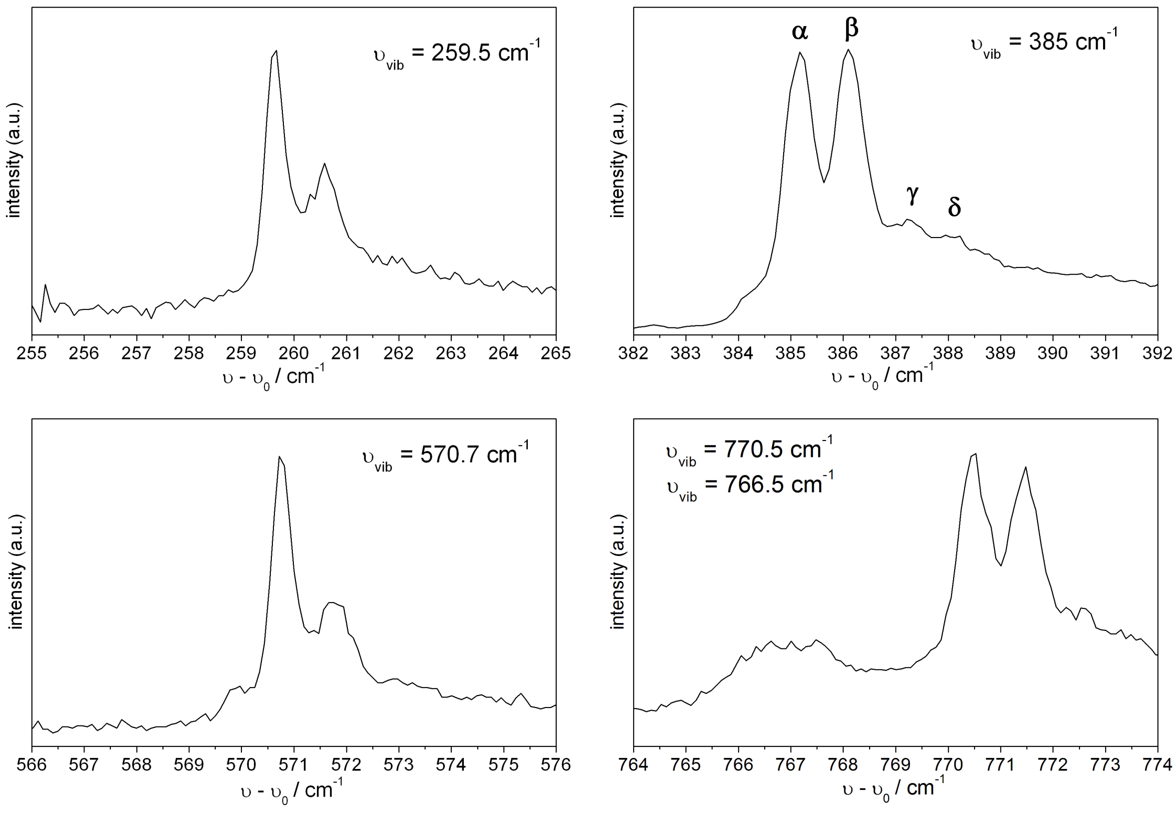

Fig. 5.4: Excitation spectra of selected vibronic transitions of AN in helium droplets on an expanded scale. $\nu_0 = 27622$ cm^{-1} . The 770.5 cm^{-1} vibration is assigned to the first overtone of the 385 cm^{-1} fundamental. [KZ85]

Some signals in fig. 5.2 are marked with asterisks. These accompany all prominent vibronic features of the bare molecule with a red shift of about 106 cm^{-1} and disappear after some time of heating the sample. Thus, these signal are attributed to a complex of AN with an impurity which evaporates from the solid AN sample. The red shift of 106 cm^{-1} is similar to the shift observed upon complexation of tetracene with single H_2O [LTV06] and thus the signals are tentatively assigned to stem from an AN(H_2O) complex. The transitions of the complex consist of a single line as is shown in fig. 5.5 for the electronic origin. Thus, they do not exhibit the fine structure observed at the transitions of the bare system similar as found for most of the van der Waals-complexes of tetracene. [HLTV98, LTV01, PVH01, HLTV01, HLTV02, LTV04, LTV06]

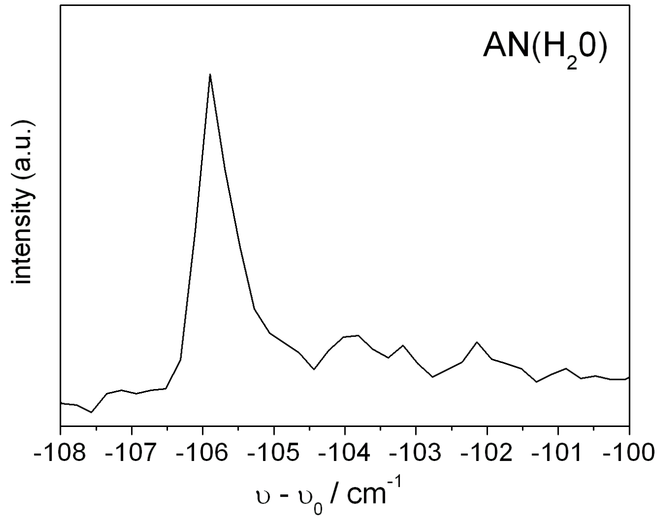

Fig. 5.5: Excitation spectrum at a transition red shifted to the electronic origin of AN in helium droplets attributed to an AN(H_2O) complex. ν_0 = 27622 cm^{-1} .(see text)

Another remarkable feature of the excitation spectrum shown in fig. 5.2 are the weak asymmetric peaks (FWHM $\approx$ 5 cm^{-1}) marked with squares which accompany each of the intense transitions shifted by about 23 cm^{-1} to the red. As for the complexes with water this feature is presumably present throughout the entire spectrum though for the weak vibronic transitions hidden below the noise limit. In contrast to the signals shifted by 106 cm^{-1} , the signals shifted by 23 cm^{-1} do not disappear with time and show the same response to the variation of experimental parameters such as stagnation conditions, sample temperature or laser intensity as observed for the intense AN resonances. A similar feature was reported for AN in a supersonic jet with a red shift of 22 cm^{-1} . [SRS^+04] However, it was observed with much lower relative intensity and therefore only at the electronic origin. Since it is still present at 0.37 K an assignment to a sequence band of the 232 cm^{-1} mode (260 cm^{-1} in helium droplets) as proposed in ref. [SRS$^+$04] can be excluded. The signals resemble a second excitation spectrum of AN shifted to the red and with reduced intensity and are thus indicative of AN complexed with another impurity. Since the same impurity was presumably present in gas phase experiments in ref. [SRS$^+$04] the impurity is likely to stem from the sample. The increased intensity ratio of this complex with respect to transitions of bare AN in helium droplets compared to the supersonic jet reflects the increased complexation cross section in the droplets [TV04] and thus corroborates the assignment.

Tab. 5.1: Transition wavenumbers $\nu - \nu_0$ (cm^{-1}) in the excitation spectrum of AN in helium droplets and their relative intensities I/I$_0$. All numbers in helium droplets are referred to the α transition at the electronic origin (ν_0 = 27622 cm^{-1} , I$_0$ = 1) and for bare AN correspond to vibrational frequencies in the excited state. α,β denotes a clearly resolved splitting with the relative intensities given in brackets. (α,β) denotes an indicated, but not clearly resolved splitting. No statement is given for weak or broad signals. For comparison vibrational frequencies in the excited state of AN in the gas phase [KZ85], ν_{vib}(jet), and a solid matrix [ZSFH94], ν_{vib}(matrix), are listed.

$\nu - \nu_0$ / cm^{-1} (droplet)	I/I$_0$ (droplet)	assignment (droplet)	ν_{vib} / cm^{-1} (jet)	ν_{vib} / cm^{-1} (matrix)	shift / cm^{-1} (droplet)
-106	0.09	AN(H_2O) (origin)	-	-	-
-23	0.05	AN(?)	-	-	-
-3	0.03	hot phonon ?	-	-	-
-1	0.08	hot phonon ?	-	-	-
0	1.00	α,β (1:1)	0	0	0
-	-		209	-	-
260	0.02	α,β (3:2)	232	320	+28
280	0.025	386-106 ,AN(H_2O)	-	-	-
361	0.015	384-23, AN(?),	-	-	-
382	0.01	385-3 (hot phonon ?)	-	-	-
385	0.34	α,β (1:1)	385	389	0
456	<0.01	broad	-	457	-
483	0.01	(α,β)	473	499	+10
571	0.03	α,β,(2:1)	541	654	+30
586	0.02	α,β, (1:1)	583	588	+3
638	0.01		-	-	-
662	0.007		-	-	-
665	0.007	771 - 106 ,AN(H_2O)	-	-	-
699	0.013	α,β, (1:1)	-	706	-
748	0.01	771-23, AN(?),	-	-	-
762	0.01	α,β, (1:1)	748	728	+14
767	0.03		755	-	+12
771	0.07	α,β, (1:1)	766	778	+5
890	0.01	(α,β)	889	870	+1
899	0.01	(α,β)	895	880	+4
904	0.01		905	908	-1
934	0.01	(α,β)	-	923	-
970	0.006	(α,β)	-	976	-
1012	0.012	α,β (1:1)	1019	997	-7
1026	0.03	(α,β)	-	1025	-
1045	0.02	α,β (1:1)	1042	1045	+3
1066	0.02	(α,β)	-	1069	-
1111-1114	< 0.01	bunch of peaks	1094	1092	+17 - +20
1118	0.015	α,β	-	1114	-

$\nu - \nu_0$ / cm^{-1} (droplet)	I/I$_0$ (droplet)	assignment (droplet)	ν_{vib} / cm^{-1} (jet)	ν_{vib} / cm^{-1} (matrix)	shift / cm^{-1} (droplet)
1137	0.01	(α,β)	1142,1146	1140	+5 - +9
1152-1159	0.02	bunch of peaks	1158	1160	-6 - +1
1167	0.01		1168	1170	-1
1178	0.04	α,β (1:1)	-	-	-
1182	0.06	(α,β)	1184	1185	-2
1292	0.01		1291	1291	+1
1321	0.01	α,β (1:1)	-	1325	-
1345	0.01	(α,β)	-	-	-
1389	0.04	(α,β)	1380	1387	+9
1391	0.06	(α,β)	-	-	-
1395	0.03	(α,β)	1389	-	-
1397	0.04	(α,β)	-	1402	-

5.1.2 Emission Spectrum of AN

The dispersed emission spectrum recorded upon excitation at ν_{exc} = 28007 cm^{-1} is shown in fig. 5.6. The electronic origin is identified at ν_0 = 27605 cm^{-1} in agreement with the origin in the excitation spectrum (ν_0 = 27622 cm^{-1}) within experimental accuracy. It is independent of the excitation frequency as is typically found in helium droplets. In particular, the emission spectrum at this resolution taken with the 1200 lines/mm grating is insensitive on excitation at an α or β transition or at a PW. The transitions have a slight asymmetric tail to the red which can be assigned to PWs. The emission spectrum has the same intensity pattern as in the gas phase recorded upon excitation at the electronic origin. [LFSZ84, AHJ88] In this case, the same state, namely the vibrational ground state of S$_1$, emits in the gas phase and in helium droplets. The vibrational frequencies of the ground state determined in helium droplets deviate from the corresponding values in the gas phase and solid matrices by less than ± 10 cm^{-1} which is the experimental accuracy. (table 5.2) In the supersonic jet an additional mode appeared at 237 cm^{-1} with an intensity of about 1 % of the electronic origin and therefore is probably too weak to be observed in the droplet experiment.
Unfortunately, no reasonable dispersed emission spectra could be detected with the laser on resonance with the signals red shifted by -23 cm^{-1} to the intense transitions of AN observed in the excitation spectrum.

Dispersed emission spectra were also recorded at higher resolution using the 2400 lines/mm grating installed in the SPEX spectrograph. The S/N ratio in emission spectra recorded upon excitation with a pulsed laser is quite limited, in particular when recorded at high resolution. (cf. chapter 3.2.6) The data acquisition time was set to 2×1800 s and further increasing this time did not gain additional information due to the increased probability of detecting cosmic events in the spectral region of interest.

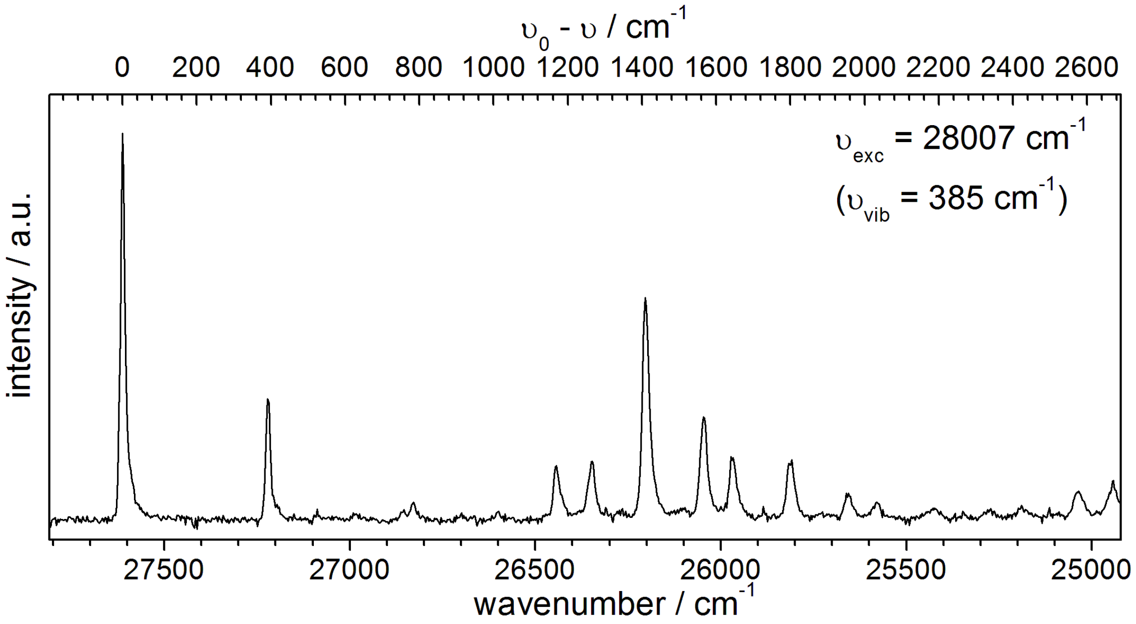

Fig. 5.6: Emission spectrum of AN in helium droplets via excitation at $\nu_{exc} = 28007$ cm^{-1} (ν_{vib} = 385 cm^{-1}). Emission is dispersed with the SPEX spectrograph (1200 lines/mm grating). ν_0 = 27605 cm^{-1} . The distance between two pixel columns amounts to about 3.2 cm^{-1} at the blue and 2.5 cm^{-1} at the red end of the spectrum.

With the improved spectral resolution emission spectra were recorded upon excitation at the α, β, γ, and δ transitions of the electronic origin (fig. 5.3) and the prominent vibronic transition at 385 cm^{-1} vibrational excess energy (fig. 5.4), respectively. From resonance to resonance the laser energies thus were tuned by about 1 cm^{-1} . The spectra recorded with the dye laser set on the resonances at the electronic origin were corrected for the background containing stray light from the laser. The spectra of pure laser stray light are shown in fig. 5.7(a) and reflect the spectral resolution for separately detected signals. The recorded stray light has a FWHM of about 3 cm^{-1} and the maxima are separated by one pixel column on the CCD-chip corresponding to about 1.4 cm^{-1} .

Sections of the emission spectra recorded upon excitation at the electronic origin at the four frequencies (α, β, γ, and δ) are shown in fig. 5.7 (b) and (c). These sections show the electronic origin and the prominent 391 cm^{-1} mode in S_0, respectively. Fig. 5.7 (d) shows the emission spectrum recorded upon excitation at α, β, γ, and δ peaks of the 385 cm^{-1} mode in S_1 at the electronic origin. Under these conditions no stray light correction is required. However, the S/N-ratio was too weak to obtain reasonable information about the 391 cm^{-1} mode in S_0.

The electronic origin in the emission spectrum in fig. 5.7(b) shows two contributions, a weaker emission at about 27612 cm^{-1} and a stronger one at about 27605 cm^{-1} . The same structure can be found in fig. 5.7(c) and (d). However, this structure is artificial and is caused by imperfect imaging of the entrance slit to the CCD-chip. In contrast to the laser stray light, the emission spectra recorded upon excitation at α, β, γ, and δ reveal

Tab. 5.2: Transition wavenumbers $\nu - \nu_0$ (cm^{-1}) in the emission spectrum of AN in helium droplets and their relative intensities I/I$_0$. Frequencies are given with respect to the electronic origin in the emission spectrum at ν_0 = 27605 cm^{-1} and correspond to vibrational frequencies in the ground state S$_0$. Vibrational frequencies in the ground state of AN observed in the gas phase [LFSZ84], ν_{vib}(jet), and in a Shpol'skii-matrix [CG82], ν_{vib}(matrix), are listed for comparison.

$\nu - \nu_0$ / cm^{-1} (droplet)	I/I$_0$ (droplet)	ν_{vib} / cm^{-1} (jet)	ν_{vib} / cm^{-1} (matrix)	shift / cm^{-1} (droplet)
0	1.00	0	0	0
-	-	237	-	-
391	0.31	390	394	+1
629	0.01	624	627	+5
758	0.03	753	759	+5
785	0.05	778	788	+7
1168	0.14	1165	1163	+3
1264	0.15	1263	1257	+1
1409	0.57	1409	1407	0
1566	0.27	1566	1566	0
1642	0.16	1643	1639	-1
1800	0.15	1797	1796,1801	+3
1957	0.07	-	1961	-
2033	0.05	-	2034	-
2188	0.03	-	-	-
2337	0.03	-	-	-
2423	0.03	-	-	-
2575	0.07	-	-	-
2670	0.10	-	-	-

only two different spectra (1) and (2). As can be seen in fig.s 5.7(b)-(d) the emission spectra recorded upon excitation at α and β coincide (emission (1)) and, shifted to the blue by one CCD-pixel (1.4 cm^{-1}), the emission upon excitation at γ and δ coincide (emission (2)). Thus, emission originates from two different excited states. One of them is populated upon excitation at α and β transitions whereas the other one is populated upon excitation at γ and δ transitions. However, within the experimental accuracy it is not clear if the transition frequencies at the electronic origin of emission (1) and of the α peak at the origin in the excitation spectra are identical. Thus, the emission spectra only provide evidence that upon excitation at β the systems relaxes into the same emissive state than upon excitation at α. Though, it is not clear if β relaxes directly into α or relaxation occurs also upon excitation at α transitions. In analogy, the δ system may relax into the γ system or both relax to populate the emissive state.

It should be noted that the laser intensity for recording the emission spectra with the 2400 lines/mm grating was higher than for excitation spectra and emission spectra with the 1200 lines/mm grating and might have caused already saturation effects.

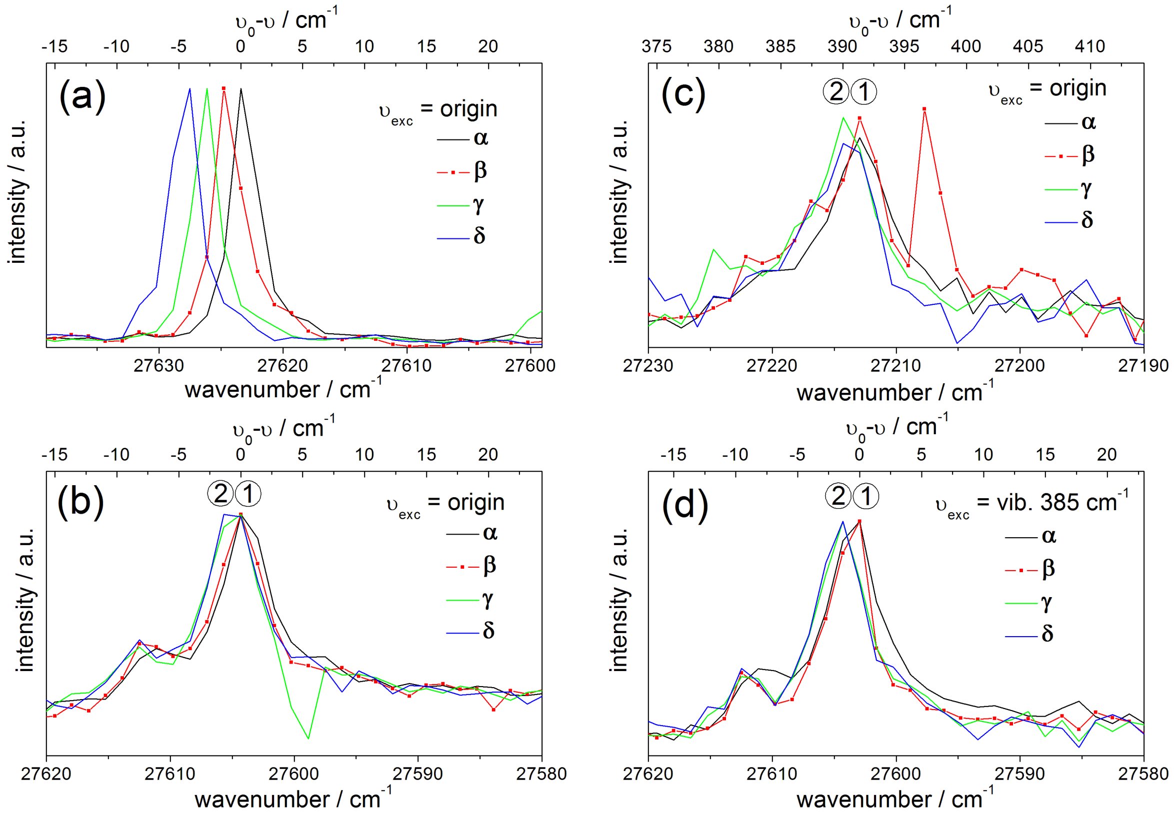

Fig. 5.7: Emission spectra of AN in helium droplets via excitation (ν_{exc}) at the transitions α, β, γ and δ of the electronic origin and the 385 cm^{-1} mode in the excitation spectrum. (b-d) The laser stray light recorded with the same laser frequencies demonstrate the spectral resolution. (a) Emission is dispersed with the SPEX spectrograph (2400 l/mm grating). $\nu_0 = 27623.41$ cm^{-1} (a), 27604.31 cm^{-1} (b,c) or 27602.95 cm^{-1} (d). The distance between two pixel columns amounts to about 1.4 cm^{-1} at the electronic origin and 1.3 cm^{-1} at the 391 cm^{-1} mode in the emission spectrum. The intense peak at 27208 cm^{-1} in (c) is a detected cosmic event.

5.1.3 Discussion

The vibrational pattern in electronic excitation and emission spectra of AN in helium droplets exhibit the typical behavior of a rigid molecule. Roughly, the spectra reflect the corresponding gas phase data. However, the transitions in the excitation spectrum show a splitting into at least two transitions separated by 1.0 cm^{-1} . This splitting has no counterpart in the gas phase. [AHJ88, SRS$^+$04] Further, all transitions are accompanied by weak asymmetric PWs, however without the phonon gap to the ZPL as expected for pure superfluid helium.

A similar splitting of the ZPLs of each transition by 1.1 cm^{-1} was observed in the electronic excitation spectra of tetracene in helium droplets. [HLTV98, LTV01, HLTV01, LS05] (Fig. 5.8(a)) Pump-probe experiments demonstrated that the splitting into the two contributions α and β is a ground state phenomenon. However, measurements of the fluorescence decay times after selective excitation of the α or β systems showed that the

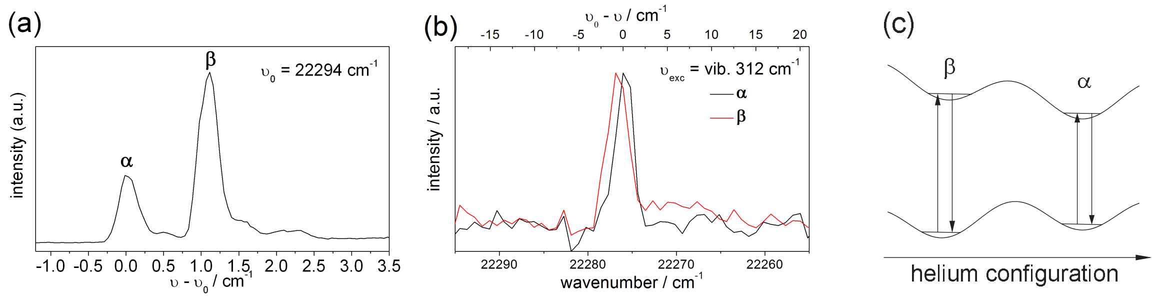

Fig. 5.8: Excitation (a) and emission (b) spectrum at the electronic origin of Tetracene in helium droplets and the configuration coordinate model to explain the experimental observations (c). The excitation spectrum was recorded with a GG475 cut-off filter in front of the PMT R 943-02 (Hamamatsu) and an oven temperature of 100°C. ν_0=22294 cm^{-1} . Dispersed emission is recorded upon excitation with 312 cm^{-1} vibrational excess energies with the CCD DU 420A-BU2 and the SPEX spectrograph (2400 lines/mm grating). The distance between two pixel columns amounts to 0.84 cm^{-1} at the electronic origin.

emission is also stemming from different excited states. [HLTV01] These results were confirmed by emission spectra [LS05]: Spectra recorded upon selective excitation at α or β transitions were shifted against each other by the amount of the splitting in the excitation spectrum. (Fig. 5.8(b)) Upon excitation with vibrational excess energy no interconversion between the two spectra was observed. Thus, α and β behave like two different species which in matrix isolation spectroscopy use to be addressed as sites. [FH84] The splitting was explained to arise from different configurations of the helium solvation layer around the dopant molecule which do not interconvert by any means. [LS05] (Fig. 5.8(c)) The existence of different solvation structures was also suggested by theoretical work. [WDW09]

The α and β transitions of tetracene are not of equal intensity in the excitation spectrum. Though, they exhibit the same saturation behavior which is different from the accompanying PW separated by a gap of about 5 cm^{-1} from the ZPLs and containing also sharp features. [HLTV02]

Various heterogeneous van der Waals-complexes of tetracene were also investigated. [HLTV98, LTV01, PVH01, HLTV01, HLTV02, LTV04, LTV06] Among them are complexes of tetracene with single H_2O molecules. [LTV06] Different isomers of the 1:1 complex could be identified by comparison with the electronic spectra of the corresponding v.d.W.-complexes formed in the supersonic jet. [LTV06] No splitting of the ZPLs of the 1:1 complexes of tetracene with water was observed. This was attributed to a perturbation of the first solvation layer of He around tetracene in agreement with studies on other v.d.W.-complexes of tetracene. [PVH01, LTV06]

In the case of AN a splitting is observed in the excitation spectrum. Upon complexation with H_2O (cf. fig. 5.5) the splitting vanishes. This suggests that, as for tetracene, the splitting is due to different solvation structures around the chromophore which is distorted upon complexation.

High resolution emission spectra recorded upon excitation at α and β as well as γ and δ resonances of the excitation spectra coincide. However, the two pairs of spectra are slightly shifted against each other by about 1 - 2 cm^{-1} which is at the limit of the resolution of the experimental setup.

In the following several models will be discussed in order to interpret the experimental observations within the configuration coordinate model successfully applied to tetracene. (Fig. 5.8(c)) In view of the large size of the droplets ($\approx 10^5$ He atoms per droplet) and the small energy difference of the four excitations inhomogeneous effects resulting from different droplet sizes can be neglected. Further, emission is assumed to stem from relaxed states, i.e. not e.g. from hot phonon states. This assumes fast dissipation of vibrational and phonon excess energy as is reported in the literature for many examples. [LTV01, TV04, LS04b, LS05, CDF$^+$06] All models are based on the presence of four distinct resonances (α, β, γ, and δ) in the excitation spectrum. α is the first intense transition on the red side and thus is assigned to a ZPL with high confidence. Different assignments of the other transitions will be discussed.

Model 1: α=ZPL; β, γ, δ = PW

In this model α is the only ZPL while all other features belong to the PW. However, β exhibits the same saturation behavior as α indicating the same transition moment. Further, the saturation behavior of γ and δ is different compared to α and β. However, the PW usually displays its own saturation behavior different to that of the ZPL. Moreover, upon excitation at β, γ, and δ the same emission as observed upon excitation at α should occur which contrasts the experimental data. (cf. fig. 5.7) Thus, this model is in contrast to the observations in both excitation and emission spectra and thus can be excluded.

Model 2: α =ZPL, β = PW ; γ = ZPL, δ = PW

In this model α and γ are ZPLs with β and δ as features of their corresponding PWs with phonon energies of 1.0 cm^{-1} . However, α and β as well as γ and δ exhibit identical saturation behavior. This is highly unlikely for a ZPL and PW of a rigid molecule yielding sharp excitation spectra with no obvious dominance of PWs. Moreover, it is rather strange to easily saturate the β-PW while not saturating the γ-ZPL.

However, this model fits to the emission behavior as illustrated in fig. 5.9. Emission stems from α and γ states (after possible relaxation of the solvation shell). Excitation at their corresponding PWs β and δ, respectively, is followed by dissipation of the phonon energy leading to emission from α and γ states. This model implies that there is no interconversion between the two different sites. However, in view of the saturation behavior in the excitation spectra this model can be excluded.

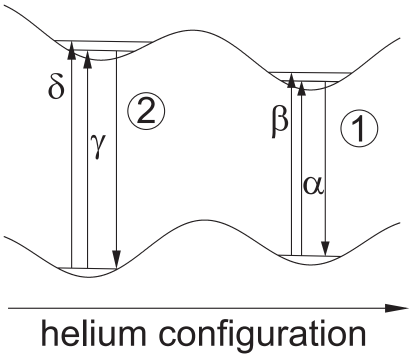

Fig. 5.9: Model 2: Configuration coordinate model for AN in helium droplets assuming $\alpha =$ ZPL, $\beta =$ PW ; $\gamma =$ ZPL, $\delta =$ PW. (see text)

Model 3: α, β =ZPL; γ, δ = PW

According to this model α and β are ZPLs with γ and δ belonging to their corresponding PWs with phonon energies of 2.0 cm^{-1} . Assigning α and β as ZPLs is in line with their identical saturation behavior. Further, γ and δ also exhibit identical saturation behavior and saturate only at higher laser intensities than α and β. Thus, model 3 is in agreement with the saturation behavior.
The emission spectra in fig. 5.7 revealed that excitation at β is followed by relaxation into the identical emissive state than excitation at α. Further, upon excitation at γ and δ the system also relaxes into the same emissive state which, however, is different to that upon excitation at α and β. Thus, according to model 3 excitation with excess phonon energy would cause relaxation into a different emissive state than excitation at the ZPLs. This is illustrated in fig. 5.10 for the case that the splitting in the excitation spectrum is only due to different ground state configurations. Alternatively, schemes with different minima only in the excited state or in both electronic states may be applied. In fig. 5.10 excitation originates from both ground states. Emission recorded upon excitation at α and β originates from the relaxed emissive state on the right side (green) while excitation at γ and δ causes emission from a different relaxed emissive state, which is indicated on the left side (red).

Model 3 is in agreement with experimental observations in both, excitation and emission spectra. However, it requires the reorganisation of the solvation layer being faster than the dissipation of excess phonon energy. Otherwise e.g. excitation at γ would lead to the

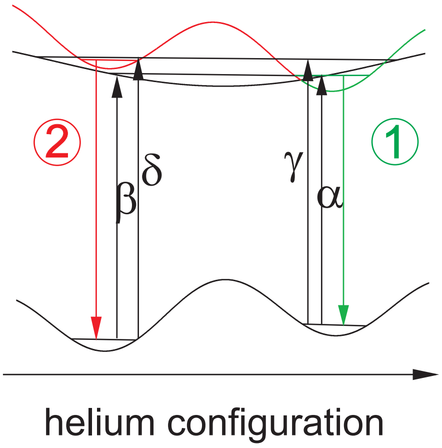

Fig. 5.10: Model 3: Configuration coordinate model for AN in helium droplets assuming α, β =ZPL; γ, δ = PW. (see text)

same emission as excitation at α. Interestingly, the line widths of all four transitions α, β, γ, and δ in the excitation spectra are broader than expected for the ZPL of anthracene at 0.37 K particularly if the rotational constant would be reduced upon solvation. [KRH05] This may be due to a reduced life time of the corresponding excited states in agreement with a relaxation process. The line width of α and β are about 0.7 cm^{-1} corresponding to a lower limit of a relaxation time of 8 ps.

From an energetic point of view a different relaxation of the helium solvation layer due to excitation with excess phonon energy seems unlikely due to the small amount of excess energy of 2 cm^{-1} (phonon energy) compared to the total excitation energy of about 27620 cm^{-1} . Relaxation effects were also observed for phthalocyanines in helium droplets [LS03, LS04a, LS04b]: The excitation spectrum of free base phthalocyanine reveals only single ZPLs. Though, the emission spectra consist of two sets of sharp lines, separated by 10.3 cm^{-1} . The intensity of the main spectrum decreases in favor of a red shifted spectrum with increasing vibrational excess energy though the red shifted spectrum already appears upon excitation at the electronic origin, i.e. without any excess energy. [LS03, LS04a, LS04b] Interestingly, an enhanced relaxation was observed upon excitation with excess phonon energy. [LS04b]

However, model 3 would require a quantitative relaxation into a different emissive state upon excitation with 2.0 cm^{-1} excess phonon energy as compared to the ZPLs. Further, additional vibrational excess energy (cf. fig. 5.7(d)) would not alter the relaxation process and thus would suggest that it has to be distinguished between vibrational and phonon excess energy. This is in contrast to the observations on the phthalocyanines. Moreover, this is not feasible due to the fast dissipation of vibrational energy observed in helium droplets which certainly involves modes of the helium environment, i.e. phonons. Thus, model 3 is in line with the experimental observations but requires circumstances which are unlikely.

Model 4: α, β = ZPL; γ, δ = PWs of other ZPLs

A modification of model 3 would be to assign α and β as ZPLs and γ and δ to PWs not corresponding to α and β, but to different, not clearly observed ZPLs. As discussed for model 3, this would explain the different saturation behavior of γ and δ compared to α and β. Dissipation of the phonon energy would lead to emission of the corresponding molecular states. The missing of the ZPLs corresponding to γ and δ could be explained by a lower transition probability of the ZPLs compared to the the PWs. However, for all molecules with PWs having a higher transition probability than the corresponding ZPLs the PW was found to be extended over more than 20 cm^{-1} which is not observed in the excitation spectrum of AN. Moreover, a large displacement of the potential energy curves with respect to the helium configuration, which is required for much smaller transition probabilities of the ZPLs compared to the corresponding PWs, would tend to shift the emission by more than 20 cm^{-1} to the red compared to the excitation energy. However, the shift compared to excitation at α and β is only about 1-2 cm^{-1} .
Due to the weak PW and its shape in the excitation spectra together with the small shift between emission (1) and (2) among themselves and compared to the excitation frequencies this model can probably be excluded.

Model 5: α, β, γ, δ = ZPL

In this model all of the distinct features α, β, γ, and δ are assigned to ZPLs as was proposed in ref. [KRH05]. However, the ZPLs should have similar transition moments and thus exhibit almost identical saturation behaviors which is in contrast to the experimental observation. The different saturation behavior could be explained by a spectral overlap of ZPLs γ and δ with PW-structures of α and β. Consequently, upon excitation at γ and δ transitions, the same emission as upon excitation at α and β (emission (1)) would be expected to contribute to the spectrum. For the laser intensities used to record the emission spectra, emission (1) should be observed upon excitation at γ and δ with about half of the intensity than upon excitation at α and β. In particular, it should be at least as intense as emission induced upon selective excitation at the γ and δ ZPLs. However, the emission spectra observed upon excitation at γ and δ are only shifted with respect to that recorded upon excitation at α and β but do not reveal a change of the line shape, in particular of the line width. Thus it can be concluded that upon excitation at γ and δ the state emitting upon excitation at α and β is not populated.
Therefore, neither the excitation nor the emission spectra are hinting to this model.

To conclude, none of the models can explain the observed spectroscopical data satisfactorily. This may indicate that the static configuration coordinate model cannot be applied and the splitting in the excitation spectrum and the peculiar emission behavior require to consider dynamic effects. [WDW09] These could possibly involve the exchange of He atoms belonging to the non-superfluid solvation layer and the superfluid surrounding. However, given the remaining uncertainties in the experimental data there is little point in further speculating about these mechanisms at this time.

Further experimental investigations would help to shine light on the spectroscopy of AN. The emission spectra upon selective excitation should be recorded with a narrowband cw laser exciting AN doped into a continuous droplet beam. This would increase the selectivity of the excitation and the S/N-ratio while saturation effects could be avoided. Further, pump-probe experiments would yield information on a possible splitting of the absorbing ground state. Pump-probe spectra recorded by monitoring the depletion of the beam using a bolometer would enable to record the stimulated emission spectra. [LTV01] These are advantageous to dispersed emission spectra recorded upon detection of spontaneous emission due to their higher spectral resolution determined by the laser instead of the dispersion of the detection unit (spectrograph). However, pump-probe experiments on AN are difficult because of the spectral overlap of the individual transitions. Further, emission decay times upon excitation at the different transitions should be recorded which may help to distinguish between emission from different states.

Other indications for the fail of the configuration coordinate model to explain the experimental observations on AN in helium droplets are provided by experiments on helium clusters of AN in supersonic jets. [EJN$^+$00, EAHJ01, HEJ01] Mass-selective excitation spectra of clusters with up to 17 He atoms attached to AN with a rotational temperature presumably of about 0.4 K were reported. [EAHJ01] The electronic origin is shifted to the red upon increasing the number of attached helium atoms and converges to a red shift of 38 cm^{-1} for more than 12 He atoms. [EAHJ01] Interestingly, also for clusters of tetracene with up to 17 He atoms only about half of the shift in the droplets is observed. [EAHJ01] The line shape at the electronic origin of helium clusters of both anthracene and tetracene do not reveal any significant variation by means of a splitting similar as in the droplet. [HEJ01] Thus, it is indicated that both the shift and the line shape depend on the presence of the superfluid helium around the chromophore together with its non-superfluid solvation layer. [KRH05]

5.2 9,10-Dichloroanthracene (9,10-DCA)

Substituting the two H-atoms of the central ring of anthracene (AN) with chloro atoms yields 9,10-dichloroanthracene (9,10-DCA) belonging to the same point group D_{2h}. Due to its high fluorescence quantum yield, 9,10-DCA is a favored molecule for electronic spectroscopy e.g. in supersonic jets [AEJ82, AJ83, ASJ84, AHJ88, TYH^{+}89, PAJN90, BHBEJ92, PA93] or solid matrices [CG82, CT90]. The excitation spectrum of 9,10-DCA in the gas phase as well as in solid matrices is similar to that of AN with respect to both the vibrational frequencies in the excited state and the intensity pattern. [AHJ88, CG82] Hence the electronic origin is the most intense transition and no prominent low-frequency modes are observed as is typical for a rigid molecule. The main difference in the excitation spectrum of 9,10-DCA compared to the parent compound AN is the C-Cl stretching vibration with about 306 cm^{-1} (see below) which also appears in progression and combination with other modes. SVL-spectra reveal similar vibrational frequencies in the ground state S_0 compared to the electronically excited state S_1. [AHJ88, TYH^{+}89] As for AN a mirror symmetry of absorption (excitation) and emission spectra recorded upon excitation at the electronic origin as typical for rigid molecules is observed only for vibrational excess energies below about 800 cm^{-1} . [AHJ88] At higher excess energies Fermi-resonance effects cause the breakdown of this mirror symmetry. [AHJ88] The emission spectrum of 9,10-DCA appears very similar to that of AN essentially differing only in the C-Cl stretching modes.

All data presented in the following were recorded with the LPD3002 dye laser (dye: DMQ / BBQ mixture). Integral emission was detected with the PMT R 943-02 (Hamamatsu) protected by a cut-off filter WG395. Emission dispersed with the MS 257 spectrograph was detected with the CCD-camera DU 420A-BU2 (Andor iDus). The oven temperature for optimum LIF signal of single 9,10-DCA while avoiding multiple doping of the helium droplets was 70 °C.

5.2.1 Excitation Spectra of 9,10-DCA

The excitation spectrum of 9,10-DCA in helium droplets is presented in fig. 5.11 with $\nu_0 = 25889\ \mathrm{cm}^{-1}$. The most intense transition exhibits the lowest transition energy and is thus assigned to the electronic origin. The solvent shift of about 60 cm^{-1} to the red compared to the gas phase [AHJ88] is in the typical range observed for rigid molecules doped into helium droplets. The variations of vibrational frequencies compared to the gas phase are also in the typical range of less than 4 %. (table 5.3) As discussed in chapter 4.2 the intensity pattern in the excitation spectrum of 9,10-DCA in helium droplets is practically identical to the pattern in the absorption spectrum, but differs significantly from the pattern in the fluorescence excitation spectrum in the gas phase.

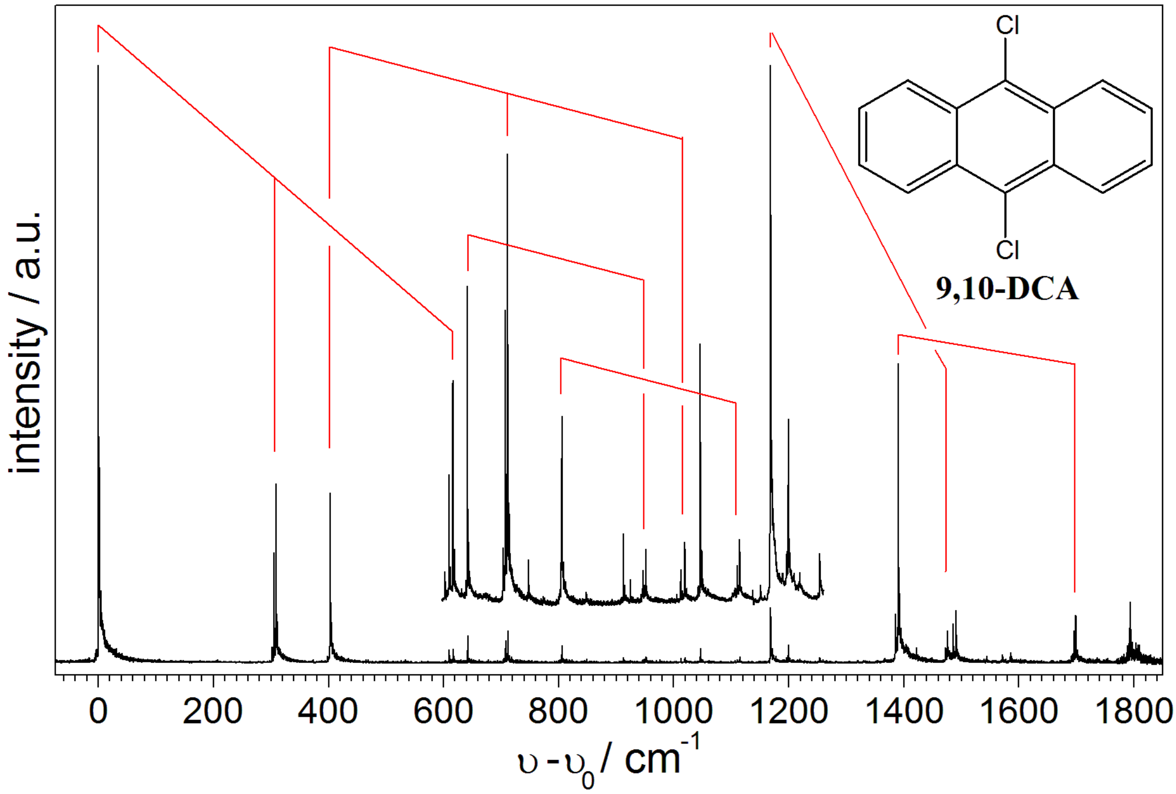

Fig. 5.11: Excitation spectrum of 9,10-DCA in helium droplets with $\nu_0 = 25889$ cm^{-1} normalized to laser intensity. The spectrum in the inset is recorded with higher laser intensity. In both spectra the laser intensity was low enough to avoid saturation effects.

All electronic transitions in the droplet spectrum reveal the same fine structure as can be seen in fig.s 5.12, 5.13 and 5.14 and which is entirely absent in the gas phase. Fig. 5.12 shows the electronic origin recorded with different laser intensities. At laser intensities lower than used for the solid line spectrum the pattern does not change whereas at higher laser intensities (dotted line) the relative intensity of the peak lowest in energy (at ν_0) decreases. As discussed in chapter 4 this indicates that only the peak at $\nu_0 = 25889$ cm^{-1} can be assigned to a ZPL. All other transitions to its blue side belong to the accompanying PW, in particular the sharp features corresponding to phonon energies of 0.8, 2.6, and 4.5 cm^{-1} .

A fine structure could also be due to the abundance of different isotopomers of 9,10-DCA in the sample. The natural abundance ratio of the isotopes ^{35}Cl and ^{37}Cl amounts to 3:1 and thus the isotopomers (^{35}Cl,^{35}Cl)-AN, (^{35}Cl,^{37}Cl)-AN, (^{37}Cl,^{37}Cl)-AN are expected in an abundance ratio of 9:6:1. [AEJ82] The different saturation behavior and the intensity ratio of the sharp transitions indicate that the fine structure observed at the electronic origin is not due to different isotopomers of 9,10-DCA. Isotopic spectral shifts are observed for vibronic transitions inducing vibrational motion of the Cl-atoms. In particular

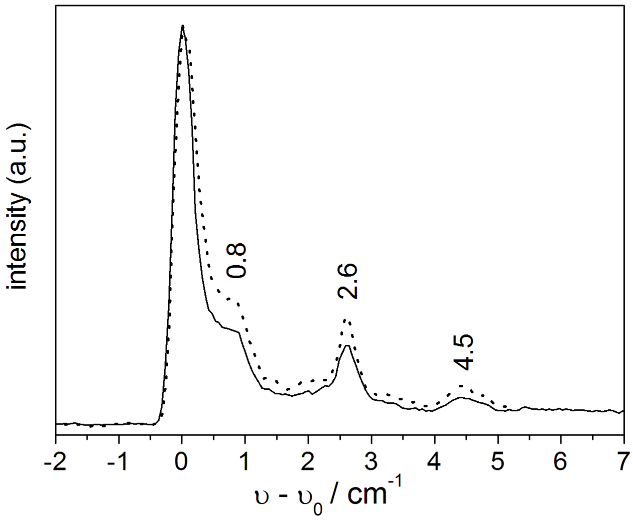

Fig. 5.12: Excitation spectrum of 9,10-DCA in helium droplets at the electronic origin recorded with different laser intensities.(see text) ν_0= 25889 cm^{-1} .

the 305 cm^{-1} vibration shown in fig. 5.13 exhibits a marked Cl isotope effect. [AEJ82] Three distinct transitions with an intensity ratio matching with the abundance ratio of the three isotopomers appear. The vibration is assigned to the symmetric C-Cl stretching vibration involving motion of both Cl-atoms. [CG82, AEJ82] The equidistant spacings of these vibronic transitions of the three different isotopomers amounts to 3.2 cm^{-1} as found in the gas phase. [AEJ82] The C-Cl stretching mode can also be found as overtone (610 cm^{-1}) and in various combinations e.g. with 403, 642, 805 (2×403), 1168 and 1390 cm^{-1} vibrations as shown in fig.s 5.13 and 5.14. Most important, the transitions of each isotopomer spectrally separated at the vibronic transitions involving the C-Cl stretching mode exhibit the same fine structure as the electronic origin. (cf. fig.s 5.12, 5.13, 5.14) The reappearance of this fine structure at the isotopically split vibronic bands provides further evidence that it is not due to different isotopomers.

The isotopic spectral shift at the electronic origin is due to the differences in the zero-point energy between the electronic ground and excited state for the different isotopomers. However, the vibrational frequencies in both electronic states hardly differ and exchange of the Cl-isotopes has only a minor effect on the zero-point energies due to the mass ratio of the different isotopes close to one. Thus, the isotopic spectral shift at the electronic origin, and many other vibronic transitions not involving excitation of significant motion of Cl-atoms, remains hidden below the corresponding line shape. (cf. fig.s 5.12, 5.13 and 5.14)

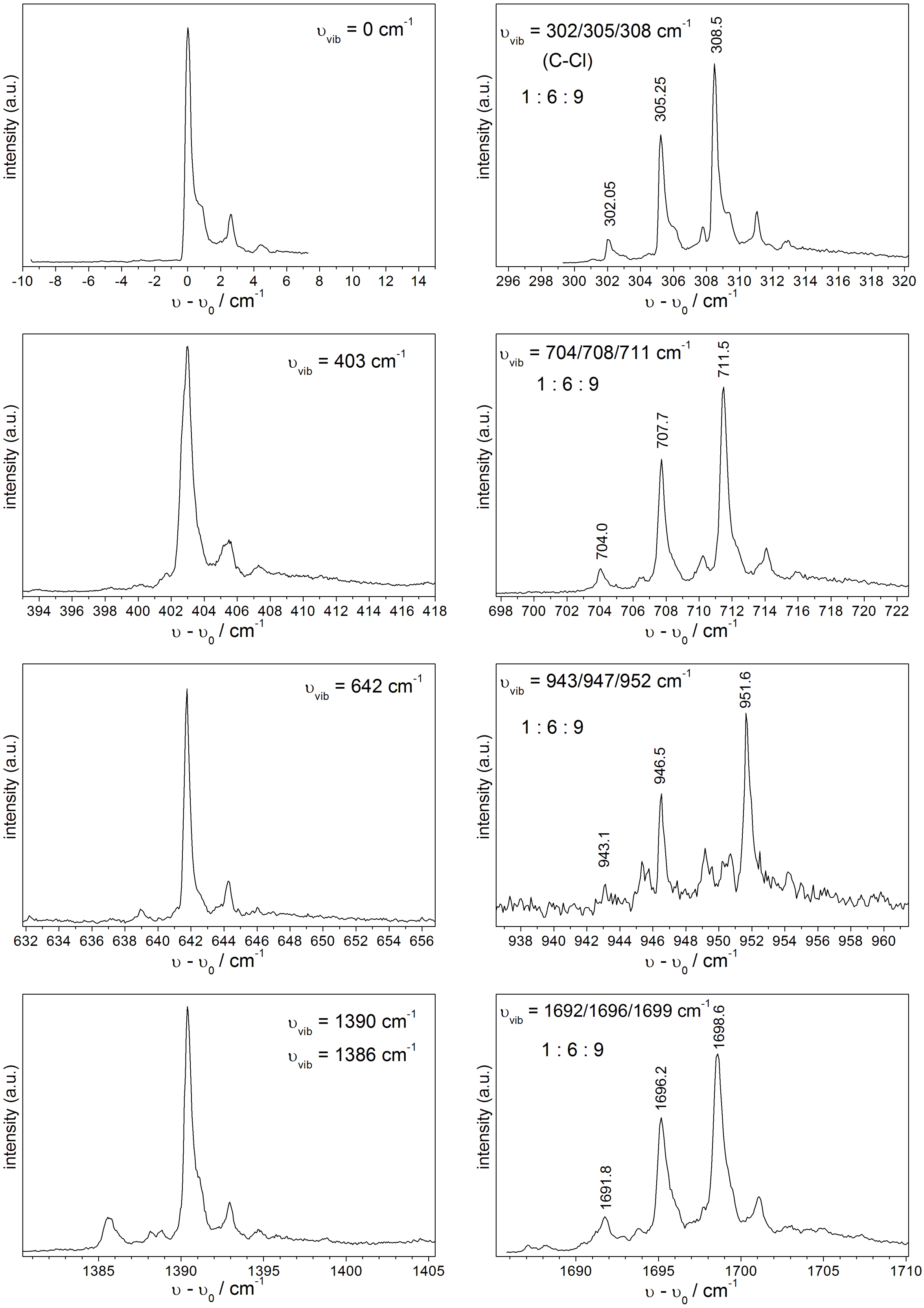

Fig. 5.13: Excitation spectra of selected vibronic bands of 9,10-DCA in helium droplets on an expanded scale. $\nu_0 = 25889$ cm^{-1} . Transitions on the right side are assigned to combinations of the transitions on the left side with the C-Cl stretching mode.

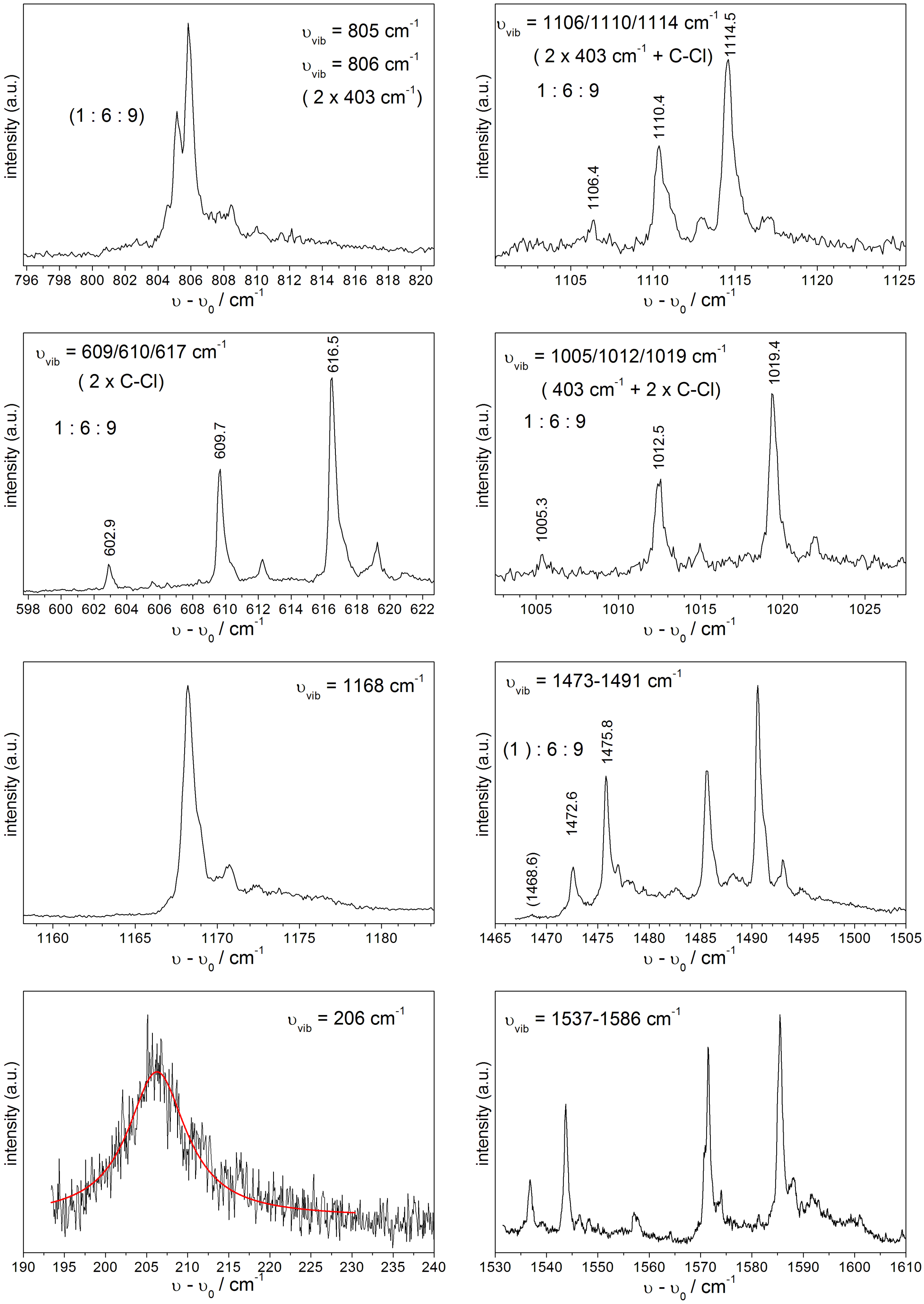

Fig. 5.14: Excitation spectra of selected vibronic bands of 9,10-DCA in helium droplets on an expanded scale. $\nu_0 = 25889$ cm^{-1} . Note the different wavenumber scaling for the lower sections. The line shape of the vibronic transition at $\nu - \nu_0 = 206$ cm^{-1} was fitted with a Lorentzian with a full width of 8 cm^{-1} . (see text)

Interestingly, the vibronic transition shown fig. 5.14 with a vibrational energy of 206 cm^{-1} in S$_1$ has a much larger line width of almost 10 cm^{-1} than all other transitions with FWHMs of typically < 1 cm^{-1} . In the gas phase spectrum the line width of the corresponding transition is similar to that of the other transitions and the fluorescence quantum yield of the excited state is close to one. [AHJ88] Thus, the line broadening is due to the helium environment. The line shape can be fitted with a Lorentzian function with a line width of 8 cm^{-1} indicating a decay time of 0.7 ps due to damping of the vibronic state. For AN a weak low energy mode with 209 cm^{-1} in the gas phase spectrum (cf. chapter 5.1) was absent in the corresponding droplet spectrum. (cf. chapter 5.1)
In contrast to AN (cf. chapter 5.1), 9-MA (cf. chapter 5.6), and 1-MA (cf. chapter 5.7) no signal red shifted to the electronic origin due to complexation with an impurity could be found even with high laser intensities.

Tab. 5.3: Transition wavenumbers $\nu - \nu_0$ (cm^{-1}) in the excitation spectrum of 9,10-DCA in helium droplets and relative peak intensities I/I$_0$. All numbers are referred to the ZPL at the electronic origin (ν_0 = 25889 cm^{-1} , I$_0$ = 1) and correspond to vibrational frequencies in the electronically excited state. The sharp features of the fine structure of each vibronic transitions are not listed. For comparison gas phase data from the literature [AHJ88], ν_{vib}(jet), are listed. However, only frequencies of the most intense transitions of 9,10-DCA are given in the literature and the splitting due to various isotopomers is not listed.

$\nu - \nu_0$ / cm^{-1} (droplet)		I/I$_0$ (droplet)	ν_{vib} / cm^{-1} (jet)	shift / cm^{-1} (droplet)
0		1.000	0	0
206		0.02	198	+8
302		0.03		
305	a	0.18	306^a	≈ -1
308		0.28		
398		0.01		
400		0.01		
403		0.28	401	+2
603		0.004		
610	a	0.022	612^a	≈ -2
617		0.03		
642		0.05		
705		0.006		
708	a	0.037	711^a	≈ -3
712		0.053		
806		0.03	805	+1
913		0.01		
943		< 0.001		
947	a	0.005		
952		0.007		
1005		0.001		
1013	a	0.008		
1020		0.009		
1047		0.024		
1106		0.001		
1110	a	0.006		
1115		0.01		
1168		0.09	1168	0
1197		0.01		

$\nu - \nu_0$ / cm^{-1} (droplet)		I/I$_0$ (droplet)	ν_{vib} / cm^{-1} (jet)	shift / cm^{-1} (droplet)
1200		0.03		
1254		0.009		
1330		0.004		
1367		0.005		
1386		0.08		
1391		0.50	1390	+1
1422		0.03		
1473	[b]	0.03		
1476		0.05	1474	+2
1486	[b]	0.07		
1491		0.09	1488	+3
1537	[b]	0.005		
1544		0.01		
1572	[b]	0.009		
1586		0.015		
1692	a	0.01		
1696		0.05	1696[a]	0
1699		0.08		
1794		0.10		

a isotopomers

[b] presumably isotopomers

5.2.2 Emission Spectra of 9,10-DCA

The dispersed emission spectrum of 9,10-DCA recorded upon excitation at the electronic origin is shown in fig. 5.15. The intensity pattern and frequency positions of the transitions are independent of the excitation frequency. Except for a solvent shift the spectrum matches with the emission spectrum recorded in the gas phase upon excitation at the electronic origin. [TYH$^+$89]

The differences in the vibrational frequencies in helium droplets and in the gas phase (table 5.6) are to a large extent due to the low spectral resolution and consequently large experimental uncertainties in the vibrational frequencies in both experiments. Note that the intense 1263 cm^{-1} vibration in the droplet spectrum is not listed in ref. [TYH$^+$89] but is clearly visible in their spectrum.

The electronic origin in the emission spectrum recorded upon excitation at the electronic origin was identified at 25893 cm^{-1} which is in agreement with the frequency of the electronic origin in the excitation spectrum at 25889 cm^{-1} within experimental accuracy. However, the emission spectrum exhibits a gradual shift to the red increasing with excess excitation energy. Fig. 5.16 shows parts of the emission spectrum on an expanded scale recorded upon excitation with vibrational excess energies as indicated. Fig. 5.16(a) and (b) demonstrate the gradual shift at the electronic origin while fig. 5.16(c) and (d) reveal the influence on some of the prominent modes. The emission spectrum recorded upon excitation with 1168 cm^{-1} vibrational excess energy is shifted by about 10 ± 3 cm^{-1}

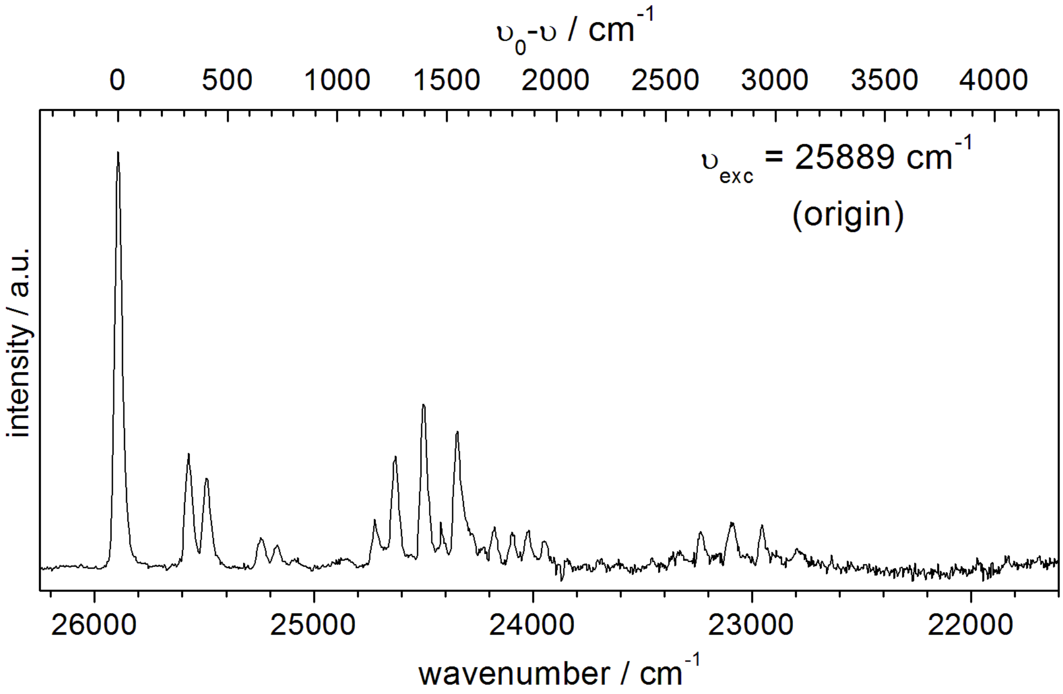

Fig. 5.15: Emission spectrum of 9,10-DCA in helium droplets via excitation at ν_{exc} = 25889 cm^{-1} (electronic origin) recorded with the CCD-camera DU 420A-BU2 (Andor iDus) attached to the MS 257 spectrograph (1200 lines/mm grating). ν_0 = 25893 cm^{-1} . The distance between two pixel columns amounts to about 3.9 cm^{-1} at the blue and 5.8 cm^{-1} at the red end of the spectrum.

compared to excitation at the electronic origin. The fluorescence was dispersed with the MS257 spectrograph. This spectrograph is less sensitive with respect to the frequency position and shape of the detected signal on the position of the imaged light source than the SPEX spectrograph used to obtain dispersed emission spectra of anthracene (AN). (cf. chapter 5.1) Moreover, a shift of the emission spectrum was not observed in the spectra of 9-cyanoanthracene (9-CNA, cf. chapter 5.4) recorded with the same detection unit and upon excitation with the same dye laser operated within a similar spectral range. Thus, a shift of the detection region upon changing the excitation frequency, i.e. a variation of the position of the imaged light source, as a reason for the shift is not obvious.

Emission spectra were also recorded at higher spectral resolution using a 3600 lines/mm grating instead of the 1200 lines/mm grating both in the MS257 spectrograph. Fig. 5.17(b) shows the spectra recorded upon misaligning the laser beam to increase the laser stray light while the nozzle was switched off. The laser was tuned to the resonance frequencies of the ZPL and two transitions of the PW at the electronic origin as indicated. The different laser frequencies can clearly be resolved. Fig. 5.17(a) reveals the emission of 9,10-DCA upon excitation with the same frequencies at the electronic origin and also upon excitation with a vibrational excess energy of 1168 cm^{-1} . Within the experimental accuracy the emission spectra recorded upon excitation at the ZPL and the sharp features of the PW at the electronic origin coincide. In contrast, emission upon excitation with vibrational excess energy appears with a red shift of about 8 ± 2 cm^{-1} . It should be noted that the upper scales in fig. 5.17 are scaled to the electronic origin in the emission spectrum (25908 cm^{-1}) recorded upon excitation at the electronic origin. The spectra recorded using the 3600 lines/mm grating were calibrated using an Ar/Ne lamp with only three lines in the recorded spectral range thus giving a larger error than the calibration of the spectra in fig.s 5.15 and 5.16 with 14 lines of the lamp. The frequencies of the recorded stray light in fig. 5.17(b) appear red shifted by up to 4 cm^{-1} with respect to the origin of the corresponding emission spectra in fig. 5.17(a). This is unreasonable and is due to the different position of the imaged light source when recording stray light of the misaligned laser beam compared to LIF from the sample. However, the spectra in fig. 5.17(b) can be compared among themselves since the recorded stray light originates from the same place. The same argument holds for the spectra shown in fig. 5.17(a) comparing fluorescence originating from the detection region. The three isotopomers could not spectroscopically be distinguished due to the limitations in the spectral resolution.

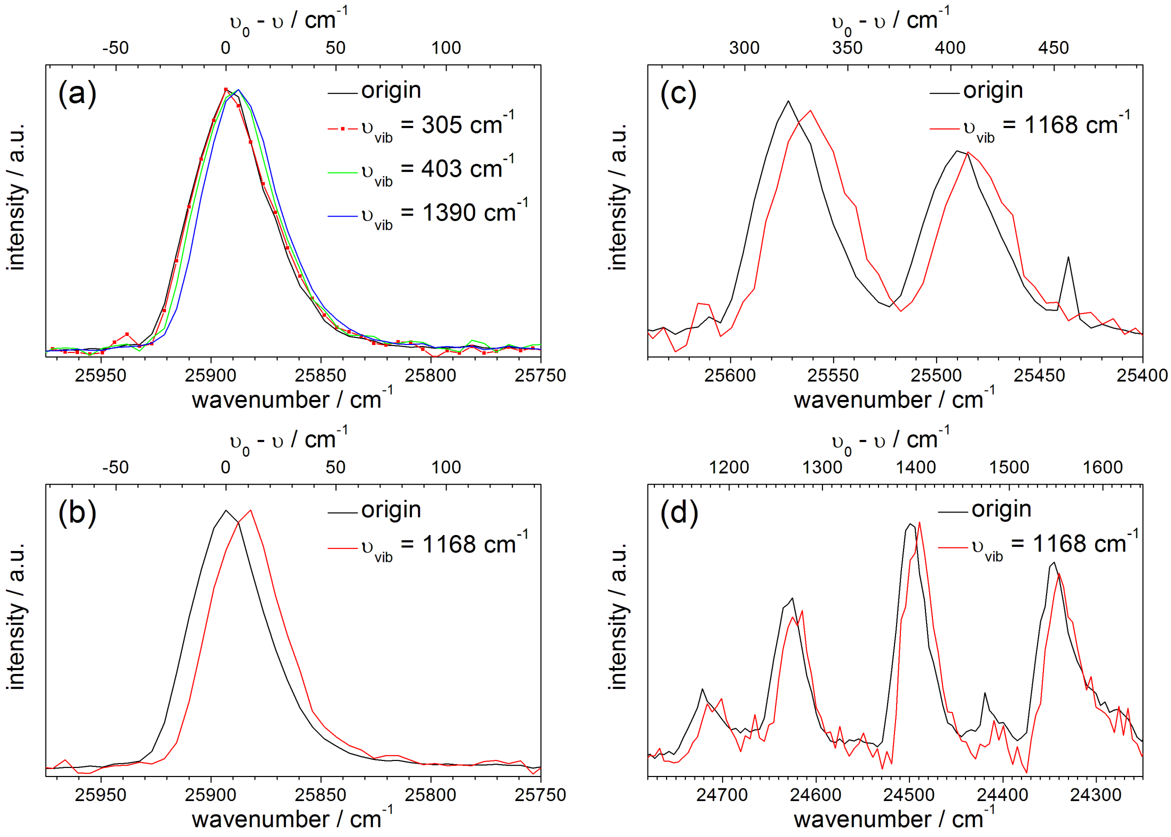

Fig. 5.16: Emission spectra of 9,10-DCA in helium droplets recorded upon excitation with vibrational excess energies as indicated. Emission is dispersed with the MS257 spectrograph (1200 lines/mm grating). ν_0 = 25893 cm^{-1} . The distance between two pixel columns amounts to about 5.6 cm^{-1} at the electronic origin, 5.5 cm^{-1} and 5.0 cm^{-1} at the vibrational satellites, respectively.

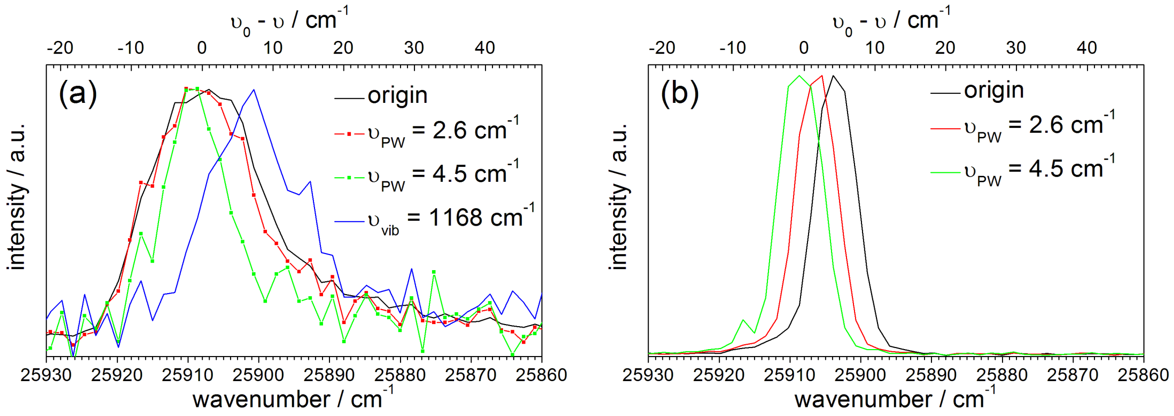

Fig. 5.17: Emission spectra (a) of 9,10-DCA in helium droplets recorded upon excitation with phonon or vibrational excess energies as indicated. Laser stray (b) recorded with the same laser frequencies demonstrates the spectral resolution. Emission is dispersed with the MS257 spectrograph (3600 lines/mm grating). $\nu_0 = 25908$ cm^{-1} . The distance between two pixel columns amounts to 1.6 cm^{-1} .

Tab. 5.4: Transition wavenumbers $\nu_0 - \nu$ (cm^{-1}) in the emission spectrum of 9,10-DCA in helium droplets and their relative intensities I/I$_0$. Frequencies are given with respect to the electronic origin in the emission spectrum at $\nu_0 = 25893$ cm^{-1} and correspond to vibrational frequencies in the ground state S$_0$. For comparison vibrational frequencies in the ground state of 9,10-DCA observed in the gas phase [TYH$^+$89], ν_{vib}(jet), are listed.

$\nu_0 - \nu$ / cm^{-1} (droplet)	I/I$_0$ (droplet)	ν_{vib} / cm^{-1} (jet)	shift / cm^{-1} (droplet)
0	1.00	0	0
321	0.28	306,309	+15,+12
403	0.22	403	0
653	0.08	641	+12
728	0.06	707,710	+21,+18,
809	0.03	805	+4
1031	0.02	1045	-14
1171	0.12	1169	+2
1263	0.26	-	-
1394	0.40	1390	+4
1473	0.12	1489	-16
1548	0.33	1582	-34
1612	0.09	-	-
1715	0.10	1696	+19
1802	0.08	1792	+10
1870	0.09	-	-
1946	0.07	-	-
2660	0.09	-	-
2802	0.11	-	-
2938	0.11	-	-

5.2.3 Discussion

The excitation spectrum of 9,10-DCA in helium droplets reflects the corresponding gas phase spectrum with the typical signature of a rigid molecule. The intensity pattern in helium droplets was found to be almost identical to the absorption spectrum in the gas phase differing from the fluorescence excitation spectrum in the gas phase as discussed already in chapter 4.2. The differences in the two gas phase spectra are ascribed to an increase of the ISC-rate mediated via IVR with increasing vibrational excess energy. [AHJ88] The intensity pattern in the helium droplets indicates that the quantum yield for the relaxation into the emissive state is close to one. Thus, this relaxation process, possibly also mediated via IVR or even ISC, is faster than the competing non-radiative processes such as IC, IVR and ISC. Since line widths as small as 0.5 cm^{-1} can be observed even with high vibrational excess energies such as 1390 cm^{-1} , a lower limit for the decay time and thus the energy dissipation for the directly excited states can be estimated to about 10 ps.
All transitions in the excitation spectrum revealed an identical fine structure which has no counterpart in the gas phase spectrum. Together with the observed saturation behavior at the electronic origin the sharp features at 0.8, 2.6, and 4.5 cm^{-1} to the blue from the most intense transition (ZPL) can presumably be assigned to features of the PW. The same fine structure appeared for each of the three isotopomers providing evidence that the fine structure is not due to an overlap of their spectra. The fine structure does not reveal a splitting of the ZPL as found for AN. Both molecules belong to the same point group D_{2h}. The fine structure will also be discussed in chapter 5.9.2.

The pattern in the emission spectrum is the same as in the gas phase spectrum originating from the vibrational ground state of S_1 and shows the typical spectral signature of a rigid molecule. The emission spectrum was found to be independent of the phonon excess energy, however, reveals a gradual shift to the red with increasing excitation energy. This may be due to an experimental artefact which, however, could not be identified. Emission from a state different than the vibrational ground state of S_1 was not yet reported in helium droplets and in view of the fast energy dissipation and low temperature this can be excluded as a reason for the shift with high confidence. The dissipation of the vibrational excess energy of less than 1400 cm^{-1} causes the evaporation of less than 300 He atoms. Due to the large droplet size in the order of 10^5 He atoms per droplet the different shrinkage in size upon excitation with different excess energies can also be excluded as a reason for the shift.
Different transition energies could be due to a slightly different configuration of the non-superfluid solvation layer around the chromophore. The different environment would alter the interaction energies between the environment and the embedded molecule in the electronic ground and excited state and thus would lead to different transition ener-

gies. A reorganisation of the non-superfluid solvation layer upon electronic excitation was found for phthalocyanines in helium droplets. [LS03, LS04a, LS04b, LSK$^+$04, LS05](cf. chapter 4) The emission spectra revealed a splitting of all transitions into two signals which were attributed to emission from two distinct configurations of the non-superfluid solvation layer. The relative intensity of the two spectra was found to depend on the vibrational excess energy which was interpreted to reflect the relative population of the two different configurations. [LS03, LS04a, LS04b, LSK$^+$04, LS05]
However, in the case of 9,10-DCA no splitting but a gradual shift is observed. The absence of a splitting and the invariance of the line shape indicate that emission originates only from one emissive state corresponding to a distinct configuration of the solvation layer. A gradual variation of this solvation layer with the excess energy would cause a gradual frequency shift of the emission.

However, a gradual variation of the configuration would be surprising since the configurations are related to localized He-atoms. To exclude a systematic experimental error to cause the shift dispersed emission spectra should be recorded upon excitation with a cw dye laser yielding better S/N ratio. Further, pump-probe experiments monitoring the depletion of the beam with a bolometer would yield stimulated emission spectra also revealing information on a possible reorganisation of the helium environment.

5.3 9-Chloroanthracene (9-CA)

Substitution of one H-atom at the central ring of anthracene by a Cl-atom yields 9-chloroanthracene (9-CA) thereby lowering the symmetry from D_{2h} to C_{2v}. Electronic spectra of 9-CA in supersonic jets are reported in ref.s [IYI87, II88, ITI88, LI95, ZLS^{+}95, ZLLB95]. In all excitation spectra the electronic origin is the most intense transition while the reported vibrational intensity pattern differs significantly among different experiments. In fluorescence excitation spectra all other vibronic transitions display a relative intensity of less than 10 % compared to the electronic origin. [IYI87, II88, ITI88, LI95] Whereas, in two-color [1+1] REMPI spectra in particular the bending mode of the anthracene chromophore with an energy of about 375 cm^{-1} has a relative intensity of almost 50 % compared to the origin. [ZLS^{+}95, ZLLB95] C-Cl stretching modes are weak in all spectra.

Fig. 5.18 shows the excitation spectrum of a sample of 9-CA in helium droplets (b) compared to the excitation spectrum of 9,10-DCA in helium droplets (a). (cf. chapter 5.2) The 9-CA sample was bought from Aldrich with a purity of 96 % and was checked by means of an NMR spectrum. However, most of the detected signals stem from contamination of the sample with 9,10-DCA. This can be clearly seen in fig. 5.18. Samples of 9-CA were found to be contaminated with 9,10-DCA also in ref. [ZLLB95]. It should be noted that 9,10-DCA was investigated after 9-CA and thus contamination of the apparatus or the pick-up cell can be excluded as source for 9,10-DCA.

From the comparison of the spectra shown in fig. 5.18 only two transitions could be attributed to 9-CA which are indicated accordingly. The lowest energetic one is found at 26726 cm^{-1} and the second one with an excess energy of 374 cm^{-1} . The former is assigned to the electronic origin of 9-CA shifted by 66 cm^{-1} to the red compared to the gas phase [LI95]. The latter can presumably be assigned to the prominent bending mode of the anthracene chromophore.

The oven temperature was optimized to 26 °C monitoring the signal at the electronic origin of 9-CA. The same optimum temperature is found detecting signals from the 9,10-DCA impurity and is far below the optimum of sublimating 9,10-DCA. However, the signals of the impurity dominate the excitation spectrum indicating a drastically reduced fluorescence quantum yield for 9-CA as compared to 9,10-DCA. In solution at room temperature 9-CA is reported to have a fluorescence quantum yield of 8 %. [HITS90] However, in view of the low relative intensity of the origin of 9-CA of only 2.5 % as compared to the estimated intensity at the electronic origin of 9,10-DCA under the conditions shown in fig. 5.18(b), the fluorescence quantum yield of 9-CA in helium droplets should be more than two orders of magnitude lower than that of 9,10-DCA with a quantum yield close to unity.

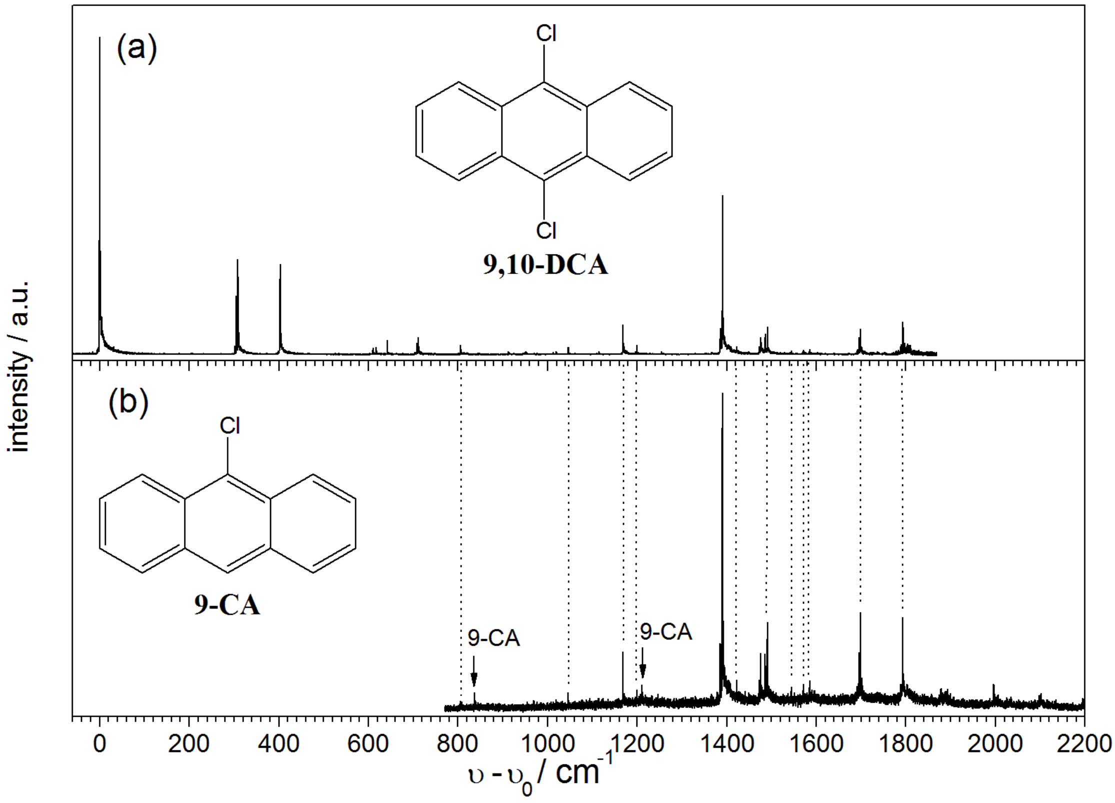

Fig. 5.18: Excitation spectrum of a sample of 9-CA in helium droplets (b) compared to the excitation spectrum of 9,10-DCA (a) to identify transitions of the former. $\nu_0 = 25896\ \mathrm{cm}^{-1}$ in both spectra. Excitation spectrum (b) were recorded with the LPD3002 dye laser (DMQ) an an edge-filter WG385 in front of the PMT (R 943-02, Hamamatsu). The spectrum of the 9-CA sample was not normalized to the laser intensity.

Fig. 5.19 shows the electronic origin of 9-CA in helium droplets on an expanded wavenumber scale. The most intense transition is assigned to a ZPL and the weaker accompanying features to the blue to distinct features of the PW. The transition shifted by 374 cm^{-1} to the blue exhibits the same fine structure within the experimental accuracy. The electronic transitions of 9-CA show a different fine structure than AN. Thus, the substitution of a single H-atom by a Cl-atom already disturbs the helium solvation strong enough to prevent a splitting of the ZPLs. The fine structure will be discussed further in chapter 5.9.2.

Due to the low fluorescence intensity no emission spectra were recorded. The low fluorescence quantum yield reduces the sensitivity of methods based on the detection of spontaneous emission. Whereas, it makes 9-CA a well suited compound to be studied with depletion methods.

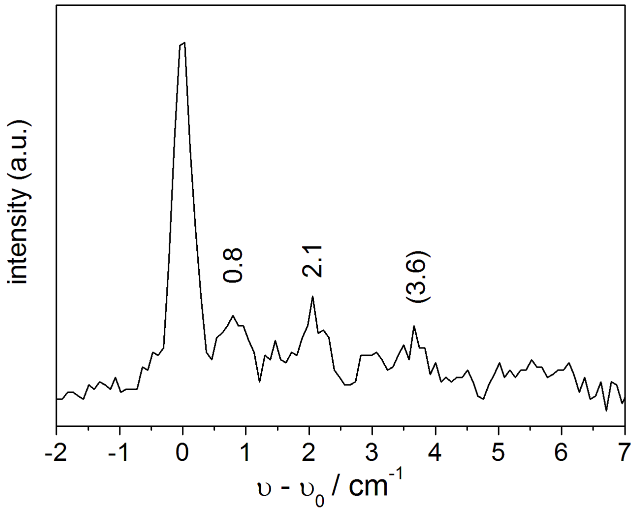

Fig. 5.19: Excitation spectrum of 9-CA in helium droplets at the electronic origin. $\nu_0 = 26726$ cm^{-1} .

5.4 9-Cyanoanthracene (9-CNA)

Substitution of one of the H-atoms of the central ring of the anthracene chromophore with a cyano group yields 9-cyanoanthracene (9-CNA) and lowers the symmetry from point group D_{2h} to C_{2v}. The fluorescence excitation and dispersed emission spectra of 9-CNA in supersonic jets were found to be similar as for the parent compound anthracene. [Hir86, AJOL86, AJTL87, Ami88, AHJ88, KKHS92, MLS^{+}05] The introduction of the cyano-group causes splittings in the C-C stretching and C-H bending regions and the appearance of the C-N stretching mode ($\approx$ 2200 cm^{-1}). [LBH^{+}98] Further, a totally symmetric low frequency mode (217 cm^{-1}) is observed also in combination with other modes of the anthracene body. [Hir86, AJOL86, Ami88, AHJ88, MLS^{+}05] A normal mode analysis in the ground state in comparison with IR spectra in a solid Ar matrix is given in ref. [LBH^{+}98].

All data presented in the following were recorded with the LPD3002 dye laser (dye: DMQ / BBQ mixture). Integral emission was detected with the PMT R 943-02 (Hamamatsu) protected by a cut-off filter WG395. Emission dispersed with the MS 257 spectrograph was detected with the CCD-camera DU 420A-BU2 (Andor iDus). The oven temperature for optimum LIF signal of single 9-CNA while avoiding multiple doping of the helium droplets was 40°C.

5.4.1 Excitation Spectrum of 9-CNA

Fig. 5.20 shows the fluorescence excitation spectrum of 9-CNA in helium droplets with $\nu_0 = 26074\ \mathrm{cm}^{-1}$. The spectrum reflects the corresponding gas phase data [Hir86, AJOL86, Ami88, AHJ88] with the electronic origin dominating the spectrum. The origin was assigned by the fact that no substantial features to the red have been observed and exhibits a solvent shift of 97 cm^{-1} to the red with respect to the gas phase. [AHJ88]

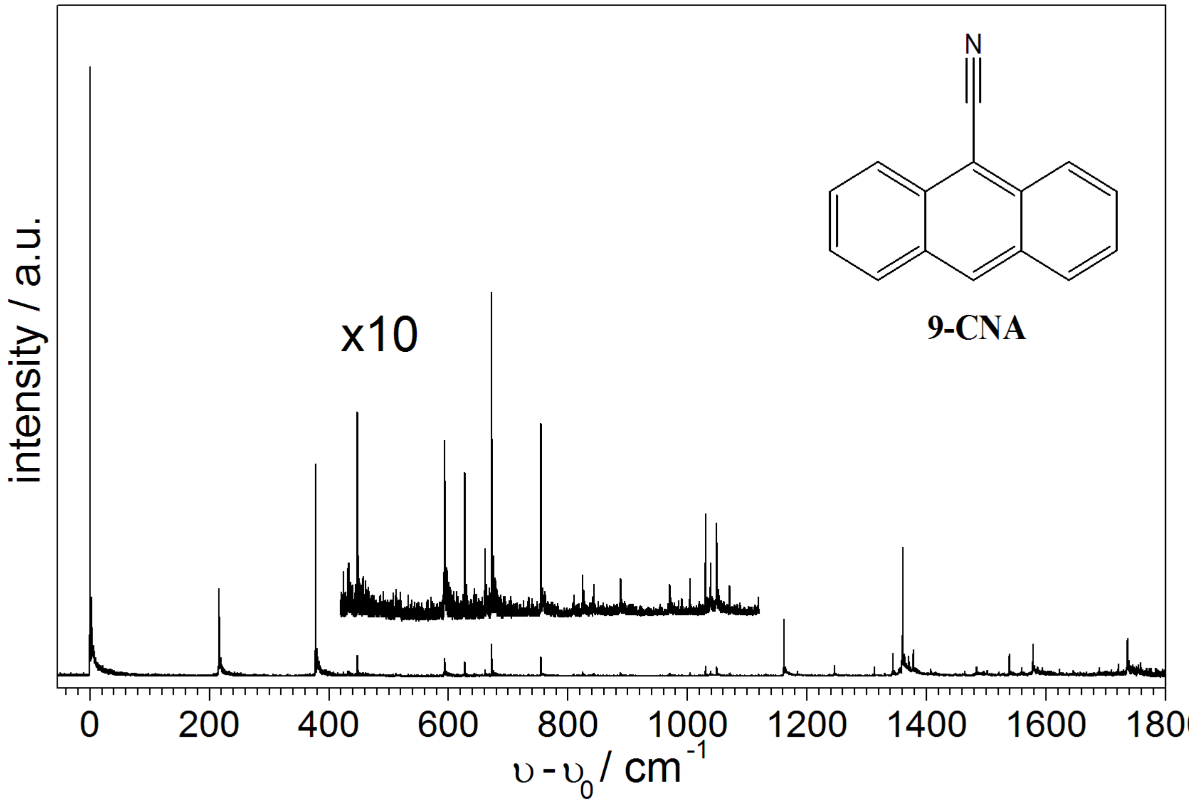

Fig. 5.20: Excitation spectrum of 9-CNA in helium droplets with $\nu_0 = 26074\ \mathrm{cm}^{-1}$. The laser intensity was low enough to avoid saturation effects.

An enlargement of the electronic origin recorded with different laser intensities is shown in fig. 5.21 and reveals a fine structure that has no counterpart in the gas phase. At laser intensities lower than for the solid line spectrum the shape does not alter whereas at higher laser intensities (dotted line) the relative intensity of the most intense peak decreases. Thus, this transition is assigned to a ZPL while the less intense sharp features are assigned to part of the PW. The features on the high energy side correspond to excitations of phonons in the excited state with phonon energies such as 0.8, 1.7, and 2.6 cm^{-1} , respectively. Consequently, the transition 0.5 cm^{-1} to the red of the ZPL is tentatively assigned to originate from a populated phonon state of the ground state, i.e. a 'hot phonon'.

All vibronic transitions exhibit (at least indicatively) a similar fine structure as at the

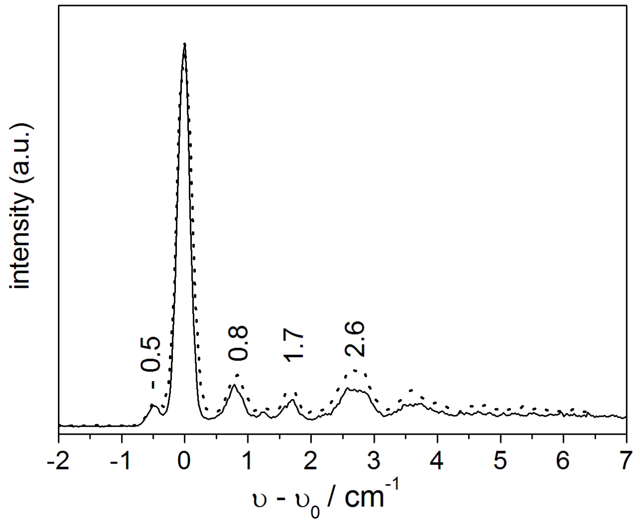

Fig. 5.21: Excitation spectrum of 9-CNA in helium droplets at the electronic origin recorded with different laser intensities.(see text) $\nu_0 = 26074$ cm^{-1} .

electronic origin as shown in fig. 5.22 for selected vibrational satellites. Deviations of the vibrational frequencies as compared to the gas phase values are within the typical range of less than 3 %. (cf. table 5.5) The intensity pattern within the vibrational fine structure is roughly an intermediate between absorption and fluorescence excitation spectra in the gas phase. [AJOL86, Ami88, AHJ88] This can be rationalized by the state specificity of the corresponding quantum yields as discussed in chapter 4.2.

However, the relative peak intensity of the totally symmetric 216 cm^{-1} mode (217 cm^{-1} in the gas phase) is lower by almost a factor of 2/3 than in both spectra in the gas phase. [AJOL86, Ami88, AHJ88] In the supersonic jet the fluorescence quantum yield was reported to be unity at the electronic origin and to hardly decrease with vibrational excess energies up to about 750 cm^{-1} . [AJOL86, Ami88, AHJ88] This is in agreement with the fluorescence decay times which were found to be almost independent of the excitation energy up to at least 590 cm^{-1} above the electronic origin. [HST85, Hir86, KKHS92] Thus, the decrease of the relative peak intensity of the 216 cm^{-1} mode in the droplet spectrum compared to the gas phase spectra indicate a mode specific enhanced non-radiative decay. This is in agreement with the increased line width compared to other vibronic transitions. (fig. 5.22) Interestingly, the fluorescence decay times of rare gas clusters of 9-CNA with one or two Ar atoms in the supersonic jet were found to be independent of vibrational excess energy up to at least 1320 cm^{-1} and almost identical to the decay time of the origin of bare 9-CNA. [KKHS92] Though, the decay time upon excitation of the 217 cm^{-1} vibronic band is lower by about half of this value indicating enhanced radiationless decay processes. [KKHS92]
A weak 128 cm^{-1} mode as found in the gas phase [Hir86, AJOL86, Ami88] corresponding

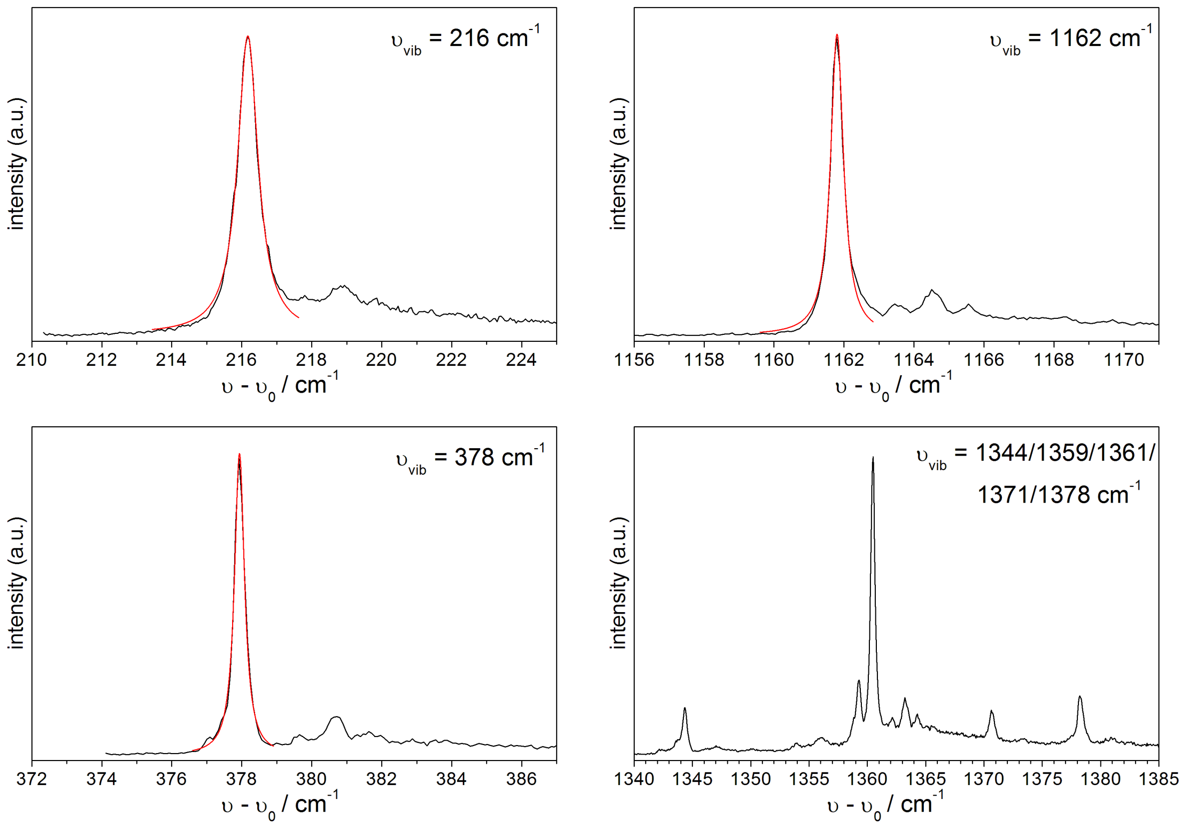

Fig. 5.22: Excitation spectra of selected vibronic bands of 9-CNA in helium droplets on an expanded scale. ν_0= 26074 cm^{-1} . Line shapes were fitted with a Lorentzian with line widths of 0.71, 0.35, and 0.45 cm^{-1} for the 216, 378, and 1162 cm^{-1} transition, respectively.

to an in plane bending mode of the CN-group [LBH$^+$98] was not observed in helium droplets. No signal red shifted to the electronic origin due to a complex with an impurity, as was the case for AN (cf. chapter 5.1), 9-MA(cf. chapter 5.6), and 1-MA (cf. chapter 5.7) was found.

Tab. 5.5: Transition wavenumbers $\nu - \nu_0$ (cm^{-1}) in the excitation spectrum of 9-CNA in helium droplets and their relative peak intensities I/I$_0$. All numbers are given with respect to the electronic origin (ν_0 = 26074 cm^{-1} , I$_0$ = 1) and correspond to vibrational frequencies in the excited state. The sharp features of the fine structure of each transition are not listed. For comparison vibrational frequencies in the excited state of 9-CNA in the gas phase from ref. [Hir86] and ref. [AHJ88], ν_{vib}(jet) are also listed.

$\nu - \nu_0$ / cm^{-1} (droplet)	I/I$_0$ (droplet)	$\nu_{vib}{}^a$ / cm^{-1} (jet)	$\nu_{vib}{}^b$ / cm^{-1} (jet)	shift / cm^{-1} (droplet)
0	1.000	0	0	0
-	-	128	128	-
216	0.144	214	217	+2/-1
378	0.35	376	377	+2/+1
432	0.008	429	-	+3
448	0.033	448	-	0

$\nu - \nu_0$ / cm^{-1} (droplet)	I/I$_0$ (droplet)	$\nu_{vib}{}^a$ / cm^{-1} (jet)	$\nu_{vib}{}^b$ / cm^{-1} (jet)	shift / cm^{-1} (droplet)
594	0.028	593	588	+1/+5
627	0.023	645	-	+18
661	0.011	-	-	-
672	0.053	661	-	+11
755	0.031	751	753	+4/+2
810	0.003	-	-	-
824	0.007	-	-	-
843	0.005	868 (?)		(-25)
888	0.005	882	-	+6
970	0.005	966	-	+4
1004	0.006	-	-	-
1020	0.002	1019	-	+1
1030	0.017	-	1027	+3
1039	0.009	-	-	-
1049	0.015		1045	+4
1071	0.005	1068	-	+3
1119	0.003	-	-	-
1129	0.002	-	-	-
1132	0.004	-	-	-
1162	0.093	1158	1160	+4/+2
1185	0.008	1181	-	+4
1238	0.004	-	-	-
1246	0.018	1242	1246	+4/0
1313	0.015	1310	-	+3
1330	0.005	-	-	-
1344	0.038	-	-	-
1359	0.043	1356	-	+3
1361	0.21	1367	-	+6
1371	0.032	-	-	-
1378	0.043	1375	1396	+3/-18
1408	0.012	-	-	-
1465	0.008	1464	1464	+1
1484	0.016	-	-	-
1502	0.009	-	-	-
1521	0.007	-	-	-
1539	0.036	1535	-	+4
1560	0.014	-	-	-
1579	0.051	1575	1577	+4/+2
1721	0.02	1730	-	+9

[a] ref. [Hir86]
[b] ref. [AHJ88]

5.4.2 Emission Spectrum of 9-CNA

The dispersed emission spectrum of 9-CNA in helium droplets is shown in fig. 5.23. It is independent of the excitation frequency at least up to 1361 cm^{-1} excess energy. The spectrum is frequency calibrated using the Ar/Ne lamp and the position of the electronic origin is determined to $\nu_0 = 26106$ cm^{-1} in accordance to the position of the electronic origin in the excitation spectrum ($\nu_0 = 26074$ cm^{-1}) within experimental accuracy.

It should be noted that the same excitation laser and detection unit were used as for 9,10-DCA where a red shift of the emission spectrum upon increasing the excitation frequency in the same range was observed. (cf. chapter 5.2) The emission spectrum is in agreement with the SVL-spectrum of 9-CNA recorded in the gas phase upon excitation at the electronic origin. [HST85, Hir86, Ami88] It is similar to the emission spectra of anthracene and 9,10-DCA though the cyano group adds the totally symmetric low frequency mode around 220 cm^{-1} and weak C-N stretching modes at around 2200 cm^{-1} . (table 5.6) Further, the lower symmetry leads to a splitting of modes, in particular in the C-C stretching and C-H bending regions. [LBH$^+$98] The amount of vibronic transitions together with the low resolution limited by the detection scheme causes the spectral congestion due to overlapping bands apparent in fig. 5.23.

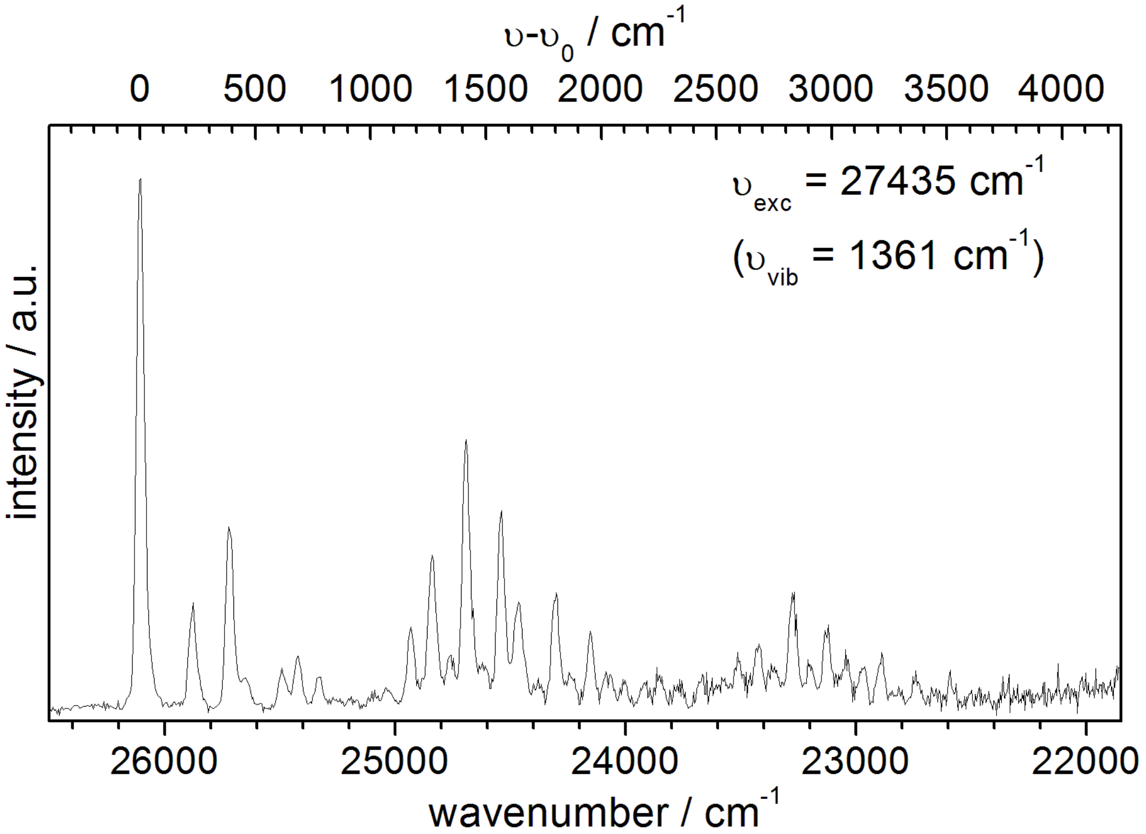

Fig. 5.23: Emission spectrum of 9-CNA in helium droplets upon excitation at ν_{exc} = 27435 cm^{-1} (ν_{vib} = 1361 cm^{-1}) recorded with the CCD-camera DU 420A-BU2 (Andor iDus) attached to the MS 257 spectrograph (1200 lines/mm grating). ν_0 = 26106 cm^{-1} . The distance between two pixel columns amounts to about 4.0 cm^{-1} at the blue and 5.8 cm^{-1} at the red end of the spectrum.

The S/N-ratio in emission spectra recorded upon excitation at the weak transitions assigned to sharp features of the PW in the excitation spectrum was too low to allow for any conclusions. This is in particular the case in emission spectra recorded at higher spectral resolution.

Tab. 5.6: Transition wavenumbers $\nu_0 - \nu$ (cm^{-1}) in the emission spectrum of 9-CNA in helium droplets and their relative intensities I/I$_0$. Frequencies are given with respect to the electronic origin in the emission spectrum at $\nu_0 = 26106$ cm^{-1} and correspond to vibrational frequencies in the ground state S$_0$. Gas phase spectra are shown in ref.s [HST85, Hir86, Ami88] though vibrational frequencies are not reported.

$\nu_0 - \nu$ / cm^{-1} (droplet)	I/I$_0$ (droplet)	$\nu_0 - \nu$ / cm^{-1} (droplet)	I/I$_0$ (droplet)
0	1.00	1952	0.15
228	0.20	2098	0.05
385	0.35	2190	0.05
457	0.06	2251	0.06
615	0.08	2338	0.04
682	0.11	2435	0.05
776	0.06	2591	0.09
1068	0.04	2685	0.12
1172	0.15	2751	0.07
1268	0.29	2835	0.22
1344	0.10	2907	0.08
1412	0.51	2983	0.15
1491	0.09	3067	0.09
1570	0.37	3140	0.08
1641	0.20	3220	0.11
1804	0.22	3362	0.06
1871	0.07	3518	0.06

5.4.3 Discussion

Excitation and emission spectra of 9-CNA in helium droplets reflect the vibrational fine structure of the corresponding gas phase spectra with the typical signature of a rigid molecule. However, a fine structure which has no counterpart in the gas phase spectra is found for all transitions in the excitation spectrum of 9-CNA in helium droplets. Each transition consists of a ZPL as the most intense transition accompanied by distinct sharp features attributed to the PW. (cf. chapter 5.9.2) These transitions correspond to additional excitation of phonons in the excited state with energies such as 0.8, 1.7, and 2.6 cm^{-1} . A weak transition with a red shift of 0.5 cm^{-1} was tentatively attributed to absorption originating from an excited phonon state in the electronic ground state. The relative intensity of this hot phonon compared to the ZPL is about 0.06 which is lower than the corresponding Boltzmann-factor of about 0.14 for a temperature of 0.37 K. Hot phonons usually are not observed in excitation spectra of rigid molecules in helium droplets due to the low temperature and a small transition moment. The transition moment seems to be larger in case of 9-CNA. The phonon energy in the ground state of 0.5 cm^{-1}

might correspond to the phonon energy of 0.8 cm^{-1} in the exited state indicating a similar non-superfluid solvation layer around the molecule in the different electronic states. The low resolution and signal to noise ratio did not allow for any investigation of the fine structure in emission spectra.

Another remarkable difference in the excitation spectrum in helium droplets compared to the gas phase is the missing of the weak 128 cm^{-1} mode and line broadening of the 216 cm^{-1} mode. The 128 cm^{-1} mode is assigned to an in plane bending mode of the CN group. [LBH^{+}98] In the gas phase this transition carries about 10 % of the peak intensity of the 217 cm^{-1} mode. [Hir86, AJOL86, Ami88] If the 128 cm^{-1} mode was present in helium droplets with a similar relative peak intensity it should have been detected which is not the case. This indicates a damping of the in plane mode in the excited state by the helium environment causing a broadening of the vibronic transition below the detection limit.

A lower relative peak intensity in the fluorescence excitation spectrum recorded in the droplets compared to the excitation and absorption spectrum in the gas phase [AJOL86, Ami88, AHJ88] was further observed for the 216 cm^{-1} mode (217 cm^{-1} in the gas phase). The line shape of the ZPL of this vibronic transition could be well fitted with a Lorentzian with a line width of 0.71 cm^{-1} which is broader than the Lorentzian widths of 0.35 cm^{-1} and 0.45 cm^{-1} for the 378 and 1162 cm^{-1} modes, respectively. Deviations in the fitting are due to overlapping signals assigned to the PW. The decreased relative peak intensity of the 216 cm^{-1} mode is in agreement with its increased line width and is indicative of an enhanced non-radiative process. This process is not effective in the gas phase as reflected by the almost constant fluorescence quantum yield of almost unity [Ami88, AHJ88] and by the fluorescence decay time, which is thus determined by the radiative decay. [HST85, Hir86, KKHS92] This was the case for vibrational excess energies up to at least 590 cm^{-1} above the electronic origin. Thus, the process is probably due to dissipation of vibrational excess energy without involving intramolecular energy redistribution (IVR). Since the ratio of the integrated intensities of the 216 and 378 cm^{-1} vibronic transitions in the droplet spectrum is similar to their ratio of peak intensities in the gas phase spectra the dissipation leads to population of the emissive state to the same extent for both excited modes.

5.5 9-Phenylanthracene (9-PA)

Substitution of the central ring of anthracene with a phenyl group yields 9-phenylanthracene (9-PA) belonging to point group C_2. Compared to the substitution of the H atom with another atom (Cl) or a linear rotor (CN) as discussed in the previous chapters, the phenyl group introduces a qualitatively new degree of freedom, namely the torsional angle around the bond between the chromophore body (anthracene) and the substituent (phenyl group). The corresponding torsional mode was found to dominate the electronic spectra of 9-PA in the gas phase as is discussed in ref.s [WGB85, WLSB85, WBGB87, SH03a]. In fluorescence excitation spectra it appears as a pronounced Franck-Condon progression (FCP) with a fundamental frequency of 49 cm^{-1} . The FCP repeats coupled to at least two other fundamentals with 387 cm^{-1} and 427 cm^{-1} . The intensity distribution within the FCP is shifted towards higher transitions and the electronic origin is hardly visible. Both is indicative for a significantly different equilibrium geometry with respect to the torsional angle in the electronic ground state S_0 and electronically excited state S_1. [WGB85, WLSB85, WBGB87] An analysis of the electronic spectra using a one-dimensional effective model potential revealed a flat torsional potential with minima at angles of 90° and 270° in S_0 and at angles of 62°, 118°, 242° and 298° in S_1. The observed anharmonicity of the progression was explained by a barrier of only 240 cm^{-1} to the perpendicular orientation of the aromatic planes (90° or 270°, respectively) in S_1. [WGB85, WLSB85, WBGB87] Further details are published in ref.s [WGB85, WLSB85, WBGB87]. The torsional potentials of 9-PA in S_0 and S_1 were also investigated by using high level ab initio calculations yielding qualitatively the same potential energy curves as the experimental studies. [SH03a]

All data presented in the following were recorded with the LPD3002 dye laser (dye: DMQ). Integral emission was detected with the PMT H5783P (Hamamatsu) protected by a cut-off filter WG400. The oven temperature for optimum LIF signal of single 9-PA while avoiding multiple doping of the helium droplets was 49 °C.

5.5.1 Excitation Spectrum of 9-PA

Fig. 5.24 shows the excitation spectra of 9-PA in helium droplets (a) and in the supersonic jet (b). The gas phase spectrum is taken from ref. [Str05] and is in agreement with the data published in ref.s [WGB85, WLSB85, WBGB87]. The droplet spectrum exhibits a substantial line broadening with the spectral shape reflecting the envelope of the gas phase spectrum. By comparison with the gas phase data the electronic origin is identified at about 26830 cm^{-1} corresponding to a red shift of about 100 cm^{-1} compared to the gas phase. The similar peak pattern in both spectra reveals rather similar intramolecular torsional potentials and masses in the gas phase and in helium droplets. The

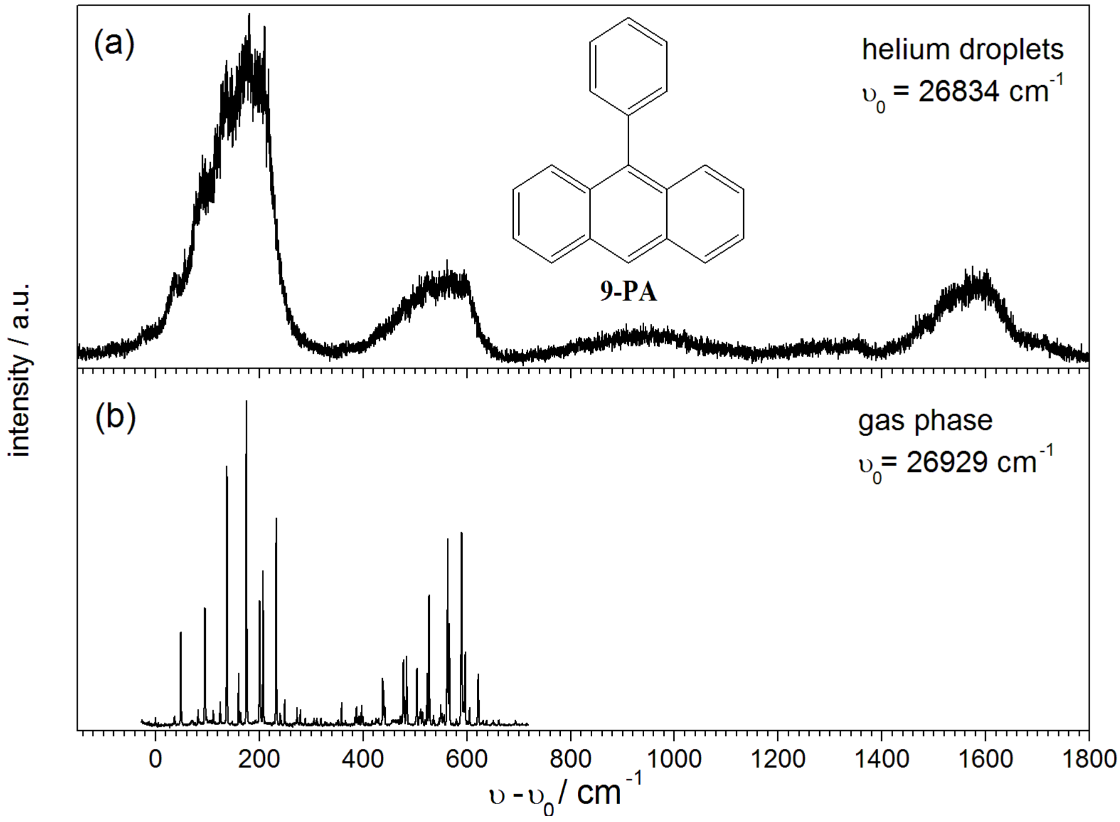

Fig. 5.24: Excitation spectra of 9-PA in helium droplets (a) and in the supersonic jet (b) with ν_0 as indicated. The laser intensity was low enough to avoid saturation effects.

relative intensity is lower in the droplet spectrum for excess energies above ≈ 230 cm^{-1} . This indicates that an excess-energy-dependent decay channel opens up on excitation of the molecule to higher vibrational levels of its S_1 state.

The laser intensities used in the droplet experiment are comparable to those used for other anthracene derivatives and by lowering the laser intensity the spectrum only looses intensity but no variations of its shape are observed. Thus, saturation effects to cause the broadening can be excluded. At the chosen temperature of the pick-up unit multiple doping and, therefore, line broadening due to cluster formation can also be excluded. Only at substantially higher temperatures the spectral shape of the excitation spectrum is further broadened as expected for complex formation.

Consequently, the line broadening can be attributed to the interaction between the dopant and the helium environment and is interpreted as damping of the nuclear rearrangement induced upon electronic excitation as will be discussed in chapter 5.9.1.

The low intensity level and the drastic line broadening do not allow for an analysis of a possible fine structure of the transitions in the excitation spectrum or for recording dispersed emission spectra.

5.6 9-Methylanthracene (9-MA)

Similar to the substitution of anthracene at the central ring with a phenyl group yielding 9-PA (point group C_2) the substitution with a methyl group yielding 9-MA (point group C_s) lowers the molecular symmetry and introduces low-frequency vibrational modes. The fluorescence excitation spectrum of 9-MA in the gas phase exhibits the prominent vibronic transitions of the anthracene body and additional low-frequency transitions. [SFS$^+$85, AHJ88, MLS$^+$05, NNS$^+$06, BMS$^+$09] The assignment of these transitions observed between about 50 and 160 cm^{-1} , especially the prominent ones at 57 and 69 cm^{-1} , is still subject of controversial discussion. [MLS$^+$05, NNS$^+$06, BMS$^+$09] The corresponding modes could also be observed in dispersed emission spectra though with different frequencies, e.g. of 79 cm^{-1} and 104 cm^{-1} corresponding to 57 cm^{-1} and 69 cm^{-1} , respectively, in the excitation spectrum. [SFS$^+$85] The low-frequency transitions are either attributed to the purely torsional mode [MLS$^+$05, BMS$^+$09] or to a mode involving torsion and out-of plane bending of the methyl moiety [NNS$^+$06]. Accordingly, different potentials and equilibrium structures in both S_0 and S_1 were proposed. [MLS$^+$05, NNS$^+$06, BMS$^+$09] Though, the different approaches agree that the potentials are quite shallow with torsional barriers lower than 120 cm^{-1} in S_0 and only 35 cm^{-1} in S_1, respectively. [MLS$^+$05, NNS$^+$06, BMS$^+$09] The low barriers are in agreement with the observed tunneling splitting of 1.0 cm^{-1} at the electronic origin. [Gre09, PGDS10]

All data presented in the following were recorded with the LPD3002 dye laser (dye: DMQ). Integral emission was detected with the PMT H5783P or R 943-02 (both Hamamatsu) protected by a cut-off filter WG385. Emission dispersed with the MS 257 spectrograph was detected with the CCD-camera DU 420A-BU2 (Andor iDus). The oven temperature for optimum LIF signal of single 9-MA while avoiding multiple doping of the helium droplets was 12 °C.

5.6.1 Excitation Spectrum of 9-MA

The excitation spectra of 9-MA in helium droplets (a) and in the gas phase (b) are shown in fig. 5.25. The gas phase spectrum is taken from ref. [Gre09] and is in agreement with the data published in ref.s [SFS$^+$85, AHJ88, MLS$^+$05, NNS$^+$06, BMS$^+$09]. The electronic origin in helium droplets is identified at $\nu_0 = 26885$ cm^{-1} shifted by about 50 cm^{-1} to the red with respect to the gas phase origin. No vibronic transitions of 9-MA could be found with less than 388 cm^{-1} excess energy even upon recording the spectrum with high laser intensity. In particular, the prominent transitions at 57 cm^{-1} and 69 cm^{-1} are absent. Other prominent modes related to vibrations of the anthracene body are observed with a typical solvent shift of the vibrational frequencies in the order of 1 %.

(table 5.7)
Most of the intensity is concentrated in the electronic origin whereas torsional and/or bending modes of the methyl group are not observed. Both observations are indicative of almost identical nuclear configuration in both electronic states. In particular, the methyl group does not seem to rotate upon electronic excitation.

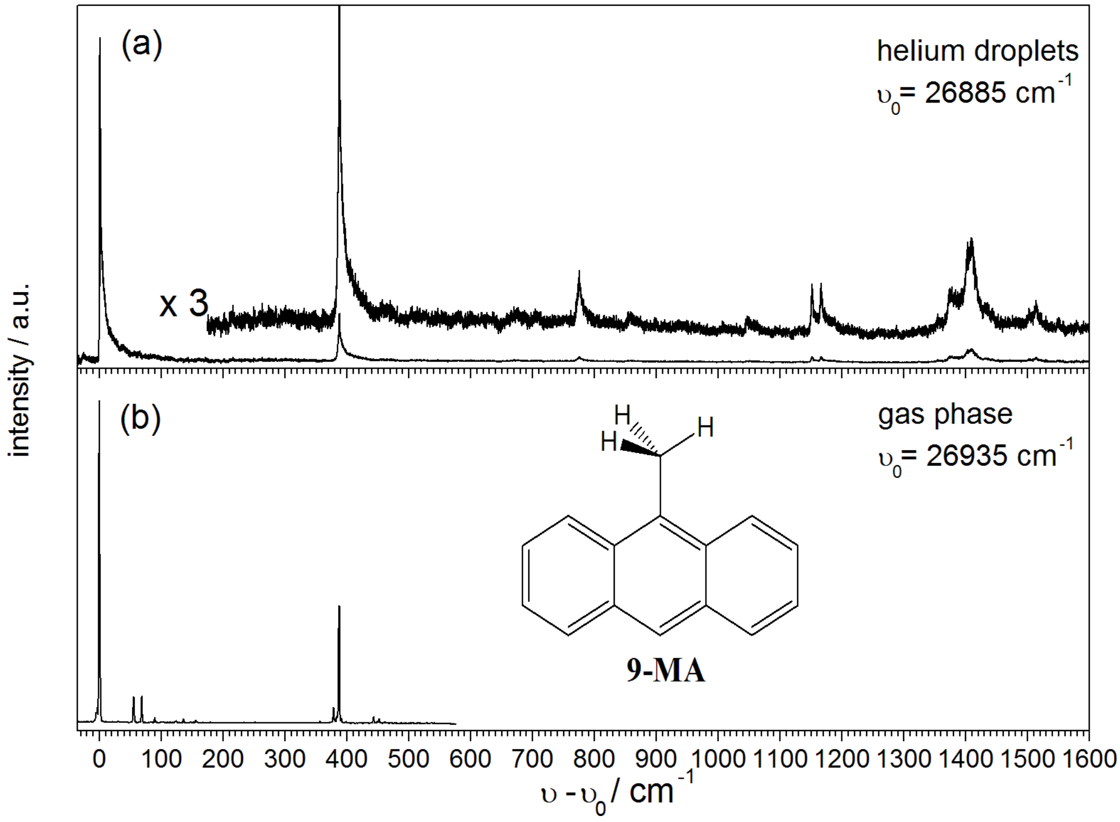

Fig. 5.25: Excitation spectra of 9-MA in helium droplets (a) and in the supersonic jet (b) with ν_0 as indicated. The data in the inset in (a) are not normalized to the laser power.

An enlargement of the electronic origin of 9-MA in helium droplets recorded with different laser intensities is presented in fig. 5.26. At laser intensities lower than for the solid line spectrum the pattern does not change whereas at higher laser intensities (dotted line) the relative intensity of the two most intense peaks at 0.0 cm^{-1} and 0.8 cm^{-1} decreases. The transitions with 1.8 cm^{-1} and 2.6 cm^{-1} display identical saturation behavior and identical relative intensities among them as compared to the two most intense peaks. Thus, the pattern of the transitions at 0.0 cm^{-1} and 0.8 cm^{-1} is repeated shifted by 1.8 cm^{-1} as indicated in fig. 5.26. As discussed in chapter 4 the different saturation behavior of transitions to the blue of those with the lowest transition energy is indicative of PWs. Thus, only the two intense transitions at 0.0 and 0.8 cm^{-1} are assigned to ZPLs whereas all other transitions are attributed to sharp features of their PWs. A similar splitting of 1.0 cm^{-1} as compared to the 0.8 cm^{-1} splitting in fig. 5.26 is found in the gas phase spectrum and is assigned to a tunneling splitting in the low-frequency mode as will be discussed below.

The relative peak intensities of the vibrational satellites compared to the electronic origin in helium droplets are lower than in the gas phase spectra. (fig. 5.25 and ref.s [SFS$^+$85, AHJ88, MLS$^+$05, NNS$^+$06, BMS$^+$09]) This is in agreement with the observed broadening of the vibronic transitions in helium droplets compared to the gas phase. The prominent 388 cm^{-1} transition shown in fig. 5.27 exhibits a FWHM of about 4 cm^{-1} and all other modes appear even broader. This is indicative of enhanced non-radiative decay processes. However, the line shapes cannot be fitted with a single Lorentzian indicating that the line shape is due to spectral overlap of various transitions and their PWs. Instead of the quartet substructure resolved at the electronic origin the fine structure of the 388 cm^{-1} mode consists of two peaks separated by ≈ 1.8 cm^{-1} and residing on top of a broad asymmetric and unstructured signal.

In the excitation spectrum recorded with high laser intensities tiny signals shifted by about 24 cm^{-1} to the red of the origin (fig. 5.27) and the 388 cm^{-1} vibrational mode appeared. As for anthracene (AN) (cf. chapter 5.1) and 1-methylanthracene (1-MA)(cf. chapter 5.7) these signals are attributed to complexes of 9-MA with some impurity.

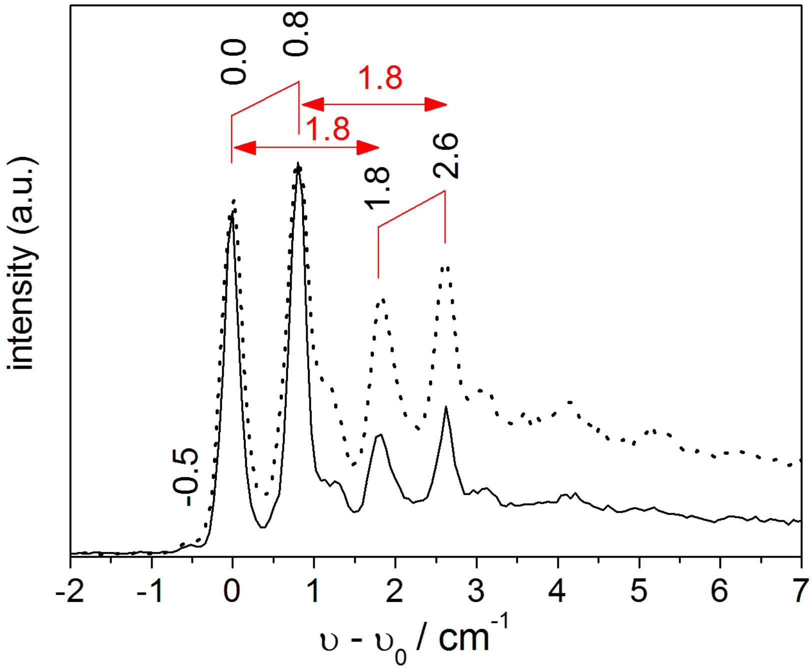

Fig. 5.26: Excitation spectrum of 9-MA in helium droplets at the electronic origin with $\nu_0 = 26885$ cm^{-1} recorded with different laser intensities (see text).

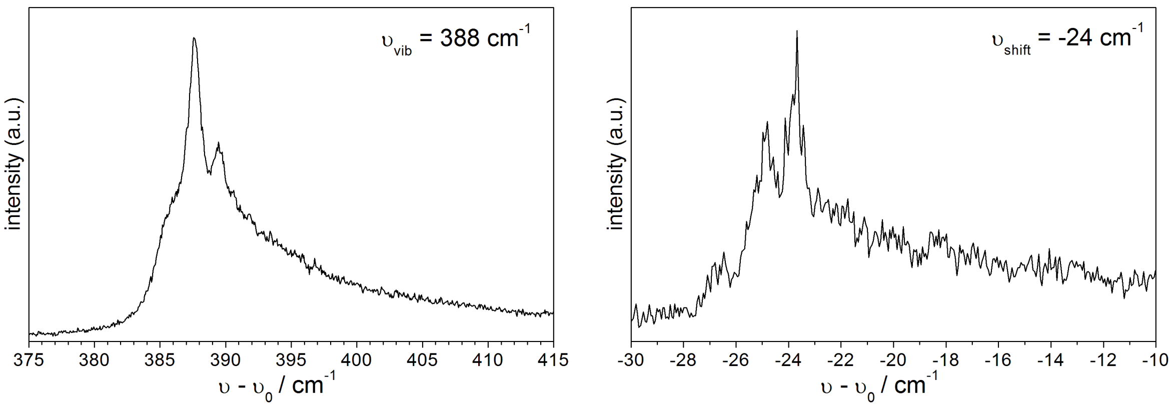

Fig. 5.27: Excitation spectra of selected transitions of 9-MA in helium droplets on an expanded scale. ν_0= 26885 cm^{-1} .

Tab. 5.7: Transition wavenumbers $\nu - \nu_0$ (cm^{-1}) in the excitation spectrum of 9-MA in helium droplets and their relative peak intensities I/I$_0$. All numbers are referred to the electronic origin ($\nu - \nu_0 = 0.0$ in fig. 5.26, I$_0$ = 1). The first column corresponds to vibrational frequencies in the excited state. The sharp features of the fine structure the transitions are not listed. The corresponding gas phase data [SFS$^+$85] are listed for comparison. These numbers are only given for the transitions observed in the droplets. Signals assigned to stem from impurities are only observed at high laser intensities and thus no relative intensities are given.

$\nu - \nu_0$ / cm^{-1}	I/I$_0$	$\nu - \nu_0$ / cm^{-1}	I/I$_0$	shift / cm^{-1}
(droplet)	(droplet)	(jet)	(jet)	(droplet)
-24	(impurity)	-	-	-
0	1.000	0	1.00	0
363 (388-25)	(impurity)	-	-	-
388	0.15	388	0.45	0
776	0.017	773	0.06	+3
857	0.004	-	-	-
1047	0.003	-	-	-
1152	0.016	1159	0.04	-7
1166	0.016			+7
1376	0.016	1360	0.02	+16
1409	0.038	1400	0.09	+9
		1405	0.08	+4
1515	0.011	1512	0.04	+3
1550	0.005	-	-	-

5.6.2 Emission Spectrum of 9-MA

The dispersed emission spectrum of 9-MA in helium droplets is presented in fig. 5.28. It was found to be independent of the excitation frequency within the experimental accuracy. The frequency was calibrated using the Ar/Ne lamp and the position of the electronic origin is determined to 26887 cm^{-1} in agreement with the position of the electronic origin in the excitation spectrum (26885 cm^{-1}). As observed in the excitation spectrum most of the intensity is concentrated in the electronic origin and the vibrational fine structure appears similar as in the emission spectra of AN (cf. chapter 5.1), 9,10-DCA (cf. chapter 5.2) and 9-CNA (cf. chapter 5.4). The emission spectrum of 9-MA recorded in helium droplets resembles the gas phase spectra recorded upon excitation at the electronic origin. [SFS+85, NNS+06, BMS+09] The SVL spectra in the gas phase revealed that vibronic transitions observed at 79 cm^{-1} and 104 cm^{-1} (table 5.8) correspond to the transitions at 56 and 69 cm^{-1} , respectively, in the excitation spectrum. [SFS+85, NNS+06] The corresponding transitions are not observed in the emission spectrum of 9-MA in helium droplets. They may be hidden due to the low S/N ratio or alternatively suffer the same fate as their counterparts in the excitation spectrum which have disappeared. The signal to noise ratio in emission spectra recorded with higher resolution using the 3600 lines/mm grating was too low to allow for a reasonable analysis. Further, a splitting of about 1.8 cm^{-1} or 0.8 cm^{-1} , respectively, as observed at the electronic origin in the excitation spectrum would be at the limit of or even below the spectral resolution using the 3600 lines/mm grating.

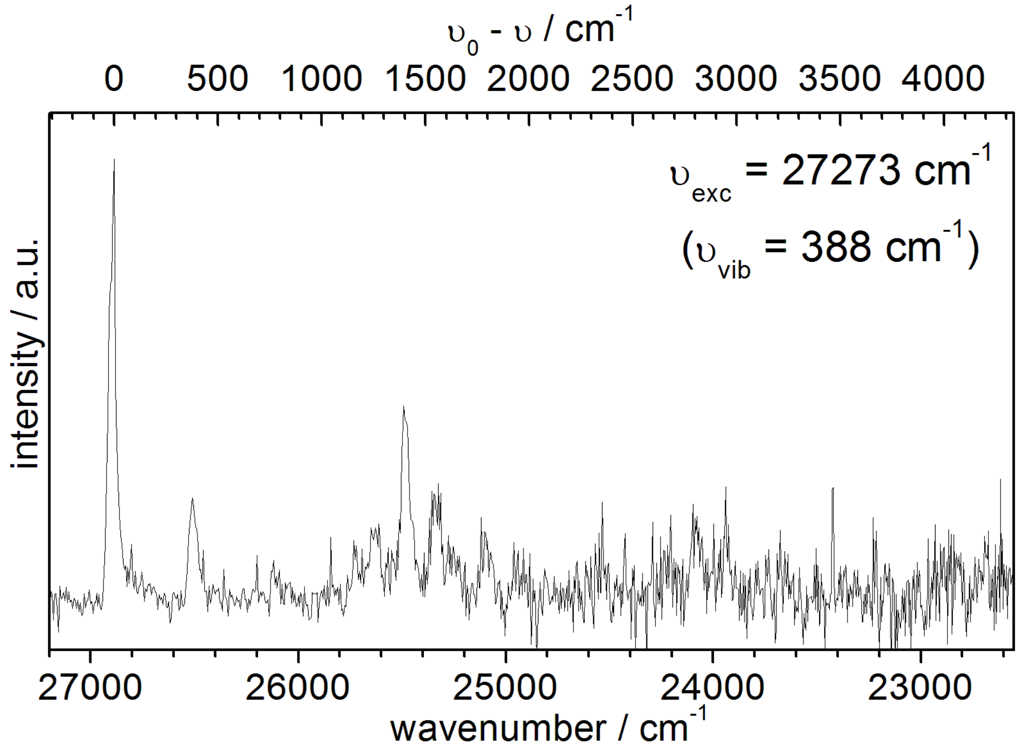

Fig. 5.28: Emission spectrum of 9-MA in helium droplets upon excitation at ν_{exc} = 27273 cm^{-1} (ν_{vib} = 388 cm^{-1}) recorded with the CCD-camera DU 420A-BU2 (Andor iDus) attached to the MS 257 spectrograph (1200 lines/mm grating). ν_0 = 26887 cm^{-1} . The distance between two pixel columns amounts to about 4.2 cm^{-1} at the blue and 6.1 cm^{-1} at the red end of the spectrum.

Tab. 5.8: Transition wavenumbers $\nu_0 - \nu$ (cm^{-1}) in the emission spectrum of 9-MA in helium droplets for excess energies below 2000 cm^{-1} and their relative intensities I/I$_0$. Frequencies are given with respect to the electronic origin in the emission spectrum at ν_0 = 26887 cm^{-1} and correspond to vibrational frequencies in the ground state S$_0$. For comparison vibrational frequencies in the ground state of 9-MA, ν_{vib} (jet), and corresponding relative intensities, I/I$_0$(jet), observed in the gas phase [SFS+85] are also listed.

$\nu_0 - \nu$ / cm^{-1} (droplet)	I/I$_0$ (droplet)	ν_{vib} / cm^{-1} (jet)	I/I$_0$ (jet)	shift / cm^{-1} (droplet)
0	1.00	0	1.00	0
-	-	79	0.04	-
-	-	104	0.02	-
-	-	123	0.02	-
380	0.23	390	0.32	-10
-	-	694	0.03	-
768	0.10	786	0.05	-18
-	-	1024	0.02	-
1166	0.13	1164	0.05	+2
-	-	1184	0.06	-
-	-	1224	0.03	-
1259	0.17	1260	0.14	-1
-	-	1283	0.06	-
-	-	1356	0.06	-
1396	0.44	1414	0.31	-18
1546	0.25	1567	0.22	-21
1636	0.13	1634	0.09	+2
1790	0.16	1806	0.08	-16
1945	0.12	1963	0.06	-18

5.6.3 Discussion

Excitation and emission spectra of 9-MA in helium droplets reflect the corresponding gas phase spectra with the typical signature of a rigid molecule. However, in helium droplets the low frequency modes with the corresponding normal coordinate depending on the torsional and possibly bending angle of the methyl group are missing in the excitation and most likely also in the emission spectrum. The prominent modes at 57 cm^{-1} and 69 cm^{-1} are definitely not observed in the excitation spectrum. They are well within the long tail of the PW coupled to the origin and thus might be efficiently damped by the helium environment. Alternatively, the torsional potential, which was determined to be shallow and hence particular sensitive to the helium environment, might be altered upon solvation. The missing of the low frequency modes is indicative either of highly efficient damping or of almost identical nuclear configurations of the methyl substituent in S$_1$ and S$_0$ enforced by the helium environment.

Corroboration for a different potential comes from an analysis of the fine structure at the electronic origin in the excitation spectra recorded in the gas phase and in helium droplets. In the gas phase a triple peak structure is observed which by applying the maximum entropy method [Fou88] can be separated into two identical rotational envelopes shifted by 1.0 cm^{-1} . [Gre09, PGDS10] These were attributed to the $0a_1 \leftarrow 0a_1$ and $1e \leftarrow 1e$ transitions within the tunneling multiplet in the torsional potential. A similar shift of 0.8 cm^{-1} is found for the two intense peaks in the corresponding droplet spectrum. (fig. 5.26) As shown in fig. 5.29 the droplet spectrum can be separated into the sum of two identical spectra shifted by 0.8 cm^{-1} with respect to each other. The relative intensity of the two subspectra is about 4.5:1 in favor of the lower energetic one in the gas phase phase whereas it is almost 1:1 in the droplets where no rotational branches are recognizable. If the change in the relative intensity of the two components was due to the reduced temperature in the droplets the blue component should be the $0a_1 \leftarrow 0a_1$ transition. Variations of the vibrational frequencies of the molecule upon solvation in helium affects the zero-point energy in S_0 and S_1 and thus the tunneling splitting. The missing of the low-frequency transitions would have to be attributed to efficient damping. Alternatively, both the different splitting and the missing of the low-frequency transitions can be explained by a variation of the potentials due to the helium solvation. A different potential would affect the transition probabilities within the vibrational

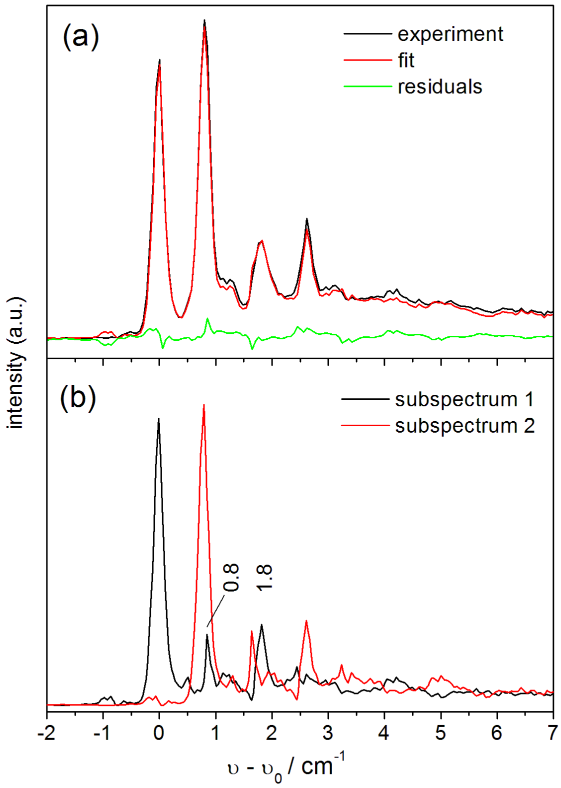

Fig. 5.29: Electronic origin of 9-MA in helium droplets. The experimental excitation spectrum (a) can be separated using the Maximum Entropy method into its two components (b). The best fit (red) and residuals (green) are also shown in (a).

satellite structure as well as at the electronic origin.

The peaks on the blue side of the intense transitions in the subspectra in the droplet in fig. 5.29 (b) are assigned to phonon excitations corresponding to phonon energies such as 0.8 and 1.8 cm^{-1} . This is in agreement with the observed saturation behavior shown in fig. 5.26.

The excitation spectrum at the electronic origin (fig. 5.26) reveals two peaks at 0.0 cm^{-1} and 0.8 cm^{-1} with an intensity ratio of about 1:1.1. The same patterns repeats shifted by 1.8 cm^{-1} though with a different saturation behavior. In case the 1.8 cm^{-1} separation would be due to the tunneling splitting the transitions at 0.0 cm^{-1} and 1.8 cm^{-1} would correspond to transitions (ZPLs) within different tunneling symmetries and the transitions at 0.8 cm^{-1} and 2.6 cm^{-1} to their PWs. Thus, ZPL and PW of each pair would have the same saturation behavior and in particular the PW at 0.8 cm^{-1} would saturate at lower laser intensities than the ZPL at 1.8 cm^{-1} which seems unlikely. Therefore, this assignment can probably be excluded.

However, it should be noted that the experimental observations could also be explained by a multiplet splitting of the ZPL due to the helium solvation instead of or in addition to the tunneling splitting in the torsional potential. Neither dispersed emission nor pump-probe experiments could unequivocally unravel the remaining uncertainty. Though, in analogy to the gas phase experiments and the findings on other substituted anthracenes the splitting by 0.8 cm^{-1} observed at the electronic origin in the excitation spectrum of 9-MA in helium droplets is most probably due to a tunneling splitting in S_0 and S_1 within the torsional potential.

To conclude, the electronic spectra of 9-MA in helium droplets are characteristic for negligible nuclear rearrangements induced upon electronic excitation. In particular, the methyl group should not rotate upon electronic excitation. Further, the low-frequency excitations at 57 cm^{-1} and 69 cm^{-1} in the gas phase spectra are way above the barrier of the corresponding potentials. The rather shallow torsional potential does not exert much of a torque to the methyl group upon electronic excitation. Thus, these excitations do not induce a significant nuclear rearrangement. The differences in the fine structure in the spectra of 9-MA in helium droplets compared to the corresponding gas phase spectra may be indicative of a slightly modified potential along the coordinate responsible for the low-frequency mode.

5.7 1-Methylanthracene (1-MA)

Substitution of one H-atom of the anthracene chromophore by a methyl group generates three isomers. In the following the isomer 1-methylanthracene (1-MA) belonging to point group D_s will be discussed. The torsional potential varies with the position of the methyl group as is reflected in the different spectroscopic behavior of 1-MA, 9-MA (cf. chapter 5.6) and 2-MA (cf. chapter 5.8).

Fluorescence excitation and dispersed emission spectra of 1-MA recorded in a supersonic jet [NNS$^+$05, Gre09] are dominated by the electronic origin accompanied by rather weak vibrational satellites and without low energy progressions. This is indicative of almost identical geometries in S_0 and S_1 in particular with respect to the torsional angle. However, vibronic transitions lower in energy than the prominent mode of the anthracene body at 399 cm^{-1} could be observed in the excitation spectrum. [Gre09] These modes not observed for AN may show up due to the reduced symmetry of 1-MA, out-of-plane bending or torsional modes of the methyl group. The most intense among them with a frequency of 345 cm^{-1} probably corresponds to the 357 cm^{-1} mode of 9-PA [WGB85] and to the 379 cm^{-1} mode of 9-MA. The electronic origin in the gas phase displays the envelope of single P- and R-branches of the rotational fine structure. The absence of an indication for a tunneling splitting at the electronic origin hints to high rotational barriers in both the S_0 and the S_1 state. Ab initio calculations confirm an identical minimum geometry of 1-MA in S_0 and S_1 with respect to the torsional angle. [NNS$^+$05] The calculations predict barriers for the methyl rotation of about 800 cm^{-1} in S_0 and about 500 cm^{-1} in S_1 [NNS$^+$05], which is in agreement with the missing of a low frequency progression of the torsional mode and the tunneling splitting at the electronic origin below experimental resolution. [Spa97]

All data presented in the following were recorded with the LPD3002 dye laser (dye: DMQ). Integral emission was detected with the PMT H5783P (Hamamatsu) protected by a cut-off filter WG385. The oven temperature for optimum LIF signal of single 1-MA while avoiding multiple doping of the helium droplets was 7°C.

5.7.1 Excitation Spectrum of 1-MA

Fig. 5.30 shows the excitation spectra of 1-MA in helium droplets (a) and in the gas phase (b). The electronic origin in helium droplets is identified at $\nu_0 = 27411$ cm^{-1} shifted by about 60 cm^{-1} to the red with respect to the gas phase origin. [NNS$^+$05, Gre09] As in the gas phase the spectrum in helium droplets is dominated by the electronic origin. All of the vibronic transitions observed in the gas phase can also be identified in the droplet spectrum with typical solvent shifts of vibrational frequencies of less than 4 %. (table 5.9)

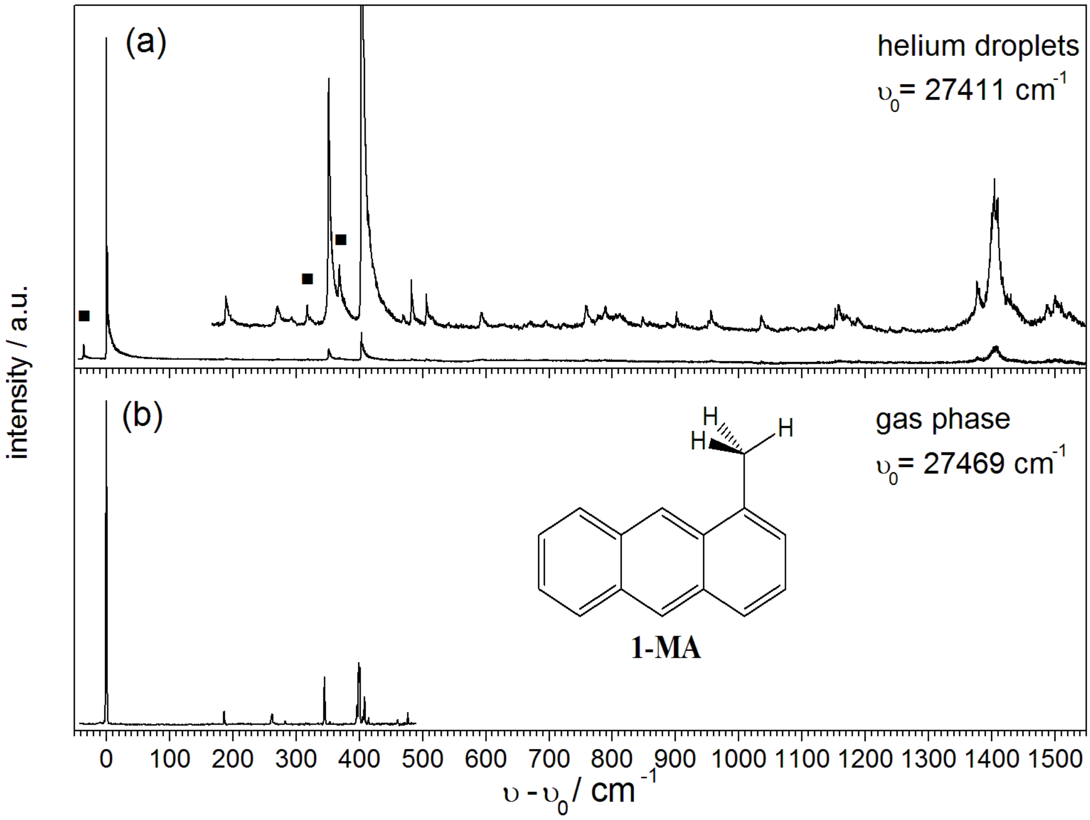

Fig. 5.30: Excitation spectra of 1-MA in helium droplets (a) and in the supersonic jet (b) with ν_0 as indicated. The spectrum of the vibrational satellite part of the droplet spectrum shown in the inset in (a) was recorded with higher laser intensity and was not normalized to the laser intensity. Signals marked with squares are attributed to complexes of 1-MA with an impurity.

The electronic origin was recorded with different laser intensities and the corresponding spectra are shown in fig. 5.31. At laser intensities lower than used for the solid spectrum the pattern does not change whereas at higher laser intensities (dotted line) only the relative intensity of the most intense peak decreases. Thus, only this transition is assigned to a ZPL while all other transitions with higher transition energies and which have no counterpart in the gas phase spectrum are attributed to the PW. In particular, the sharp features to the blue of the ZPL correspond to phonon energies of 0.6, 1.4, 2.4, and 3.5 cm^{-1} in S_1 while the weak transitions to the red of the ZPL correspond to phonon energies of 0.8 and 1.2 cm^{-1} in S_0. Despite of the smaller line width in helium droplets ($\approx$ 0.25 cm^{-1}) as compared to the supersonic jet ($\approx$ 1.3 cm^{-1} [Gre09]) no indication for a tunneling splitting is observed.

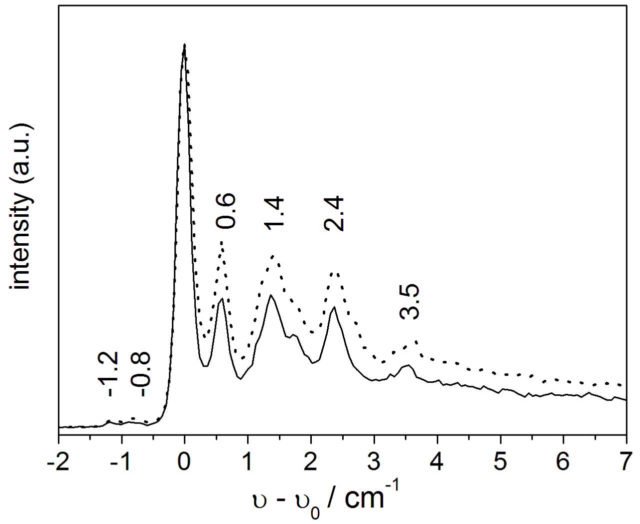

Fig. 5.31: Excitation spectrum of 1-MA in helium droplets at the electronic origin (ν_0 = 27411 cm^{-1}) recorded with different laser intensities (see text).

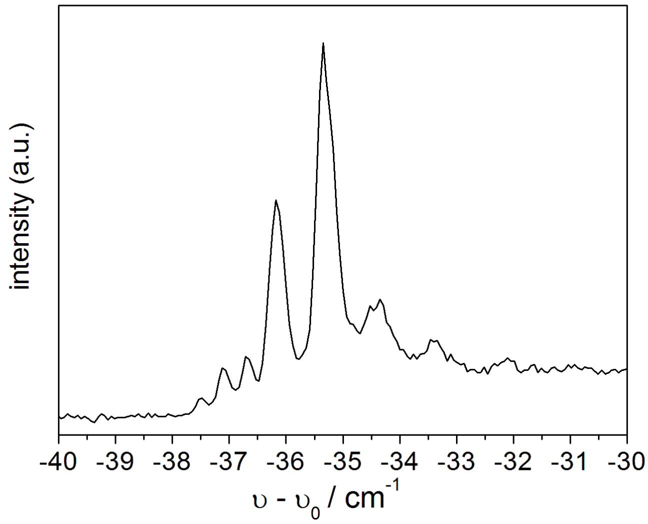

Fig. 5.32: Signal red shifted to the electronic origin of 1-MA in helium droplets with ν_0 = 27411 cm^{-1} .

The fine structure observed at the electronic origin repeats for all other vibronic transitions in the droplet spectrum, however, modified in the width of the individual peaks. Similar as found in the excitation spectra of AN (chapter 5.1) and 9-MA (chapter 5.6) some signals red shifted by about 35 cm^{-1} to the most intense vibronic transitions are observed in the droplet spectrum. (fig. 5.30) Fig. 5.32 shows an enlargement of the signal red shifted to the origin. It shows a distinct fine structure and is accompanied by a broad background extending over about 30 cm^{-1} to the blue. In the case of 9-MA a less pronounced fine structure was observed whereas in the case of AN only a broad signal without fine structure was found. However, the signals extend over a similar frequency range. As for AN and 9-MA these signals are attributed to complexes of 1-MA with some impurity from the sample. Additional doping with suspect impurities such as solvents used in the synthesis may help to identify the impurity.

Tab. 5.9: Transition wavenumbers $\nu - \nu_0$ (cm^{-1}) in the excitation spectrum of 1-MA in helium droplets and their relative peak intensities I/I$_0$. All numbers are referred to the electronic origin (ν_0 = 27411 cm^{-1} , I$_0$ = 1). The sharp features of the fine structure of the transitions are not listed. For comparison vibrational frequencies in the exited state of 1-MA and corresponding relative intensities observed in the gas phase [Gre09], $\nu - \nu_0$(jet) and I/I$_0$(jet), are also given.

$\nu - \nu_0$ / cm^{-1} (droplet)	I/I$_0$ (droplet)	$\nu - \nu_0$ / cm^{-1} (jet)	I/I$_0$ (jet)	shift / cm^{-1} (droplet)
-35 (impurity)	0.04	-	-	-
0	1.00	0	1.00	0
188	< 0.01	186	0.05	+2
271	< 0.01	263	0.03	+8
293	< 0.01	283	0.01	+10
318 (352-34) (impurity)	< 0.01	-	-	-
352	0.03	345	0.13	+7
369 (403-34) (impurity)	< 0.01	-	-	-
403	0.08	399	0.16	+4
on PW	?	408	0.07	?
	?	415	0.02	?
470	< 0.01	461	0.02	+9
482	< 0.01	476	0.04	+6
506	< 0.01	-		-
594	< 0.01		-	-
670	< 0.01	-	-	-
696	< 0.01	-	-	-
759	< 0.01	-	-	-
778	< 0.01	-	-	-
789	< 0.01	-	-	-
811	< 0.01	-	-	-
848	< 0.01	-	-	-
902	< 0.01	-	-	-
956	< 0.01	-	-	-
1036	< 0.01	-	-	-
1153,1158	< 0.01	-	-	-
1188	< 0.01	-	-	-
1378	< 0.01	-	-	-
1404,1408	0.04	-	-	-
1488	< 0.01	-	-	-
1501	< 0.01	-	-	-
1523	< 0.01	-	-	-

5.7.2 Discussion

The excitation spectrum of 1-MA in helium droplets reflects the corresponding gas phase spectrum as is typical for rigid molecules. The intensity pattern of the vibronic transitions, in particular the absence of a low-frequency progression, is indicative of a similar geometry of the molecule in the electronic ground and excited state. Thus, the torsional angle is not altered upon excitation. Tunneling doublets at the electronic origin could be identified in neither the gas phase nor the droplet spectrum. This is indicative of very high barriers in the torsional potential in both S_0 and S_1 and, thus, negligible tunneling probability. Both the similar geometry and the high barriers were confirmed by ab intio calculations. [NNS$^+$05]

The electronic origin in helium droplets exhibits a distinct fine structure which is absent in the gas phase spectra. On the basis of the saturation behavior only the most intense transition was assigned to a ZPL while the sharp transitions were attributed to the PW. The corresponding phonon energies are similar as for other anthracene derivatives as will further be discussed in chapter 5.9.2.

5.8 2-Methylanthracene (2-MA)

The third isomer with one methyl substituent is 2-Methylanthracene (2-MA) which belongs to point group C_s. The different position of the methyl group leads to a significant change of the torsional potential reflected in the electronic spectra: In contrast to the spectra of 9-MA and 1-MA, the excitation spectrum of 2-MA in a supersonic jet exhibits a low-frequency progression attributed to the torsional mode of the methyl group. [LHP93, NNS$^+$05] The fully resolved Franck-Condon progression (FCP) repeats coupled to the prominent mode of the anthracene body with 395 cm^{-1} and at least two other modes with 290 and 470 cm^{-1} . The intensity distribution within the FCP peaks at higher transitions and the series of resonances are rather irregular. The extended FCP is indicative of a significant change of the equilibrium torsional angle upon electronic excitation. The irregular spacings are indicative of excitations into levels energetically close to the torsional barrier in S_1. An analysis of the gas phase spectra using a one-dimensional free-rotor model revealed barriers of 70 cm^{-1} and 300 cm^{-1} to 335 cm^{-1} in the torsional potentials for S_0 and S_1, respectively. [LHP93, NNS$^+$05] Further, a phase shift in the potentials with respect to each other, i.e. a change of the equilibrium torsional angle by 60°, was determined. [LHP93, NNS$^+$05] An analysis of the line shape at the electronic origin in the excitation spectrum revealed a tunneling splitting of about 1.7 cm^{-1} . [Gre09, PGDS10]

The phase shift and the barrier heights of the torsional potentials in S_0 and S_1 deduced from fluorescence excitation spectra in the gas phase were confirmed by quantum chemical calculations. [NNS$^+$05]

All data presented in the following were recorded with the LPD3002 dye laser (dye: DMQ). Integral emission was detected with the PMT H5783P (Hamamatsu) protected by a cut-off filter WG385. The oven temperature for optimum LIF signal of single 2-MA while avoiding multiple doping of the helium droplets was 25 °C.

5.8.1 Excitation Spectrum of 2-MA

Fig. 5.33 shows the excitation spectra of 2-MA in helium droplets (a) and in the gas phase (b). The gas phase spectrum is taken from ref. [Gre09] and is in agreement with literature spectra. [LHP93, NNS$^+$05] The droplet spectrum reflects the envelope of the gas phase spectrum and thus reveals substantial line broadening. Obviously, the vibrational frequencies are almost identical to those in the gas phase. By comparison with the gas phase data the helium solvation shift can be estimated to about 45 cm^{-1} to the red compared to the gas phase.

For similar reasons as discussed for 9-PA (cf. chapter 5.5), saturation or multiple doping

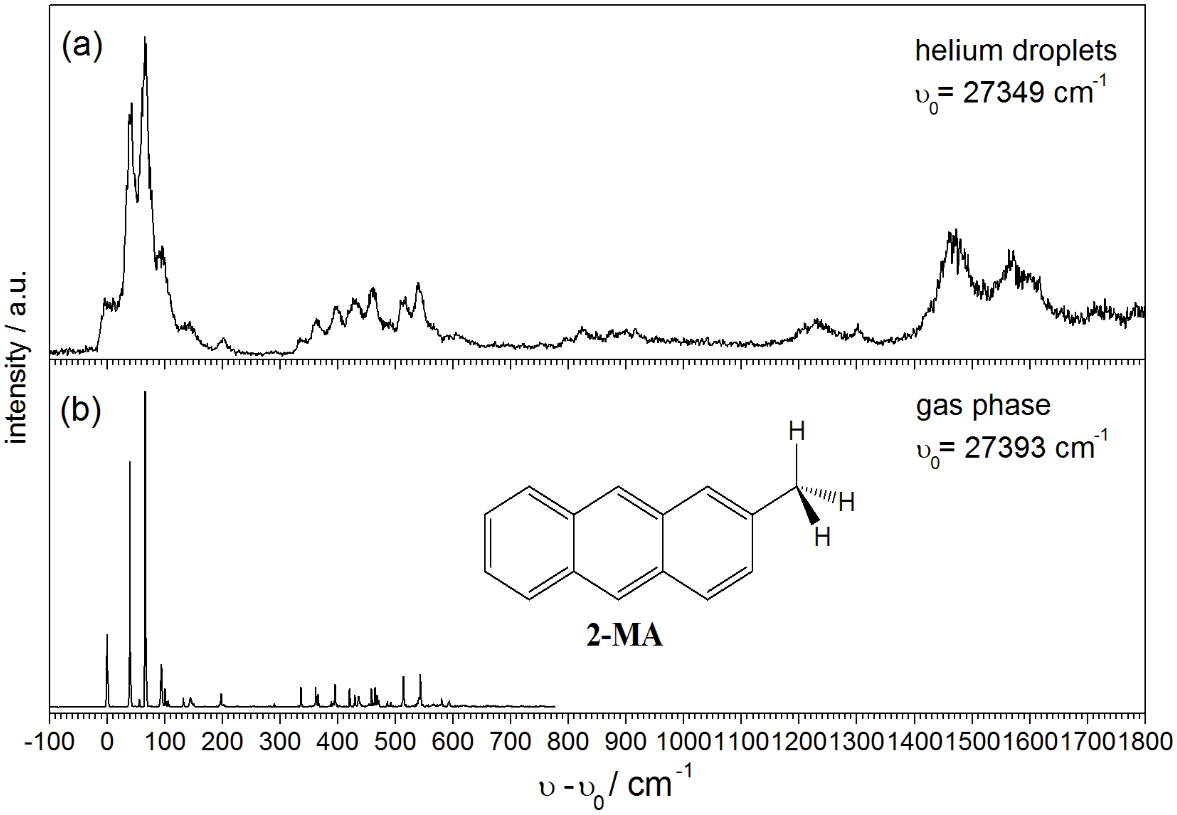

Fig. 5.33: Excitation spectra of 2-MA in helium droplets (a) and in the supersonic jet (b) with ν_0 as indicated. The laser intensity was low enough to avoid saturation effects.

can be excluded to be responsible for the spectral broadening: Upon lowering the laser intensity or the oven temperature only the entire signal level decreases while the overall spectral shape of the spectrum is not affected. Significantly increasing the oven temperature further broadens the spectrum and extends it to the red as is typically found in electronic spectra when oligomers start to grow in the droplets.

The broadening observed in the electronic spectrum in fig. 5.33 (a) is attributed to damping of the nuclear rearrangement induced upon electronic excitation as will discussed in chapter 5.9.1.

The low intensity level and the drastic line broadening do not allow for resolving a possible fine structure of the individual vibronic transitions in the excitation spectrum or for recording dispersed emission spectra.

5.9 Comparative Discussion

Within this chapter, two peculiarities of the electronic spectra of anthracene derivatives in helium droplets became apparent. These are a substantial line broadening in the excitation spectra of 9-PA and 2-MA and a pronounced fine structure of electronic transitions of the other derivatives. The fine structure consists of ZPL(s) accompanied by a PW with distinct sharp features. These observations will be discussed in the following.

5.9.1 Line Broadening in Electronic Excitation Spectra

Line broadening in the electronic excitation spectrum recorded in helium droplets was observed for 9-PA and 2-MA. As pointed out in the presentation of the experimental data the anthracene derivatives differ in the nuclear response to electronic excitation. The spectra of most derivatives in the gas phase as well as in helium droplets revealed the typical sparse spectroscopic signature of a rigid molecule. The rigidity concerning the substituent is reflected in particular by the absence of a low-frequency ($\nu_{vib} \leq 100$ cm^{-1}) Franck-Condon progression (FCP) and was confirmed by quantum chemical calculations. [Ohn79, ZZ88, ZSFH94, GNB94, ZHS95, JWKJ96, LBH^{+}98, JK97, NNS^{+}05, NNS^{+}06] In contrast, extended low-frequency FCP characteristic for a significant change of the geometry upon electronic excitation was observed in the gas phase spectra of 9-PA and 2-MA. The geometry change was attributed to a variation of the equilibrium torsional angle by 28° (9-PA) and 60° (2-MA), respectively. This assignment was corroborated by quantum chemical calculations. [NNS^{+}05, NNS^{+}06, LHP93, WGB85, WBGB87, SH03a]

Droplet spectra of those derivatives without extended FCP resemble the corresponding gas phase spectra and consist of sharp signals. The droplet spectra of 9-PA and 2-MA exhibit a similar intensity pattern and spacings between the individual transitions as in their gas phase spectra, however, with significant line broadening.

The broad spectra appear as the envelope of the corresponding gas phase spectra and can be reproduced reasonably well by a convolution of the gas phase spectra with an appropriate broadening function. In contrast to the broad spectral features observed for fluorazene (FPP) (chapter 6) and reported for phenol and aniline [LRD05, Log08] the spectra of 9-PA and 2-MA reveal rather symmetric line shapes. Convolution of the gas phase spectra with a Lorentzian fitted much better to the droplet spectrum than with a Gaussian. Reasonable agreement of the convoluted gas phase spectra with the experimental droplet spectra is obtained for line widths (FWHM) of 50 cm^{-1} and 20 cm^{-1} for 9-PA (fig. 5.34(a)) and 2-MA (fig. 5.34(b)), respectively. It should be noted that the simulated spectra were obtained for a single line width as the only fitted parameter.

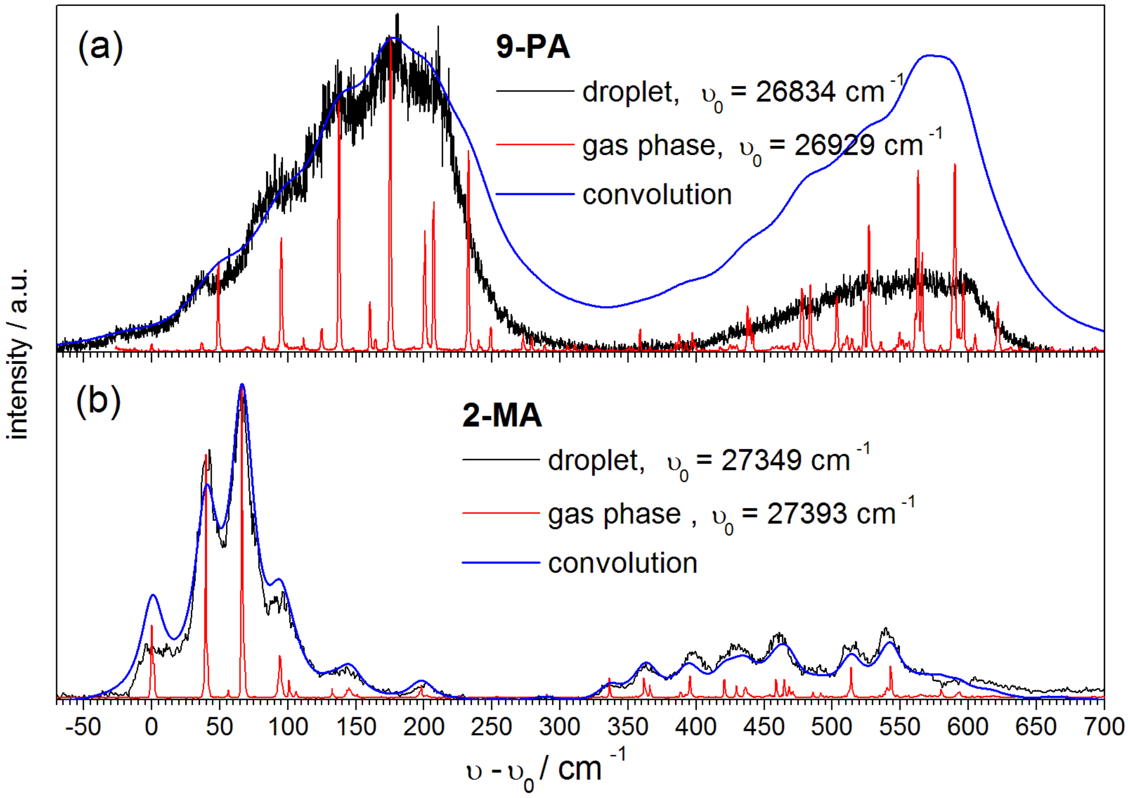

Fig. 5.34: Simulation (blue) of spectral broadening by convolution of the jet spectrum (red) with a Lorentzian. The spectrum obtained in helium droplets is shown for comparison (black). The upper panel (a) shows data for 9-PA (Lorentzian width 50 cm^{-1}), the lower panel (b) for 2-MA (Lorentzian width 20 cm^{-1}).

The almost perfect agreement in the frequency position contrasts to the deviations in the intensity pattern between the convoluted jet and the experimental droplet spectrum. Since none of the spectra consists of hot bands the differences cannot be due to a thermal effect. The deviations might partly arise from neglecting helium solvation effects such as the occurrence of PWs. A similar fine structure, consisting of ZPL and PW, as observed for the other anthracene derivatives would slightly change the shape of the simulated spectrum. However, it would be of minor influence on the relative intensity pattern since all of the transitions are expected to have the same fine structure. Though, a different intensity pattern can arise from a different fluorescence quantum yield of the individual transitions in the gas phase and in helium droplets. As was discussed in chapter 4.2 this is due to the different emissive states in helium droplets and in the gas phase. In case of 9-PA (fig. 5.34(a)) the simulated spectrum overestimates the fluorescence intensity for excess energies $\nu - \nu_0 \gtrsim 230\ \mathrm{cm}^{-1}$. This indicates that a decay channel into a dark state opens up in the droplets on excitation with higher vibrational excess energies. This may be accounted for by a scaling of the intensity of the gas phase spectrum used for the convolution by a factor of 0.25 for excess energies above 225 cm^{-1} . Fig. 5.35 (a) shows this modified gas phase spectrum and its convolution with a single Lorentzian (FWHM

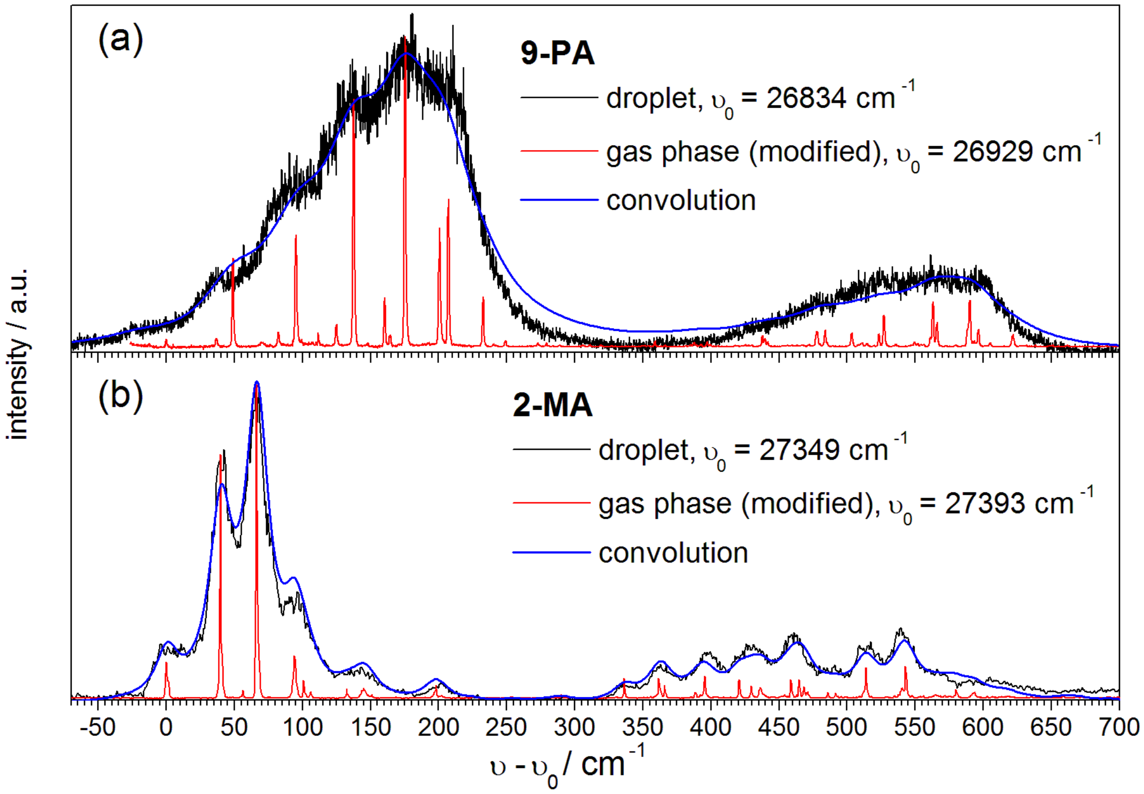

Fig. 5.35: Simulation (blue) of spectral broadening by convolution of the modified jet spectrum (red)(see text) with a Lorentzian. The spectrum obtained in helium droplets is shown for comparison (black). The upper panel (a) shows data for 9-PA (Lorentzian width 50 cm^{-1}), the lower panel (b) for 2-MA (Lorentzian width 20 cm^{-1}).

50 cm^{-1}) which is in better agreement with the experimental droplet spectrum. In case of 2-MA (fig. 5.34(b)) the largest deviations are observed at the electronic origin. An arbitrary scaling of the relative intensity at the electronic origin to about half of the experimental gas phase value leads to a much better agreement. (fig. 5.35(b)) This could be due to a decrease of the fluorescence quantum yield in the gas phase upon excitation with excess energy similar as discussed for 9,10-DCA in chapter 4.2.

The remaining discrepancies could be further reduced by introducing mode specific line widths, frequency shifts, and changes in relative intensity. For example, the line shape shown in fig. 5.36 for 2-MA was simulated by a superposition of individual Lorentzians taking into account slightly different widths and relative intensities for all transitions. The relative intensity of the split electronic origin was scaled to about the half and that of the other transitions by less than 10 % compared to the experimental gas phase values. However, the convolutions shown in fig. 5.34 and fig. 5.35 are most convincing due to the low number of fit parameters necessary to obtain reasonable agreement. In particular, all transitions reveal approximately the same homogeneous line width.

Convolution with asymmetric broadening functions did not improve the agreement between the simulated and experimental droplet spectrum. As a result of the convolution it

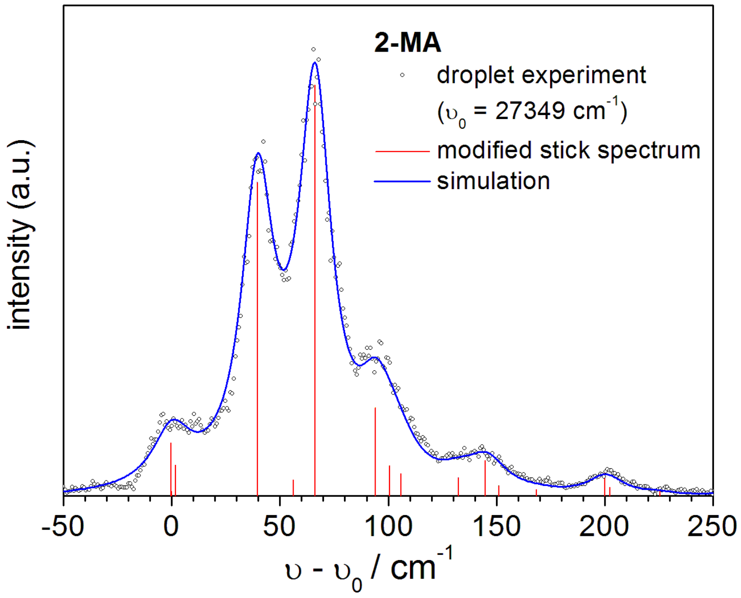

Fig. 5.36: blue: simulation of spectral broadening by superposition of Lorentzians at center frequencies and with relative intensities as indicated by the modified stick spectrum (red)(see text). The experimental data points obtained in helium droplets are shown for comparison (open circles).

is obvious that the vibrational fine structure in the electronic spectra of these two molecules in helium droplets are spectrally broadened but not changed in the frequencies. Consequently, the torsional potential and the corresponding mass of the dopant system are almost not affected by the helium environment.

Lorentzian line shapes are indicative of homogeneous broadening effects which is consistent with the assumption of an exponential decay of the excited molecular level. Line widths of 50 cm^{-1} and 20 cm^{-1} correspond to a damping time constant of 0.1 and 0.3 ps, respectively. This contrasts to the line width in the electronic spectra of the other anthracene derivatives in the order of 0.2 cm^{-1} which reflects the experimental spectral resolution. It corresponds to a lower limit for the decay time of 25 ps which is in the typical range of vibronic levels of closed shell molecules doped into helium droplets. (cf. chapter 4)

The observed broadening can be explained by a Lorentzian shape of the transitions which is in contrast to a different broadening effect, namely the PW dominating over the ZPL. This effect is discussed in chapter 6 and was reported e.g. in ref. [LRD05, Log08] for phenol and aniline in helium droplets. Characteristic for this broadening are asymmetric PWs extending over at least 50 cm^{-1} accompanying weak but sharp ZPLs. However, the spectra of 9-PA and 2-MA contain neither an indication for any sharp ZPL nor for an asymmetric spectral shape.

To conclude, substantial line broadening obtained for extended FCP in the electronic spectra of molecules in helium droplets is explained by damping of the corresponding nuclear rearrangements such as the variation of the equilibrium torsional angle. The damping cannot be solely due to the dissipation of vibrational excess energy because it is also effective on the vibrational ground state of S_1. This is reflected by the broadening of the electronic origin in the excitation spectrum of 2-MA. In the excitation spectrum of 9-PA in the gas phase the electronic origin is hardly visible and thus may be hidden below the noise in the droplet spectrum.

In general, the life time of an excited state is determined by radiative and non-radiative decay processes such as IVR, IC, and ISC. These processes are known to be state specific. [AHJ88] Torsional modes can be an efficient promoter for electronic non-radiative decay. [VF82, WGB85, PS86] In helium droplets these isoenergetic non-radiative processes may have different rate constants than in the gas phase and, most important, energy dissipation adds as a further non-radiative decay process.

The gentle interaction of the helium environment reflected by solvent shifts of electronic and vibrational transitions indicates a negligible variation of the relative energies of electronic and vibrational levels. Thus, the rate constants for isoenergetic intramolecular processes such as IC, IVR, and ISC are not expected to be significantly altered as compared to the gas phase and thus presumably are not responsible for the damping. This is corroborated by the decay times of vibronic levels of various fluorescing anthracene derivatives in the supersonic jet: Upon complexation with rare gas atoms the decay times are typically not altered by more than one order of magnitude. [HST85, KKHS92, PA93] In contrast, dissipation of vibrational excess energy or vibrational relaxation, respectively, was found to be faster than the competing radiative decay in the order of a few ns for all organic molecules yet investigated in helium droplets. [LS03, LS04b, LSK$^+$04, ST08] However, it is typically not faster than about 3 to 30 ps as determined from line shape analyses of excitation spectra of various molecules in helium droplets. (cf. chapter 4) Thus, the broadening may indicate an energy dissipation enhanced by nuclear rearrangements induced upon electronic excitation. In the case of 2-MA the damping process affects also the electronic origin indicating that not only the dissipation of vibrational excess energy but also of electronic energy, mediated by IC (or ISC) is enhanced.

An efficient energy dissipation requires a coupling of the molecular degrees of freedom with the surrounding environment. The coupling depends on the specific kind of interaction reflected by a coupling constant or operator, respectively, and the density of states both of the molecule (donor modes) and the helium environment (acceptor modes). For polyatomic molecules the density of states tends to increase with excess energy and strongly depends on the normal modes of the specific molecule. The density of states of the helium surrounding is quasi-continuous as is reflected by the shape of the broad PWs of molecules embedded in helium droplets. (cf. chapter 4 and the following section) The coupling to the helium environment was shown to be efficient for vibrational and rotational degrees of freedom as is reflected in the depletion of droplet beams upon excitation of embedded species and in dispersed emission spectra. [CLSS01, TV04, LS05, CDF$^+$06] Time constants for rotational relaxation were reported in the range of 5 ps $\leq \tau \leq$ 25 ns depending on the rotational constants of the dopant molecule. [CDF$^+$06] From line widths in IR and electronic spectra a lower limit for the vibrational relaxation times was determined in the order of 10 ps for most vibrational modes. (cf. chapter 4) The specificity of vibrational relaxation is reflected by the broadening of individual transitions in electronic spectra. For example, a broadening of vibrational modes in electronic spectra in helium droplets compared to the gas phase was observed for out of plane modes of pentacene (85, 207, and 304 cm^{-1}) resulting in line widths of about 7 cm^{-1} while an in plane mode with comparable vibrational energy of 265 cm^{-1} exhibited a line width of only 0.2 cm^{-1} . [LS05] Similarly, the 206 cm^{-1} mode of 9,10-DCA appears broadened with a line width of 8 cm^{-1} (chapter 5.2) wheras other modes of similar vibrational energy such as the 217 cm^{-1} mode of 9-CNA (chapter 5.4) exhibit line widths <1 cm^{-1} . Even low frequency modes of 1-MA having a methyl moiety (chapter 5.7), e.g. with 188 cm^{-1} , remain as sharp as in the gas phase.

In the case of 9-PA and 2-MA the low frequency torsional modes unambiguously increase the density of molecular states compared to other anthracene derivatives. The efficient coupling is attributed to the significant nuclear rearrangement induced upon electronic excitation and distorting the solvation. Note that both the high density of molecular states and the large coupling due to the geometry change do not only enhance the dissipation of pure vibrational excess energy but also of electronic excitation energy leading to a broadening of the electronic origin. This is in qualitative agreement with the observed low fluorescence intensity. As in any other host system [Tur78, KM95], the dissipation of electronic excitation energy thereby is thought to involve a redistribution over vibrational degrees of freedom (vibrational relaxation). In case the electronic excitation induces a 'smaller' geometry change only the dissipation of pure vibrational excess energy is enhanced. This is reflected by a broadening of the vibrational satellite structure while the electronic origin remains sharp. This was observed e.g. in the excitation spectra of the Pyrromethene dyes PM567 and PM650 in helium droplets and is discussed in chapter 7.

In summary, substantial line broadening of electronic spectra in helium droplets is explained by damping of nuclear rearrangements induced upon electronic excitation. The change of the geometry together with the increased density of molecular states enable fast energy dissipation. Without low-energy FCP and, thus, without nuclear rearrangement the electronic transitions in helium droplets remain at least as sharp as in the gas phase. This damping mechanism is expected to affect the dynamics of intra- and intermolecular processes involving significant nuclear rearrangements such as isomerizations and (photo)chemical reactions.

5.9.2 Fine Structure of Electronic Transitions

The electronic transitions in the excitation spectra of all anthracene derivatives yielding sharp spectra exhibit a distinct fine structure that has no counterpart in the gas phase. On the right side of fig. 5.37 a section of 9 cm^{-1} including the electronic origin of the molecules indicated on the left side of fig. 5.37 is shown. The vibronic transitions at least indicated the same fine structure though often cannot be fully resolved due to an increased line width.

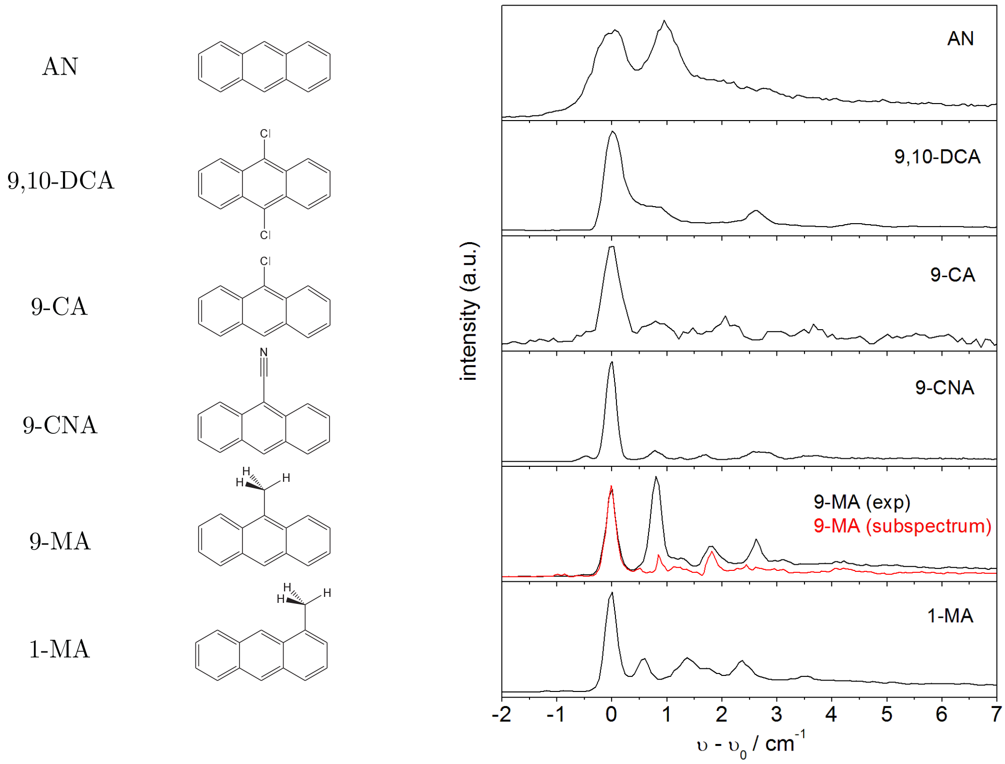

Fig. 5.37: Molecular structures (left) and excitation spectra at the electronic origin (right) of all investigated anthracenes yielding sharp spectra. ν_0 as given in the corresponding chapters. The experimental spectrum (black) and a single subspectrum (red) are plotted for 9-MA.(cf. chapter 5.6)

The fine structure was argued to consist of ZPls and accompanying PWs. The most intense transition was thereby assigned to the ZPL since it is the first significant transition on the red side of the spectrum and saturates at lower laser intensities than the other transitions. Consequently, transitions to the blue of the ZPL(s) that have no counterpart in the corresponding gas phase spectrum were attributed to features of the PW(s). For all derivatives the PW contains distinct sharp features and in addition a broad contribution extending over more than 10 cm^{-1} . The contribution of the PW cannot be reduced further than shown in fig. 5.37 upon changing any experimental parameter, in particular the laser intensity.

Interestingly, in none of the spectra the PW is separated from the ZPL by a gap of about 5 - 6 cm^{-1} as was found in the excitation spectra of other molecules such as glyoxal, phthalocyanine, tetracene and pentacene. [HMTV96, HLTV02, LS05] The gap was interpreted in terms of the density of states of superfluid helium as was discussed in chapter 4. However, only in the case of glyoxal the PW could be shown to reflect the density of states of superfluid helium. Sharp features of PWs e.g. in the spectra of perylene [LS05], as well as the broad PWs observed e.g. in the spectra of aniline, phenole or FPP (cf. chapter 6.3) revealed a different spectral shape. Interestingly, no PW was observed in the excitation spectrum of benzene in helium droplets. [ScD+04, BBC+05, LBD08] The spectrum of naphthalene does not contain a PW within 2 cm^{-1} excess energy. [Lin99] It should be noted that the PW in the excitation spectra of AN (chapter 5.1), tetracene, and phthalocyanine [PRD+09] recorded in the pulsed droplet beam is identical to that observed in the continuous droplet beam. [KRH05, HLTV02] Thus, the missing of the phonon gap cannot be attributed to any property of the droplets.

As discussed in the previous chapters only the excitation spectrum of AN revealed a multiplet splitting of the ZPL due to the helium solvation. In case of 9-MA the double structure separated by 0.8 cm^{-1} at the electronic origin was attributed to an overlap of two subspectra within different tunneling symmetries. The excitation spectrum could be separated into the two subspectra as discussed in chapter 5.6. Fig. 5.37 shows the experimental spectrum and one of the extracted subspectra.

The fine structures in the excitation spectra shown in fig. 5.37 of anthracene with different substituents are not identical, but render some similarities: The sharp features display a similar relative intensity compared to the ZPL and correspond to similar phonon energies in the excited state S_1 and in the ground state S_0. (table 5.10) These quasi-localized phonons are assigned to excitations of the non-superfluid helium solvation layer around the chromophores. [HLTV02] (cf. chapter 4) Thus, the similarity of the PW structure indicates a similar solvation layer as is expected for molecules with similar molecular structures and properties. As was discussed in chapter 4 the relative intensity of ZPL and PW reflects the absorption cross section and quantum yield for relaxation into the emissive state. According to the configuration coordinate model, the anthracene derivatives belong to an intermediate case of electron-phonon coupling strength. (cf. chapters 4 and 8)

The observed sharp features of the PWs corresponding to phonon energies below 5 cm^{-1} (table 5.10) are attributed to excitations of the non-superfluid solvation layer of localized He atoms. Excitation spectra of van der Waals clusters of AN with He atoms in supersonic jets revealed vibrational lines with low frequencies in particular of about 8 cm^{-1} and 22 cm^{-1} . [EJN+00, EAHJ01] Additionally very weak vibronic bands at

Tab. 5.10: Phonon energies in S_1 and S_0 states of anthracene derivatives yielding sharp excitation spectra in helium droplets.

molecule	phonon energy S_1 / cm^{-1}	phonon energy S_0 / cm^{-1}
AN	≈ 2	
9,10-DCA	0.8 , 2.6, 4.5	
9-CA	0.8, 2.1, (3.6)	(0.5)
9-CNA	0.8, 1.7, 2.6	0.5
9-MA	≈ 0.8, 1.8	0.5
1-MA	0.6, 1.4, 2.4, 3.5	0.8, 1.2

2.0 cm^{-1} , 3.6 cm^{-1} and 7.0 cm^{-1} were reported for the cluster with 4 He atoms. However, all of these modes disappear upon increasing the cluster size and no v.d.W.-modes were observed for clusters with more than 7 He atoms. [EJN$^+$00, EAHJ01] The lower vibrational frequency of the quasi-localized phonons in the droplets compared to the v.d.W.-modes for the smaller clusters could be attributed to a weaker v.d.W. bond or a larger effective mass due to the helium surrounding. However, there is no indication for the correspondence of the phonons to certain v.d.W.-modes of the clusters in the jet.

As mentioned above, only the unsubstituted AN exhibits a multiplet splitting of the ZPLs due to the helium solvation. The splitting of the AN signals was found to vanish upon complexation with a single water molecule. The same behavior was observed for tetracene: The excitation spectrum of bare tetracene reveals a double splitting of the ZPLs whereas only single ZPLs are observed for the 1:1 complexes with water. [LTV06] The excitation spectrum of clusters of tetracene with single Ar atoms revealed the formation of two configurations of the 1:1 complex. [PVH01] These were attributed to complexes with the single Ar atom above or in the aromatic plane. No splitting is observed for the former complex. In contrast, it remains for the latter though with a different splitting and intensity ratio of the two ZPLs. [PVH01] The absence of the splitting for the complex with the Ar atom above the aromatic plane was attributed to a perturbation of the first solvation layer of localized He atoms around tetracene. [PVH01, LTV06]

Upon substitution of the anthracene body the splitting of the ZPL vanishes. This is even the case upon substitution of an H-atom by a chloro- (9-CA) or a cyano-group (9-CNA) which are arranged within the aromatic plane and upon symmetric substitution as for 9,10-DCA maintaining the molecular symmetry. Obviously any of the substituents significantly alters the solvation and perturbs the mechanism causing the splitting.
Interestingly, the line width at the electronic origin in the spectra shown in fig. 5.37(b) decreases upon substitution and approaches the experimental spectral resolution given by the laser width. The larger line width of the transitions of AN may be indicative for a relaxation process as discussed in chapter 5.1.

5.10 Summary

In this chapter electronic spectra of eight anthracene derivatives were presented and discussed. The spectra of unsubstituted anthracene (AN) were found to be similar as in the gas phase though exhibiting a splitting of the ZPLs into at least two contributions similar as previously found for tetracene in helium droplets. Emission spectra revealed a pairwise coincidence of the emission spectra upon excitation at two transitions exhibiting the same saturation behavior. However, the pairwise identical emission spectra were found to be slightly shifted against each other by 1-2 cm^{-1} . Applying the configuration coordinate model successfully used to explain the spectroscopic behavior of tetracene and other molecules in helium droplets no satisfactory interpretation could be found. This could be due to the necessity to consider dynamic effects. However, emission spectra were recorded with a pulsed excitation source at the limit of the spectral resolution of the detection unit which shows some artefacts. Thus, further experiments were suggested to clarify the remaining experimental uncertainties.

The peculiar multiplet splitting in the excitation spectrum of AN was not observed for 9,10-DCA belonging to the same point group D_{2h}. However, the transitions in the excitation spectrum exhibit a fine structure consisting of a single ZPL accompanied by a PW including sharp features. Contributions of different isotopomers of 9,10-DCA could be separated at vibronic transitions involving the excitation of the symmetric C-Cl stretching mode. These revealed the same fine structure for each isotopomer. Emission spectra recorded upon excitation with phonon excess energy were found to coincide with emission induced upon excitation at the electronic origin whereas a gradual red shift of the emission increasing with vibrational excess energy was observed. This may be attributed to a gradual variation of the non-superfluid solvation layer though was argued to be unlikely. However, emission spectra recorded with the same detection unit and excitation laser tuned over about the same spectral range did not cause a shift of the emission spectrum of 9-CNA.

The electronic spectra of anthracene substituted with moieties such as a Cl atom (9-CA) or a cyano group(9-CNA) at the central ring of AN resembled the corresponding gas phase spectra. The electronic transitions revealed a fine structure similar as for 9,10-DCA.

The electronic spectra of the isomers 9-MA and 1-MA also exhibited a fine structure of the transitions. For the former a splitting was observed which was attributed to be due to a tunneling splitting within the torsional potential. The different splitting and vibrational fine structure of 9-MA in helium droplets compared to the gas phase was tentatively assigned to variations in the shallow torsional potential. The spectra revealed no indication for a change of the geometry, in particular of the torsional angle, upon electronic excitation. For the latter molecule 1-MA the excitation spectrum in helium droplets resembled the gas phase spectrum and indicated that no significant geometry change is induced upon electronic excitation.

In contrast, the spectra of 9-PA and 2-MA exhibited extended Franck-Condon progressions (FCPs) of the torsional mode with the peak intensity at higher transitions. The torsional potential and vibrating mass is not significantly altered upon the solvation in helium droplets as was reflected by the vibrational frequencies and intensity pattern in the excitation spectra recorded in helium droplets and in the gas phase. However, the individual transitions were found to be drastically broadened with the droplet spectrum resembling the envelope of the gas phase spectrum.

This broadening was analyzed in the comparative discussion and was attributed to a damping of nuclear rearrangements induced upon electronic excitation. The time constant of the damping was determined to be about 0.1 ps in the case of 9-PA and 0.3 ps for 2-MA. The damping is expected to affect the dynamics of intra- and intermolecular processes such as isomerisations or (photo)chemical reactions.

At the end of the chapter the fine structure observed in fluorescence excitation spectra of those anthracene derivatives exhibiting sharp spectra was discussed and revealed similar features of the PWs. These were attributed to similar phonon energies in the electronic (ground and) excited states indicative of similar non-superfluid helium solvation layers around the molecules in line with chemical intuition.

For all of the molecules discussed, vibrational frequencies were only weakly perturbed by the droplet environment. Only in the case of 9-MA differences in the electronic spectra in helium droplets compared to the gas phase were attributed to a variation of the torsional potential. However, in the case of 9-MA the potential was found to be quite shallow and thus pronounced sensitive to interactions with an environment, even with helium.

6 Intramolecular Charge Transfer Systems

Dual fluorescence in polar solvents is observed for many molecules containing both electron donor and acceptor moieties. [GR03, YGD$^+$03, GRBPR05] Along with normal fluorescence from the locally excited (LE) state red shifted anomalous fluorescence gains intensity with increasing polarity of the solvent. The transition frequency of the former hardly depends on the solvent whereas the anomalous fluorescence exhibits a red shift, which increases with the solvent polarity. The pronounced solvatochromic shift is due to the large dipole moment of the emitting state which is therefore assigned to an intramolecular charge transfer (ICT) state. The LE and ICT-states correspond to minima on the surface of the first excited singlet state S_1 with the former usually lower in energy in nonpolar solvents and the latter in polar media. The decreasing emission from the LE state in favor of emission from the ICT state observed for increasing polarity of the solvent is thus ascribed to a stronger stabilization of the ICT state in S_1. [GR03, GRBPR05, CZH06]

Various models for the structural conformation and the mechanism of the formation of ICT states in flexible donor-acceptor molecules have been proposed. [GR03, GRBPR05] The most frequently used are the TICT (twisted ICT) model with the donor and acceptor moieties perpendicular to each other and the PICT (planar ICT) model corresponding to a planar configuration. Though, the essential difference between the TICT and other ICT models is rather the absence of electronic coupling between the donor and acceptor groups in the TICT state (principle of zero electronic overlap) than the different geometries. [GR03, YDZ04, GRBPR05, SHD05] The ICT state can be formed via an adiabatic reaction pathway from the LE to the ICT state or via a nonadiabatic reaction path from the Franck-Condon structure of S_2 to either ICT or LE via a conical intersection. [GRBPR05, CZH06]

N-Phenylpyrrole (PP, fig. 6.1) is a typical flexible donor-acceptor molecule showing dual fluorescence and has been studied extensively experimentally [ONOS98, BHR02, YGD$^+$03, YDZ04, SBH$^+$05, SHD05] and theoretically [PMSA00, Par00, ZH02, CZH06, XCZ06, HL07]. [GR03] However, the nature of the ICT state responsible for the anomalous emission and the mechanism of its formation after excitation into the LE state is still under controversial discussion. [GR03, YDZ04, SHD05, CZH06, DKS^{+}08] The PICT state of PP has a quinoidal structure with shortened central bonds of the benzene ring and a shortened C-N bond between the aromatic rings. On the contrary, the TICT state has an antiquinoid structure with lengthened bonds in the benzene ring and between the rings. [SHD05] In ab initio calculations both structures were found to be minima of the same potential surface with only slightly different energies. [SHD05] The LE state was found to be lower in energy than the ICT states for the bare molecule which is in line with the experimental observations in supersonic jets. [BHR02, ONOS98] In the molecular beam even clusters of PP with acetonitrile showed only emission from the LE state. [BHR04] In contrast, clusters of the cyano-substituted PP (PBN) with acetonitrile revealed emission from the ICT state for clusters with at least four acetonitrile molecules. The different behavior of the substituted compound was attributed to the larger binding energy between acetonitrile and the substituted chromophore compared to the parent compound. [BHR04]

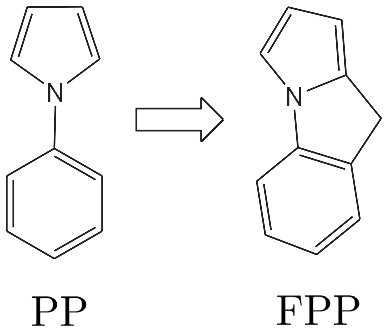

Fig. 6.1: Molecular structures of N-phenylpyrrole (PP) and its rigidized counterpart fluorazene (FPP).

Recently, fluorazene (FPP, fig. 6.1) was found to have a similar spectroscopical behavior as PP, in particular with respect to the emission from an ICT state. [YDZ04] The ratio of emission from the ICT state compared to the LE state under the same conditions was found to be even larger and to increase with increasing polarity of the solvent and by lowering the temperature. However, for FPP the donor (pyrrole) and acceptor (benzene) moieties of PP are rigidly connected by a methylene bridge preventing appreciable nuclear rearrangements. [YDZ04] Thus, it was suggested that also for PP the ICT state is not accessed via a geometrical change. [YDZ04, XCZ06, HL07, DKS^{+}08]

PP was also studied in neat Ar matrices where only emission from the LE state was found. [SH03b, SBH^{+}05, SHD05] In Ar matrices containing also acetonitrile dual fluorescence was observed. However, excitation and emission spectra of sites attributed to PP with acetonitrile in its vicinity were broad and thus information on the structure of the complexes remained hidden. [SH03b, SBH^{+}05, SHD05] Since the formation of the

ICT state may be related to geometrical changes of the molecule or the complex of PP with acetonitrile(s), respectively, rigid matrices in general may not be suitable to study the ICT phenomenon. [SHD05] Instead, supersonic jets and superfluid helium droplets should be better suited for this purpose.

However, the size distribution as well as the conformation of solvated complexes created in a seeded beam expansion is often only ill defined. Further, these clusters are often not efficiently cooled during the expansion. [Sco88, EJN$^+$00, EAHJ01, BHR04, SHD05] In contrast, clusters formed in helium droplets are cooled to the droplet temperature of only 0.37 K within picoseconds. [TV04, CDF$^+$06, ST08] The droplet environment allows for the investigation of metastabile complexes, and under certain circumstances only a small number of isomeric clusters are formed. [TV04, CDF$^+$06, ST08] Spectrally isolated transitions can be assigned to clusters of a defined stoichiometry by fitting a Poissonian distribution to the signal intensity measured as function of the particle density of the sample in the pick-up cell. [TV04, CDF$^+$06, ST08] Selective excitation of different clusters can yield information on their emissive behavior. In the particular case of molecules capable of dual fluorescence, possibly the number of solvent molecules around the chromophores necessary to switch from normal to anomalous emission can be determined. Further, heights of possible barriers necessary to overcome for the formation of ICT states might become accessible. This strategy was successfully applied for example to clusters of 3-hydroxyflavon with water. [LPV$^+$09] In the following, the spectroscopic results on PP and FPP in helium droplets will be presented and compared to the respective gas phase data. For both molecules broad spectra were found in helium droplets. In the case of FPP the broadening arises from the dominance of PWs due to strong electron-phonon coupling as will be discussed in the last section also with respect to other systems.

Helium droplets were generated at a stagnation pressure of 80 bar, nozzle temperatures ranging from 20 K to 23 K and a repetition rate of 20 Hz or 50 Hz. The frequency doubled output of the LPD3002 or Scanmate dye laser system (dyes: Coumarin 153) was used for excitation. Integral emission was detected with the PMT H5783P or PMT R 943-02 (all Hamamatsu) protected by various cut-off filters. (see text) Gas phase data are taken from ref. [Gre09]

6.1 Phenylpyrrole (PP)

Fig. 6.2 shows the excitation spectra of PP in a supersonic jet and in helium droplets. The gas phase spectrum (red) with the electronic origin found at 35497 cm^{-1} is in agreement with literature data though exhibits a higher spectral resolution and a slightly different intensity pattern. [ONOS98, BHR02] Long progressions of a low frequency mode with irregular spacings appear in the excitation spectrum and were also observed in single vibronic level dispersed emission spectra. [ONOS98] This low frequency mode is assigned to the torsional mode of PP. [ONOS98, BHR02, XCZ06, HL07] The pattern of the torsional mode for excess energies < 700 cm^{-1} observed in excitation and emission spectra can be well fitted with the model of an one-dimensional rotor. [ONOS98] The minima of the deduced torsional potential are found at dihedral angles of 38.7° in S_0 and 19.8° in S_1, respectively. [ONOS98] The irregular spacings are due to the low barriers to planarity of 457 cm^{-1} in the torsional potential in S_0 and of only 105 cm^{-1} in S_1. [ONOS98] From the excitation spectrum shown in fig. 6.2 a dihedral angle of 18.9° and a barrier of 108 cm^{-1} are determined for S_1 in good agreement with the literature values. [Gre09] Ab initio calculations provide various absolute values for the dihedral angles, though all approaches agree with a decrease of the dihedral angle by up to 20° upon electronic excitation. [PMSA00, CZH06, XCZ06, HL07] Isolated PP in the gas phase was found to emit only normal fluorescence which is in accordance with the findings in the literature [ONOS98, BHR02] and with experiments on other molecules capable of dual fluorescence such as the well-known DMABN. [NMB$^+$05]

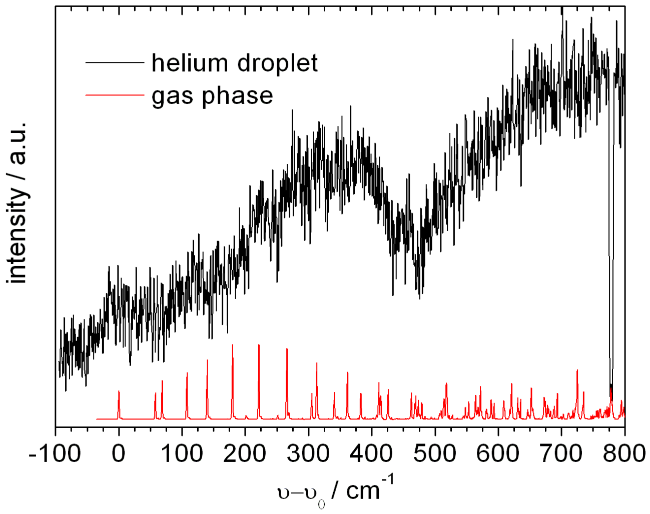

Fig. 6.2: Excitation spectra of bare PP in the gas phase and helium droplets with $\nu_0 =$ 35497 cm^{-1} and 35279 cm^{-1} , respectively. For the gas phase spectrum a cut-off filter WG295 and for the droplet spectrum a filter WG305 was used, respectively. At an excess energy of about 780 cm^{-1} the droplet beam was switched off.

Fig. 6.2 also shows the excitation spectrum of PP in helium droplets with $\nu_0 = 35279$ cm^{-1} . It appears broader than in the gas phase and seems to follow roughly its envelope. The large shift of about 220 cm^{-1} to the red is surprisingly large.

The excitation spectrum was recorded with an oven temperature of 10°C which is in the expected temperature range for optimum single doping with PP and is the same as for

FPP. Additionally, the PP sample was wrapped with aluminium foil with a small hole. In the gas phase experiments similar sample and nozzle temperatures were used for both molecules. [Gre09] At lower oven temperatures the spectrum only looses intensity, but no variations of its shape are observed. Increasing the sample pressure further broadens the spectrum as is typically found in electronic spectra when oligomers start to grow in helium droplets. The amount of sample evaporated during the measurements was typical for experiments on single doped droplets. The shape of the spectrum roughly describes the envelope of the gas phase spectrum of the monomer indicating that the droplet signal also stems from the monomer. Thus, multiple doping seems to be rather unlikely to cause the spectral broadening.

Broad excitation spectra can also arise from saturation effects. However, the laser intensities used are comparable to those used for other molecules and upon lowering the laser intensity the spectrum only looses intensity but does not change its shape. Thus, saturation effects can be excluded to cause the broadening with high confidence.

From the gas phase experiments and ab initio calculations the potential energy curves in S_0 and S_1 were deduced and revealed a distinct change of the torsional angle by almost 20° upon electronic excitation. As discussed in chapter 5.9.1 and in ref. [PGDS10] such a change of the geometry can lead to a damping of the nuclear rearrangement which causes spectral broadening. Further, electronic spectra in helium droplets also appear broad in the case of strong electron-phonon coupling which may also occur for PP.

The LIF signal level of PP in helium droplets is rather low. In broad electronic spectra the intensity is not concentrated in few transitions with a low FWHM, but is distributed over a larger spectral range therefore causing a low signal to noise ratio. Due to the low signal level and broad spectrum of bare PP its clusters with solvent molecules such as acetonitrile were not investigated.

6.2 Fluorazen (FPP)

As mentioned in the previous chapter, electronic spectra of flexible molecules possibly undergoing nuclear rearrangements upon electronic excitation can be broadened in helium droplets. Thus, these molecules are not well suited to study ICT in helium droplets since the formation of the ICT state may be related to changes of the geometry, e.g. of a torsional angle. However, ICT has also been reported for molecules that cannot undergo substantial nuclear rearrangements. In particular, dual emission has been observed from fluorazen (FPP). [YDZ04](Fig. 6.1) It even shows a more pronounced ICT behavior compared to PP. In FPP the two aromatic rings of PP are connected by a methylene-bridge and thus the torsional motion is inhibited.

Fig. 6.3(b) shows the excitation spectrum of FPP in the supersonic jet with $\nu_0 =$

34310 cm^{-1} corresponding to the transition with the lowest energy, therefore, assigned to the electronic origin. The origin is the most intense signal and no intense low frequency modes appear which is the typical spectroscopic signature of a rigid molecule. A normal mode analysis of the LE state is discussed in ref. [Gre09]. SVL spectra in the gas phase revealed only emission stemming from the LE state independent of the excitation energy. These spectra show only a small number of vibronic transitions corresponding to similar vibrational frequencies as found in the excitation spectrum. [Gre09] The almost mirror symmetry of excitation and emission spectrum (recorded via excitation at the electronic origin) provides further evidence for the invariance of the geometry of the molecule upon electronic excitation.

Ab initio studies on FPP in the gas phase confirmed that no significant geometry changes are induced by electronic excitation. [XCZ06, HL07] The molecule remains perfectly planar and upon excitation into the LE state only the bonds within the phenyl ring are slightly expanded while the C-N bond connecting the two aromatic rings is slightly shortened. [XCZ06, HL07]

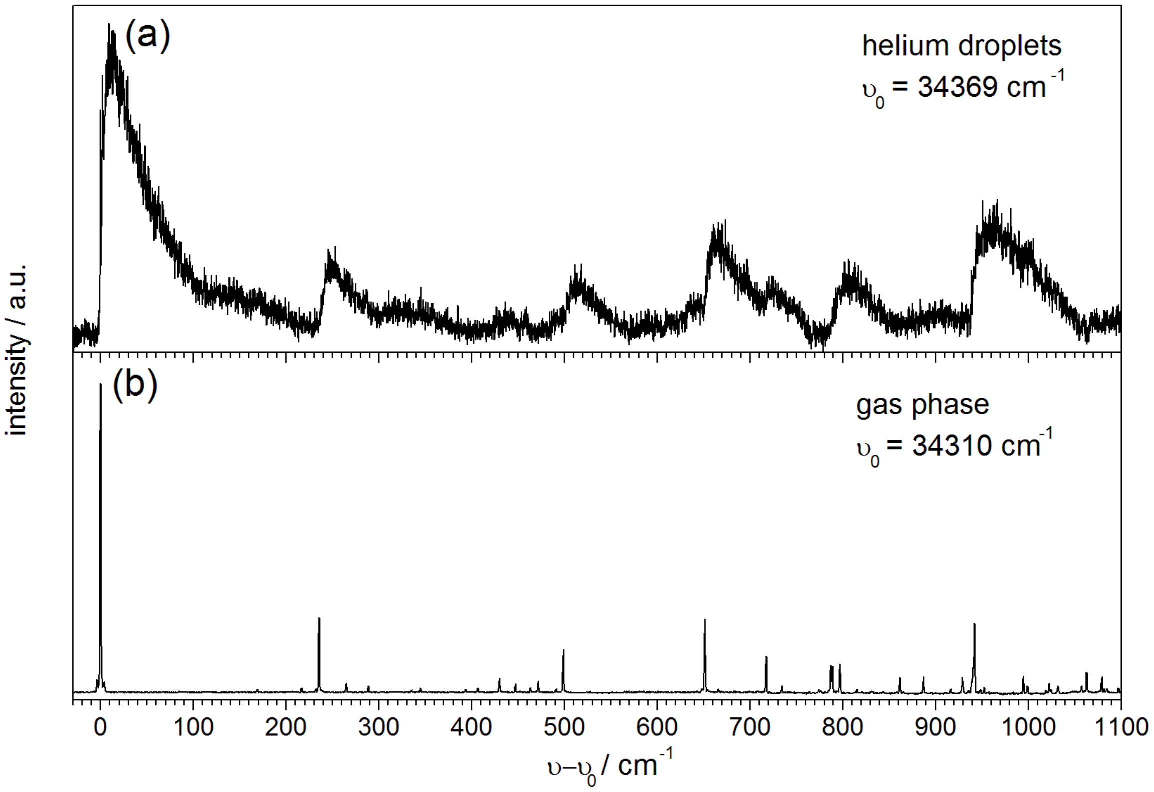

Fig. 6.3: Excitation spectra of bare FPP in helium droplets (a) and in the gas phase (b) with ν_0 as indicated. The droplet spectrum was recorded without a cut-off filter due to the weak fluorescence, the gas phase spectrum with a filter WG305. The temperature of the pick-up cell was 10°C.

The excitation spectrum of FPP in helium droplets with $\nu_0 = 34369$ cm^{-1} is presented in fig. 6.3(a). No signal was found to the red of this transition which is therefore assigned to the electronic origin. The solvent shift of about 60 cm^{-1} compared to the gas phase is in the typical range observed for rigid molecules doped into helium droplets. The spectrum displays the same pattern as in the gas phase and thus corroborates the assignment. However, each transition found in the gas phase spectrum appears as a sharp line accompanied by a broad asymmetric band with a FWHM of about 35 cm^{-1} as can also be seen in fig. 6.4. This pattern is typical for weak ZPLs followed by strong PWs. Vibrational frequencies of the prominent lines in helium droplets for which the ZPL can clearly be identified are listed in table 6.1 compared to the corresponding gas phase values. The variations of the vibrational frequencies are in the typical range of less than 1 %.

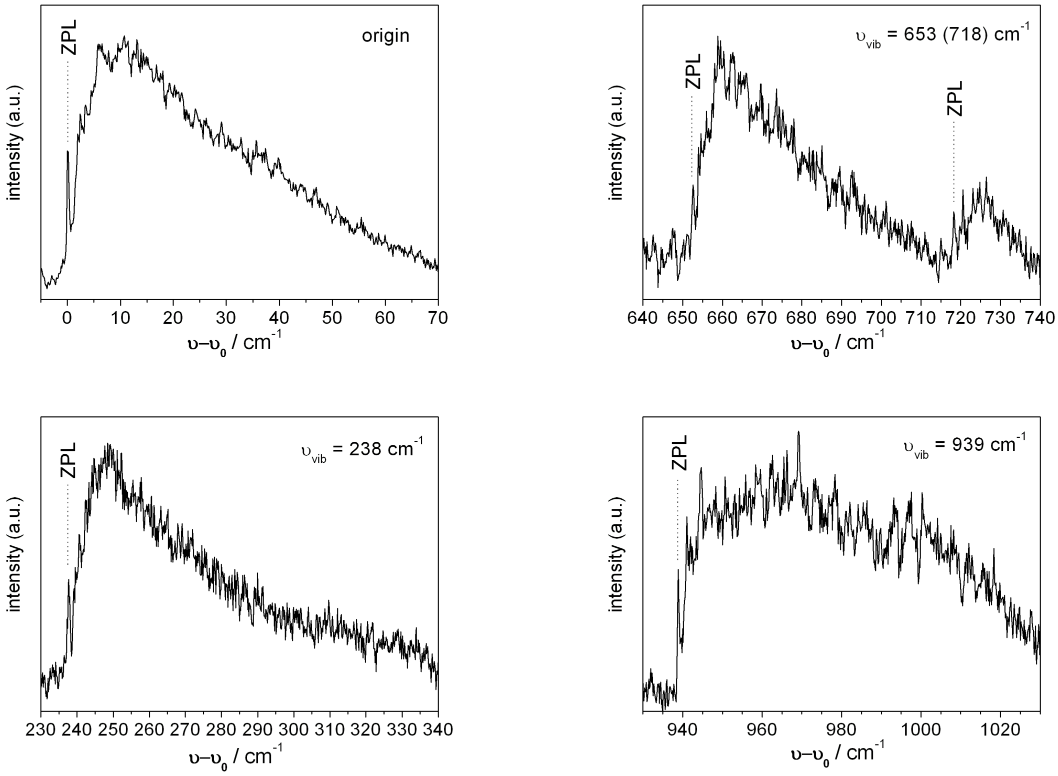

Fig. 6.4: Excitation spectra of selected bands of FPP in helium droplets on an expanded scale. Despite of the low signal to noise ratio the sharp ZPLs are reproducible.

PWs often have smaller absorption cross sections, and the life times of the respective excited states are shorter, as compared to the corresponding ZPLs. (cf. chapter 4) Therefore, intense PWs are often observed when high laser intensities already saturating the corresponding ZPLs are used. Fig. 6.5 shows the electronic origin recorded with different laser intensities demonstrating that the intensity ratio of ZPL and PW is not altered in the range of laser intensities used. An invariance of the intensity ratio is expected only if none or both transitions are saturated. For the intensities used a saturation of the PW can be excluded and, therefore, saturation effects can be excluded to cause the

Tab. 6.1: Relative wavenumbers $\nu - \nu_0$ (cm^{-1}) of the transitions of FPP in the supersonic jet ($\nu_0 = 34310$ cm^{-1}) and in helium droplets ($\nu_0 = 34369$ cm^{-1}) and their differences.

$\nu - \nu_0$(droplet)/cm^{-1}	$\nu - \nu_0$(jet)/cm^{-1}	shift/cm^{-1}
0	0	0
238	236	+2
502	499	+3
653	651	+2
718	717	+1
939	942	-3

intensity pattern in the excitation spectrum in fig. 6.3(a). This is also indicated by the intensity pattern within the vibrational fine structure resembling that found in the gas phase spectrum recorded without saturation. (fig. 6.3)

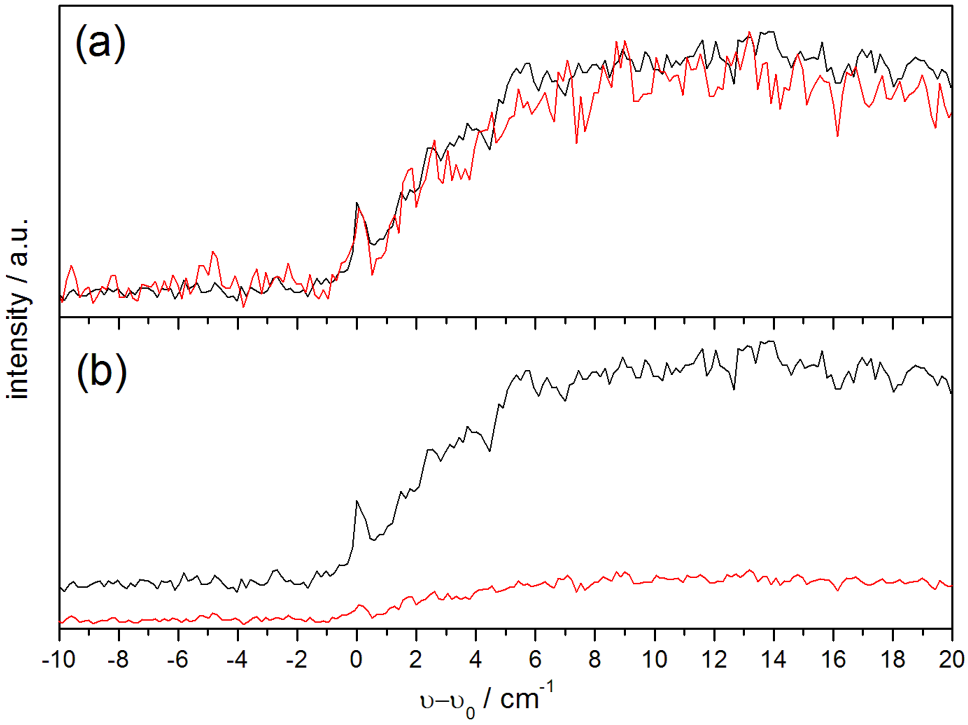

Fig. 6.5: Excitation spectrum at the electronic origin of FPP in helium droplets recorded with different laser intensities on a relative (a) and absolute (b) intensity scale.

Unfortunately, for FPP in helium droplets LIF is only weak and distributed over a large spectral range. Hence, dispersed emission spectra could not be obtained with reasonable signal to noise ratio. Instead, excitation spectra were recorded using different cut-off filters in front of the PMT. Thereby, the spectral pattern as shown in fig. 6.3 has not changed. Comparing the integral emission induced upon excitation with a fixed laser frequency thus yields information on the spectral distribution of the emission and thereby on the nature of the emissive state. On the right side of fig. 6.6 the integral emission recorded without a filter and using a WG305, WG325, and WG385 cut-off filter, respectively, is plotted. In order to distinguish between LIF and scattering, the intensity was recorded with each filter once with the nozzle opening synchronized to the laser pulses (syn) and once asynchroneous (asyn). The differences of two corresponding signal levels indicated by arrows in fig. 6.6 reveal bare molecular fluorescence.

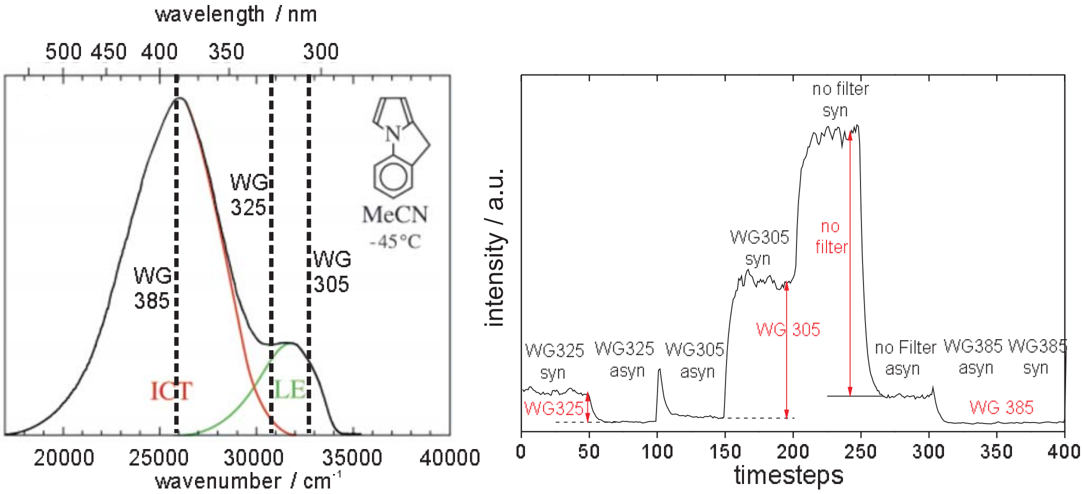

Fig. 6.6: Left: Emission spectrum of FPP in acetonitrile at -45°C. Figure taken from ref. [YDZ04]. Right: Fluorescence intensity in helium droplets recorded with different cut-off filters as indicated on the left side. Syn/asyn: nozzle openings synchronized/asynchroneous to the laser pulses.

The spectral position of the cut-off filters in the emission spectrum of FPP in acetonitrile at -45°C is shown in fig. 6.6 (left) and displays the spectral distributions of the emission stemming from the LE and ICT state, respectively. The dispersed emission spectrum in helium droplets is expected to be similar with respect to the red shift of the ICT-emission by at least 40 nm compared to the LE-emission. The decrease of signal displayed in fig. 6.6(right) with increasing the cut-off wavelength of the filter is in accordance to emission exclusively from the LE-state. Thus, as found in the gas phase, the emission of the bare system exclusively stems from the LE-state, but not from an ICT-state.

Clusters of FPP with solvent molecules such as acetonitrile were not investigated in helium droplets due to the low fluorescence intensity of the bare molecule and its broad spectrum. Signals of the clusters are expected to overlap with signals of the bare system at least in the excitation spectra and to be also weak. Thus, an unequivocal assignment of the signals to certain clusters and their selective excitation to probe the emissive behavior, i.e. to distinguish between emission from a LE or ICT state, would be impossible.

6.3 Discussion

PP was found to be twisted in S_0 and S_1 (LE-state) though with different dihedral angels of about 39° and 20°, respectively. As discussed in chapter 5.9.1 and ref. [PGDS10] a significant change of a torsional angle upon electronic excitation can lead to a broadening of the ZPLs in electronic spectra due to damping of the respective excited states. This was e.g. found for 9-phenylanthracene with a change in the torsional angle by 28°. A damping of all excited states including the vibrational ground state of S_1 also lowers the fluorescence quantum yield and distributes the intensity of single transitions over a large spectral range both attributing to a low signal to noise ratio.
The spectroscopy of FPP shows the typical signature of a rigid molecule with no significant nuclear rearrangements induced upon electronic excitation. This is also confirmed by ab initio calculations. [XCZ06, HL07] Emission of bare FPP in the gas phase and helium droplets was shown to stem exclusively from the LE-state indicating that the ICT states are higher in energy or lower in energy but not accessible due to a barrier preventing relaxation from LE to ICT states. Quantum chemical calculations confirm the LE state to be the global minimum of the S_1 potential energy surface of the bare molecule. [XCZ06, HL07] From PP and other molecules capable of dual fluorescence such as DMABN, emission in supersonic jets was reported to stem only from the LE state. [ONOS98, BHR02, NMB+05]

Each transition in the electronic excitation spectrum of FPP in helium droplets consists of a weak ZPL accompanied by an intense asymmetric PW indicating a strong electron-phonon coupling. According to the configuration coordinate model the coupling strength is reflected by the size of the displacement of the potential energy curves of the electronic ground and excited state with respect to an environmental coordinate (helium configuration) as was discussed in chapter 4 (cf. fig. 4.3). The displacement of the potential energy curves determines the PW-structure found in the excitation and also emission spectra of molecules embedded in helium droplets. Thus, the intensity ratio of ZPLs and PWs depends on the change of the configuration of the helium solvation layer induced by the electronic excitation. This configuration is determined by the perturbation of the helium droplet due to the embedded molecule. Variations of molecular properties alter this perturbation and thus induce a reorganisation of the helium solvation layer.
The geometry of FPP is not significantly altered upon excitation. In particular, the geometry changes are not larger than for other rigid molecules such as anthracene or tetracene. In the electronic spectra of these molecules the PWs are only minor contributions. Large geometry changes upon excitation lead to a rather symmetric broadening of the ZPLs due to damping of the corresponding excited states as discussed in chapter 5.9.1 and ref.[PGDS10]. In contrast, the width of the leading ZPLs in the excitation spectrum of FPP is almost constant throughout the entire spectrum. Thus, it can be

concluded that the dominance of the PWs related to a reorganisation of the helium solvation layer is not induced by changes of the geometry of the embedded molecule.

Instead, the coupling to the environment is ascribed to changes in the electron density inevitably induced by electronic excitations. The coupling strengths to phonons in other media are known to depend on the change of the electron density. [FH84] Electron density redistribution is often reflected by a change of the electric dipole moment. [KBBP01] The emission of FPP was shown to stem exclusively from the LE state and thus the phonon-coupling is not caused by the formation of an ICT state. For FPP dipole moments of $\mu(\mathrm{GS}) = 1.7$ D and $\mu(\mathrm{LE}) \approx 1$ D were determined experimentally for the ground and LE state, respectively. [YDZ04] The dipole moments are assumed to point in the same direction with the negative charge on the pyrrole moiety. [YDZ04] The direction of the dipole moment in the LE state compared to the ground state was determined with ab initio calculations and in analogy to PP. [YGD$^+$03, YDZ04, XCZ06, HL07] As can be followed from ab initio calculations, the significant reduction of the dipole moment to almost half of its value upon excitation into the LE state is due to the transfer of substantial amount of charge from the nitrogen atom at the pyrrole ring to the phenyl ring. [ZH02, XCZ06, HL07]

The same behavior as observed for FPP was already described in refs. [LRD05, Log08] for aniline and phenol. The excitation spectra in helium droplets are dominated by asymmetric broad PWs with FWHMs of about 100 and 50 cm^{-1} , respectively. The vibrational pattern in the spectra are similar as in the corresponding gas phase spectra. The reorganisation of the helium environment was tentatively ascribed to be due to changes of the geometry or of the electron density of the molecules upon electronic excitation. [LRD05, Log08] Information about the geometry of aniline in S_0 and S_1 is provided by rotationally resolved excitation spectra in a supersonic jet. [SP96, KBBP01] In the ground state (S_0) the amino group is pyramidally distorted with an angle of about 38° between the planes of the amino and phenyl groups (inversion angle). Upon excitation into S_1 the molecule becomes quasi-planar with slightly increased aromatic bond lengths and a shortened C-N bond. [SP96] Stark experiments revealed an electric dipole moment changing from $\mu(S_0) = 2.8$ D to $\mu(S_1) = 1.1$ D upon excitation. [KBBP01] By comparison with ab initio calculations the variation of the dipole moment was attributed to the transfer of substantial amount of charge from the lone pair electrons on the nitrogen to the π^* orbitals of the phenyl ring which is in line with the observed geometry changes. [SP96, KBBP01] For a van der Waals-complex of aniline with a single Ar atom rotationally resolved excitation spectra also have been reported. Therein, the Ar atom was found to be located on the opposite side of the two hydrogen atoms in the ground state. [SP96] This was attributed to an anisotropic attractive interaction between Ar and the lone pair electrons of the amino group. [SP96] Upon electronic excitation the equilibrium position of the Ar atom is altered which is attributed to significant differences in the intermolecular potential energy surfaces of the two electronic states. [SP96] This demonstrates the sensitivity of surrounding rare gas atoms on changes in the electron density, especially in lone pair orbitals. In helium droplets a similar rearrangement of localised He atoms may occur corresponding to changes in the helium solvation layer.

The geometry of phenol is modified upon electronic excitation by a slight increase of the C-C bond lengths in the ring and of the C-O-H angle, whereas the C-O bond length decreases. [BMSK96, SGR+96] The latter is indicative of a transfer of electron density from the oxygen into the phenyl ring which is reflected also in the increasing acidity of phenol upon electronic excitation. [BMSK96, SGR+96]

In the electronic excitation spectrum of 3-aminophthalimide in helium droplets only PWs with a FWHM of about 30 cm^{-1} were found. [Mor07] However, in this case the pronounced PWs might be due to saturation effects. [Mor07] Recently, the excitation spectrum of 4-Aminophthalimide was recorded in our lab consisting of weak ZPLs accompanied by strong PWs and with a vibrational pattern similar as in the excitation spectrum in the gas phase [SOK+09]. For this molecule a large increase of the dipole moment from $\mu(S_0) = 5.0$ D to $\mu(S_1) = 10.6$ D upon excitation is found in high level ab initio calculations. [SOK+09]

Further evidence that the reorganisation of the helium solvation layer is caused by variations of the electron density distribution is provided by rotationally resolved excitation spectra of glyoxal in helium droplets. [P01̈, SV01, PPV02] Rotational constants found in helium droplets differ from the corresponding values in the gas phase. This is considered by a separation of the determined moments of inertia into contributions from the molecule and the helium environment. [P01̈, SV01, PPV02] The contribution from the helium surrounding to the moments of inertia depends on the rotational axis and changes by up to 61 % upon electronic excitation. In contrast, variations of only a few percent are observed upon vibrational excitation. [P01̈, SV01, PPV02] The changes in case of electronic excitation are interpreted in terms of a considerable reorganisation of the helium environment induced by changes in the electron density of the molecule upon excitation. [SV01, PPV02]

Additionally, PWs are usually not observed in IR spectra and only some indications for weak PWs observed at high laser powers are reported.[RWvHH07] These observations display the stronger coupling of the helium environment to electronic excitation than to vibrational excitations in the electronic ground state and reflects the influence of changes in the electron density on the coupling strength. [SV01, PPV02] The weak coupling of vibrational excitations to phonons is also reflected by the fact that the PW structure in electronic spectra is largely independent of the vibrational frequencies as found for FPP but also for molecules with distinct features in the PW.(cf. chapter 5) Also rotational excitations of embedded molecules couple only weakly to phonons as indicated by the absence of PWs in microwave spectra. [SV01, TV04, CDF+06]

It should be noted that the PWs in the excitation spectrum of FPP are not only blue shifted to the corresponding ZPLs but the ZPLs coincide with the rising edge of the PWs. A PW transition lower in energy than the ZPL could be due to absorption originating from populated matrix states in the electronic ground state, often called 'hot phonons'. Due to the low temperature of only 0.37 K the population of these states usually can be neglected. However, the phonon and ripplon states with vanishing small energy exist and therefore are populated. (cf. chapter 4) Since the intensity of the corresponding transitions in the excitation spectrum does not only depend on the thermal population but also on the transition moments, the latter seems to be in favor in the case of FPP. This is in line with the observation of the dominance of the PW indicating a large rearrangement of the helium environment upon electronic excitation. The shift of the corresponding potential energy curves (cf. fig. 4.3 in chapter 4) with respect to the helium configuration alters the transition probabilities.

PWs are also observed in the electronic spectra of alkali and alkaline-earth atoms and clusters on the surface of helium droplets and often dominate the spectra. [SV01] In particular, each of the transitions in the electronic excitation spectrum of singlet Na_2 consists of a relatively sharp ZPL (FWHM ≈ 0.5 cm^{-1}) accompanied by a PW on the blue side. The width of the PW thereby depends on the size of the droplets and decreases from 110 cm^{-1} to about 30 cm^{-1} by decreasing the droplet size from several thousands to several hundreds He atoms per droplet. [SV01] The pronounced size dependence was interpreted to suggest that the coupling of the electronic transitions is to the surface modes. [SV01] Interestingly, the PW in the excitation spectrum of triplet Na_2 is narrower though no ZPLs could be observed. [SV01]

The dipole moment of PP was found to change upon electronic excitation experimentally and in ab initio calculations though the values reported differ. [SH03b, YGD+03, XCZ06, CZH06] The variation of the dipole moment corresponds to a change in the electron density and thus may cause strong electron phonon coupling as found for FPP. Together with the broadening due to damping this explains the extremely broad excitation spectrum of PP in helium droplets and its weak fluorescence.

6.4 Conclusion

The investigation of PP and FPP aimed to study the intramolecular charge transfer as a photochemical reaction in helium droplets. It was shown that fluorescence of bare FPP in the gas phase and helium droplets stems only from the LE state. The substituted FPP 4-Cyanofluorazene (FPP4C) as well as its flexible counterpart PBN show dual fluorescence also in nonpolar solvents such as hexane. [DKS$^+$08] Dual emission of PBN was also found in neat Ar matrices. [SBH$^+$05, SHD05] The large increase in the efficiency of the ICT reactions of PBN and FFP4C compared to PP and FPP is attributed to a smaller gap between the lowest two singlet excited states. [DKS$^+$08] Therefore, FPP4C is an interesting candidate for the observation of emission from an ICT state in helium droplets and should be investigated in future experiments. It might be speculated that due to the low temperature and the dissipative medium in helium droplets only emission from the ICT state will be observed.

The excitation spectrum of FPP recorded in helium droplets revealed a strong electron-phonon coupling. By comparison with other experimental and theoretical studies the coupling was attributed to changes of the electron density. The helium environment seems to be in particular sensitive to redistributions of the electron density at heteroatoms such as nitrogen. In this case strong electron phonon-coupling occurs which is reflected by the dominance of broad asymmetric PWs in electronic spectra.
The excitation spectrum of PP in helium droplets was found to be broad which is attributed to damping of the excited state due to changes of the geometry of the molecule and additionally to strong electron-phonon coupling due to changes of the electron density.
Electron-phonon coupling in helium droplets will further be discussed in chapter 8.

7 Pyrromethene Dyes

Pyrromethene-BF_2 (PM) dyes are another class of compounds whose electronic spectroscopy in helium droplets was investigated within this work. Many PM dyes are commercially available laser dyes and exhibit high extinction coefficients and high fluorescence quantum yields in solution at room temperature. [LABnM+05, KKY+05, UZH08, HSJ08] The geometry of the chromophore consisting of two pyrrole rings linked by a methene bridge and rigidified by a BF_2-group (fig.7.1) is essentially planar in all of the investigated dyes. [ABC03, LABnPMM+04] The molecular structures often contain alkyl or aryl groups introducing low-frequency modes. These large amplitude modes have shallow potentials compared to other modes with higher vibrational frequencies and thus are particularly sensitive to the environment. Therefore, PM dyes are attractive for investigations of the interaction between embedded molecules and the environment present in helium droplets.
In case electronic excitation induces a significant change of the geometry such as an equilibrium torsional angle a substantial line broadening was observed in the excitation spectra of anthracene derivatives in helium droplets. (cf. chapter 5) This was attributed to a damping of the nuclear rearrangement and thus may occur also for the PM dyes.

The investigated PM dyes are shown in fig.7.1 together with their abbreviations used in the literature and in this work. The parent compound BDP is expected to exhibit the spectroscopic signature of a rigid molecule and serves as a reference for the other compounds. All other investigated dyes contain a single aryl (8-PhPM) or a variety of alkyl groups capable of low-frequency modes such as torsional or bending modes. However, only 8-PhPM contains a single rotor whereas the other molecules contain more than one rotor. In these cases coupled torsional modes are expected exhibiting rather complicated spectral signatures which are not easily analyzed.

In the following the electronic spectroscopy of each of the compounds starting with BDP will be presented and discussed with respect to the corresponding gas phase data. At the end of the chapter common features of the spectroscopic signatures, in particular the broadening of the vibrational satellite structure in the excitation spectra of the substituted PM dyes, will be discussed.
The electronic spectroscopy of these molecules by means of fluorescence excitation and emission studies and also pump-probe experiments in the supersonic jet was recently

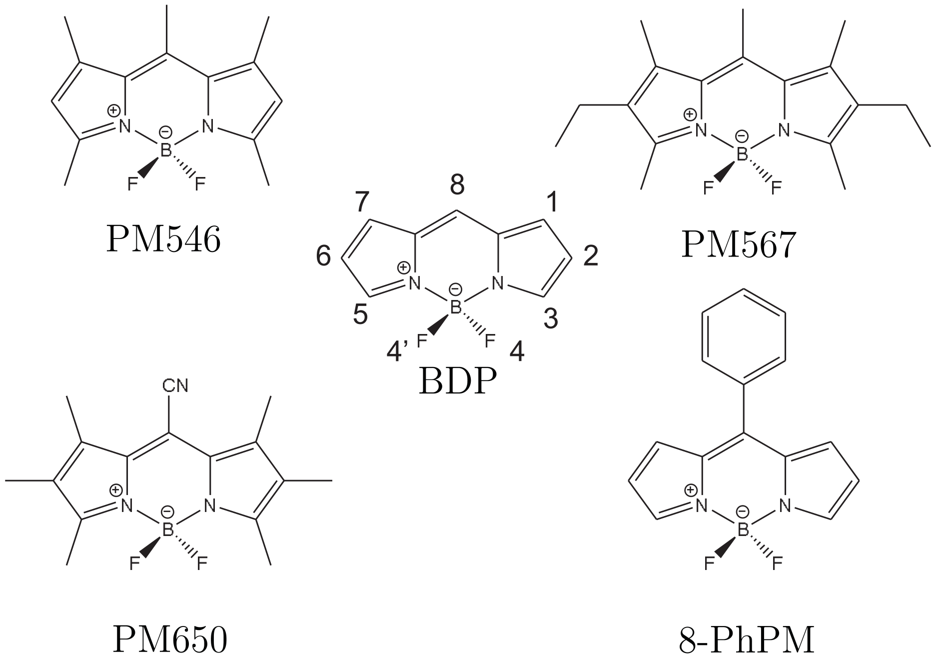

Fig. 7.1: Molecular structures of the investigated pyrromethene dyes and their abbreviations: 4-bora-3a,4a-diaza-s-indacene or Borondipyrromethene (BDP), 8-phenylpyrromethene-difluoroborat (8-PhPM), 1,3,5,7,8-pentamethylpyrromethene-difluoroborat (PM546), 1,3,5,7,8-pentamethyl-2,6-diethylpyrromethene-difluoroborat (PM567), and 1,2,3,5,6,7-hexamethyl-8-cyanopyrromethene-difluoroborat (PM650). PM dyes are commonly also called BODIPY (BOron-DIPYrromethene) dyes. The numbering of the substituents follows rules set up for the carbon polycycle indacene. [UZH08] A different numbering according to the IUPAC nomenclature for dipyrromethanes is less common. [WL96]

reported in ref. [SF09]. Gas phase spectra shown in this work are taken from ref. [SF09]. Therein, also some of the aspects of the spectroscopy of these compounds in helium droplets are discussed. It should be noted that the absolute wavenumbers given in ref. [SF09] are not corrected for vacuum and thus differ from the values given in this work.

The helium droplets were generated with a stagnation pressure of 80 bar, nozzle temperatures ranging from 20 K to 23 K and a repetition rate of 20 Hz if not denoted otherwise. Laser intensities measured at the entrance window of the vacuum apparatus were typically varied from less than 10 μJ up to at most 100 μJ. To avoid saturation effects typically less than 10 μJ had to be used.

7.1 BDP

The parent compound BDP shows the expected spectral signature of a rigid molecule in solution at room temperature. [SHWJ09] However, the fluorescence excitation spectrum in the supersonic jet revealed an unexpected anharmonic progression with transitions at 21.5 cm^{-1} , 44.5 cm^{-1} , and 79.2 cm^{-1} . (fig. 7.2(b)) The low frequency progression peaks at the second transition and appears also coupled to other modes of the molecule. Pump-probe experiments provided evidence that the four transitions of the progression with the irregular spacings originate from the same ground state. SVL spectra revealed a progression of a low-frequency mode with 65 ± 7 cm^{-1} in the ground state. The emission spectrum recorded upon excitation at the electronic origin does not reveal a mirror symmetry to the excitation spectrum, as would be typical for a rigid molecule. The frequency and intensity pattern in the SVL-spectrum recorded upon excitation at the most intense transition at 21.5 cm^{-1} deviates strongly from other SVL spectra. Interestingly, it exhibits similarities to the emission spectrum recorded upon excitation at the peak shifted by 58 cm^{-1} to the red of the origin. This transition was attributed to a complex of BDP formed with an impurity and is marked with an asterisk in fig. 7.2(b). The reason for the appearance of the strongly anharmonic low-frequency progression in the excitation spectrum and the 65 cm^{-1} progression in emission spectra is not yet understood. [SF09] (see below)

All data presented in the following were recorded with the Scanmate dye laser system (dye: Coumarin102). Integral emission was detected with the PMT R 943-02 (Hamamatsu) protected by a cut-off filter OG515. Emission dispersed with the SPEX spectrograph was detected with the CCD-camera DU 420A-BU2 (Andor iDus). The oven temperature for optimum LIF signal of single BDP while avoiding multiple doping of the helium droplets was 29 °C.

7.1.1 Excitation Spectra of BDP

Fig. 7.2 (a) shows the fluorescence excitation spectrum of BDP in helium droplets with $\nu_0 = 20504\ \mathrm{cm}^{-1}$. The most intense transition is assigned to the electronic origin due to the fact that no substantial signal can be observed with a lower transition energy. The weak signal marked with an asterisk is assigned to a complex of BDP with an impurity from the sample since it decreases in intensity with time. Thus, the impurity probably stems from the sample. Signals of the complex probably appear also to the red of the vibronic transitions, though, too weak to be distinguished from the background noise.

The spectrum is dominated by the electronic origin and exhibits few vibronic transitions as is expected for a rigid molecule. The vibrational frequencies are in agreement with those observed in the gas phase. [SF09] However, in the gas phase all of the respecti-

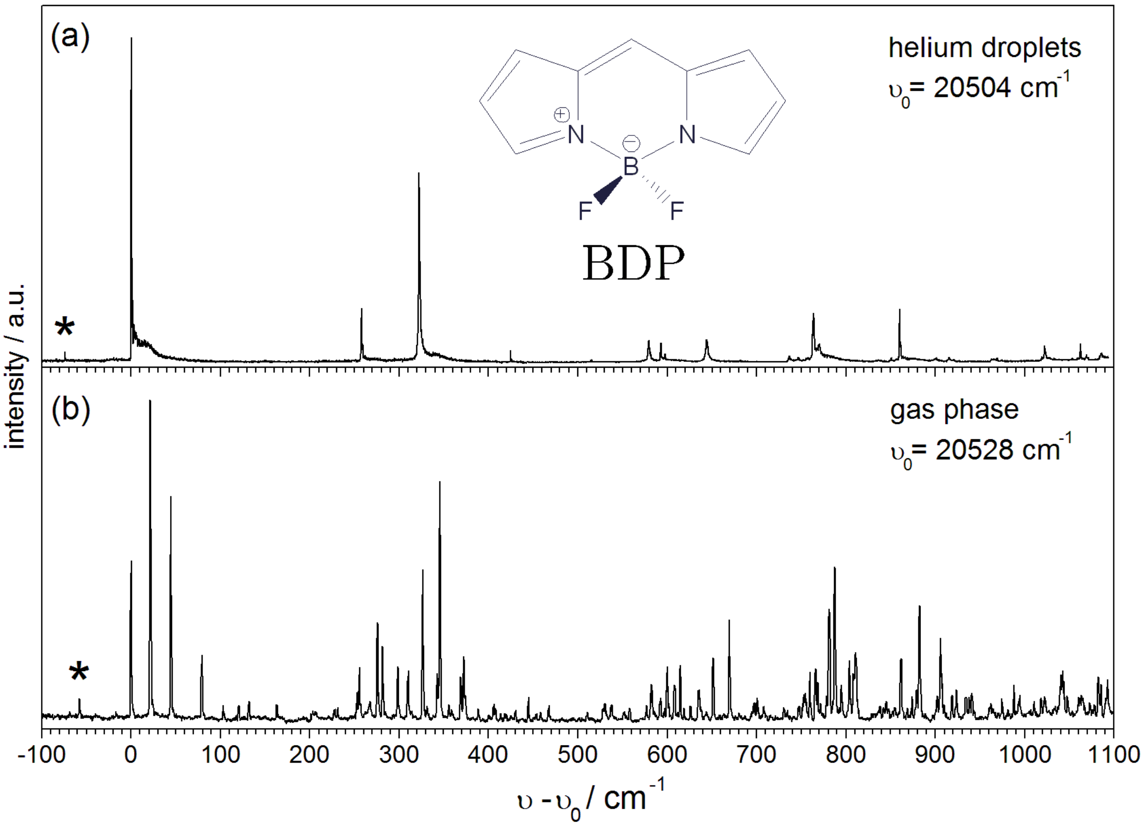

Fig. 7.2: Excitation spectra of BDP in helium droplets (a) and in the supersonic jet (b) with ν_0 as indicated. The laser intensity was low enough to avoid saturation effects. Laser intensity was kept constant. Signals marked with asterisks are attributed to complexes of BDP with an impurity.

ve transitions appear coupled to the anharmonic low frequency progression mentioned above.

All vibronic transitions in the droplet spectrum consist of a sharp transition accompanied by an asymmetric tail to the blue extending over more than 50 cm^{-1} . Due to the line shape of the tail and its low relative peak intensity it can only be clearly recognized at the electronic origin and the most intense vibronic transitions e.g. at 322 cm^{-1} and 763 cm^{-1} . Enlargements of the electronic origin recorded with different laser intensities are shown in fig. 7.3. At laser intensities lower than used for the solid line spectrum the spectral shape did not alter whereas at higher laser intensities (dotted spectrum) the relative intensities change in favor of the blue tail. Thus, the most intense peak lowest in energy can be assigned to a ZPL while the accompanying features to its blue side, which have no counterpart in the gas phase spectrum, can be attributed to the PW. (cf. chapter 4) The PW thus consists of sharp features, e.g. at 1.8 cm^{-1} , followed by a broad asymmetric band to the blue. The laser intensities required to avoid saturation of the ZPL are by at least one order of magnitude lower compared to the anthracene derivatives. (cf. 5) This reflects the much larger absorption cross section or extinction coefficients, respectively, of the PM dyes. [STS$^+$90, LABnPMM$^+$04, UZH08, SHWJ09]

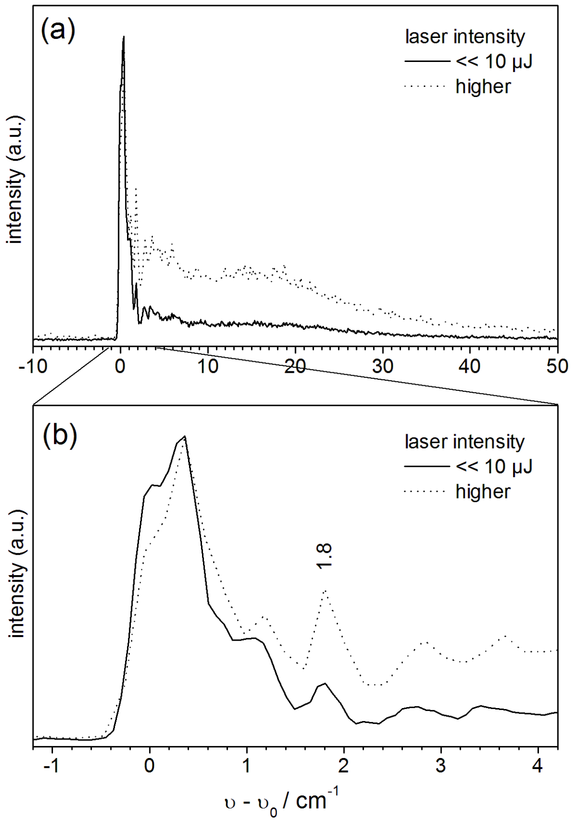

Fig. 7.3: Excitation spectrum of BDP in helium droplets recorded with different laser intensities.(see text) ν_0= 20504 cm^{-1} .

The line shape of the ZPL at the electronic origin in fig. 7.3 (b) reveals a triple peak structure, which is not fully resolved. This was also observed at the electronic origin of BDP in the supersonic jet. [SF09] BDP contains a boron-atom with a natural abundance ratio of the isotopes ^{11}B and ^{10}B of 4:1. Differences in the zero-point energy of the two resulting isotopomers ^{11}BDP and ^{10}BDP, respectively, in S_0 and S_1 may lead to a isotopic spectral shift at the electronic origin. Indeed, as shown in fig. 7.4, the line shape at the electronic origin (fig. 7.4 (a)) can be separated into two identical subspectra with the intensity ratio of 4:1 (fig. 7.4 (b)) by applying the maximum entropy method [Fou88]. Each of the subspectra reveal a rotational contour similar as in the gas phase though with a smaller spectral width as is typical for helium droplets. [SF09]

The isotopic spectral shift amounts to 0.81 cm^{-1} which is in agreement with the values of 0.85 cm^{-1} at the electronic origin and of 0.92 cm^{-1} at 21.5 cm^{-1} excess energy found in the gas phase spectrum. [SF09] Pump-probe experiments in the gas phase revealed that these transitions have contributions originating from different ground states which confirms the assignment to different isotopomers. [SF09] In both the gas phase and the helium droplet spectrum the transition of the lighter isotopomer ^{10}BDP is shifted to the blue compared to the transition of the heavier isotopomer ^{11}BDP indicating an increase of vibrational frequencies upon excitation.

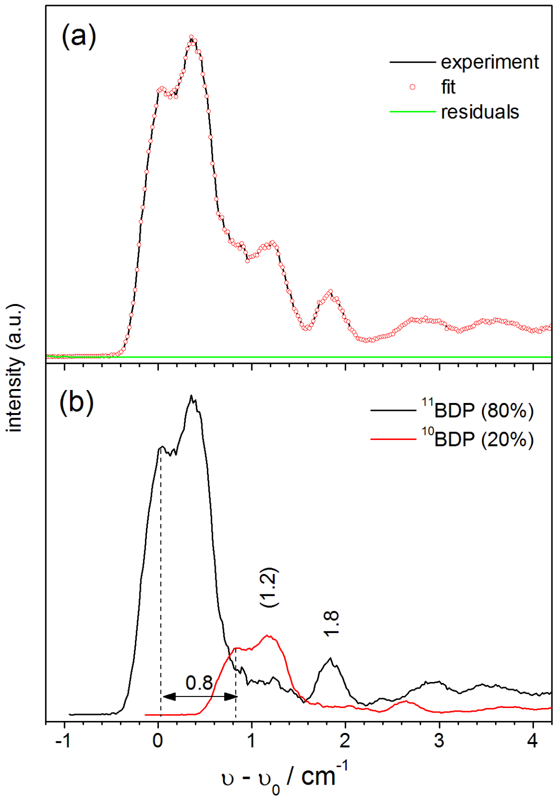

Fig. 7.4: Electronic origin of BDP in helium droplets. The experimental excitation spectrum (a) can be separated using the Maximum Entropy method into the spectra of the two isotopomers (b). The best fit (red) and residuals (green) are also shown in (a).

The feature at 1.8 cm^{-1} in the spectrum of ^{11}BDP in fig. 7.4 (b) has no counterpart in the gas phase spectrum. In accordance with the saturation behavior displayed in fig. 7.3 (b) this transition can be assigned to a sharp feature of the PW of the ^{11}BDP isotopomer. Interestingly, the line width of this peak at 1.8 cm^{-1} is only $\approx$ 0.4 cm^{-1} which is half the width of the rotational envelope of the ZPL. This might indicate that the PW is coupled to only one rotational branch, e.g. the Q-branch.

Larger isotopic shifts than at the electronic origin are expected for vibronic transitions involving excitations of vibrational modes which depend on the nuclear coordinate of the B-atom. The vibronic transitions at 257.9 cm^{-1} and 259.3 cm^{-1} , 424.7 cm^{-1} and 425.6 cm^{-1} , as well as 860.0 cm^{-1} and 861.2 cm^{-1} , respectively, display an intensity ratio of 4:1 as observed at the origin however separated by 1.4 cm^{-1} , 0.9 cm^{-1} , and 1.2 cm^{-1} , respectively. The vibronic transitions at 592.9 cm^{-1} and 597.4 cm^{-1} are separated by 4.5 cm^{-1} and appear with the same intensity ratio of 4:1. Pump-probe experiments or emission spectra recorded upon selective excitation could provide further evidence for the assignments to the two different isotopomers.

7.1.2 Emission Spectra of BDP

The dispersed emission spectrum of BDP in helium droplets recorded upon excitation at $\nu_{exc} = 20826$ cm^{-1} (322 cm^{-1} above the electronic origin) is shown in fig. 7.5 (a). The emission spectrum does not depend on the excitation frequency. The most intense transition is found at the blue end of the spectrum at 20505 cm^{-1} therefore assigned to the electronic origin. The coincidence of the electronic origin in the emission (20505 cm^{-1}) and in the excitation spectrum (20504 cm^{-1}) within experimental accuracy together with the almost perfect mirror symmetry of the two spectra (fig. 7.5) corroborates the assignment of the electronic origin in the excitation and emission spectra.

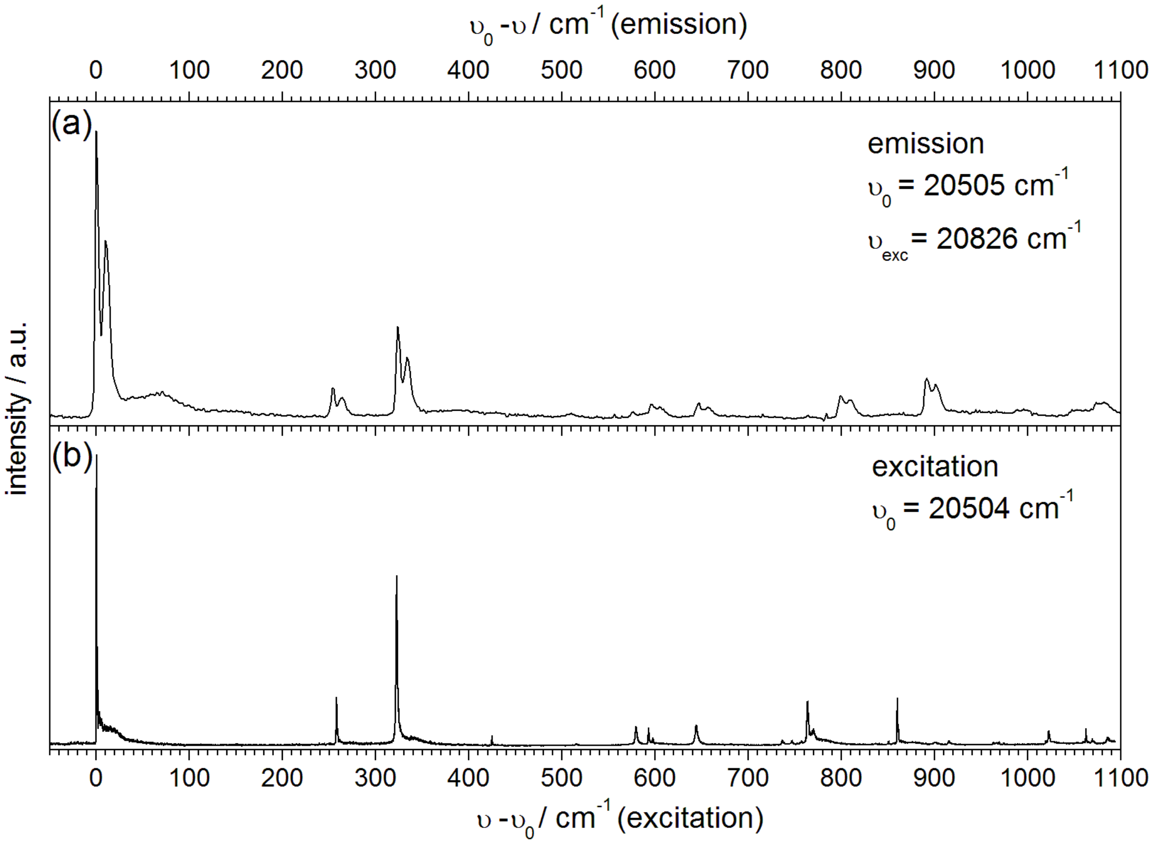

Fig. 7.5: Emission spectrum (a) recorded upon excitation at $\nu_{exc} = 20826$ cm^{-1} and excitation spectrum (b) of BDP in helium droplets with ν_0 as indicated. For the emission spectrum light was dispersed with the 1200 lines/mm grating. The distance between two pixel columns amounts to about 1.7 cm^{-1} at the blue and 1.4 cm^{-1} at the red end of the emission spectrum.

The vibrational frequencies of corresponding modes in S_1 (excitation spectrum) and S_0 (emission spectrum) deviate by less than 1 % for vibrational excess energies up to about 650 cm^{-1} and thus are assigned accordingly. (table 7.1) At higher excess energies the deviations are larger. The relative intensities indicate a correspondence of the 764 cm^{-1} and 860 cm^{-1} modes in S_1 to the 799 cm^{-1} and 892 cm^{-1} modes in S_0.

Tab. 7.1: Transition wavenumbers $\nu - \nu_0$ (S_1) and $\nu_0 - \nu$ (S_0) (cm^{-1}) in the excitation and emission spectrum, respectively, of BDP in helium droplets and their relative peak intensities I/I_0. All numbers are given with respect to the electronic origin ($\nu_0 = 20504\ cm^{-1}$ in excitation and $\nu_0 = 20505\ cm^{-1}$ in emission spectra) and correspond to vibrational frequencies in the excited state S_1 and ground state S_0, respectively. A shift of vibrational frequencies is given for transitions presumably corresponding to the same modes. A splitting of transitions in the emission spectrum is only listed when clearly resolved.

$\nu - \nu_0$ (S_1) / cm^{-1}	I/I_0	$\nu_0 - \nu$ (S_0) / cm^{-1}	I/I_0	shift / cm^{-1}
-74 (impurity)	0.03	-	-	-
0	1.00	0	1.00	0
-	-	10^a	0.62	-
258	0.16	254	0.11	-4
259	0.05	-	-	-
-	-	264^a	0.08	
322	0.58	324	0.32	+2
-	-	334^a	0.22	-
425	0.03	-	-	-
426	< 0.01	-	-	-
515	< 0.01	509	0.02	-6
579	0.06	576	0.03	-3
593	0.06	595	0.05	+2
597	0.02			-2
-	-	605^a	0.04	-
644	0.06	647	0.06	+3
-	-	657^a	0.04	-
736	0.02	-	-	-
747	0.01	-	-	-
757	< 0.01	-	-	-
764	0.15	799	0.08	-
-	-	809^a	0.06	-
770	0.05	-	-	-
851	0.01	-	-	-
860	0.16	892	0.14	-
-	-	902^a	0.12	-
861	0.05	-	-	-
900	< 0.01	-	-	-
915	0.01	-	-	-
920	< 0.01	-	-	-
963	< 0.01	-	-	-
966	< 0.01	-	-	-
969	< 0.01	-	-	-
974	< 0.01	-	-	-
1019	0.01	-	-	-
1022	0.04	996	0.03	-
1053	< 0.01	1053	0.03	-
1059	< 0.01			
1062	0.05	1079	0.06	-
1069	0.01	-	-	-
1070	< 0.01	-	-	-
1086	0.02	-	-	-

[a] red shifted emission spectrum

All of the transitions in the emission spectrum in fig. 7.5(a) reveal a fine structure independent of the excitation energy. Fig. 7.6 (a) shows the emission spectrum recorded at higher spectral resolution. Each transition consists of three contributions, namely a sharp feature at the blue end followed by a slightly broader feature and a broad tail. The latter can probably be assigned to a PW due to its shape. The first is assigned to a ZPL due to the fact that it exhibits the highest transition frequency. The second peak exhibits a significantly different spectral shape as compared to the third feature and is thus tentatively assigned to a further ZPL. Accordingly, each vibronic transition consists of two ZPLs separated by 10.1 ± 0.2 cm^{-1} with a relative peak intensity of 3:2. The spectral shape at the electronic origin (fig. 7.6 (b),(c)) and vibronic transitions (fig. 7.6 (d),(e)) can be fitted with Lorentzians. Gaussians fitted worse in particular to the second features. The ZPL at the blue side exhibits a line width of 1.8 cm^{-1} (b,c), 2.2 cm^{-1} (d) and 2.5 cm^{-1} (e), respectively. Deviations are observed in particular to the blue side of this transition at the electronic origin. The observed line width is not limited by the spectrograph, though, it is at the limit of the spectral resolution of the detection unit. Laser stray light recorded under the same conditions exhibited a line width of about 1.3 cm^{-1} .

The line shape at the electronic origin was fitted with two (fig. 7.6(b)) or three (fig. 7.6(c)) Lorentzians, respectively. The shape of the second ZPL is well described by a Lorentzian with a width of 7.4 cm^{-1} . (fig. 7.6(b)) The third Lorentzian is centered at 63 cm^{-1} with a width of 71 cm^{-1} . This contribution is too weak to be clearly observed for the other transitions. These reveal a width of the second peak of 8.0 cm^{-1} (fig. 7.6(d)) and 7.8 cm^{-1} (fig. 7.6(e)), respectively.

Note that all of the transitions exhibit the same splitting of the first two peaks. In view of the splitting of 10.2 cm^{-1} an isotope spectral shift can be excluded as a reason for the splitting. The isotope spectral splitting e.g. of about 1 cm^{-1} as resolved in excitation cannot be resolved though may contribute to the deviations from pure Lorentzian line shapes. The S/N ratio in emission spectra recorded upon excitation at 259.3 cm^{-1} , 425.6 cm^{-1} , 861.2 cm^{-1} , or 597.4 cm^{-1} , which were tentatively assigned to stem only from ^{10}BDP was too low to allow for a detailed analysis.

The emission spectrum recorded in helium droplets exhibits a mirror symmetry to the excitation spectrum. (fig. 7.5) In addition to the fine structure of each transition this behavior is in contrast to the corresponding gas phase spectra. [SF09] SVL spectra in the gas phase exhibit a low-frequency progression with 65 cm^{-1} spacings which reappears coupled to higher frequency modes such as the 322 cm^{-1} mode. Similar as in the excitation spectrum, only the high frequency vibrational modes are observed in helium droplets whereas the low-frequency mode itself is absent. Interestingly, the emission spectrum recorded in the gas phase upon excitation with 21.5 cm^{-1} excess energy is very similar to the helium droplet spectrum in fig. 7.5 (a) whereas the SVL spectrum in the gas phase recorded upon excitation at the electronic origin strongly deviates from the droplet spectrum. [SF09]

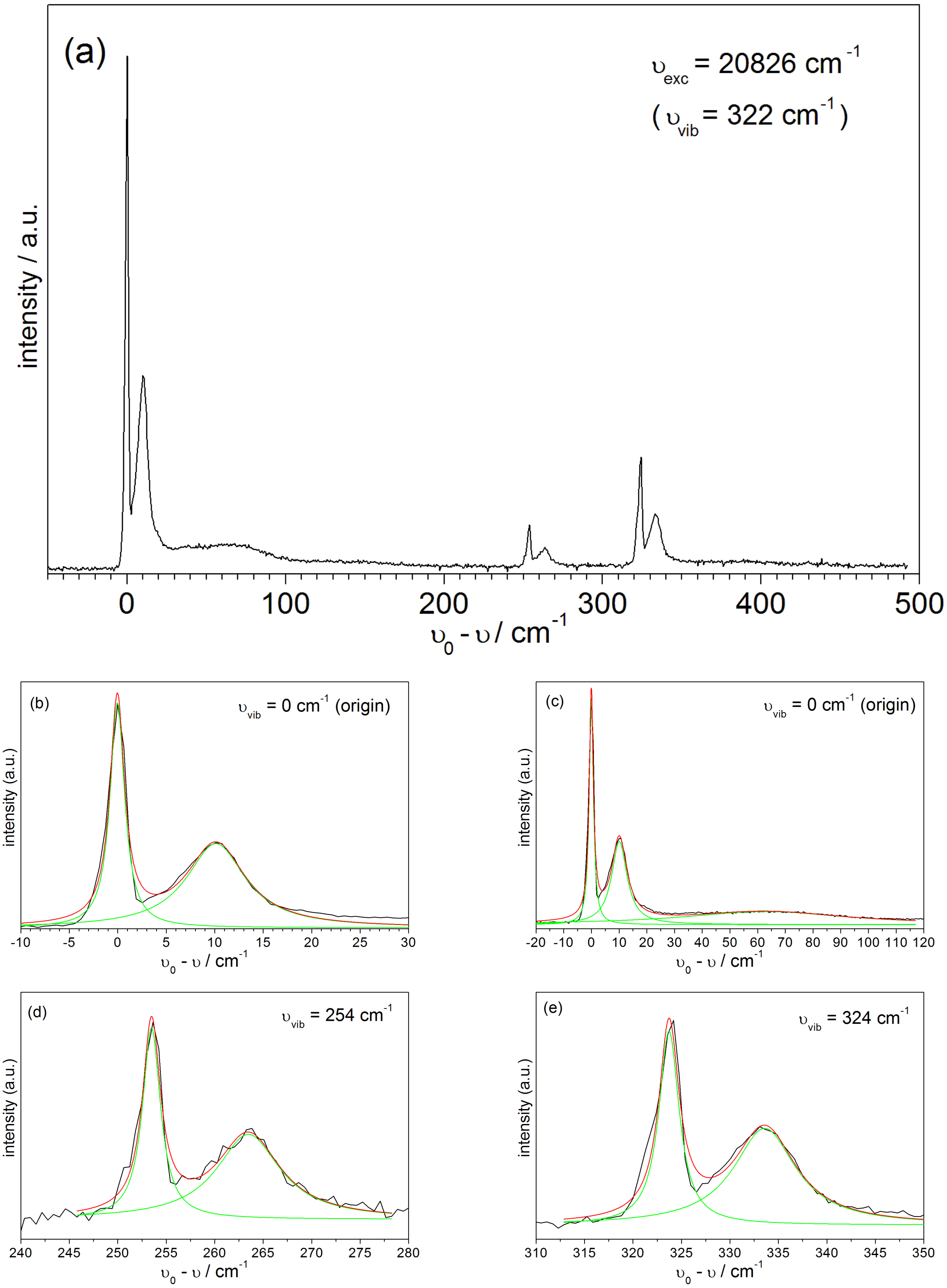

Fig. 7.6: Emission spectrum of BDP in helium droplets recorded upon excitation at $\nu_{exc} = 20826\ \mathrm{cm}^{-1}$ ($\nu_{vib} = 322\ \mathrm{cm}^{-1}$). $\nu_0 = 20505\ \mathrm{cm}^{-1}$. The distance between two pixel columns amounts to 0.65 cm^{-1} at the blue and 0.57 cm^{-1} at the red end of the spectrum (2400 lines/mm grating). (a) The line shape at the electronic origin can fitted with two (b) or three (c) Lorentzians (see text). Line shapes of the vibronic transitions (d and e) are well described by two Lorentzians.

7.1.3 Discussion

The fluorescence excitation and dispersed emission spectra of BDP in helium droplets display the typical spectroscopic signature of a rigid molecule. The electronic origin is the most intense transition and no low-frequency modes with $\mid \nu - \nu_0 \mid < 250$ cm^{-1} are observed. Further, the excitation and emission spectra reveal an almost perfect mirror symmetry. The saturation behavior in the excitation spectrum revealed a broad asymmetric PW and a single quasi-localized phonon with a phonon energy of 1.6 cm^{-1} (with respect to the center of the rotational envelope of the ZPL). The emission spectra revealed a splitting of each vibronic transition into three contributions. The transitions highest in energy with a line width of about 2 cm^{-1} , which is close to the spectral resolution, are assigned to the ZPLs. They are followed by transitions of Lorentzian shape with line widths of about 8 cm^{-1} shifted by 10 cm^{-1} to the red. The third contribution is a broad tail with a center frequency separated by about 60 cm^{-1} from the ZPL. The latter can presumably be assigned to a PW. However, it should be noted that a 65 cm^{-1} low-frequency mode is observed in the emission spectra in the supersonic jet. [SF09] Thus, the broad transition might also be due to a damped 60 cm^{-1} mode in the ground state.

The transitions in the emission spectrum shifted by about 10 cm^{-1} to the red of the sharp ZPLs have no counterpart in the supersonic jet spectrum. Since their line shape is different to that of the PW they can presumably be assigned to ZPLs. Further, PWs with such a high relative peak intensity usually exhibit a broad asymmetric spectra shape. (cf. chapter 6) The different transition frequencies compared to the sharp ZPLs at the blue side of each vibronic transition are indicative for a different solvation layer. The relative intensity of the two ZPLs and the splitting by 10 cm^{-1} is independent of the excitation excess energy. This indicates that both emissions originate from the same excited state. Thus, the splitting is presumably due to different configurations of the non-superfluid solvation layer in the electronic ground state as illustrated in fig. 7.7 (a). Thus, the 10 cm^{-1} shift reflects the difference in the zero-point energy of the two ground state configurations.

The homogeneous line width of the red shifted ZPL amounts to about 8 cm^{-1} and indicates a fast decay process of the corresponding ground state. This process is only active for the configuration higher in energy and thus is attributed to a relaxation of the solvation layer of the meta-stable ground state configuration with a time constant of about 0.7 ps as indicated in fig. 7.7 (a).

The time constant for the relaxation is almost identical for all vibrational states in the electronic ground state. Further, the splitting and relative peak intensities of the two ZPLs are almost identical for all transitions.

Note that also the excited state might be split into two configurations which can be

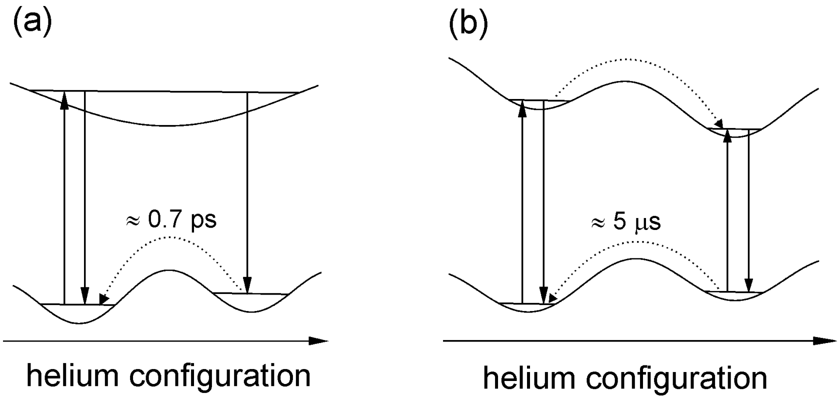

Fig. 7.7: Configuration coordinate models to explain the splitting in the emission spectra of BDP (a) and phthalocyanine (b) in helium droplets. (see text) Model (b) according to ref.s [LS04b, LS04a, LS05, ST08]

interconverted. However, there is no indication for a splitting in the excited state such as a dependence of the relative intensities of the ZPLs in the emission spectrum on the excitation excess energy as observed for phthalocyanines (see below), or a broadening of the transitions in the excitation spectrum hinting to a fast process.

Interestingly, about the same splitting was observed in the emission spectra of various phthalocyanines. [LS03, LS04a, LS04b, LSK$^+$04, LS05] For example, the emission spectra of the free base phthalocyanine (Pc) consist of two sets of sharp lines separated by 10.3 cm^{-1} . The intensity of the main spectrum decreases in favor of a red shifted spectrum with increasing excess energy. This was explained by two different configurations of the helium solvation layer around the molecule in the electronically excited state separated by a barrier as shown in fig. 7.7 (b). Pump-probe experiments revealed that not only the excited state but also the ground state is split. The relaxation time in the ground state was determined to about 5 μs in the pump-probe experiments. [ST08] Thus, in contrast to BDP where the 10 cm^{-1} splitting is identical to the difference of the zero-point energy levels of the two ground state configurations, in the case of Pc the splitting reflects the sum of the energy differences of the two configurations in S_0 and S_1, i.e. the difference between the transition energies within one configuration. Path-integral Monte Carlo calculations identified the two configurations as the totally incommensurate and a mixed incommensurate/commensurate configuration of a localized first layer of helium. [WHKW05] Note that the relaxation time of 5 μs is almost seven orders of magnitude (!) longer than in the case of BDP.

In both excitation and emission spectra broad features attributed to PWs are observed. Calculations predict an orientation of the transition dipole moment along the long molecular axis, i.e. perpendicular to the electric dipole moment along the short axis of the molecular plane with its negative end at the BF_2 group. [BMH$^+$02, ABC03, LABnM$^+$05, KKY$^+$05] This is in agreement with the spectral shape of the rotational envelope at the electronic origin in the excitation spectrum recorded in helium droplets as well as in the gas phase. [SF09] The dipole moment of PM dyes in the ground state is typically in the order of 5 D and is reduced by about 10 % upon electronic excitation. [BMH$^+$02, BnPLAMM$^+$04b, BnPLAMM$^+$04a, LABnM$^+$05, KKY$^+$05] Excitation induces symmetric changes of the electron density at the atoms of the chromophore with respect to the short molecular axis, thus maintaining the orientation of the dipole moment as well as the C_{2v} symmetry of the molecule. [BMH$^+$02, ABC03, KKY$^+$05] According to the configuration coordinate model as discussed in chapters 4 and 6.3 the occurrence of PWs is indicative of reorganisations of the non-superfluid solvation layer induced by variations of the electron density upon excitation. A variation of the solvation layer is in agreement with the model for the configuration potential proposed in fig. 7.7(a). Note that in the case of Pc electronic transitions occur among global and local minima in the configuration potential (fig. 7.7(b)) which are not shifted with respect to each other. Thus, the PW is much weaker corresponding to weak electron-phonon coupling.

As discussed, both excitation and emission spectra of BDP in helium droplets exhibit the expected typical spectroscopic signature of a rigid molecule. However, therefore the spectra in helium droplets differ significantly compared to the spectra recorded in the supersonic jet by the missing of low-frequency transitions. [SF09] The vibronic transitions observed in helium droplets were also observed in the gas phase though only coupled to an anharmonic low frequency progression at 21.5 cm^{-1} , 44.5 cm^{-1} , and 79.2 cm^{-1} in the excitation spectrum and a rather harmonic progressive mode with spacings of $\approx$ 65 cm^{-1} in the emission spectra. [SF09]
The progression in the excitation spectrum was attributed to a low frequency mode in the excited state S_1. [SF09] The irregular spacings and relative intensities could be due to a double minimum potential in S_1 together with a rather shallow single minimum potential in S_0. (fig. 7.8 (a)) According to the vibrational spacings only the lowest vibrational state is below the barrier, the second is already slightly above the barrier and the third is above the barrier. [SF09] Consequently, the barrier (between the zero-point energies) in the potential in S_1 would be in the order of 40 cm^{-1} .

The missing of the corresponding low frequency transitions in the excitation spectrum of BDP in helium droplets may be due to a fast damping of the corresponding vibrational excitations or to a variation of the potential energy surface in S_1 as illustrated in fig. 7.8 (b). The potential is quite shallow and thus is expected to be particularly sensitive to interactions with the environment.
The nature of the unexpected low-frequency mode observed exclusively in the supersonic jet is not yet understood. In case the vibrational mode is non-totally symmetric, e.g. an out-of plane bending mode, only every second overtone (0→2, 0→4, etc.) is observed in

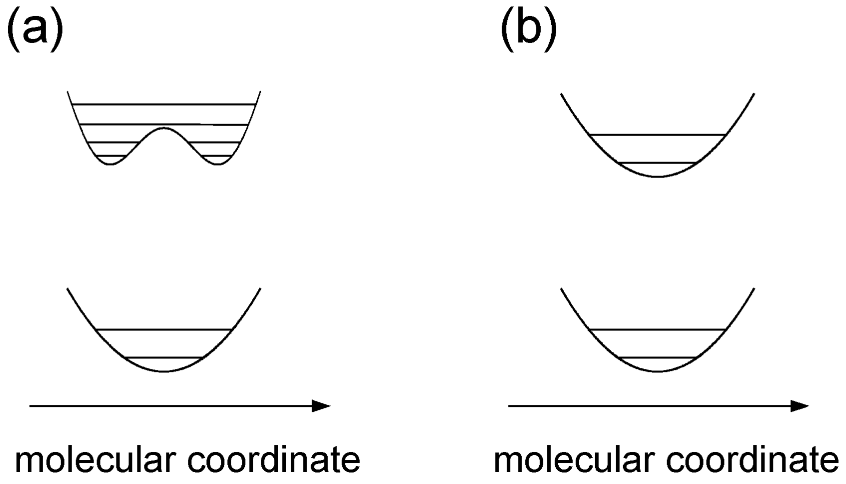

Fig. 7.8: Approach to explain the occurrence of low frequency modes in the jet spectrum (a) and their absence in helium droplets (b). (see text)

the electronic spectrum. Possible low frequency modes are vibrations involving in-plane or out-of plane bending of the BF_2-group. In case the vibration depends significantly on the nuclear coordinate of the B-atom a larger isotopic shift would be expected at the vibrational satellites as compared to the electronic origin. However, the observed shifts at the electronic origin and at the transition with 21.5 cm^{-1} excess energy are identical. [SF09]

Other possible candidates for low-frequency modes are butterfly modes. The fundamental frequency would amount to only 11 cm^{-1} which is below typical values. [ZSGL04] The butterfly mode of pentacene is the most intense transition in the gas phase [AEJ80b] whereas it is strongly damped (Lorentzian width 7 cm^{-1}) in helium droplets. [LS05] Further, the 16 cm^{-1} out-of plane mode of Chloroaluminium-phthalocyanine is damped in helium droplets. [Rie07]

7.2 8-PhPM

Introduction of a phenyl group at the central position (meso) of BDP lowers the symmetry from C_{2v} to C_2. As found for 9-PA compared to AN (cf. chapter 5.5), the substitution at the central position with a phenyl group alters the spectroscopic behavior compared to the parent compound (BDP). For example, the fluorescence quantum yield of 8-PhPM in solution at room temperature was determined to 5-6 % which is untypically low for PM dyes. [KKY$^+$05] This was attributed to an enhanced non-radiative decay process promoted by the torsional mode of the phenyl group. [KKY$^+$05]

The excitation spectrum of 8-PhPM in the supersonic jet shown in fig. 7.9 (b) reveals an anharmonic low-frequency progression similar as found for the parent compound BDP (chapter 7.1) though at slightly smaller excess energies of 15.5 cm^{-1} , 26.9 cm^{-1} , 43.0 cm^{-1} , and 63.7 cm^{-1} . [SF09] Further, the substitution with the phenyl group introduces a rather harmonic low-frequency progression with 60 cm^{-1} spacings assigned to the phenyl torsion. The phenyl progression can be found also coupled to other modes, in particular to a 222 cm^{-1} mode and its overtone. This prominent vibration may correspond to the 326 cm^{-1} (322 cm^{-1} in helium droplets) mode of the parent compound BDP. The irregular mode couples to all vibronic transitions, however, spectral congestion due to overlapping bands makes assignments difficult for excess energies $\nu - \nu_0$ larger than about 200 cm^{-1} . Pump-probe experiments provided evidence that all transitions originate from the same ground state. [SF09]

Progressions of the torsional mode could also be observed in SVL-spectra recorded in the supersonic jet. However, the spectral resolution did not allow for any conclusions on the irregular low frequency mode found in the excitation spectra. [SF09]

The assignment of the 60 cm^{-1} mode to the phenyl torsion was confirmed by quantum chemical calculations. [KKY$^+$05, SF09] Thereby, the minima of the torsional potential in S_0 were found at angles of 52°, 128°, 232°, and 308°, i.e. the most stable conformation is a twisted form with a dihedral angle of 52°. The minima are separated by barriers of 600 cm^{-1} to the perpendicular orientation (90°, 270°) and of more than 4000 cm^{-1} to planarity (0°, 180°). [SF09] This is in agreement with a dihedral angle of about 60° with respect to the essentially planar framework of the chromophore determined from the X-ray structure. [KKY$^+$05] Calculations predict structural minima in the excited state S_1 with a dihedral angle of 42° and barriers of 1160 cm^{-1} and 2200 cm^{-1} to the perpendicular and planar orientation of the chromophore and phenyl plane, respectively. The calculated torsional potentials were found in agreement with the progression of the torsional mode observed in both excitation and emission spectra in the gas phase. [SF09]

All data presented in the following were recorded with the Scanmate dye laser system (dye: Coumarin102). Integral emission was detected with the PMT R 943-02 (Hamamatsu) protected by a cut-off filter GG505. The oven temperature optimum for single

8-PhPM doping while avoiding multiple doping of the helium droplets was 24 °C.

7.2.1 Excitation Spectra of 8-PhPM

The excitation spectrum of 8-PhPM recorded in helium droplets is shown in fig. 7.9 (a) in comparison to the excitation spectrum of the free molecule in the gas phase in fig. 7.9 (b). The droplet spectrum appears broader than the gas phase spectrum though roughly describes its envelope. Thus, together with the fact that no signal is observed further to the red, the transition at 20390 cm^{-1} is assigned to the electronic origin, corresponding to a solvent shift of 28 cm^{-1} to the red compared to the gas phase.

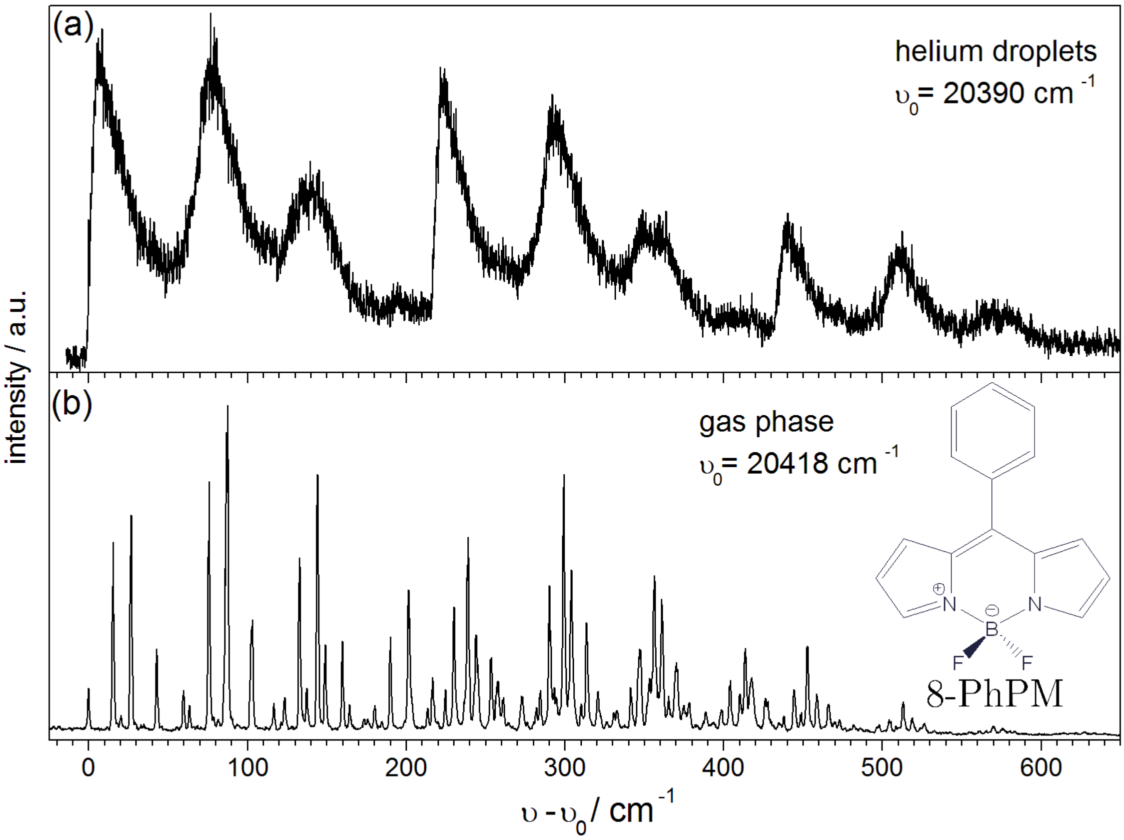

Fig. 7.9: Excitation spectra of 8-PhPM in helium droplets (a) and in the supersonic jet (b) with ν_0 as indicated. The laser intensity was low enough to avoid saturation effects. Both spectra were normalized to the laser intensity.

The excitation spectrum in fig. 7.9 (a) shows only one sharp transition with a line width of about 0.4 cm^{-1} at the electronic origin. Decreasing the oven temperature does not affect the shape of the spectrum.

An enlargement of the excitation spectrum at the electronic origin recorded with different laser intensities is presented in fig. 7.10. Lowering the laser intensity does not

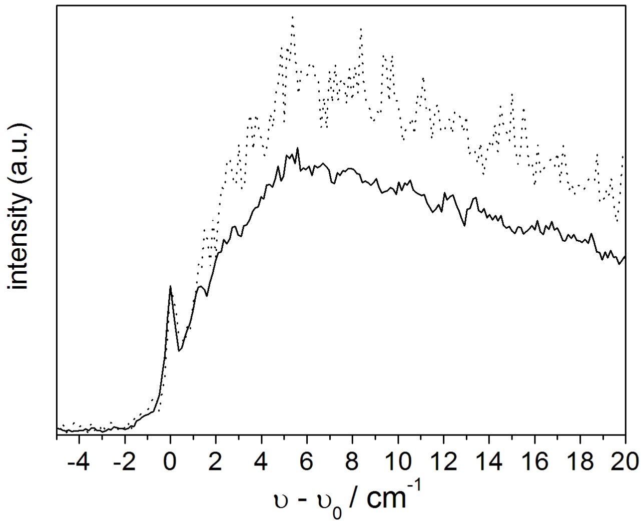

Fig. 7.10: Excitation spectrum of 8-PhPM in helium droplets recorded with different laser intensities.(see text) ν_0= 20390 cm^{-1} .

alter its shape compared to the solid line spectrum but only decreases its intensity. Thus, saturation effects can be excluded to cause the broadening. Increasing the laser intensity by about an order of magnitude slightly decreases the relative intensity of the sharp transition. This reflects a different saturation behavior of the leading peak and the broad feature to its blue side. Together with the fact that the broad contribution has no counterpart in the gas phase spectrum the saturation behavior is indicative for a sharp ZPL accompanied by an intense PW. The PW appears as a broad asymmetric feature similar as observed for fluorazene (FPP) in helium droplets discussed in chapter 6. However, in contrast to the spectrum of FPP a sharp ZPL is observed only at the electronic origin. Further, not all of the broad bands in the spectrum shown in fig. 7.9 (a) resemble the same asymmetric broad line shape.

In particular, the steep rise and asymmetric tail observed at the electronic origin reappears only at the fundamental and first overtone of a 217 cm^{-1} mode, which is also observed in the supersonic jet with a vibrational frequency of 222 cm^{-1} . In contrast, the other bands reveal a rather symmetric spectral shape. The peak intensities of the first three bands following the electronic origin appear shifted by about 80 cm^{-1} , 140 cm^{-1} and 195 cm^{-1} from the electronic origin. These bands are assigned to the members of the progression of the torsional mode. The intensity pattern of the progression indicates different equilibrium positions in the torsional potential in S_0 and S_1.

The S/N ratio and the drastic line broadening do not allow to resolve any fine structure of the vibrational satellites in the excitation spectrum. Due to the low signal level recording dispersed emission spectra was also not possible .

7.2.2 Discussion

The excitation spectrum of the phenylated PM dye 8-PhPM appears broadened compared to its spectrum in the gas phase. A similar broadening was observed for meso-phenylated anthracene (9-PA). (cf. chapter 5.5) In case of 9-PA the broadening could be attributed to a damping of the nuclear rearrangement induced upon excitation. This lead to a homogeneous broadening of all transitions in the excitation spectrum as discussed in chapter 5.9.1. However, in the spectrum of 8-PhPM different spectral shapes are observed. The electronic origin as well as the fundamental and the first overtone of a 217 cm^{-1} mode exhibit an intense and broad asymmetric band typical for a PW.
These bands exhibit a steep rise on the red side and a more moderate decline on the blue side. They were tentatively fitted with the phenomenological function

$$y = \begin{cases} 0, & \text{for } \nu < \nu_c \\ B(\nu - \nu_c) exp(-\frac{\sqrt{\nu-\nu_c}}{C}), & \text{for } \nu \geq \nu_c \end{cases} \tag{7.1}$$

with ν_c the frequency of the onset of the broad bands as shown in fig. 7.11 for the electronic origin. Therein, a Lorentzian function was added to describe the ZPL. The parameters B and C in fig. 7.11 were 14.5 cm and 1.35 cm^{-1} , respectively.
Similarly, the PW of pyrene observed in the excitation spectrum in helium droplets was simulated with an exponential decay as reported in ref. [RKH$^+$04]. Therein, the steep rise was assumed to be vertical and the PW to be separated from the ZPL by 5 cm^{-1} .

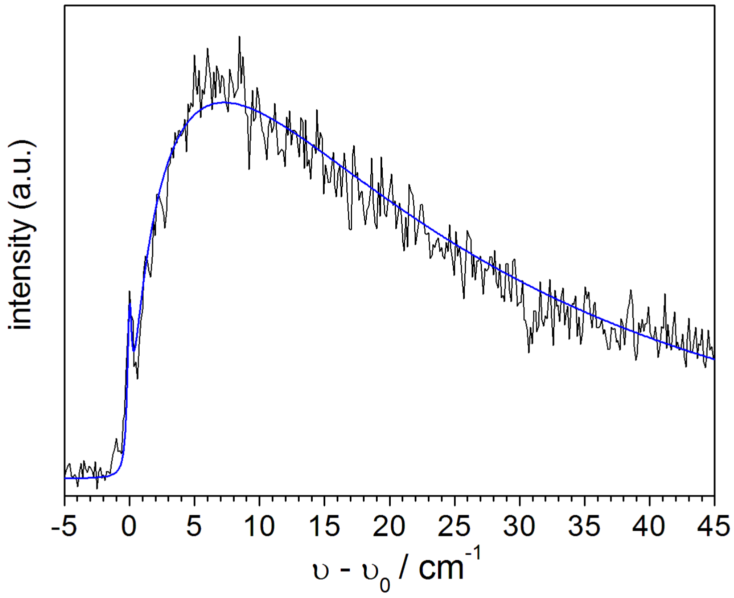

Fig. 7.11: Fit of the excitation spectrum of 8-PhPM in helium droplets at the electronic origin. (see text) $\nu_0 = 20390$ cm^{-1} .

The excitation spectrum of 8-PhPM in the gas phase for excess energies $\nu - \nu_0$ below 200 cm^{-1} mainly consists of the harmonic progression of the phenyl torsion. Each transition of this progression is additionally coupled to the anharmonic low-frequency progression with transitions at 15.5 cm^{-1} , 26.9 cm^{-1} , 43.0 cm^{-1} , and 63.7 cm^{-1} . [SF09] This anharmonic low-frequency progression was also present in the gas phase spectrum of the parent compound BDP though was completely missing in the droplet spectrum (cf. chapter 7.1). Assuming this low-frequency mode to be absent also in the droplet spectrum of 8-PhPM, it consists mainly of the progression of the phenyl torsion built on the electronic origin and the 217 cm^{-1} mode. Fig. 7.12 shows a simulation (blue) of the progression of the phenyl torsion built on the electronic origin. This pattern repeats coupled to the fundamental and the first overtone of the 217 cm^{-1} mode. The simulation used is a linear combination of equ. 7.1 to describe the first broad band and four Lorentzians. One of them describes the sharp ZPL at the electronic origin. The other Lorentzians have center frequencies of 79.5 cm^{-1} , 140 cm^{-1} , and 195 cm^{-1} with line widths (FWHM) of 36 cm^{-1} and relative intensities as indicated in fig. 7.12.
The simulation in fig. 7.12 (blue) demonstrates that transitions involving excitations of the torsional mode can roughly be described by Lorentzians. In contrast, the first band is ill-described by a Lorentzian (as well as any other symmetric function such as a Gaussian) function. The line widths of the torsional modes would correspond to a decay time of 0.15 ps similar as determined for 9-PA. (cf. chapter 5.9.1)

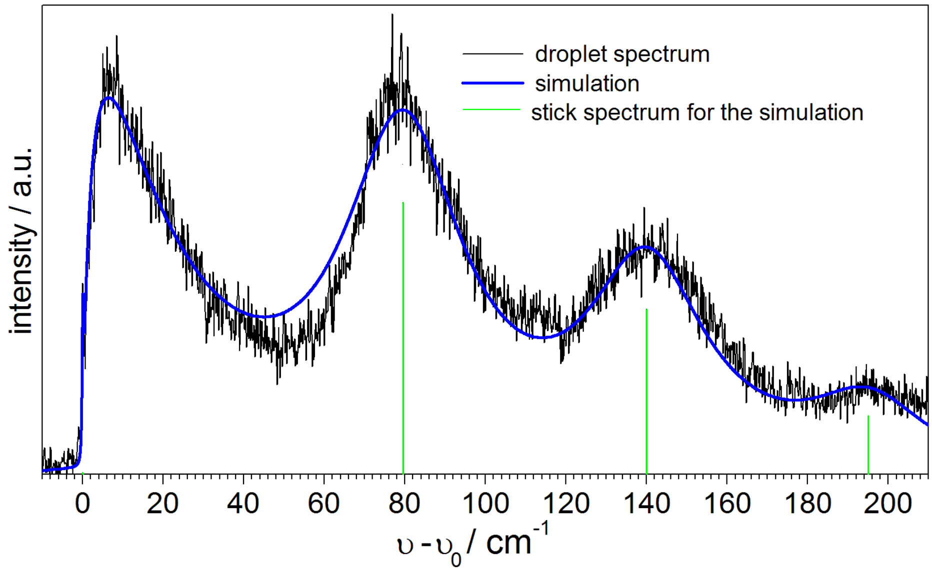

Fig. 7.12: Simulation (blue) of the excitation spectrum of 8-PhPM in helium droplets by a linear combination of an exponential and four Lorentzian functions. (see text) The center frequencies and relative intensities of the vibrational satellites are indicated by vertical lines (green). The experimental droplet spectrum (black) is shown for comparison.

To account for other vibronic transitions observed in the supersonic jet the spectrum in helium droplets was further simulated by a linear combination of the function presented in equ. 7.1 to describe the electronic origin and the fundamental and the overtone of the 217 cm^{-1} and Lorentzians for all others. Fig. 7.13 shows the simulated spectrum (blue) compared to the experimental droplet spectrum (black). The red stick spectrum illustrates the relative peak intensities and frequencies of all transitions observed in the supersonic jet omitting the unidentified low-frequency mode which was absent in helium droplets in the case of BDP.

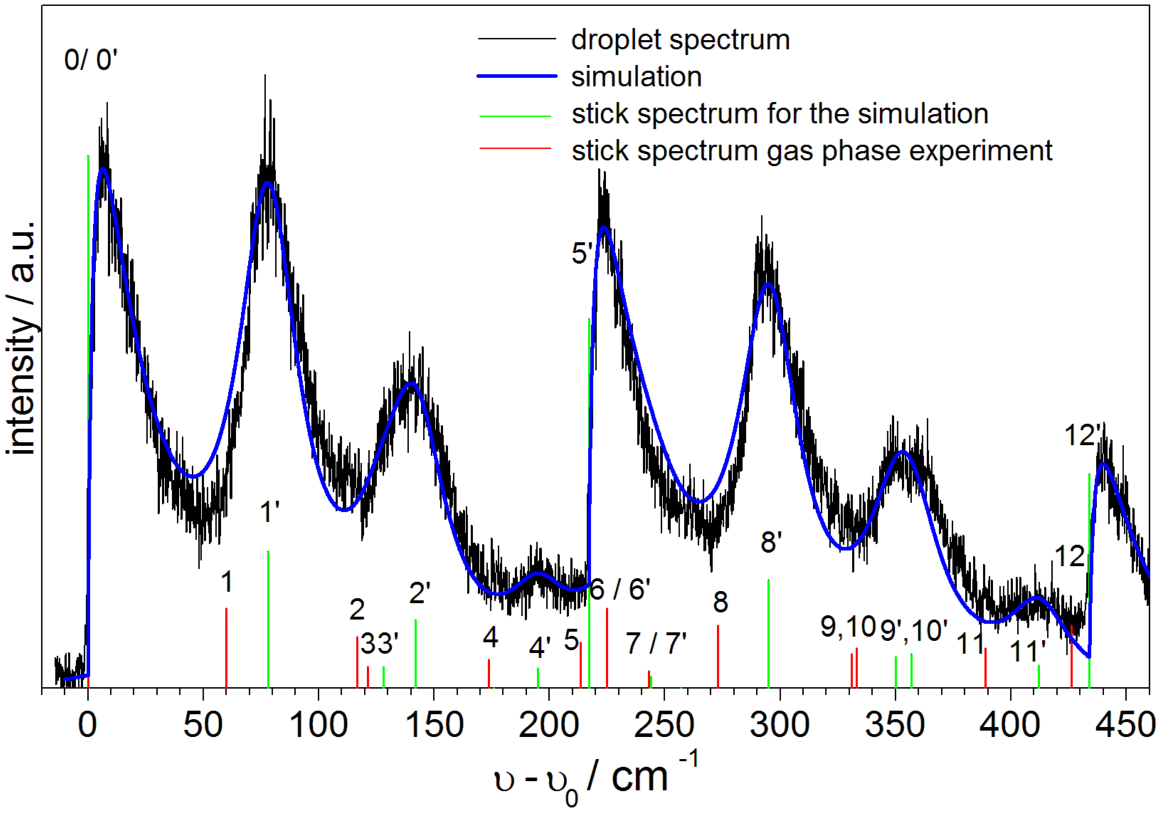

Fig. 7.13: Simulation (blue) of the excitation spectra of 8-PhPM in helium droplets by a linear combination of an exponential and Lorentzian functions. (see text) The stick spectrum for the simulation (green) and of parts of the experimental gas phase spectrum (red) are also shown. Corresponding transitions of the red and green spectra are labeled with the same number though with an additional prime for the transitions in the green spectrum. The experimental droplet spectrum (black) is shown for comparison.

For the simulation the parameters B and C in equ. 7.1 were fixed to 14.5 cm and 1.25 cm^{-1} , respectively, for the asymmetric bands with $\nu - \nu_0 = 0$ cm^{-1} , 217 cm^{-1} and 434 cm^{-1} . All Lorentzians have the same line width of 32 cm^{-1} corresponding to a decay time of about 0.2 ps. The center frequencies of the vibrational satellites were altered to obtain better agreement. Corresponding transitions in the gas phase and in helium droplets have the same number with a prime added to label the droplet transitions. In particular the center frequencies of the torsional mode were altered from 60 cm^{-1} (1), 117 cm^{-1} (2), and 174 cm^{-1} (4) as observed in the gas phase (red) to 78 cm^{-1} (1'), 142 cm^{-1} (2'), and 195 cm^{-1} (4') (green), respectively, for the fundamental and the two overtones. A similar scaling was used for these modes coupled to the 217 cm^{-1} mode. The relative intensities were altered as indicated by the green stick spectrum in fig. 7.13. The relative intensities used for the PWs at 0 cm^{-1} , 217 cm^{-1} and 434 cm^{-1} cannot be compared with the relative intensities for the Lorentzians.

The members of the progression of the phenyl torsion 1', 2' and 4' in helium droplets are shifted compared to the gas phase frequencies ($\nu - \nu_0$) of 1, 2, and 4, respectively, by about 20 cm^{-1} to higher energies. Thus, the origin of the progression would be expected at $\nu - \nu_0 \approx 20$ cm^{-1} which is in contrast to the observation of a sharp transition at $\nu - \nu_0 = 0$ cm^{-1} readily assigned to the electronic origin. This may indicate that the low frequency anharmonic progression observed in the gas phase spectrum is not absent in the droplet spectrum of 8-PhPM. In this case the peak positions of the broad bands in the droplet spectrum correspond to the center of the anharmonic progression coupled to the members of the torsional progression. This position is separated by about 20 cm^{-1} from the first transition of the anharmonic progression. (cf. fig. 7.9(b)) In contrast, the electronic origin in the droplet spectrum may correspond to the transition lowest in energy of the anharmonic progression built on the electronic origin. The anharmonic progression may cause the deviations between the simulated (blue) and experimental (black) droplet spectrum in fig. 7.13.

To conclude, the electronic origin and the vibrational satellites of the 217 cm^{-1} mode not coupled to the phenyl torsion reveal a rather asymmetric broadening typical for the dominance of a PW. This is in agreement with the observed saturation behavior and indicates a strong electron-phonon coupling. All transitions coupled to the phenyl torsion appear broadened in helium droplets. However, it is not clear if the anharmonic low-frequency progression observed in the gas phase is completely absent, as observed for BDP, or if it contributes to the observed band widths. The latter is indicated by the center frequency of the broad bands of the phenyl torsion. Therefore, only a lower limit for the decay time can be estimated to 0.2 ps. Since the broadening does not occur in the gas phase or at the electronic origin it can presumably be attributed to a fast dissipation of vibrational excess energy following the arguments in chapters 7.4 and 7.5.

Regardless of the presence or absence of the anharmonic low-frequency mode in the droplet spectrum the electronic origin is the only sharp ZPL that could be resolved. Sharp ZPLs might also be found in the steep rise of the transitions at 217 cm^{-1} and 434 cm^{-1} though could not unequivocally be assigned. In view of the S/N-ratio and the relative peak intensity of the sharp transition at the electronic origin compared to the broad signal in fig. 7.10 a sharp signal with half of the intensity of the sharp origin, as to be expected at 217 cm^{-1} , would be hidden below the noise.

Interestingly, both broadening mechanisms, namely the dominance of PWs and the damping of excited states, seem to appear in the spectrum of 8-PhPM. The latter dominates for vibronic transitions involving excitation of the phenyl torsion. However, at this stage it is not clear why it dominates over the electron-phonon coupling. If both processes would be affective for the transitions involving the phenyl torsion the line shape could not be described by a symmetric function with a line width similar as observed for the asymmetric PW at the electronic origin.

The driving force for both, electron-phonon coupling based on a variation of the configuration of the non-superfluid solvation layer and the damping based on a variation of an intramolecular coordinate (such as a torsional angle), is the change of the electron density induced upon electronic excitation. One might speculate that only upon excitation of the torsional mode the damping is faster than the rearrangement of the solvation layer thus dominating the line shape of transitions involving excitation of the torsional mode.

7.3 PM546

Substitution of the parent compound BDP with a methyl group at position 8 and two methyl groups on each pyrrole ring at positions 1, 3, and 5, 7, respectively, gives the commercially available laser dye PM546.

The excitation spectrum of PM546 in a supersonic jet is shown in fig. 7.14 (b) and reveals a harmonic progression of a 29 cm^{-1} mode. [SF09] The electronic origin is hardly recognizable and the peak intensity is at the sixth transition of the progression indicative of a significant change of the geometry induced upon electronic excitation. A similar harmonic progression is not observed in the spectra of BDP or 8-PhPM and thus is attributed to vibrational modes involving the methyl groups. Progressions with similar spacings of about 30 cm^{-1} are observed in the spectra of PM567 (cf. chapter 7.4) and PM650 (cf. chapter 7.5) all containing methyl groups at positions 1, 3, 5, and 7. Quantum chemical calculations provided evidence that the mode is not a torsional mode of single methyl groups. [SF09] Thus, it is indicated that the normal coordinate of this vibrational mode depends on the torsional and bending angles of all of the distinct methyl-groups at positions 1, 3, 5, and 7.

Each transition of the progression reveals a double peak splitting of 3 cm^{-1} . Pump-probe experiments provided evidence that the transitions of a doublet originate from different ground states, though are not due to hot bands. For example, the different ground state could be due to different conformers (possibly differing by the configuration of the methyl-group at position 8) or a tunneling splitting.

SVL-spectra recorded in the supersonic jet indicate a low-frequency mode of $\approx$ 30-40 cm^{-1} in the ground state. However, more detailed information remained hidden due to spectral congestion and limitations of the spectral resolution.

All data presented in the following were recorded with the Scanmate dye laser system (dye: Coumarin102). Integral emission was detected with the PMT R 943-02 (Hamamatsu) protected by a cut-off filter OG515. Emission dispersed with the 1200 lines/mm grating installed in the SPEX spectrograph was detected with the CCD-camera DU 420A-BU2 (Andor iDus). The oven temperature for optimum LIF signal of single PM546 while avoiding LIF-signals from multiple doped helium droplets was 42 °C.

7.3.1 Excitation Spectrum of PM546

The excitation spectrum of PM546 recorded in helium droplets is shown in fig. 7.14 (a) in comparison to the excitation spectrum of the free molecule in the gas phase (fig. 7.14 (b)). The droplet spectrum appears drastically broadened as compared to the gas phase spectrum though roughly describes its envelope. The electronic origin is expected to

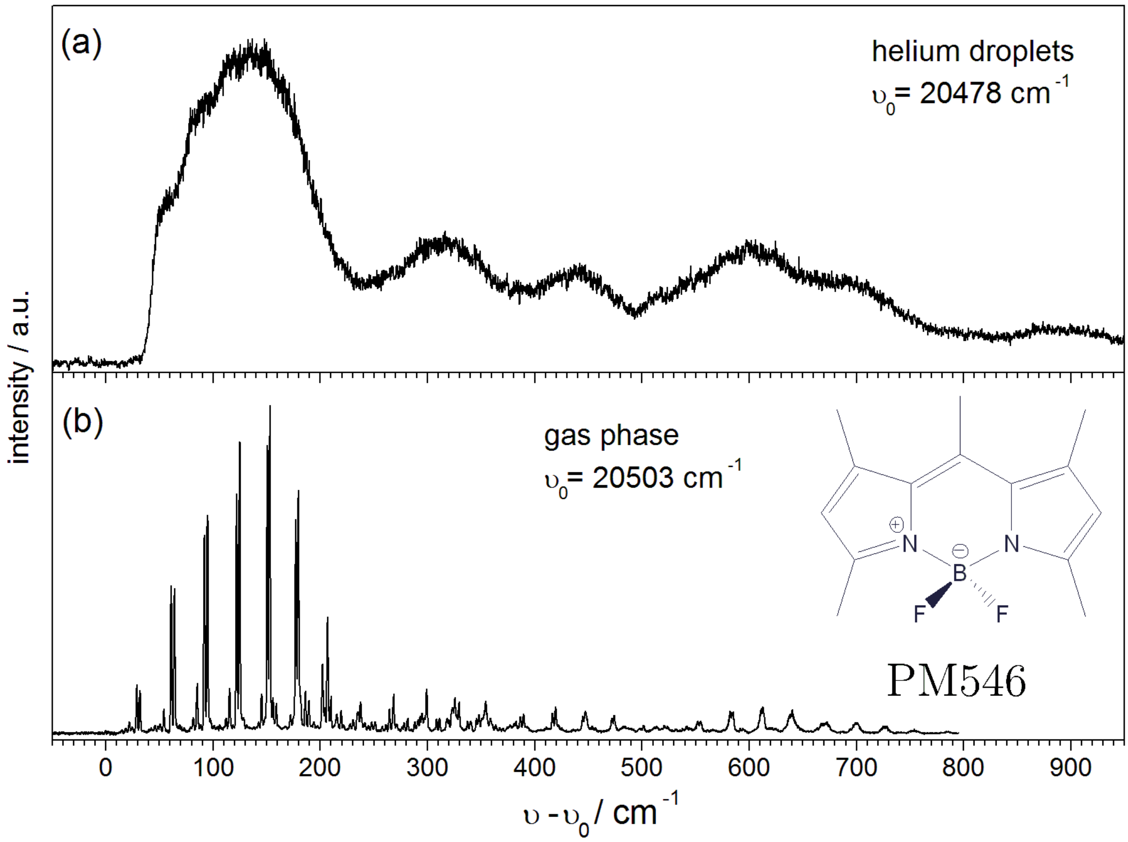

Fig. 7.14: Excitation spectra of PM546 in helium droplets (a) and in the supersonic jet (b) with ν_0 as indicated. The laser intensity was low enough to avoid saturation effects and was kept constant.

be very weak as found in the gas phase and thus its position is determined to about 20478 cm^{-1} by comparing the shape of the gas phase and helium droplet spectra. This frequency corresponds to a helium solvent shift of about 25 cm^{-1} to the red.

No sharp transitions could be observed independent of experimental conditions such as laser intensity or oven temperature. Upon lowering the oven temperature or the laser intensity the spectrum only looses intensity while its spectral shape is not affected. Thus, the droplet spectrum stems from the monomer and is not broadened by saturation effects. Upon increasing the oven temperature the spectrum further broadens and a new band appears to the red of the spectrum which is assigned to stem from oligomers.

The droplet spectrum shown in fig. 7.14 (a) appears as the broad envelope of the 29 cm^{-1} mode progression built onto the electronic origin and other modes such as a $\approx$ 200 cm^{-1} mode. This mode presumably corresponds to the 217 cm^{-1} mode of 8-PhPM. (cf. chapter 7.2)

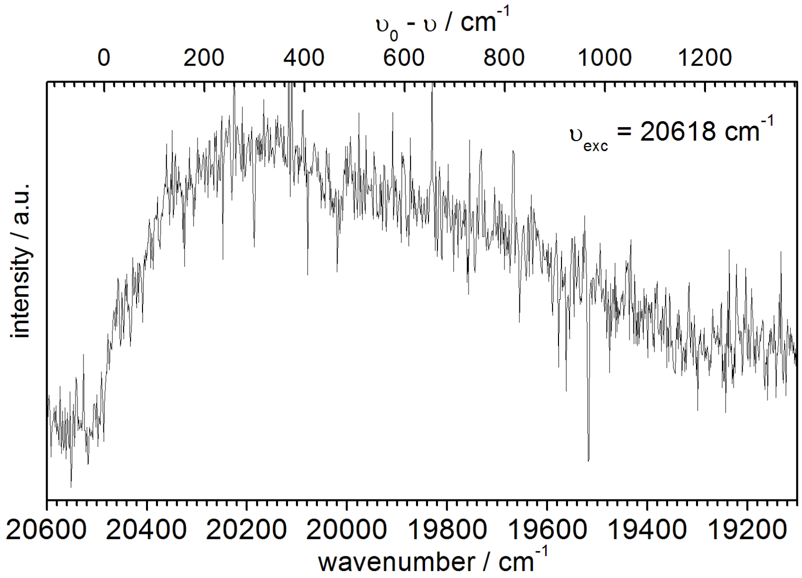

Fig. 7.15: Emission spectrum of PM546 in helium droplets recorded upon excitation at ν_{exc} = 20618 cm^{-1} with ν_0 = 20485 cm^{-1} . The distance between two pixel columns amounts to about 1.7 cm^{-1} at the blue and 1.4 cm^{-1} at the red end of the spectrum.

7.3.2 Emission Spectrum of PM546

The dispersed emission spectrum of PM546 in helium droplets is shown in fig. 7.15. Its spectral shape was found to be independent of the excitation frequency within the spectrum shown in fig. 7.14 (a). Low fluorescence intensity distributed over a large spectral range cause the low S/N-ratio despite of the accumulation time of one hour. The broadening is not caused by experimental conditions such as the width of the entrance slit of the spectrograph.

The rise of the signal starts at roughly 20485 cm^{-1} at the given experimental accuracy, which is in agreement with the frequency of the electronic origin in the excitation spectrum. It should be noted that the SVL spectrum in the supersonic jet recorded upon excitation with 29 cm^{-1} excess energy appears slightly more structured but in well agreement with the emission spectrum observed in helium droplets. [SF09]

7.3.3 Discussion

The excitation spectrum of PM546 in helium droplets appears only with very broad spectral features and without any sharp ZPL. The shape of the excitation spectra recorded in helium droplets as well as in the gas phase indicates that significant nuclear rearrangements are induced upon electronic excitation. A similar broadening was observed in the excitation spectrum of 2-methylanthracene (2-MA) in helium droplets and was attributed to a damping of the nuclear rearrangement induced upon excitation. (cf. chapter 5.9.1) In the case of 2-MA the spectrum in helium droplets was found in reasonable agreement with the experimental gas phase spectrum convoluted with a single Lorentzian. Fig. 7.16 shows the experimental excitation spectrum of PM546 recorded in the supersonic jet convoluted with a Lorentzian with a full width of 42 cm^{-1} .

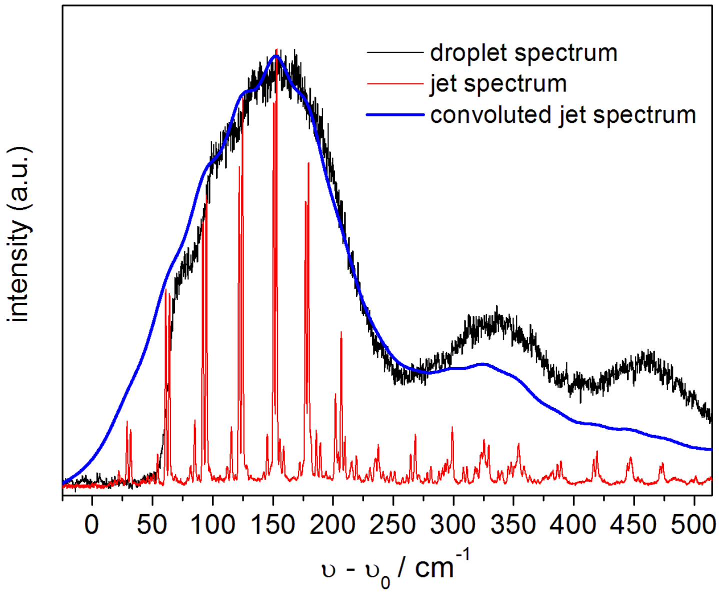

Fig. 7.16: Convolution (blue) of the excitation spectra of PM546 in the supersonic jet (red) with a Lorentzian with a line width of 42 cm^{-1} . The experimental droplet spectrum (black) is shown for comparison. $\nu_0 = 20458$ in the droplet spectrum, and 20503 cm^{-1} in the supersonic jet spectrum.

The convoluted spectrum reveals significant discrepancies compared to the experimental droplet spectrum in the rising part (red edge) and at excess energies above $\nu - \nu_0 \approx$ 270 cm^{-1} . The latter can be attributed to the different dependence of the fluorescence quantum yield in helium droplets and in the gas phase on excess excitation energy $\nu - \nu_0$ as discussed in chapters 4 and 5.9.1. The former represents the larger deviation and will be discussed in more detail.

A comparison of the experimental excitation spectra in helium droplets (black) and in the gas phase (red) or the convoluted gas phase spectrum (blue), respectively, shown in fig. 7.16 reveals that the width of the progression of the 29 cm^{-1} mode in the gas phase is larger than the width of the first band in helium droplets. This indicates that the vibrational frequency of this mode decreases upon solvation of PM546 in helium. This is corroborated by the excitation spectra of PM567 and PM650 revealing a decrease of the vibrational frequency of the 26.5 cm^{-1} and 32 cm^{-1} mode, respectively, presumably corresponding to the 29 cm^{-1} mode of PM546. (cf. chapters 7.4 and 7.5) The lower frequency in helium droplets may be attributed to a more shallow potential of this mode in the excited state or a larger effective mass involved. In the former case not only the vibrational frequency but also the intensity pattern (FC-factors) of the progression is altered. Both, different frequencies and relative intensities in helium droplets and in the gas phase contribute to deviations of the convoluted gas phase spectrum compared to the experimental droplet spectrum in fig. 7.16.

Another reason for the deviation is the presence of hot bands in the gas phase spectrum. Only few of them, e.g. at 22 cm^{-1} or 54 cm^{-1} are spectrally well separated from transitions originating from the vibrational ground state, whereas most of the hot bands overlap with transitions of ’cold’ PM546. In particular, hot bands were observed to overlap with the transitions at 29 cm^{-1} and 32 cm^{-1} . [SF09] Due to the spectral overlap it is not possible to unequivocally extract the excitation spectrum of ’cold’ isolated PM546 from the experimental gas phase spectrum. Thus, parts of the deviations in fig. 7.16 are attributed to thermal effects.

Most of the transitions in the gas phase spectrum reveal a splitting by roughly 3 cm^{-1} . The splitting slightly decreases from 2.8 cm^{-1} at the electronic origin e.g. to 2.3 cm^{-1} at 177 cm^{-1} vibrational excess energy. Further, the relative intensity of the two transitions within a doublet varies slightly. At excess energies $\nu - \nu_0 \gtrsim 200$ cm^{-1} spectral congestion due to overlapping bands makes an assignment difficult. Some prominent transitions, e.g. at 202 cm^{-1} are either not split or exhibit a significant larger splitting of 4.7 cm^{-1} . [SF09] As discussed above, the splitting may be e.g. due to a tunneling splitting or the presence of different conformers of PM546 in the supersonic jet. However, it is not clear if both, only one, or a different contribution is reflected by the droplet spectrum. This may also cause deviations of the simulated spectrum shown in fig. 7.16 based on the experimental gas phase spectrum as compared to the experimental droplet spectrum.

It should be noted that, similar as found in the excitation spectrum of 8-PhPM in helium droplets, the excitation spectrum of PM546 reveals a steep rise at the red side. However, no sharp transition can be found in the case of PM546. The steep rise may indicate that PWs contribute to the spectrum in helium droplets.

To conclude, the electronic spectra of PM546 in helium droplets are significantly broadened compared to the corresponding gas phase spectra. In analogy to the discussion in chapter 5.9.1 this can presumably be attributed to a damping of the nuclear rearrangement induced upon electronic excitation. However, the shape of the excitation spectrum in helium droplets could not be reproduced by a convolution of the corresponding gas phase spectrum. It is indicated that the vibrational frequency of the progressive mode decreases upon embedding PM546 in helium droplets which may also affect the intensity ratios of the individual transitions. Further possible reasons for the deviation of the simulated spectrum as compared to the experimental droplet spectrum are the occurrence of hot bands in the gas phase spectrum as well as PWs in the droplet spectrum. Moreover, the gas phase spectrum consists of transitions originating from two different ground states and it is not clear if both, only one, or a different ground state contributes to the droplet spectrum.

7.4 PM567

Additional introduction of ethyl groups at positions 2 and 6 to the molecular structure of PM546 yields PM567.

The excitation spectrum of PM567 recorded in the supersonic jet is shown in fig. 7.17(b) and is dominated by an extended progression of a 26.5 cm^{-1} mode. [SF09] The electronic origin is not the most intense transition but the progression peaks at a higher transition. This is characteristic for a significant change of the equilibrium geometry upon excitation. The progression repeats coupled to other modes such as a $\approx$ 50 cm^{-1} and a $\approx$ 200 cm^{-1} mode. However, spectral congestion due to overlapping transitions and increasing line width with increasing vibrational excess energy make the assignments difficult. A similar progression was observed in the excitation spectra of PM546 (cf. chapter 7.3) and PM650 (cf. chapter 7.5). The transitions of the progression of PM567 in the gas phase exhibit a splitting into triplets with spacings of about 6 cm^{-1} at the electronic origin and the first few members of the progression. However, the splitting tends to decrease with increasing vibrational excess energy and is presumably below the line width e.g. at the transition at 256 cm^{-1} with a line width of 5.5 cm^{-1} .

Pump-probe experiments indicated that the transitions within a triplet originate from different ground states. [SF09] A similar splitting into triplets and doublets with spacings of about 3 cm^{-1} was observed in the gas phase excitation spectra of PM650 (cf. chapter 7.5) and PM546 (cf. chapter 7.3), respectively.

SVL spectra recorded in the supersonic jet indicated progressions of a low-frequency mode of about 27 cm^{-1} also in S_0. [SF09]

All data presented in the following were recorded with the Scanmate dye laser system (dye: Coumarin307). Integral emission was detected with the PMT R 943-02 (Hamamatsu) protected by a cut-off filter OG530. Emission dispersed with the 1200 lines/mm grating installed in the SPEX spectrograph was detected with the CCD-camera DU 420A-BU2 (Andor iDus). The oven temperature for optimum LIF signal of single PM567 while avoiding LIF-signals from multiple doped helium droplets was 62 °C.

7.4.1 Excitation Spectrum of PM567

Fig. 7.17 (a) shows the excitation spectrum of PM567 recorded in helium droplets in comparison to the excitation spectrum of the free molecule in the gas phase (fig. 7.17(b)). The transition lowest in energy, therefore assigned to the electronic origin, is the only sharp transition. It is split into a triple peak structure with the first transition at $\nu_0 =$ 19476 cm^{-1} (cf. fig. 7.18) corresponding to a red shift of 19 cm^{-1} compared to the gas phase. The broad dominant bands in the spectrum of PM567 in helium droplets appear

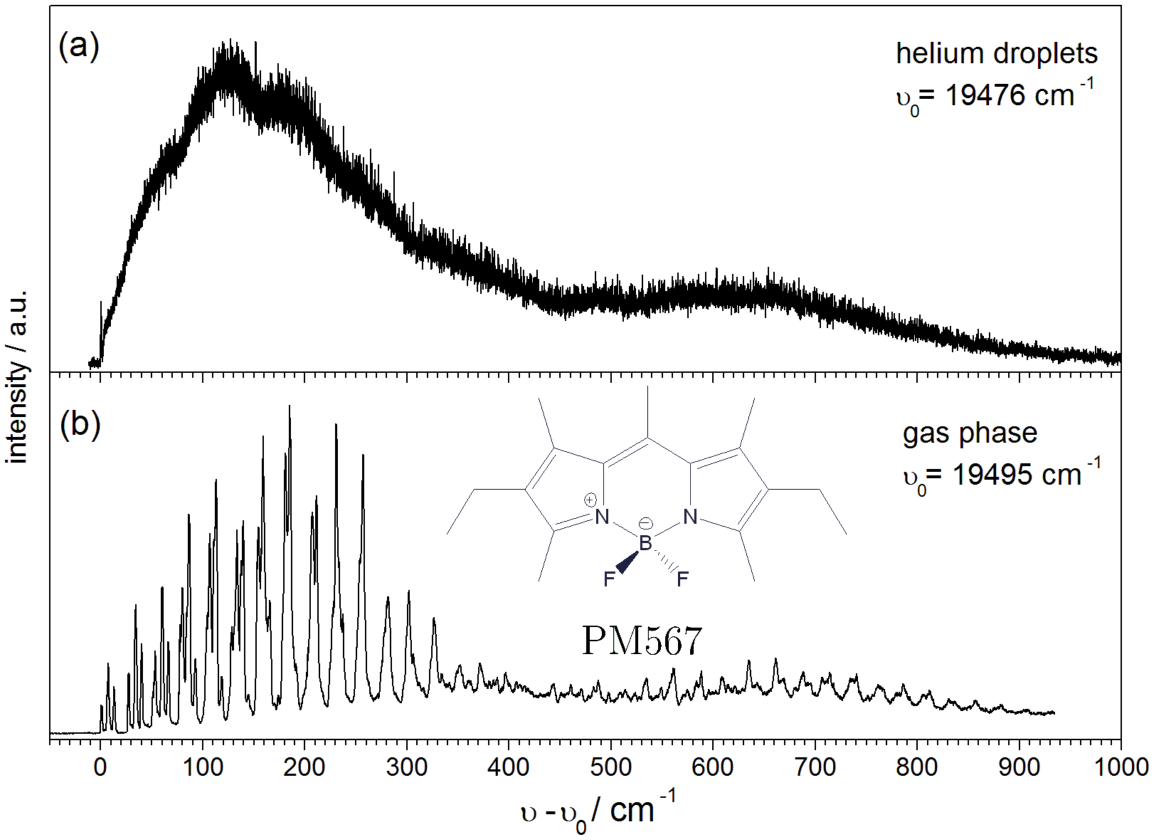

Fig. 7.17: Excitation spectra of PM567 in helium droplets (a) and in the supersonic jet (b) with ν_0 as indicated. The laser intensity was kept constant in the droplet experiment. The excitation spectrum recorded in the supersonic jet was normalized to the laser intensity.

roughly as the envelope of the gas phase spectrum. However, the droplet spectrum exhibits a steeper rise on the red side and peaks already at an excess energy of $\nu - \nu_0 \approx 125$ cm^{-1} much lower than the gas phase spectrum peaking at $\nu - \nu_0 \approx 185$ cm^{-1} .

Upon decreasing the oven temperature the spectrum looses intensity but the spectral shape is not affected. Variations of the laser intensity, however, are of influence on the spectral shape in particular at the electronic origin as shown in fig. 7.18.

Excitation spectra recorded with laser intensities of less than 10 μJ (solid line) and of about 80 μJ (dotted line) are presented in fig. 7.18 (a). Upon increasing the laser intensity the relative intensity of the leading triple peak structure decreases compared to the broad accompanying signal to the blue. Further decreasing the laser intensity than for the solid line spectrum may slightly increase the relative intensity of the sharp transitions as shown in fig. 7.18 (b). The dotted spectrum was recorded with a polarizer in almost perpendicular orientation to the polarization of the laser beam. Under these conditions the weak fluorescence could only be distinguished from the noise when recorded without a cut-off filter in front of the PMT. The excitation spectra in fig. 7.18 (b) are almost identical within the S/N ratio. This indicates that, at the utmost, small satura-

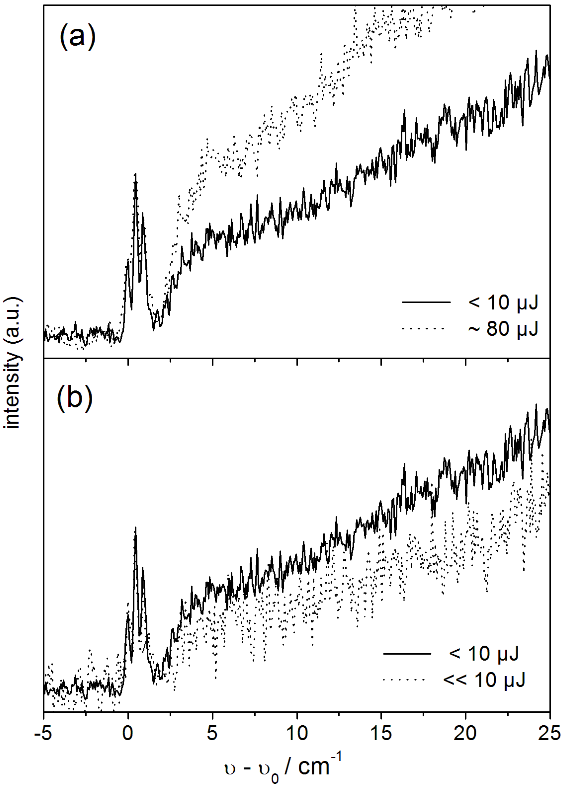

Fig. 7.18: Excitation spectrum of PM567 in helium droplets recorded with different laser intensities.(see text) ν_0= 19476 cm^{-1} .

tion effects may occur in the solid line spectrum. Conditions of the solid line spectrum in fig.s 7.18(a) and (b) were used for all other excitation spectra shown.
The different saturation behavior indicates that only the sharp transitions can be assigned to ZPLs. (cf. chapter 4) Consequently, the broad contribution with the steep rise separated by about 2 cm^{-1} from the origin, which has no counterpart in the gas phase spectrum is dominated by the corresponding PW.
An enlargement of the excitation spectra of PM567 in helium droplets (black) and in the gas phase (red) at the electronic origin is shown in fig. 7.19.

It clearly reveals that already the second peak in the gas phase spectrum centered at $\nu-\nu_0$ $\approx$ 7.2 cm^{-1} , and thus shifted from the center of the first peak by about 6.4 cm^{-1} , is not observed as a sharp ZPL in the droplet spectrum. The electronic origin in helium droplets appears split into a triplet structure with a spacing of 0.45 cm^{-1} between two subsequent transitions. This triplet structure is also indicated though not fully resolved in the gas phase spectrum with similar spacings between the peaks. It may be due to a tunneling splitting in addition to an overlap of rotational band contours of the two different isotopomers containing ^{11}B or ^{10}B, respectively. Further, solvation effects cannot be excluded to cause the triplet structure in the droplet spectrum, though, are unlikely due to the similar structure indicated in the gas phase spectrum.

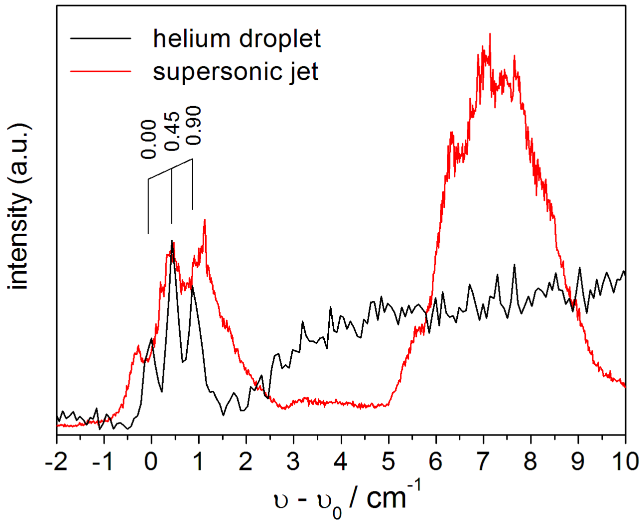

Fig. 7.19: Excitation spectrum of PM567 at the electronic origin recorded in helium droplets (black, ν_0= 19476 cm^{-1}) and in the supersonic jet (red, ν_0= 19495 cm^{-1}).

7.4.2 Emission Spectrum of PM567

The dispersed emission spectrum of PM567 recorded in helium droplets upon excitation at ν_{exc} = 20101 cm^{-1} is shown in fig. 7.20. It appears independent of the excitation frequency as a single broad band similar as for PM546. The onset is observed at $\nu_0 \approx$ 19460 cm^{-1} which is in agreement with the electronic origin in the excitation spectra at ν_0 = 19476 cm^{-1} within experimental accuracy. The emission spectrum recorded upon excitation at the sharp electronic origin was too weak to be clearly distinguished from the noise. Due to the low S/N-ratio despite of the long acquisition time of 1.5 hours it remains unclear if the emission spectrum contains also sharp transitions, in particular at the electronic origin. For a similar intensity ratio of a sharp electronic origin to the peak of the broad band as observed in the excitation spectra, the sharp origin would be hidden below the noise.

7.4.3 Discussion

The excitation spectrum of PM567 in helium droplets revealed only a single sharp transition at the electronic origin. All other transitions appear broadened. The excitation spectrum in the gas phase provides evidence for a significant change of the geometry upon electronic excitation. In this case a broadening of the transitions is often obser-

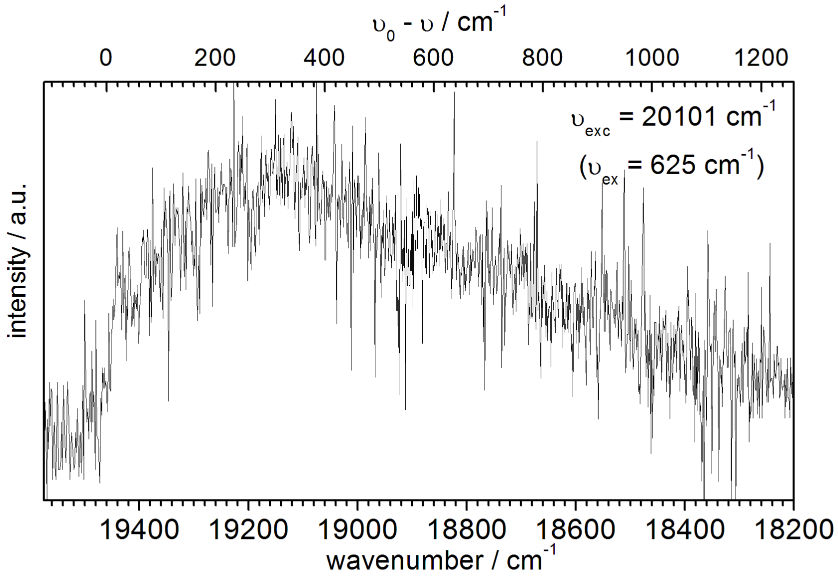

Fig. 7.20: Emission spectrum of PM546 in helium droplets recorded upon excitation at $\nu_{exc} = 20101$ cm^{-1} (excess energy $\nu_{ex} = 625$ cm^{-1}) with $\nu_0 = 19460$ cm^{-1} . The distance between two pixel columns amounts to about 1.5 cm^{-1} at the blue and 1.3 cm^{-1} at the red end of the spectrum.

ved in helium droplets and is attributed to a damping of the nuclear rearrangement as discussed in chapter 5.9.1. In the case of PM567 the electronic origin remains sharp indicating that the nuclear rearrangement only drives the damping of vibrational excited states. The broadening observed only in helium droplets may be due to an enhancement of isoenergetic non-radiative decay processes such as IC, IVR, or ISC also affective in the gas phase or the dissipation of vibrational excess energy (vibrational relaxation) into the helium environment. (cf. chapter 5.9.1) The gentle interaction of the helium environment revealed by the small solvent shifts of electronic and vibrational transitions indicates only minor variations of the energy spacings of electronic and vibrational levels. Thus, the rate constants for isoenergetic intramolecular processes, such as IC, IVR, and ISC, are not expected to be altered by orders of magnitude as compared to the gas phase and thus presumably do not cause the damping. ISC was reported to the be negligible for PM567 and most other PM dyes in all media yet investigated despite of large solvent shifts such as 10 nm (≈ 400 cm^{-1} at 500 nm). [ABC03, CGMG+02, BnPLAMM+04a, UZH08] In contrast, in helium droplets dissipation of vibrational excess energy was found to occur within picoseconds for all fluorescing organic molecules yet investigated in helium droplets. [LS03, LS04b, LSK+04, ST08] (cf. chapters 4 and 5.9.1) The observed broadening thus presumably can be attributed to an enhanced dissipation of the vibrational excess energy. On the other hand, since the electronic origin remains sharp, the dissipation of purely electronic excitation energy, mediated by IC or ISC, is not enhanced.

According to this broadening mechanism the experimental droplet spectrum might be obtained by convolution of the vibrational satellites in the corresponding gas phase spectrum with a Lorentzian function. Fig. 7.21 shows the experimental excitation spectrum of PM567 recorded in the supersonic jet convoluted with a Lorentzian with a full width of 40 cm^{-1} .

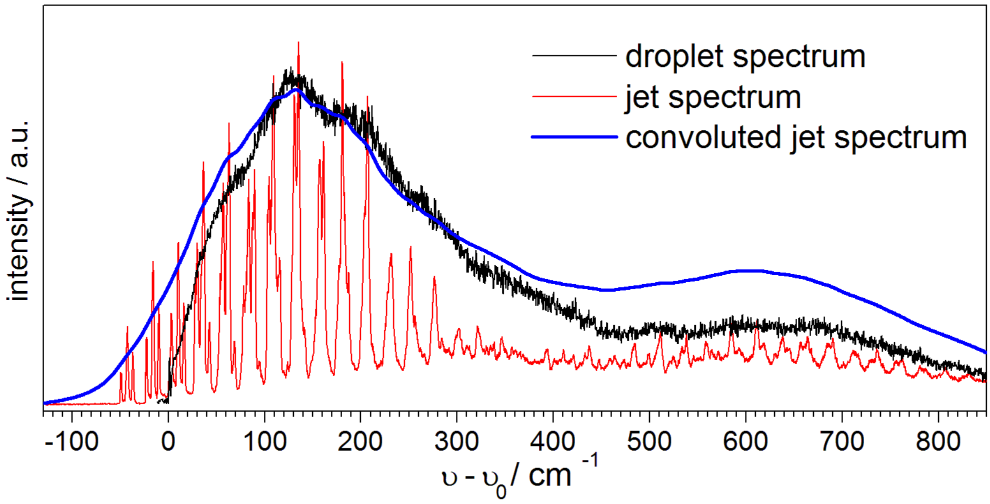

Fig. 7.21: Convolution (blue) of the excitation spectra of PM567 in the supersonic jet (red) with a Lorentzian with a line width of 40 cm^{-1} . A 1 Hz low-pass FFT-filter was applied to the droplet spectrum (black) shown for comparison. $\nu_0 = 19476\ \mathrm{cm}^{-1}$ in the droplet spectrum, and 19445 cm^{-1} in the supersonic jet spectrum.

For the convolution, the gas phase spectrum in fig. 7.21 was shifted further to the red by 50 cm^{-1} compared to the spectrum shown in fig. 7.17 (b). Thereby, the convoluted spectrum is in reasonable agreement with the experimental gas phase spectrum for excess energies $\nu - \nu_0 \gtrsim 70\ \mathrm{cm}^{-1}$. Deviations at higher excess energies such as 400 cm^{-1} can be attributed to different fluorescence quantum yields in helium droplets and the gas phase as discussed in chapter 5.9.1. Larger deviations are found at lower frequencies where the convoluted spectrum extends further to the red than the experimental droplet spectrum. The electronic origin is also broadened in the simulation shown in fig. 7.21 though this plays a minor role for the deviation. Whereas, they may be due to a reduction of the vibrational frequency of the progressive mode upon solvation in the helium droplets as indicated also for PM546 (cf. chapter 7.3) and PM650 (cf. chapter 7.5). A variation of the vibrational frequency may be due to a different effective mass or a different potential. The latter would also affect the intensity pattern (FC-factors). The triplet structures observed in the gas phase spectrum ($\approx 6\ \mathrm{cm}^{-1}$ spacings) may be a further reason for the deviation since it is indicated that the spacings and the relative intensities within the triplets depend on the excess energy $\nu - \nu_0$. These transitions originate from different ground states e.g. due to tunneling splittings or the presence of different conformers. The sharp ZPLs in the helium droplet spectrum correspond to only one of these transitions of a triplet. This may indicate that the other transitions do not contribute significantly

to the droplet spectrum or appear with a much larger line width.
A sharp ZPL in the excitation spectrum of PM567 in helium droplets is observed only at the electronic origin. In case the broadening would be due a dominance of PWs, sharp ZPLs would be expected to occur also for all vibronic transitions, as observed for fluorazene (FPP, cf. chapter 6). Since the relative intensity of the vibronic transitions increases with the excess energy up to $\nu - \nu_0 \approx 125$ cm^{-1} the sharp ZPLs should be clearly recognizable. Thus, the broadening can be excluded to be solely due to a dominance of PWs in the spectrum with high confidence. However, PWs contribute to the spectrum and cause further deviations of the simulated spectrum in fig. 7.21 as compared to the experimental droplet spectrum.

To conclude, the excitation spectrum of PM567 in helium droplets reveals a broadening of the vibrational satellite structure while the electronic origin remains sharp. Emission spectra also indicate a broadening though the S/N ratio does not allow for a reasonable analysis of the line shape at the electronic origin. The shape of the vibrational satellite structure indicates a rather symmetric broadening. Convolution of the gas phase spectra with a Lorentzian indicate a line width in the order of 40 cm^{-1} corresponding to a decay time of 0.1 ps. The fast decay can presumably be attributed to the dissipation of vibrational excess energy. Deviations between the convoluted spectrum and the experimental gas phase spectrum may be due to a variation of the vibrational frequency of the progressive mode. However, PWs may also contribute to the deviations.

7.5 PM650

The introduction of additional methyl groups at positions 2 and 6 to the molecular structure of PM546 together with a substitution of the methyl group at position 8 by a cyano group yields PM650. Alternatively, the molecular structure of PM650 can be seen to arise from PM567 by substituting the ethyl groups at positions 2 and 6 by methyl groups and the methyl group at position 8 by a cyano group.

The excitation spectrum of PM650 recorded in the supersonic jet is shown in fig. 7.22 (b) and reveals a progression of a low-frequency mode with 31.9 cm^{-1} spacings similar as observed for PM546 (cf. chapter 7.3) and PM567 (cf. chapter 7.4). [SF09] This mode repeats coupled to other modes such as a 47 cm^{-1} and a 56 cm^{-1} mode. However, spectral congestion due to overlapping transitions inhibits straight assignments already for excess energies $\nu - \nu_0 \gtrsim 50\ \mathrm{cm}^{-1}$. The electronic origin and the second feature of the progression are of almost equal intensity and the progression ends after four transitions. Both are indicative for a smaller geometrical change induced upon electronic excitation as compared to PM546 and PM567 exhibiting extended progressions and weak origins in the electronic spectra.

Similar as found for PM567, the electronic origin and most of the vibrational satellites in the excitation spectrum of PM650 appear split into a triplet though with smaller spacings of 3 cm^{-1} between two subsequent transitions. Pump-probe experiments provided evidence that the transitions within a triplet originate from three different ground states.

SVL spectra in the supersonic jet revealed a short progression of a 27 cm^{-1} mode corresponding to the 32 cm^{-1} mode in the excitation spectrum. The 27 cm^{-1} mode of the electronic ground state appears also coupled to similar modes as the 32 cm^{-1} mode of the excited state. The 27 cm^{-1} mode in SVL spectra is in agreement with hot bands observed in excitation spectra recorded at higher temperatures in the supersonic jet. These hot bands revealed a triplet structure with the same 3 cm^{-1} spacings as for the transitions shown in fig. 7.22 (b).

All excitation spectra presented in the following were recorded with the Scanmate dye laser system (dye: Coumarin153). Integral emission was detected with the PMT R 943-02 (Hamamatsu) protected by a cut-off filter OG590. Emission spectra were recorded upon excitation with the cw dye laser (dye: Rhodamine6G) with the nozzle operated at 200 Hz, a stagnation pressure of 80 bar and a nozzle temperature of 18 K. Light was dispersed with the 1200 lines/mm grating installed in the MS257 spectrograph and detected with the CCD-camera DU 401-BV (Andor iDus). The oven temperature for optimum LIF signal of single PM650 while avoiding LIF-signals from multiple doped helium droplets was 65 °C.

7.5.1 Excitation Spectrum of PM650

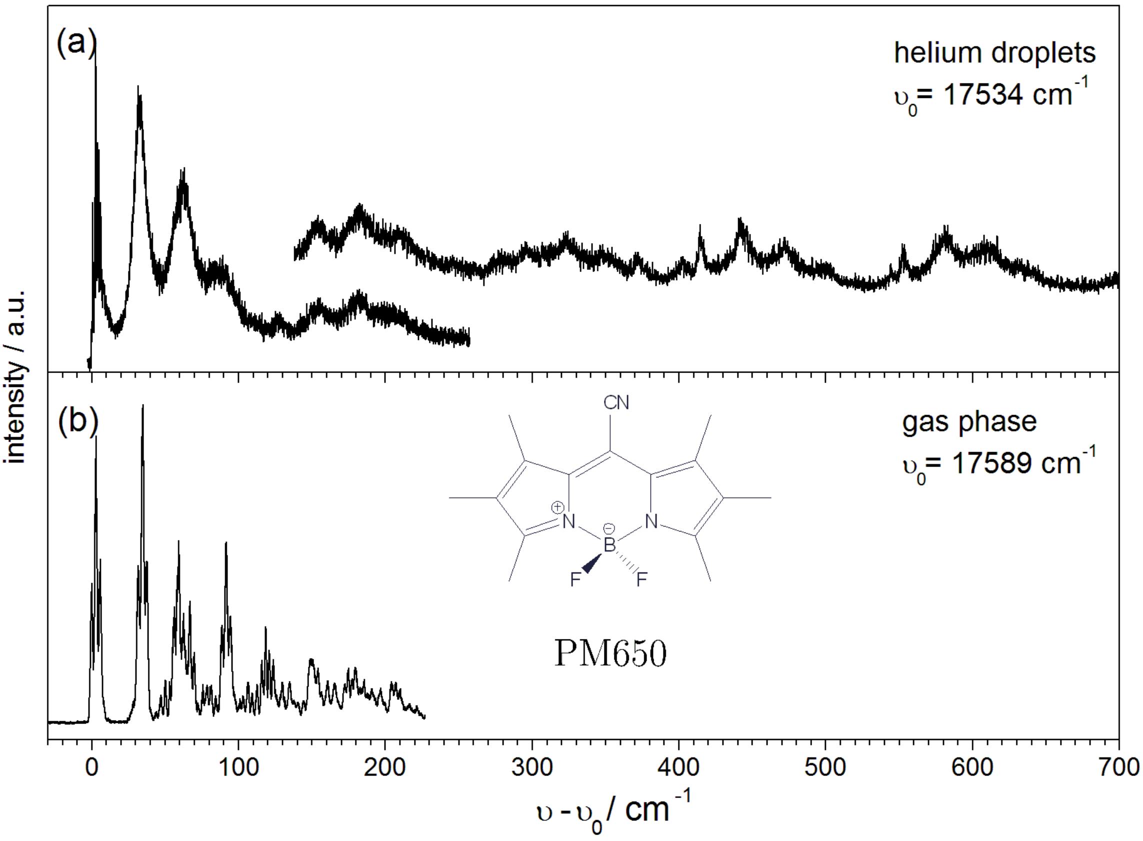

Fig. 7.22: Excitation spectra of PM650 in helium droplets (a) and in the supersonic jet (b) with ν_0 as indicated. The laser intensity was kept constant in the droplet experiment and was low enough to avoid saturation effects. The inset spectrum in (a) starting at 140 cm^{-1} is identical to the dotted spectrum in fig. 7.23 and was recorded with higher laser intensity causing saturation effects at the origin.

The excitation spectrum of PM650 recorded in helium droplets is presented in fig. 7.22 (a). No transitions were found to the red of the signal at $\nu_0 = 17534$ cm^{-1} therefore assigned to the electronic origin. This corresponds to a solvent shift of 55 cm^{-1} to the red compared to the gas phase. The shape of the spectrum is in qualitative agreement with the spectrum in the gas phase in fig. 7.22 (b) corroborating the assignment. However, only the electronic origin reveals sharp transitions in the droplet spectrum. All vibronic transitions appear with a larger line width than in the gas phase.

Multiple doping of the droplets as a reason for the broadening can be excluded since upon lowering the oven temperature the spectral shape is not altered. In contrast, significantly increasing the oven temperature further broadens the spectrum and extends it to the red of the origin.

Varying the laser intensity strongly affects the spectral shape of the excitation spectrum as shown in fig. 7.23.

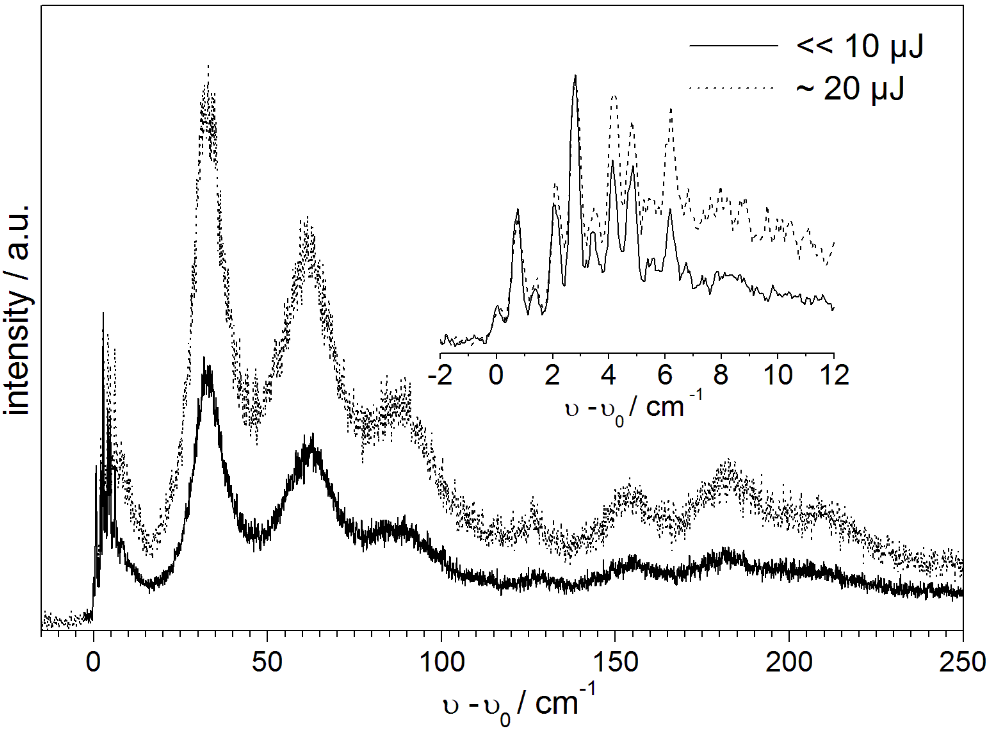

Fig. 7.23: Excitation spectra of PM650 in helium droplets recorded with different laser intensities as indicated. ν_0= 17534 cm^{-1} .

The two spectra recorded with different laser intensities are both normalized to the peak intensity at the electronic origin. At laser intensities lower than for the solid line spectrum the intensity decreases while the spectral shape remains constant. The part of the excitation spectrum at the electronic origin shown in the inset was also recorded upon excitation with an attenuated cw dye laser. It confirmed the relative intensities and did not increase the spectral resolution.

The spectral region around the electronic origin shown in the inset of fig. 7.23 exhibits sharp features on top of a broad background. The relative signal contribution of the broad feature cannot be reduced below of what is shown in the solid line spectrum. It presumably arises from spectral overlap of the sharp transitions and of PWs. The relative intensity of the broad background and of single sharp transitions increases with the laser intensity. (dotted line)

Upon increasing the laser intensity beyond that used for the solid line spectrum also the vibrational satellites gain relative intensity compared to the electronic origin as can be seen in the main spectrum of fig. 7.23. The different saturation behavior can arise from different absorption cross sections and different life times of the corresponding excited states. (cf. chapter 4) The solid line spectrum reflects the different absorption cross sections (weighted by the probability for relaxation into the emissive state). The intensity

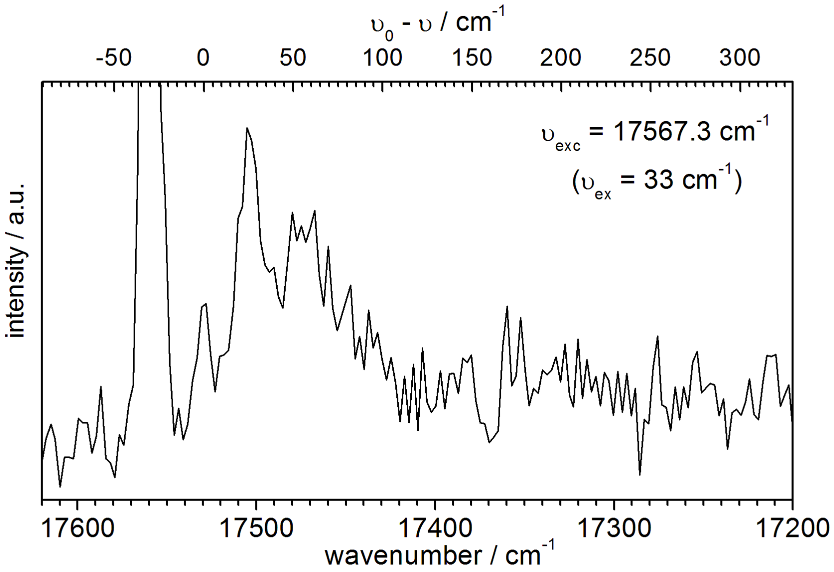

Fig. 7.24: Emission spectrum of PM650 in helium droplets recorded upon excitation at ν_{exc} =17567.3 cm^{-1} (excess energy ν_{ex} = 33 cm^{-1}). ν_0 = 17529 cm^{-1} . The intense signal at 17561 cm^{-1} ($\nu - \nu_0$ = -32 cm^{-1}) is identified as stray light from the excitation laser. The distance between two pixel columns amounts to about 2.5 cm^{-1} .

ratio (peak intensities) of the sharp transition at 2.8 cm^{-1} and the first broad transition at 32.8 cm^{-1} amounts to 1:0.8 in the solid line spectrum indicative of similar absorption cross sections. This ratio decreases by a factor of two in the dotted spectrum which is consequently attributed mainly to different life times of the corresponding excited states.

7.5.2 Emission Spectrum of PM650

The dispersed emission spectrum of PM650 recorded in helium droplets upon excitation at the first broad band beyond the electronic origin (ν_{exc} = 17567.3 cm^{-1}) with the cw dye laser is shown in fig. 7.24. The electronic origin can be identified at ν_0 = 17529 cm^{-1} in agreement with the electronic origin in the excitation spectrum (ν_0 =17534 cm^{-1}) within the experimental accuracy. The emission spectrum was found to be independent of the excitation frequency and indicates the progression of a low-frequency mode with spacings of about 27 cm^{-1} similar as in the excitation spectrum and in agreement with emission spectra recorded in the supersonic jet. The spectral resolution and S/N ratio did not allow for resolving a possible fine structure at the electronic origin as observed in the excitation spectrum. The vibrational satellites appear slightly broader than the electronic origin though the S/N ratio does not allow for a detailed analysis of the line shape.

7.5.3 Discussion

The excitation spectra of PM650 in helium droplets reveal sharp transitions at the electronic origin and broadened vibrational satellites.
Fig. 7.25 shows a comparison of the fine structure at the electronic origin observed in the excitation spectra recorded in helium droplets (a) and in the gas phase (b).

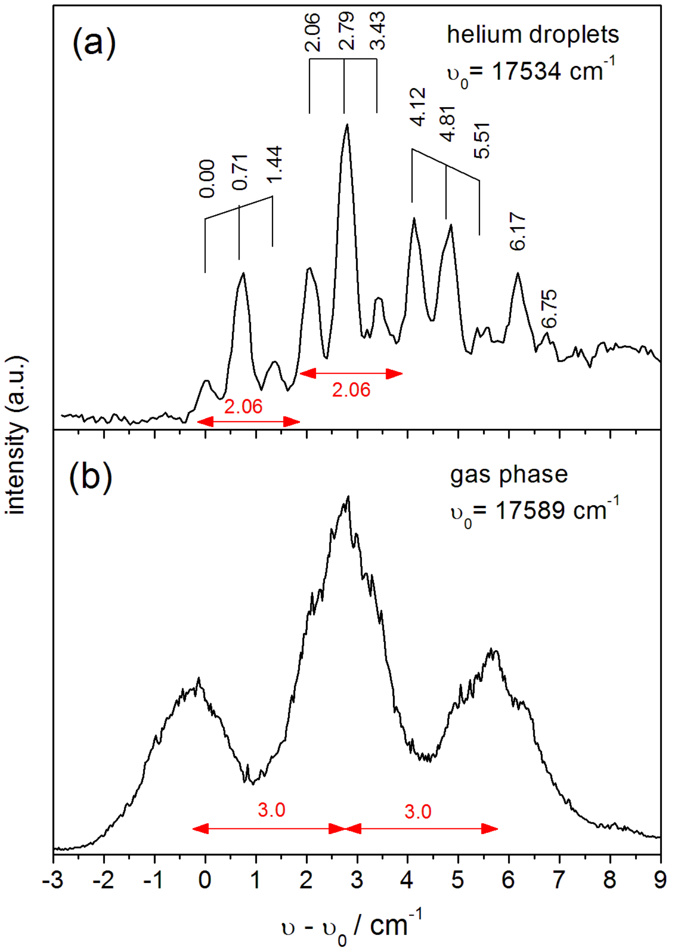

Fig. 7.25: Excitation spectrum of PM650 at the electronic origin in helium droplets (a) and in the supersonic jet (b) with ν_0 as indicated. The gas phase spectrum was shifted to obtain a frequency match of the most intense transitions in (a) and (b).

The sharp transitions in helium droplets are extended over the spectral region of the three transitions of the triplet structure in the gas phase spectrum. The three contributions in the gas phase spectra were shown to originate from three different ground states. [SF09] Thus, the droplet spectrum may indicate that in the case of PM650 also the droplet spectrum consists of sharp transitions originating from the corresponding different ground states. This is in contrast to the observations at the electronic origin in the excitation spectrum of PM567 in helium droplets. (cf. chapter 7.4) In the spectrum of PM567 only one of the three transitions of the triplet observed in the gas phase spectrum yields sharp signals also in the droplet spectrum. The line width of the distinct transitions in the droplet spectrum of PM650 at the electronic origin is significantly smaller as compared to the gas phase.

In analogy to the spectra of PM567 the transitions may be gathered into groups of three as indicated in fig. 7.25 (a). A similar splitting may be indicated in the gas phase spectrum in particular at the second and third transition separated from the first by 3.0 and 6.0 cm^{-1} , respectively, though could not be fully resolved. The spacing between two subsequent transitions within a triplet structure in the droplet spectrum amounts to 0.7 cm^{-1} on average. (fig. 7.25(a)) The spacing between these triplets amounts to 2.05 cm^{-1} on average and might correspond to the splitting of 3.0 cm^{-1} found in the gas phase. (cf. fig. 7.25)

However, the intensity pattern within the second and third triplet centered at 2.79 cm^{-1} and 4.81 cm^{-1} , respectively, are different to the pattern in the first triplet centered at 0.71 cm^{-1} . (fig. 7.25(a)) In particular, the first transitions of these triplets at 2.06 cm^{-1} and 4.12 cm^{-1} , respectively, are of higher relative intensities. Further, a significant sharp transition is observed at 6.17 cm^{-1} . Each of the transitions at 2.06 cm^{-1} , 4.12 cm^{-1} , and 6.17 cm^{-1} are separated from the center peak of the preceding triplet at 0.71 cm^{-1} , 2.79 cm^{-1} and 4.81 cm^{-1} , respectively, by 1.33 ± 0.03 cm^{-1} . Thus, the larger relative intensities at 2.06 cm^{-1} and 4.12 cm^{-1} may be due to distinct features of the PW of the preceding triplet overlapping with the first signals of the triplets centered at 2.79 cm^{-1} and 4.81 cm^{-1} , respectively. Accordingly, the signal at 6.17 cm^{-1} may be a distinct feature of the PW of the transition at 4.81 cm^{-1} .

This interpretation is in agreement with the observed saturation behavior presented in fig. 7.23. In particular from the inset in fig. 7.23 it becomes apparent that transitions at 2.06 cm^{-1} and 4.12 cm^{-1} saturate only at higher laser intensities than transitions at 2.79 cm^{-1} and 4.81 cm^{-1} , respectively. Further, the relative intensity of the transition at 6.17 cm^{-1} compared to that at 4.81 cm^{-1} increases with increasing laser intensity. However, it should be noted that the transition at 6.17 cm^{-1} fits in a series from 0.00 cm^{-1} to 2.05 cm^{-1} to 4.12 cm^{-1} .

Pump-probe experiments could help to unravel the fine structure at the electronic origin by providing evidence which transitions originate from the same ground state. However, spectral overlap (of ZPLs and PWs) makes these experiments difficult.

The spectral overlap together with PWs cause the broad background below the sharp transitions at the electronic origin. In contrast, only broad signals could be observed at the vibrational satellites. Due to the broadening in the droplet spectrum and spectral overlap of transitions in the gas phase spectrum the broadening can be analyzed separately only for the second member of the progression. The corresponding broad band in the helium droplet spectrum peaks at a lower frequency of 32.8 cm^{-1} as compared to the

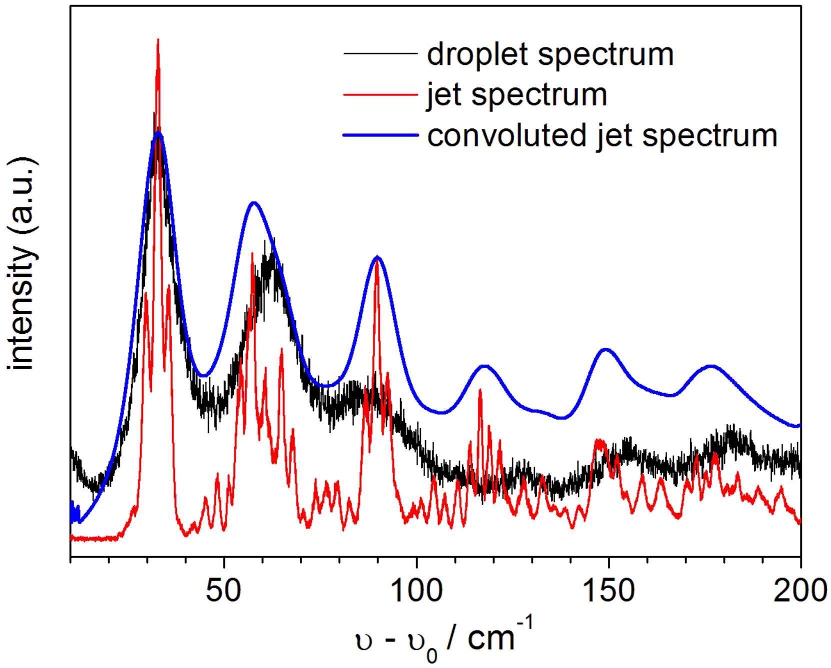

Fig. 7.26: Convolution (blue) of the excitation spectra of PM650 in the supersonic jet (red) with a Lorentzian with a full width of 10 cm^{-1} . The experimental droplet spectrum (black) is shown for comparison. $\nu_0 = 17534$ in the droplet spectrum, and 17587 cm^{-1} in the supersonic jet spectrum.

peak intensity at 34.8 cm^{-1} in the gas phase spectrum. Thus, the vibrational frequency of the progressive mode slightly decreases upon solvation in helium droplets similar as indicated in the spectra of PM546 (cf. chapter 7.3) and PM567 (cf. chapter 7.4).

Fig. 7.26 shows a convolution of the gas phase spectrum (for $\nu - \nu_0 > 12$ cm^{-1}) with a Lorentzian with a line width of 10 cm^{-1} to account for the rather symmetric broadening. The gas phase spectrum was shifted by 2 cm^{-1} to the red compared to fig. 7.22(b) to obtain a match in the peak position of the first band at 32.8 cm^{-1} . The deviation between the simulated spectrum and the droplet spectrum for $\nu - \nu_0 \lesssim 20$ cm^{-1} is due to the contribution of the electronic origin to the droplet spectrum. The peak positions and relative intensities of the following broad bands of the simulated spectrum (blue) and the experimental droplet spectrum (black) are not in agreement. This can be attributed to different vibrational frequencies in the excited state and different fluorescence quantum yields upon excitation at the distinct transitions in helium droplets and in the gas phase. In particular, lower relative fluorescence induced upon excitation at transitions involving the 56 cm^{-1} mode in helium droplets compared to the gas phase would shift the peak intensity of the second broad band of the simulation in fig. 7.26 from 57.7 cm^{-1} to a higher energy. Further, this would decrease the relative intensities of this and the

following two bands centered at 89.5 cm^{-1} and 117.5 cm^{-1} .
In analogy to the discussion of the broadening of the vibrational satellite structure in the droplet spectrum of PM567 (chapter 7.4), the broadening can presumably be attributed to a fast dissipation of vibrational excess energy. Assuming that the droplet spectrum is a superposition of the spectra of the three different ground states as in the gas phase spectrum, the broadening causes a homogeneous line width of 10 cm^{-1} corresponding to a decay time of about 0.5 ps.

To conclude, the excitation spectrum of PM650 in helium droplets exhibit sharp transitions at the electronic origin while all vibrational satellites appear broadened. The fine structure at the electronic origin indicates the transitions to originate from more than one ground state as found in the supersonic jet. An analysis of the vibrational satellites indicated a homogeneous broadening by about 10 cm^{-1} attributed to the dissipation of vibrational excess energy with a time constant of about 0.5 ps.

7.6 Comparative Discussion

The transitions of all of the investigated PM dyes were found to be easily saturated and laser intensities lower than 10 μJ had to be used to avoid saturation effects. This saturation behavior is in agreement with the typical high extinction coefficients of PM dyes. [STS$^+$90, LABnPMM$^+$04, UZH08, SHWJ09] For example, the extinction coefficients are almost one order of magnitude larger than for anthracene. [KM95] Even without saturating the molecular transitions PW-structures could be identified in the spectra of most of the molecules. However, due to a broadening of the vibrational satellites and overlap of transitions the PWs were not spectrally separated from other transitions in the spectra of the substituted PM dyes 8-PhPM, PM546, PM567, and PM650 and thus could not be analyzed independently.

According to the configuration coordinate model discussed in chapter 4 part of the PWs are due to different non-superfluid helium solvation layers around the embedded molecule in the electronic ground and excited state. A reorganisation of the solvation layer is induced by a variation of the electron density upon electronic excitation. Different electron densities in the electronic ground and excited state are often reflected by changes of the dipole moments upon electronic excitation. The dipole moment in the ground state of the PM dyes is oriented along the short molecular axis of the chromophore with its negative end at the BF_2 group and is typically in the order of 5 D. [BMH$^+$02, BnPLAMM$^+$04b, BnPLAMM$^+$04a, LABnM$^+$05, KKY$^+$05, UZH08] Upon excitation it is reduced by about 10 % as was found in solvatochromic studies and quantum chemical calculations. [BMH$^+$02, ABC03, BnPLAMM$^+$04b, BnPLAMM$^+$04a, LABnM$^+$05, KKY$^+$05] Only in the case of PM650 quantum chemical calculations predict dipole moments in the ground state below 1 D increasing upon electronic excitation to about 1.3 D. [LABnPMM$^+$04] This is in agreement with the observed solvatochromic shifts and was attributed to the electron withdrawing property of the cyano-group. [LABnPMM$^+$04]

The transition dipole moment of the chromophore was found to be oriented along its long molecular axis and thus perpendicular to the electric dipole moment. [BMH$^+$02, LABnM$^+$05, KKY$^+$05] Electronic excitation induces symmetric changes of the electron density at the atoms of the chromophore with respect to the short molecular axis thus maintaining the orientation of the dipole moment. [BMH$^+$02, ABC03, KKY$^+$05] This may indicate that in case of the PM dyes the change of the dipole moment is not a proper measure for the changes of the electron density induced upon electronic excitation causing the electron-phonon coupling.

Broadening of the Vibrational Satellite Structure

A common feature of the electronic spectra of the substituted PM dyes is the broadening of the vibrational satellite structure.

The excitation spectra of the PM dyes PM546, PM567, and PM650 containing alkyl substituents reveal a rather harmonic progression of a low-frequency mode of about 30 cm^{-1} in the gas phase. [SF09] Quantum chemical calculations exclude an assignment of this mode to a torsional mode of single methyl groups. [SF09] All of these molecules contain four methyl groups at the same positions 1, 3, 5, and 7 of the chromophore. Thus, it is indicated that the corresponding normal coordinate of the 30 cm^{-1} mode depends on the nuclear coordinates, reflected by torsional and bending angles, of these four methyl groups, which are not independent from each other. The transitions of the progressions exhibit a splitting into two (PM546) or three (PM567, PM650) transitions separated by 3 cm^{-1} (PM546, PM650) or 6 cm^{-1} (PM567), respectively. These splittings may be attributed e.g. to different conformers or tunneling splittings. Unfortunately, this was not addressed in the quantum chemical calculations in ref.s [BMH$^+$02, ABC03, BnPLAMM$^+$04b, BnPLAMM$^+$04a, LABnM$^+$05, KKY$^+$05, SF09].

The relative intensity of the electronic origin compared to the other members of the progression increases in the row PM546, PM567, and PM650 while at the same time the progression of the 30 cm^{-1} mode becomes shorter. Both is indicative of a less significant nuclear rearrangement induced upon electronic excitation. In the case of PM546 no sharp transitions were observed in the helium droplet spectra. However, the relative intensity of the electronic origin in the excitation spectrum of PM546 in the gas phase is only in the order of 1 % compared to the peak intensity. For a similar relative intensity in the droplet spectrum the electronic origin would eventually be hidden below the noise and thus it is not clear if it remains sharp or is broadened. In the spectra of PM567 and PM650 the electronic origin carries about 20 % (PM567) and 90 % (PM650), respectively, of the relative intensity in the gas phase spectrum and remains sharp in the droplet spectrum. Fig. 7.27 shows excitation spectra of PM567 and PM650 at the electronic origin in helium droplets (black) and the supersonic jet (red). A comparison of the spectra indicates that in case of PM567 only one of the transitions of the triplet in the gas phase spectrum contributes to the sharp transitions observed in the droplet spectrum. Whereas, the droplet spectrum of PM650 indicates sharp transitions corresponding to all three transitions of the triplet in the gas phase spectrum. The line width at the electronic origin is smaller in the droplet spectra as compared to the corresponding gas phase spectra. The droplet spectra reveal a fine structure which is indicated, though not fully resolved, in the gas phase spectra. This fine structure may be due to

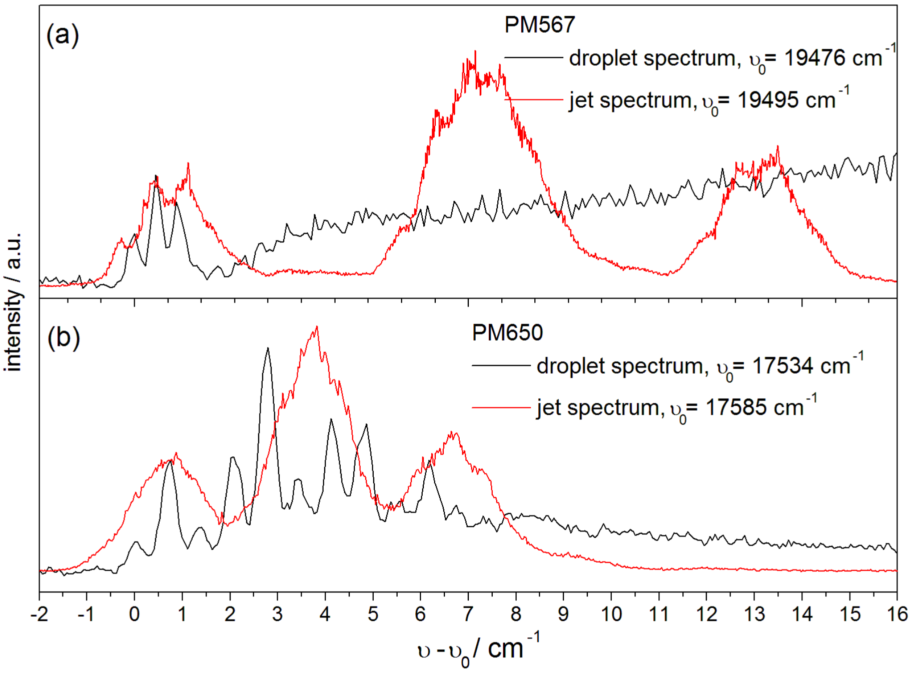

Fig. 7.27: Excitation spectra of PM567 (a) and PM650 (b) in helium droplets (black) and the supersonic jet (red) with ν_0 as indicated.

tunneling splittings in addition to an overlap of the rotational band contours of the two different isotopomers containing ^{11}B or ^{10}B, respectively. Further, solvation effects cannot be excluded in the droplet spectrum, though, are unlikely to cause the triplet structure in the droplet spectrum due to the similar structure indicated in the gas phase spectrum.

However, in the spectra of both, PM567 and PM650, sharp transitions are observed only at the electronic origin. The vibrational satellite structure appears broadened as for PM546. The broadening appears rather symmetric, which is indicative of a damping of the corresponding excited state. A broadening solely due to the dominance of PWs as observed e.g. for fluorazene (cf. chapter 6) was excluded since in this case sharp transitions would be expected to be observed also at the transitions.

The broadening is observed only in helium droplets and affects only the vibrational satellite structure. It may be due to an enhancement of isoenergetic non-radiative decay processes such as IC, IVR, or ISC, which are also affective in the gas phase or due to the dissipation of vibrational excess energy into the helium environment. The gentle interaction of the helium environment expressed in the solvents shifts of electronic and vibrational transitions indicates only minor variations of the energy spacings between electronic and vibrational levels. For the PM dyes ISC was reported to be negligible small in all media despite of large solvent shifts such as 10 nm. ($\approx$ 400 cm^{-1} at 500 nm) [BMH$^+$02, CGMG$^+$02, ABC03, BnPLAMM$^+$04a, LABnM$^+$05, KKY$^+$05, UZH08] Thus, the rate constants for isoenergetic intramolecular processes such as IC, IVR, and ISC are not expected to be altered by orders of magnitude and thus presumably do not cause the damping. In contrast, dissipation of vibrational excess energy, or vibrational relaxation, respectively, was found to be faster than the competing radiative decay for all fluorescing molecules yet investigated in helium droplets. [LS03, LS04b, LSK$^+$04, ST08] However, it is typically not faster than about 3 to 30 ps as determined from line shape analyses of excitation spectra of various molecules in helium droplets. (cf. chapters 4 and 5.9.1) The observed broadening thus presumably can be attributed to an enhanced dissipation of the vibrational excess energy. An enhanced damping is typically observed in electronic spectra of molecules where excitation induces a significant change of their equilibrium geometry. (cf. chapters 5.9.1 and 8)

Unfortunately, the broadened part of the droplet spectra could not be simulated satisfactorily by convoluting the corresponding gas phase spectra with a broadening function such as a Lorentzian. Among the possible reasons for the deviations are slightly different vibrational frequencies of the progressive mode in helium droplets as compared to the gas phase. This may be due to a different vibrating mass or a different shape of the corresponding potential. The latter would also affect the relative intensities of the members of the progression. The excitation spectra in the gas phase exhibit spectral overlap of many transitions and thus the progression is not spectrally separated from progressions coupled to other modes. Therefore, the influence of the progression cannot be analyzed separately. Further, the gas phase spectra contain hot bands which overlap with transitions originating from the vibrational ground state of S_0 and thus also cannot unequivocally be separated for the simulation. In addition, the gas phase spectrum was shown to be a superposition of the spectra originating from different ground states. [SF09] These spectra are not only shifted against each other by a constant wavenumber offset but display slightly different intensity and frequency patterns. As discussed above and shown in fig. 7.27 the influence of this splitting on the droplet spectra is not obvious. Further, any contribution of PW structures were neglected for the simulation. However, the discussion of the excitation spectra indicated that PWs appreciably affect the spectral shape of the broad excitation spectra.

A line broadening was also observed in the excitation spectrum of 8-PhPM in helium droplets. The excitation spectrum recorded in the gas phase revealed a progression of a low-frequency mode similar as for PM546, PM567 and PM650. In case of 8-PhPM this harmonic 60 cm^{-1} mode was assigned to the torsional mode. [SF09]

Similar as in the spectra of the alkylated PM dyes the electronic origin is the only sharp transition. However, only the vibrational satellites involving excitations of the torsional mode revealed a symmetric broadening, whereas other vibronic transitions displayed an asymmetric broad line shape typical for dominating PWs. The line widths of both, the symmetric and asymmetric broad bands, are about 25-30 cm^{-1} . This may indicate that the asymmetric broadening is not affective for transitions involving excitation of the torsional mode.

However, this is only speculative and would require a more detailed analysis. In particular, the excitation spectrum of isolated 8-PhPM in the gas phase, serving as reference for the droplet spectrum, is not yet understood. It contains an unexpected strongly anharmonic low-frequency mode similar as observed in the excitation spectrum of BDP in the gas phase. [SF09] This mode was found to be absent in the spectra of BDP in helium droplets which was attributed to damping of the corresponding excited states or a variation of the corresponding potential energy curves. (cf. chapter 7.1) In case of 8-PhPM the spectra in helium droplets appear broadened and do not allow for an unequivocal statement on the absence or presence of this mode. The corresponding mode is not observed in the gas phase spectra of the methyl substituted PM dyes PM546, PM567, and PM650.

Nevertheless, for PhPM in helium droplets only the electronic origin remains sharp while the vibrational satellites appear with a larger line width. The progression in the excitation spectra recorded in the gas phase as well as in helium droplets indicate a change of the equilibrium geometry induced upon electronic excitation as confirmed by quantum chemical calculations. [SF09] In analogy to the discussion of the broadening of the vibrational satellite structure in the excitation spectra of the alkylated PM dyes the broadening in the spectra of 8-PhPM is indicative of an enhanced dissipation of vibrational excess energy.

7.7 Summary

The electronic spectroscopy of the investigated PM dyes in helium droplets discussed in this chapter revealed significant differences compared to the supersonic jet. These are counterintuitive for what is expected for sub-Kelvin temperatures in a non-viscous cryogenic environment.

Only the parent compound BDP revealed the spectroscopic signature of a rigid molecule with sharp transitions in both excitation and emission spectra. Whereas, the spectra of the substituted compounds containing aryl or alkyl substituents appeared broadened. Though, the electronic origin remained sharp. The broadening was attributed to fast dissipation of vibrational excess energy.

However, many questions in the gas phase spectra are not yet unraveled. Thus, the PM dyes are not very well suited model compounds for the study of the interaction of the embedded species with the helium environment. In particular the study of broadening effects requires a detailed understanding of the corresponding sharp reference spectrum of the isolated molecule.

8 Conclusion

The electronic spectra of various organic molecules recorded in helium droplets were discussed in chapters 5 to 7 and revealed distinct differences compared to the corresponding gas phase spectra taken in a supersonic jet. These unexpected and counterintuitive features cannot be readily attributed to the significantly reduced temperature and reveal new details on the perturbation of electronic transitions of organic molecules embedded in helium droplets. In particular, a substantial line broadening in the spectra of a few molecules and the occurrence of a fine structure of electronic transitions, i.e. ZPLs accompanied by PWs, was observed. Both effects were discussed in chapters 5.9, 6.3, and 7.6. The following concluding remarks aim to provide a comprehensive picture of the influence of the helium environment on electronic transitions of organic molecules.

Line Broadening of Electronic Transitions

Single vibronic transitions appear broadened in the spectra of numerous organic molecules in helium droplets as reported in the literature and observed within this work. For example, a mode specific broadening was found for out of plane modes of pentacene (85, 207, and 304 cm^{-1}) resulting in line widths of about 7 cm^{-1} whereas an in plane mode with a comparable vibrational energy of 265 cm^{-1} exhibited a line width of only 0.2 cm^{-1} . [LS05] Similarly, the 206 cm^{-1} mode of 9,10-DCA appears broadened with a line width of 8 cm^{-1} (chapter 5.2) whereas other modes of similar vibrational energy such as the 217 cm^{-1} mode of 9-CNA (chapter 5.4) exhibit line widths < 1 cm^{-1} .

All vibronic transitions are broadened in the electronic spectra of the anthracene derivatives 2-MA and 9-PA (cf. chapter 5) and all substituted pyrromethene (PM) dyes (cf. chapter 7). For all of these molecules the electronic excitation was argued to induce a significant change of the equilibrium geometry with respect to the molecular coordinate of a low-frequency vibrational mode ($\nu_{vib} \leq 100$ cm^{-1}). This change of the equilibrium geometry can be rationalized using potential energy diagrams as is well-known from the discussion of Franck-Condon factors to explain the intensity pattern of vibronic transitions. [KM95] Three cases can be distinguished as illustrated in fig. 8.1 for the relative positions of the potential energy curves of the electronic ground and excited state with respect to a molecular coordinate.

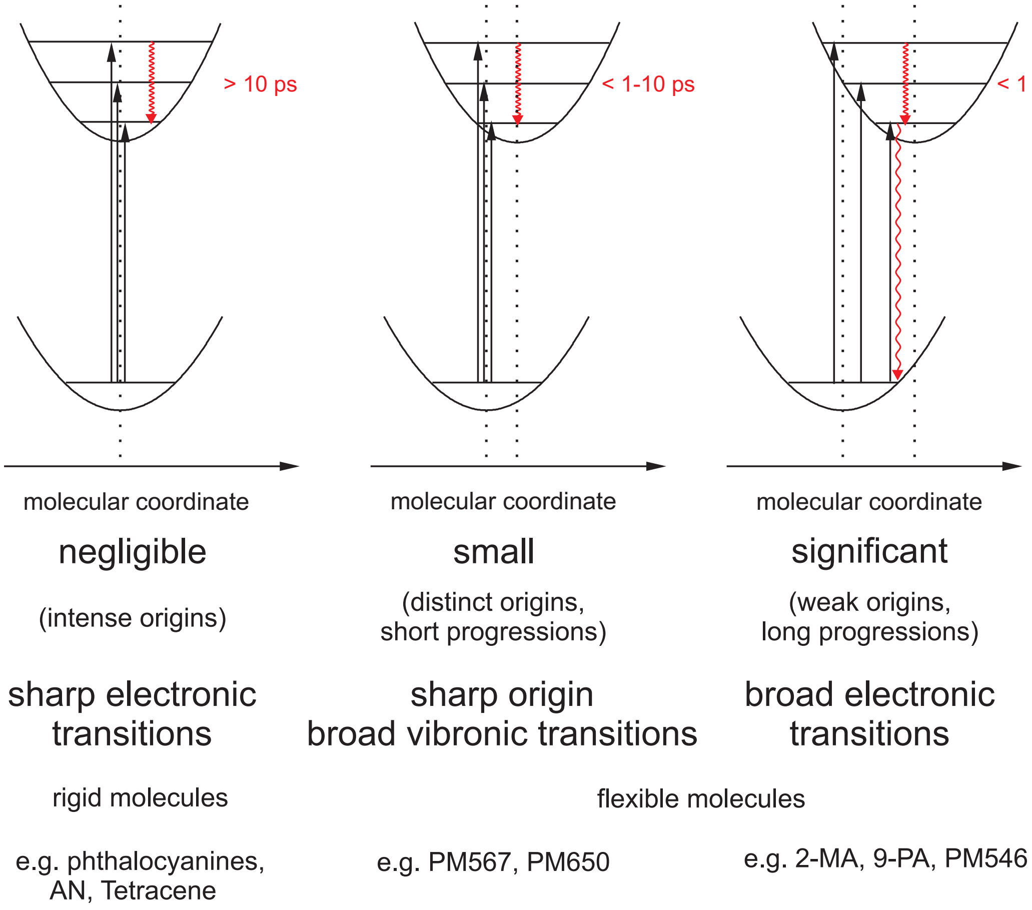

Fig. 8.1: Schematic representations of potential energy curves with respect to a molecular coordinate together with the effect on electronic spectra and examples. Note that the qualitative statements and numbers given can serve only as guidelines. (see text)

The relative positions of the potential energy curves are reflected in the electronic spectra of the corresponding molecules: A negligible displacement is typically reflected by intense origins dominating the spectra together with the missing of low-frequency progressions. On the contrary, a significant displacement leads to relatively weak origins and long progressions with higher peak intensities than at the origin. In the intermediate case of 'small' displacements the origin carries significant relative intensity and is accompanied by a short progression with peak intensities often similar as compared to the electronic origin. These experimental indications for the relative positions of the potential energy curves are usually in agreement with quantum chemical calculations.

In the first case of a negligible displacement of the potential energy curves sharp vibronic transitions with line widths typically smaller than in the corresponding gas phase spectra are observed in helium droplets. However, mode specific line broadening as mentioned above may occur. Typical rigid molecules such as phthalocyanine and polyaromatic hydrocarbons belong to this first type of molecules. In the intermediate case the electronic origin is observed as the only sharp transition in the droplet spectra while all vibronic transitions appear substantially broadened as compared to the corresponding gas phase spectra. This can be observed in the excitation spectra of 'flexible' molecules such as PM567 and PM650. In the last case with significant displacement only broad transitions are observed in the spectra of 'flexible' molecules such as 2-MA, 9-PA or PM546 in helium droplets. However, it should be noted that except in the case of 2-MA the relative intensity of the electronic origin in the gas phase spectra of these molecules is very small and thus sharp electronic origins in the droplet spectrum might be hidden below the noise.

The broadening appears rather symmetric, which is indicative of a damping of the corresponding excited state. The broadening is observed only in helium droplets but not in the spectra of isolated molecules in the gas phase. The damping may be due to an enhancement of non-radiative isoenergetic decay processes such as IC, IVR, or ISC which also occur in the gas phase, or the dissipation of energy into the helium environment. The gentle interaction of the helium environment reflected by solvent shifts of electronic and vibrational transitions indicates a negligible variation of the relative energies of electronic and vibrational levels. Thus, the rate constants for isoenergetic intramolecular processes such as IC, IVR, and ISC are not expected to be significantly altered by orders of magnitudes and thus presumably do not cause the damping. (cf. chapters 5.9.1 and 7.6)
On the other hand, dissipation of vibrational excess energy or vibrational relaxation, respectively, was found to be faster than the competing radiative decay in the order of a few ns for all organic molecules yet investigated in helium droplets. [LS03, LS04b, LSK$^+$04, ST08] However, for rigid molecules belonging to the first case in fig. 8.1 it is typically not faster than about 3 to 30 ps as determined from line shape analyses of the corresponding excitation spectra. (cf. chapters 4 and 5.9.1) Thus, a time constant for the dissipation typically longer than about 10 ps is indicated in fig. 8.1 (left scheme).
In the excitation spectra of 'flexible' molecules such as PM567 and PM650 belonging to the second type of molecules in fig. 8.1 the electronic origin in the droplet spectra exhibits a line width smaller than in the corresponding gas phase spectra. Further, it is comparable to the line width at the electronic origin in excitation spectra of rigid molecules (first type of molecules in fig. 8.1) recorded in helium droplets. In contrast, the vibronic transitions appear broader than in the corresponding gas phase spectra and in the spectra of rigid molecules inside helium droplets. According to the discussion above this damping of the vibrational satellites can presumably be attributed to an enhanced dissipation of purely vibrational excess energy corresponding to a time constant shorter than about 1 to 10 ps depending on the specific molecule. (fig. 8.1, middle scheme)
The damping process was found to be even faster corresponding to time constants below 1 ps for molecules belonging to the third type in fig. 8.1. Thus, the broadening indica-

tes an energy dissipation enhanced by nuclear rearrangements induced upon electronic excitation. In the case of 2-MA the damping process affects also the electronic origin indicating that not only the dissipation of vibrational excess energy but also of electronic energy, mediated via IC (or ISC), is enhanced.
The enhanced energy dissipation if geometrical changes are induced upon electronic excitation may indicate an enhanced coupling to the helium environment. In other words, the change of the geometry leads to a distortion of the helium environment and acts as the driving force for the enhanced energy dissipation.

Electron-Phonon-Coupling in Helium Droplets

Electronic transitions of organic molecules inside helium droplets may exhibit a fine structure that has no counterpart in the corresponding gas phase spectra. This fine structure consists of sharp ZPLs and accompanying PWs which can carry negligible small relative intensities but can also dominate the spectra. According to the configuration coordinate model (cf. chapters 4, 5.9.2 and 6.3) the occurrence of PWs is due to a displacement of potential energy curves of the electronic ground and excited state with respect to an environmental coordinate, i.e. the configuration of the non-superfluid helium solvation layer.
In fig. 8.2 three different cases of this model with different displacements of the potential energy curves of S_0 and S_1 are shown, which correspond to different electron-phonon coupling strengths.

In the first case the potentials are not shifted and thus the spectra are dominated by ZPLs while PWs are only minor contributions. This corresponds to weak electron-phonon coupling. In the intermediate case the potentials are slightly shifted and most of the intensity is in the ZPLs though the PWs also have appreciable intensities. In case of a large shift or strong electron-phonon coupling, respectively, weak ZPLs are accompanied by intense PWs.
In the excitation spectra of phthalocyanines recorded at low enough laser intensities almost no PW is observed. [HLTV02, LS04b] Thus, phthalocyanines are examples for weak electron-phonon coupling. [HLTV02] At higher intensities saturating the ZPL of the electronic origin the accompanying PW strongly gains relative intensity. [HLTV02, PRD$^+$09]
In contrast, for most of the molecules studied in helium droplets so far, the relative peak intensities of PWs with respect to the corresponding ZPLs in excitation spectra are in the range of $\approx$ 5 to 20 % (cf. chapter 5) corresponding to an intermediate electron-phonon coupling strength. (fig. 8.2) Similar values are also found in dispersed emission spectra reflecting the transition probabilities due to the underlying spontaneous radiative process.

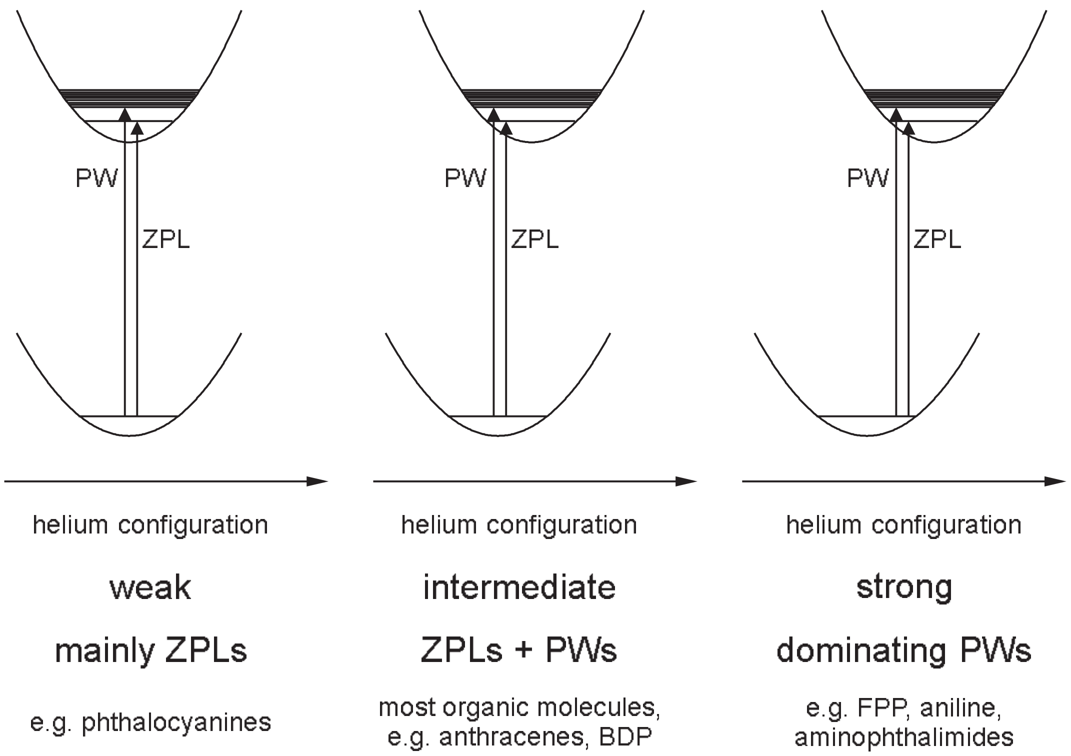

Fig. 8.2: Three different displacements of potential energy curves with respect to the helium configuration corresponding to weak, intermediate and strong electron-phonon coupling strengths. Also listed is the effect on electronic spectra and examples for the various cases.

The third case corresponds to strong electron-phonon coupling due to a large displacement of the potential energy curves with respect to the environmental coordinate. The intensity of the PWs can be even larger than that of the corresponding ZPLs which is found e.g. for FPP and aniline [LRD05, Log08]. (cf. chapter 6)

The displacements of the potential energy curves with respect to the helium configuration were argued to arise from a distinct change of the electron density induced upon electronic excitation. (cf. chapters 4, 5.9.2 and 6.3) The variation of the electron density thus corresponds to a perturbation of the helium environment driving its reorganisation.

Electronic Excitation of Molecules inside Helium Droplets

To conclude, electronic excitation of organic molecules inside helium droplets may be viewed as illustrated in fig. 8.3.

Therein, both the electronic ground and excited state are represented by a potential energy surface with respect to two different coordinates, an (intra-)molecular and an environmental coordinate. The latter describes the configuration of the non-superfluid helium solvation layer. Both coordinates are of higher dimension so that fig. 8.3 is a

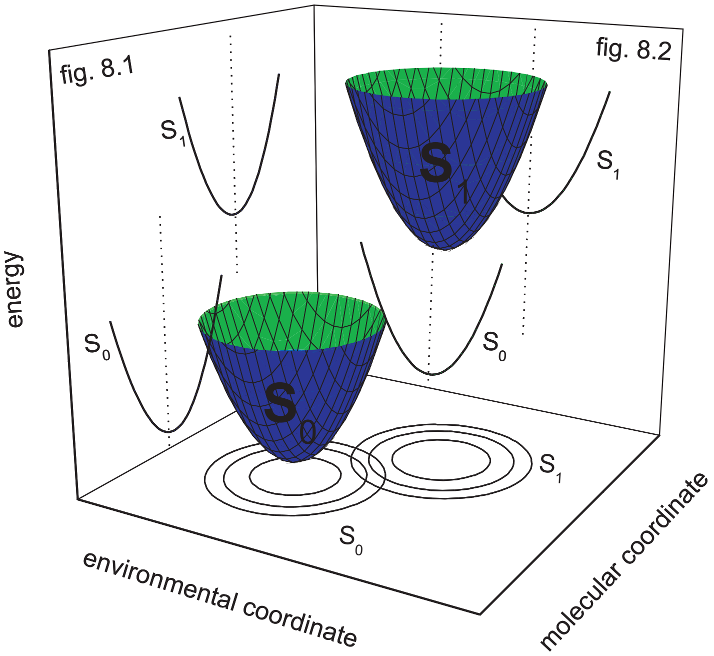

Fig. 8.3: Schematic potential energy surfaces of S_0 and S_1, respectively, with respect to an environmental coordinate (helium configuration) and a molecular coordinate. (see text)

simplified picture nevertheless illustrating the features obtained so far.

The potential energy curves in fig. 8.1 and fig. 8.2 are the projections of the potential energy surfaces in fig. 8.3 as indicated, which depend only on the molecular (fig. 8.1) or environmental (fig. 8.2) coordinate, respectively.

The discussions above thus indicate that a significant displacement of the potential energy surfaces of S_0 and S_1 shown in fig. 8.3 with respect to a molecular or environmental coordinate corresponds to a large perturbation of the helium environment. The displacements are caused by changes of the electron density inherently induced upon electronic excitation. The variation of the electron density may lead to a change of the geometry of the molecule, a reorganisation of the helium environment, or both. (fig. 8.3) In case the variation of the geometry dominates the perturbation of the helium environment an enhanced damping of the excited state reflected in a broadening of ZPLs in electronic spectra is induced. A 'significant' variation of the non-superfluid solvation layer is reflected by the occurrence or even dominance of PWs in electronic spectra.

Thus, large displacements of the potential energy surfaces in fig. 8.3 by any means are reflected by perturbations of electronic transitions.

9 Summary

Within this work the Even-Lavie valve was successfully employed as a new pulsed helium droplet source and was used for the electronic spectroscopy of various organic molecules. The detailed characterization of the pulsed helium droplet beam revealed a significantly different dependence of the droplet size on the stagnation conditions as compared to the common continuous helium droplet beams. The stagnation conditions were found to vary mainly the relative abundance of very large droplets and a leading fraction of smaller droplets. Laser induced fluorescence (LIF) from molecules inside helium droplets could only be observed from the smaller droplets. Their size could be varied in the range from more than 10^4 to less than 10^6 helium atoms per droplet. This range is rather small as compared to the size tunability observed in continuous droplet beams ranging from below 10^3 to more than 10^7 helium atoms per droplet. [TV04] However, the droplet size generated by the Even-Lavie valve is well-suited for electronic spectroscopy. Further, for repetition rates up to 500 Hz, the density of the droplets within the time interrogated by pulsed lasers was found to be about 20 times higher than in the continuous droplet beam. Thus, the Even-Lavie valve is a very well-suited helium droplet source for electronic spectroscopy with pulsed lasers and was used throughout this work.

The electronic spectra of a series of organic molecules doped into the pulsed helium droplet beam were recorded and compared to the corresponding spectra of the isolated molecules in a supersonic jet. Thereby, significant differences which could not be reduced to the lower temperature in the helium droplets, and which are consequently attributed to the interaction between the helium environment and the embedded molecules, could be observed. The perturbations of the electronic transitions are reflected by substantial line broadening, the occurrence of a fine structure of electronic transitions (zero phonon lines (ZPLs) accompanied by phonon wings (PWs)), and in rare cases a multiplet splitting of ZPLs. In particular, a systematic broadening of vibronic transitions was found in the spectra of flexible molecules if the electronic excitation induces a significant nuclear rearrangement. This broadening was attributed to a fast damping of the corresponding excited states with decay times below 1 ps.

The PWs in the sharp spectra of most of the investigated molecules included sharp features and contributed to less than about 20 % to the spectra corresponding to an intermediate electron-phonon coupling strength. However, broad asymmetric PWs ex-

tending over more than 50 cm^{-1} dominating the electronic spectra could also be observed. The different PW structures could qualitatively be explained by variations of the non-superfluid solvation layer induced upon electronic excitation.
Thus, the electronic spectroscopy of the investigated molecules revealed two broadening mechanisms, namely the broadening of ZPLs due to damping of the corresponding excited states and the dominance of broad PWs over sharp ZPLs. In both cases the broadening was attributed to a significant perturbation of the helium environment induced upon electronic excitation. Unfortunately, this limits the applicability of helium droplets as a host system for high resolution electronic spectroscopy. However, in particular the fast damping of excited states is expected to influence also the dynamics of intra- and intermolecular processes such as isomerization or proton transfer reactions. For the latter process line broadening has been observed already. [LPV$^+$09] Future experiments may profit from the fast damping.

To conclude, the electronic spectroscopy of the investigated molecules contributes to the understanding of the interaction between the helium environment and the embedded molecules. Future experiments, in particular the study of dynamic processes, are mandatory for a full understanding of this interaction. For example, pump-probe experiments with pulsed lasers, promoted by the new pulsed helium droplet source, enable to study dynamic processes in the time domain. A combination of the complementary LIF and depletion methods would gain insight into decay channels and processes induced upon excitation.

References

[ABC03] P. Acebal, S. Blaya, and L. Carretero. Ab initio study of absorption and emission spectra of pm567. *Chem. Phys. Lett.*, 374:206–214, 2003.

[AEJ80a] A. Amirav, U. Even, and J. Jortner. Cooling of large and heavy molecules in seeded supersonic beams. *Chem. Phys.*, 51:31–42, 1980.

[AEJ80b] A. Amirav, U. Even, and Joshua Jortner. Butterfly motion of the isolated pentacene molecule in its first-excited singlet state. *Chem. Phys. Lett.*, 72(1):21–24, 1980.

[AEJ82] Aviv Amirav, Uzi Even, and Joshua Jortner. Analytical Applications of Supersonic Jet Spectroscopy. *Anal. Chem.*, 54:1666–1673, 1982.

[AHJ88] Aviv Amirav, Chanan Horwitz, and Joshua Jortner. Optical selection studies of electronic relaxation from the S_1 state of jet-cooled anthracene derivatives. *J. Chem. Phys.*, 88:3092–3110, 1988.

[AJ83] Aviv Amirav and Joshua Jortner. Laser-free absorption and fluorescence spectroscopy of large molecules in planar supersonic expansions. *Chem. Phys. Lett.*, 94:545–548, 1983.

[AJOL86] Aviv Amirav, Joshua Jortner, S. Okajima, and E. C. Lim. Manifestation of intramolecular vibrational energy redistribution on electronic relaxation in large molecules. *Chem. Phys. Lett.*, 126(6):487–494, 1986.

[AJTL87] Aviv Amirav, Joshua Jortner, M. Terazima, and B.C. Lim. Rotational effects on intramolecular radiationless transitions in a large molecule. *Chem. Phys. Lett.*, 133(2):179–184, 1987.

[Ami87] Aviv Amirav. Rotational effects on energy resolved emission of anthracene. *J. Chem. Phys.*, 86:4706–4707, 1987.

[Ami88] Aviv Amirav. Rotational and vibrational energy effect on energy-resolved emission of anthracene and 9-cyanoanthracene. *Chem. Phys.*, 124(2):163–175, 1988.

[Api] *Apiezon N - Cryogenic High Vacuum grease.*

[ASJ84] Aviv Amirav, Mark Sonnenschein, and Joshua Jortner. Spectroscopy and Dynamics of 9,10-Dichloroanthracene$\cdot$Ar$_n$ van der Waals complexes. *Chem. Phys.*, 88:199–207, 1984.

[BBC$^+$05] Adrian Boatwright, Nicholas A. Besley, Sharon Curtis, Rossana R. Wright, and Anthony J. Stace. A systematic shift in the electronic spectra of substituted benzene molecules trapped in helium nanodroplets. *J. Chem. Phys.*, 123(2):021102–1–3, 2005.

[BHBEJ92] Narda Ben-Horin, Dar Barhatt, Uzi Even, and Joshua Jortner. Spectroscopic Interrogation of heterocluster isomerization. II. Spectroscopy of (9,10-dichloroanthracene)$\cdot$(rare gas)$_n$ heteroclusters. *Chem. Phys.*, 97:6011–6031, 1992.

[BHR02] Leonid Belau, Yehuda Haas, and Wolfgang Rettig. Jet cooled spectra of pyrrolobenzene and of pyrrolobenzonitrile: the nature of the excited states. *Chem. Phys. Lett.*, 364:157–163, 2002.

[BHR04] Leonid Belau, Yehuda Haas, and Wolfgang Rettig. Dual Emission of 4-(1H-Pyrrol-1-yl)benzonitrile Clusters with Acetonitrile in a Supersonic Jet and Its Absence in Phenylpyrrole Clusters. *J. Phys. Chem. A*, 108:3916–3925, 2004.

[BHT93] Jaap H. M. Beijersbergen, Qin Hui, and Michio Takami. Spectroscopy and dynamics of trapped alkaline earth atoms in superfluid helium. *Phys. Lett. A*, 181:393–403, 1993.

[BKN$^+$90] H. Buchenau, E. L. Knuth, J. Northby, J. P. Toennies, and C. Winkler. Mass spectra and time-of-flight distributions of helium cluster beams. *J. Chem. Phys.*, 92:6875–6889, 1990.

[BMB$^+$93] A. J. Bell, J. M. Mestdagh, J. Berlande, Biquard X., J. Cuvellier, A. Lallement, P. Meynadier, O. Sublemontier, and J.-P. Visticot. Mean cluster size by Rayleigh scattering. *J. Phys. D: Appl. Phys.*, 26:994–996, 1993.

[BMH$^+$02] F. Bergström, I. Mikhalyov, P. Hägglöf, R. Wortmann, T. Ny, and L. B.-A. Johansson. Dimers of dipyrrometheneboron difluoride (bodipy) with light spectroscopic applications in chemistry and biology. *J. Am. Chem. Soc.*, 124(2):196–204, 2002.

[BML08] Özgür Birer, Paolo Moreschini, and Kevin K. Lehmann. Electronic spectroscopy of benzo[g,h,i]perylene and corone inside helium nanodroplets. *Phys. Chem. Chem. Phys.*, 10:1648–1657, 2008.

[BMLS07] Özgür Birer, Paolo Moreschini, Kevin K. Lehmann, and Giacinto Scoles. Electronic Spectroscopy of Nonalternant Hydrocarbons Inside Helium Nanodroplets. *J. Phys. Chem. A*, 111:12200–12209, 2007.

[BMS$^+$09] Masaaki Baba, Koichi Mori, Motohisa Saito, Yasuyuki Kowaka, Yuki Noma, Shunji Kasahara, Takaya Yamanaka, Katsuhiko Okuyama, Takayoshi Ishimoto, and Umpei Nagashima. CH_3 Internal Rotation in the S_0 and S_1 States of 9-Methylanthracene. *J. Phys. Chem. A*, 113:2366–2371, 2009.

[BMSK96] Giel Berden, W. Leo Meerts, Michael Schmitt, and Karl Kleinermanns. High resolution UV spectroscopy of phenol and the hydrogen bonded phenol-water cluster. *J. Chem. Phys.*, 104:972–982, 1996.

[BnPLAMM$^+$04a] J. Bañuelos Prieto, F. López Arbeloa, V. Martínez Martínez, T. Arbeloa López, F. Amat-Guerri, M. Liras, and I. López Arbeloa. Photophysical properties of a new 8-phenyl analogue of the laser dye PM567 in different solvents: internal conversion mechanisms. *Chem. Phys. Lett.*, 385(1-2):29–35, 2004.

[BnPLAMM$^+$04b] Jorge Bañuelos Prieto, Fernando López Arbeloa, Virginia Martínez Martínez, Teresa Arbeloa López, and Iñigo López Arbeloa. Structural and spectroscopic characteristics of Pyrromethene 567 laser dye. A theoretical approach. *Phys. Chem. Chem. Phys.*, 6:4247–4253, 2004.

[BS90] D. M. Brink and S. Stringari. Density of states and evaporation rate of helium clusters. *Z. Phys. D.*, 15:257–263, 1990.

[Cam84] R. Campargue. Progress in Overexpanded Supersonic Jets and Skimmed Molecular Beams in Free-Jet Zones of Silence. *J. Phys. Chem.*, 88:4466–4474, 1984.

[CDF$^+$06] M. Y. Choi, G. E. Douberly, T. M. Falconer, W. K. Lewis, C. M. Lindsay, J. M. Merritt, P. L. Stiles, and R. E. Miller. Infrared spectroscopy of helium nanodroplets: novel methods for physics and chemistry. *Int. Rev. Phys. Chem.*, 25:15–75, 2006.

[CG82] Thomas P. Carter and G. D. Gillispie. Site-Selected Fluorescence Study of Anthracene and Its Halogenated Derivatives in Shpol'skii Matrices. *J. Phys. Chem.*, 86:2691–2695, 1982.

[CGMG+02] A. Costela, I. García-Moreno, C. Gomez, R. Sastre, F. Amat-Guerri, M. Liras, Fernando López Arbeloa, Jorge Bañuelos Prieto, and Iñigo López Arbeloa. Photophysical and Lasing Properties of New Analogs of the Boron-Dipyrromethene Laser Dye PM567 in Liquid Solution. *J. Phys. Chem. A*, 106:7736–7742, 2002.

[Cha07] Sayan Chakraborti. Verification of the Rayleigh scattering cross section. *Ann. J. Phys.*, 75:824–826, 2007.

[CLSS01] Carlo Callegari, Kevin K. Lehmann, Roman Schmied, and Giacinto Scoles. Helium nanodroplet isolation rovibrational spectroscopy: Methods and recent results. *J. Chem. Phys.*, 115:10090–10110, 2001.

[CT90] C. Crépin and A. Tramer. Rare-gas matrix as an infinte rare-gas cluster: a spectroscopic study of 9,10-dichloroanthracene in argon matrices. *Chem. Phys. Lett.*, 170:446–450, 1990.

[CZH06] Semyon Cogan, Shmuel Zilberg, and Yehuda Haas. The Electronic Origin of Dual Fluorescence in Donor-Acceptor Substituted Benzene Derivatives. *J. Am. Chem. Soc.*, 128:3335–3345, 2006.

[Dem08] Wolfgang Demtröder. *Laser Spectroscopy.* Springer, 2008.

[DH81] Bernhard Dick and Georg Hohlneicher. Two-Photon Spectroscopy of Dipole-Forbidden Transitions. The low-lying Singlet States of Anthracene. *Chem. Phys. Lett.*, 83:615–621, 1981.

[Dic] Bernhard Dick. Vorlesung Laserspektroskopie, Regensburg 2005.

[DKS+08] Sergey I. Druzhinin, Sergey A. Kovalenko, Tamara A. Senyushkina, Attila Demeter, Reinhard Machinek, Mathias Noltemeyer, and Klaas A. Zacchariasse. Intramolecular Charge Transfer with the Planarized 4-Cyanofluorazene and its Flexible Counterpart 4-Cyano-N-Phenylpyrrole. Picosecond Fluorescence Decays and Femtosecond Excited State Absorption. *J. Phys. Chem. A.*, 112:8238–5253, 2008.

[DS01] Bernhard Dick and Alkwin Slenczka. Inhomogeneous line shape theory of electronic transitions for molecules embedded in superfluid helium droplets. *J. Chem. Phys.*, 115:10206–10213, 2001.

[EAHJ01] U. Even, I. Al-Hroub, and J. Jortner. Small He clusters with aromatic molecules. *J. Chem. Phys.*, 115:2069–2073, 2001.

[EJN+00] U. Even, J. Jortner, D. Noy, N. Lavie, and C. Cossart-Magos. Cooling of large molecules below 1 k and he cluster formation. *J. Chem. Phys.*, 112(18):8068–8071, 2000.

[Eve] Uzi Even. personal communication, 2007.

[FH84] Josef Friedrich and Dietrich Haarer. Photochemical Hole Burning: A Spectroscopic Study of Relaxation Processes in Polymers and Glasses. *Angew. Chem. Int. Ed.*, 23:113–140, 1984.

[FHL80] P. S. H. Fitch, Ch. A. Haynam, and D. H. Levy. The fluorescence excitation spectrum of free base phthalocyanine cooled in a supersonic free jet. *J. Chem. Phys.*, 73:1064, 1980.

[Fou88] P. F. Fougere. Maximum entropy calculations on a discrete probability space. In G. J. Erickson and C. R. Smith, editors, *Maximum-Entropy and Bayesian Methods in Science and Engineering*, volume 1: Foundations, pages 205–234. Kluwer Academic Publishers, Dordrecht, 1988.

[FWL78] P. S. H. Fitch, L. Wharton, and D. H. Levy. Fluorescence excitation spectrum of free base phthalocyanine cooled in a supersonic expansion. *J. Chem. Phys.*, 69:3424, 1978.

[GEA02] V. Ghazarian, J. Eloranta, and V. A. Apkarian. Universal molecule injector in liquid helium: Pulsed cryogenic doped helium droplet source. *Rev. Sci. Instrum.*, 73:3606–3613, 2002.

[GHH$^+$00] S. Grebenev, M. Hartmann, M. Havenith, B. Sartakov, J. P. Toennies, and A. F. Vilesov. The rotational spectrum of single ocs molecules in liquid ^{4}he droplets. *The Journal of Physical Chemistry*, 112(10):4485–4495, März 2000.

[GNB94] Daniel Gruner, An Nguyen, and Paul Brumer. Theoretical study of the $S_1 \leftrightarrow S_0$ spectroscopy of anthracene. *J. Chem. Phys.*, 101:10366–10381, 1994.

[GR03] Zbigniew R. Grabowski and Krystyna Rotkiewicz. Structural Changes Accompanying Intramolecular Electron Transfer: Focus on Twisted Intramolecular Charge-Transfer States and Structures. *Chem. Rev.*, 103:3899–4031, 2003.

[GRBPR05] Isabel Gómez, Mar Reguero, Martial Boggio-Pasqua, and Michael A. Robb. Intramolecular Charge Transfer in 4-Aminobenzonitriles Does Not Necessarily Need the Twist. *J. Am. Chem. Soc.*, 127:7119–7129, 2005.

[Gre09] Christian Greil. Spektroskopie an Verbindungen mit intramolekularem Elektronentransfer, Diplomarbeit, Universität Regensburg, 2009.

[GSS92] S. Goyal, D. L. Schutt, and G. Scoles. Vibratrional Spectroscopy of Sulfur Hexafluoride Attached to Helium Clusters. *Phys. Rev. Lett.*, 69:933–936, 1992.

[GTV98] Slava Grebenev, J. Peter Toennies, and Andrei F. Vilesov. Superfluidity Within a Small Helium-4 Cluster: The Microscopic Andronikashvili Experiment. *Science*, 279:2083–2086, 1998.

[HEJ01] Andreas Heidenreich, Uzi Even, and Joshua Jortner. Nonrigidity, delocalization, spatial confinement and electronic-vibrational spectroscopy of anthracene-helium clusters. *J. Chem. Phys.*, 115:10175–10185, 2001.

[HHTV97] J. Harms, M. Hartmann, J. P. Toennies, and A. F. Vilesov. Rotational structure of the ir spectra of single sf_6 molecules in liquid ^{4}he and ^{3}he droplets. *Journal of Molecular Spectroscopy*, 185(1):204–206, September 1997.

[Hir86] Satoshi Hirayama. A comparative study of the fluorescence lifetimes of 9-cyanoanthracene in a bulb and supersonic free jet. *J. Chem. Phys.*, 85:6867–6873, 1986.

[HITS90] Satoshi Hirayama, Yutaka Iuchi, Fujio Tanaka, and Kosuke Shobatake. Natural radiative lifetimes of anthracene derivatives and their dependence on refractive index. *Chem. Phys.*, 144:401–406, 1990.

[HL07] Rong-Xing He and Xiang-Yuan Li. An anti-quinoid structure in dual fluorescence of fluorazene molecule and solvent effect of intramolecular charge transfer. *Chem. Phys.*, 332:325–335, 2007.

[HLTV98] Matthias Hartmann, Albrecht Lindinger, J. Peter Toennies, and Andrei F. Vilesov. Laser-induced fluorescence spectroscopy of van der Waals complexes of tetracene-Ar_N ($N \leq 5$) and pentacene-Ar within ultracold liquid He droplets. *Chem. Phys.*, 239:139–149, 1998.

[HLTV01] Matthias Hartmann, Albrecht Lindinger, J. Peter Toennies, and Andrej F. Vilesov. Hole-Burning Studies of the Splitting in the Ground and Excited Vibronic States of Tetracene in Helium Droplets. *J. Phys. Chem. A*, 105:6369, 2001.

[HLTV02] Matthias Hartmann, Albrecht Lindinger, J. Peter Toennies, and Andrej F. Vilesov. The phonon wings in the ($S_1 \leftarrow S_0$) specta of tetracene, pentacene, porphin and phthalocyanine in liquid helium droplets. *Phys. Chem. Chem. Phys.*, 4:4839–4844, 2002.

[HMTV95] M. Hartmann, R. E. Miller, J. P. Toennies, and A. Vilesov. Rotationally Resolved Spectroscopy of SF_6 in Liquid Helium Clusters: A Molecular Probe of Cluster Temperature. *Phys. Rev. Lett.*, 75(8):1566–1569, Aug 1995.

[HMTV96] M. Hartmann, F. Mielke, J. P. Toennies, and A. F. Vilesov. Direct Spectroscopic Observation of Elementary Excitations in Superfluid He Droplets. *Phys. Rev. Lett.*, 76:4560–4563, 1996.

[HPS+99] Matthias Hartmann, Nikolaus Pörtner, Boris Sartakov, J. Peter Toennies, and Andrej F. Vilesov. High resolution infrared spectroscopy of single SF_6 molecule in helium droplets. I. Size effects in ^{4}He droplets. *J. Chem. Phys.*, 110:5109–5123, 1999.

[HSJ08] Babette Hinkeldey, Alexander Schmitt, and Gregor Jung. Comparative photostability studies of BODIPY and fluorescine dyes by using fluorescence correlation spectroscopy. *ChemPhysChem*, 9:2019–2027, 2008.

[HST85] Satoshi Hirayama, Kosuke Shobatake, and Kiyohiko Tabayashi. Lack of a heavy-atom effect on fluorescence lifetimes of 9-cyanoanthracene-rare gas clusters in a supersonic free jet. *Chem. Phys. Lett.*, 121(3):228–232, 1985.

[HTD98] Jan Harms, J. Peter Toennies, and Franco Dalfovo. Density of superfluid helium droplets. *Phys. Rev. B*, 58(6):3341–3350, Aug 1998.

[HTK97] J. Harms, J. P. Toennies, and E. L. Knuth. Droplets formed in helium free-jet expansion from states near the critical point. *J. Chem. Phys.*, 106:3348–3357, 1997.

[II88] Totaro Imasaka and Nobuhiko Ishibashi. Supersonic jet spectrometry of aromatic hydrocarbons. *Spectrochimica Acta B*, 43:661–669, 1988.

[ITI88] Totaro Imasaka, Katsunori Tanaka, and Nobuhiko Ishibashi. Supersonic Jet Fluorimetry Using Spectrometric Multichannel Analyzer for Detection in Gas Chromatography. *Analytical Sciences*, 4:31–35, 1988.

[IYI87] Totaro Imasaka, Noriyuki Yamaga, and Nobuhiko Ishibashi. High Performance Liquid Chromatography with Supersonic Jet/Laser Fluorimetric Detection. *Anal. Chem.*, 59:419–422, 1987.

[JK97] Gouri S. Jas and Krysztof Kuczera. Ab initio calculations of S_1 excited state vibrational spectra of benzene, naphthalene and anthracene. *Chem. Phys.*, 214:229–241, 1997.

[JN92] T. Jiang and J. A. Northby. Fragmentation clusters formed in supercritical expansions of *he*4. *Phys. Rev. Lett.*, 68(17):2620–2623, Apr 1992.

[Jor92] J. Jortner. Cluster size effects. *Z. Phys. D - Atoms, Molecules and Clusters*, 24:247–275, 1992.

[JWKJ96] Gouri S. Jas Jas, Chaozhi Wan, Krysztof Kuczera, and Carey K. Johnson. Picosecond Time-Resolved Fourier-Transform Raman Spectroscopy and Normal-Mode Analysis of the Ground State and Singlet Excited State of Anthracene. *J. Phys. Chem.*, 100:11857–11862, 1996.

[KBBP01] T. M. Korter, D. R. Borst, C. J. Butler, and D. W. Pratt. Stark Effects in Gas-Phase Electronic Spectra. Dipole Moment of Aniline in its excited S_1 State. *J. Am. Chem. Soc.*, 123:96–99, 2001.

[KH99] E. L. Knuth and U. Henne. Average size and size distribution of large droplets produced in a free-jet expansion of a liquid. *J. Chem. Phys.*, 110:2664–2668, 1999.

[KKHS92] Mitsuhiko Kono, Yoshiharu Kubo, Satoshi Hirayama, and Kosuke Shobatake. Radiative lifetime and electronic relaxation of 9-cyanoanthracene in rare-gas clusters and in rare-gas matrices. *Chem. Phys. Lett.*, 198:214–219, 1992.

[KKY$^+$05] H. L. Kee, C. Kirmaier, L Yu, P. Thamyongkit, W. J. Youngblood, M. E. Calder, L. Ramos, B. C. Noll, D. F. Bocian, W. R. Scheidt, R. R. Birge, J. S. Lindsey, and D. Holten. Structural control of the photodynamics of boron-dipyrrin complexes. *J. Phys. Chem. B*, 109:20433–20443, 2005.

[KM95] Martin Klessinger and Josef Michl. *Excited States and Photochemistry of Organic Molecules*. VCH, 1995.

[KM07] Jochen Küpper and Jeremy M. Merritt. Spectroscopy of free radicals and radical containing entrance-channel complexes in superfluid helium nano-droplets. *Int. Rev. Phys. Chem.*, 26:249–287, 2007.

[KMP$^+$02] M. Kunze, P. R. L. Markwick, N. Pörtner, J. Reuss, and M. Havenith. Infrared–microwave double resonance spectroscopy of OCS in pure ^{4}He and mixed ^{4}He/^{3}He clusters. *J. Chem. Phys.*, 116(17):7473–7485, 2002.

[KRH05] Serge Krasnokutski, Gael Rouillé, and Friedrich Huisken. Electronic spectroscopy of anthracene molecules trapped in helium nanodroplets. *Chem. Phys. Lett.*, 406:386–392, 2005.

[KZ85] Brian W. Keelan and Ahmed H. Zewail. Rotational band contour analysis of symmetries and interactions of vibrational levels in anthracene S_1. *J. Chem. Phys.*, 82:3011–3019, 1985.

[LABnM+05] F. López Arbeloa, J. Bañuelos, V. Martínez, T. Arbeloa, and I. López Arbeloa. Structural, photophysical and lasing properties of pyrromethene dyes. *Intern. Rev. Phys. Chem.*, 24(2):339–374, 2005.

[LABnPMM+04] F. López Arbeloa, J. Bañuelos Prieto, V. Martínez Martínez, T. Arbeloa López, and I. López Arbeloa. Intramolecular charge transfer in pyrromethene laser dyes: photophysical behaviour of pm650. *ChemPhysChem.*, 5:1762–1771, 2004.

[LBD08] Evgeniy Loginov, Andreas Braun, and Marcel Drabbels. A new sensitive detection scheme for helium nanodroplet isolation spectroscopy: application to benzene. *Phys. Chem. Chem. Phys.*, 10:6107–6114, 2008.

[LBH+98] Stephen R. Langhoff, Charles W. Bauschlicher, Douglas M. Hudgins, Scott A. Sandford, and Louis J. Allamandola. Infrared Spectra of Substituted Polycyclic Aromatic Hydrocarbons. *J. Phys. Chem. A*, 102:1632–1646, 1998.

[Leh04] Rudolf Lehnig. *Anregungs- und Emissionsspektroskopie von organischen Molekülen in ^{4}He-Tröpfchen.* PhD thesis, Universität Regensburg, 2004.

[Lev80] D. H. Levy. Laser spectroscopy of cold gas-phase molecules. *Ann. Rev. of Phys. Chem.*, 31:197–225, 1980.

[LFSZ84] W. R. Lambert, P. M. Felker, J. A. Syage, and A. H. Zewail. Jet spectroscopy of anthracene and deuterated anthracenes. *J. Chem. Phys.*, 81:2195–2208, 1984.

[LHP93] H. Lin, J. A. Hunter, and J. Pfab. Laser-induced fluorescence spectroscopy of jet-cooled 2-methylanhtracene S_1 (π, π^*). Evidence for methyl conformation change upon electronic excitation. *Chem. Phys. Lett.*, 210:38–44, 1993.

[LI95] Cheng-Huan Lin and Totaro Imasaka. Prediction of chemical structure of aromatic hydrocarbons by pattern recognition of spectral lines obtained by fluorescence spectrometry in a supersonic jet. *Talanta*, 42:1111–1119, 1995.

[Lin99] Albrecht Lindinger. *Vibronische Spektroskopie von organischen und biologischen Molekülen in ^{4}He-Clustern.* PhD thesis, Georg-August-Universität Göttingen, 1999.

[LLTV01] Albrecht Lindinger, Eugene Lugovoj, J. Peter Toennies, and Andrei F. Vilesov. Splitting of the Zero Phonon Lines of Indole, 3 Methyl Indole, Tryptamine and N-Acetyl Tryptophan Amide in Helium Droplets. *Z. Phys. Chem.*, 215:401–416, 2001.

[Log08] Evgeniy Loginov. *Photoexcitation and Photoionization Dynamics of Doped Liquid Helium-4 Nanodroplets.* PhD thesis, EPFL Lausanne, 2008.

[LPV$^+$09] R. Lehnig, D. Pentlehner, A. Vdovin, B. Dick, and A. Slenczka. Photochemistry of 3-hydroxyflavone inside superfluid helium nanodroplets. *J. Chem. Phys.*, 131:194307–1–8, 2009.

[LRD05] Evgeniy Loginov, Dominic Rossi, and Marcel Drabbels. Photoelectron Spectroscopy of Doped Helium Nanodroplets. *Phys. Rev. Lett.*, 95:163401–1–4, 2005.

[LS03] R. Lehnig and A. Slenczka. Emission spectra of free base phthalocyanine in superfluid helium droplets. *J. Chem. Phys.*, 118:8256–8262, 2003.

[LS04a] R. Lehnig and A. Slenczka. Quantum solvation of phthalocyanine in superfluid helium droplets. *J. Chem. Phys.*, 120:5064–5066, 2004.

[LS04b] Rudolf Lehnig and Alkwin Slenczka. Microsolvation of Phthalocyanines in Superfluid Helium Droplets. *ChemPhysChem*, 5:1014–1019, 2004.

[LS05] R. Lehnig and A. Slenczka. Spectroscopic investigation of the solvation of organic molecules in superfluid helium droplets. *J. Chem. Phys.*, 122:244317–1–9, 2005.

[LSK$^+$04] Rudolf Lehnig, Mikhail Slipchenko, Susumu Kuma, Takamasa Momose, Boris Sartakov, and Andrey Vilesov. Fine structure of the ($S_1 \leftarrow S_0$) band origins of phthalocyanine molecules in helium droplets. *J. Chem. Phys.*, 121:9396–9405, 2004.

[LSS07] Rudolf Lehnig, Joshua A. Sebree, and Alkwin Slenczka. Structure and

Dynamics of Phthtalocyanine-Argon$_n$ (n = 1-4) Complexes Studied in Helium Nanodroplets. *J. Phys. Chem. A*, 111:7576–7584, 2007.

[LST93] M. Lewerenz, B. Schilling, and J. P. Toennies. A new scattering deflection method for determining and selecting the sizes of large liquid clusters of ^{4}He. *Chem. Phys. Lett.*, 206:381–387, 1993.

[LST95] M. Lewerenz, B. Schilling, and J. P. Toennies. Successive capture and coagulation of atoms and molecules to small clusters in large liquid helium clusters. *J. Chem. Phys.*, 102:8191–8207, 1995.

[LTV01] Albrecht Lindinger, J. Peter Toennies, and Andrej F. Vilesov. Pump-Probe study of the reconstruction of helium surrounding a tetracene molecule inside a helium droplet. *Phys. Chem. Chem. Phys.*, 3:2581–2587, 2001.

[LTV04] Albrecht Lindinger, J. Peter Toennies, and Andrej F. Vilesov. The effects of isotope substitution and nuclear spin modifications on the spectra of complexes of tetracene with hydrogen molecules in ultracold 0.37 K He droplets. *J. Chem. Phys.*, 121:12282–12292, 2004.

[LTV06] Albrecht Lindinger, J. Peter Toennies, and Andrey F. Vilesov. Laser-induced fluorescence spectra of tetracene complexes with Ne, H_2O, D_2O He droplets. *Chem. Phys. Lett.*, 429:1–7, 2006.

[MLS$^+$05] A. Mordziński, A. Leś, Y. Stepanenko, J. Rycombel, and L. Adamowicz. S_0 and S_1 spectroscopy of jet cooled 9-cyano-10-methylanthracene: The methyl group as a molecular rotor. *Journal of Molecular Spectroscopy*, 233:98–109, 2005.

[Mor07] Paolo Moreschini. *Spectroscopy and Dynamics of Polyaromatic Hydrocarbons in Helium Nanodroplets.* PhD thesis, Princeton University, 2007.

[MXJ07] A. R. W. McKellar, Yunjie Xu, and Wolfgang Jäger. Spectroscopic Studies of OCS-Doped ^{4}He Clusters with 9-72 Helium Atoms: Observation of Broad Oscillations in the Rotational Moment of Inertia. *J. Phys. Chem. A*, 111:7329–7337, 2007.

[NM99] K Nauta and R. E. Miller. Nonequilibrium Self-Assembly of Long Chains of Polar Molecules in Superfluid Helium. *Science*, 283:1895–1897, 1999.

[NM00] K. Nauta and R. E. Miller. Metastable vibrationally excited HF (v=1) in helium nanodroplets. *J. Chem. Phys.*, 113:9466–9469, 2000.

[NM01] K Nauta and R. E. Miller. Rotational and vibrational dynamics of methane in helium nanodroplets. *Chem. Phys. Lett.*, 350:225–232, 2001.

[NMB+05] A. E. Nikolaev, G. Myszkiewicz, G. Berden, W. Leo Meerts, J.F. Pfanstiel, and D. W. Pratt. Twisted intramolecular charge transfer states: Rotational resolved fluorescence excitation spectra of 4,4'-dimethylaminobenzonitrile in a molecular beam. *J. Chem. Phys.*, 122:084309, 2005.

[NMM99] K. Nauta, D. T. Moore, and R. E. Miller. Molecular orientation in superfluid liquid helium droplets: high resolution infrared spectroscopy as a probe of solvent-solute interactions. *Faraday Discuss.*, 113:261–278, 1999.

[NNS+05] Masayuki Nakagaki, Eriko Nishi, Kenji Sakota, Kaori Nishi, Haruyuki Nakano, and Hiroshi Sekiya. Internal rotation of methyl group in 2- and 1-methylanthracene studied by electronic spectroscopy and DFT calculations. *Chem. Phys.*, 316:178–184, 2005.

[NNS+06] Masayuki Nakagaki, Eriko Nishi, Kenji Sakota, Haruyuki Nakano, and Hiroshi Sekiya. A model two-dimensional potential for internal rotation of 9-methylanthracene studied by electronic spectroscopy and DFT calculations. *Chem. Phys.*, 328:190–196, 2006.

[noz] *The Even-Lavie Valve, Cryogenic Pulsed Valve for Supersonic Expansion, Type E.L.-5-C-2005, 1kHz, High Repetition Rate, Operating Manual.*

[Ohn79] Koichi Ohno. Normal Coordinate calculations of Benzoid Hydracarbons. *J. of Molecular Spectroscopy*, 77:329–348, 1979.

[ONOS98] K. Okuyama, Y. Numata, S. Odawara, and I. Suzuka. Electronic spectra of jet-cooled 1-phenylpyrrole: large-amplitude torsional motion and twisted charge-transfer phenomenon. *J. Chem. Phys.*, 109(17):7185–7196, November 1998.

[OPS73] I. S. Osad'ko, R. I. Personov, and E. V. Shpol'skii. Line spectra of guest molecules in n-paraffin matrices and the theory of the impurity centre. *J. of Lumin.*, 6:369–375, 1973.

[OS98] Vahur Oja and Eric M. Suuberg. Vapor Pressures and Enthalpies of Sublimation of Polycyclic Aromatic Hydrocarbons and Their Derivatives. *J. Chem. Eng. Data*, 43:486–492, 1998.

[Pö01] Nikolas Pörtner. *Hochauflösende elektronische Spektroskopie von Molekülen in ^{4}He- und ^{3}He- Tröpfchen.* PhD thesis, Georg-August-Universität Göttingen, 2001.

[PA93] Abraham Penner and Aviv Amirav. Vibratrional predissociation of 9,10-dichloroanthracene - Mixed and homo rare gas atom clusters. *J. Chem. Phys.*, 99:9616–9628, 1993.

[PAJN90] Abraham Penner, Aviv Amirav, Joshua Jortner, and Abraham Nitzan. Solvation effects on molecular pure radiative lifetime and absorption oscillator strength in clusters. *J. Chem. Phys.*, 93:147–158, 1990.

[Par00] Andreas B. J. Parusel. A dft/mrci study on the excited state charge transfer states of n-pyrrolobenzene, n-pyrrolobenzonitrile and 4-n,n-dimethylaminobenzonitrile. *Phys. Chem. Chem. Phys.*, 2:5545–5552, 2000.

[PGDS10] D. Pentlehner, Ch. Greil, B. Dick, and A. Slenczka. Line broadening in electronic spectra of anthracene derivatives inside superfluid helium nanodroplets. *J. Chem. Phys.*, 133:114505–1–9, 2010.

[PMSA00] Boris Proppe, Manuela Merchán, and Luis Serrano-Andrés. Theoretical study of the twisted intramolecular charge transfer in 1-phenylpyrrole. *J. Phys. Chem A.*, 104:1608–1616, 2000.

[PPV02] N. Pörtner, Toennies J. P., and A. F. Vilesov. The observation of large changes in the rotational constants of glyoxal in superfluid helium droplets upon electronic excitation. *J. Chem. Phys.*, 117(13):6054–6060, 2002.

[PRD$^+$09] Dominik Pentlehner, Ricarda Riechers, Bernhard Dick, Alkwin Slenczka, Uzi Even, Nachum Lavie, Ravie Brown, and Kfir Luria. Rapidly pulsed helium droplet source. *Rev. Sci. Instrum.*, 80:043302–1–9, 2009.

[PS86] Charles S. Parmenter and Bradley M. Stone. The methyl rotor as an accelerating functional group for IVR. *J. Chem. Phys.*, 84:4710–4711, 1986.

[PVH01] Nikolas Pörtner, Andrej F. Vilesov, and Martina Havenith. The formation of heterogeneous van der Waals complexes in helium droplets. *Chem. Phys. Lett.*, 343:281–288, 2001.

[Rie07] Ricarda Riechers. Optische Spektroskopie von Molekülen in superflüssigen Heliumtropfen. Untersuchung von Schwingungsmoden im elektronischen Grundzustand und in elektronisch angeregten Zuständen, Diplomarbeit, Universität Regensburg, 2007.

[RKH$^+$04] Gael Rouillé, Serge Krasnokutski, Friedrich Huisken, Thomas Henning, Oleksandr Subkhorukov, and Angela Staicu. Ultraviolet spectroscopy of pyrene in a supersonic jet and in liquid helium droplets. *J. Chem. Phys.*, 120:6028–6034, 2004.

[RkR] Y. Ralchenko, A. E. kramida, J. Reader, and NIST ASD Team (2008). NIST Atomic Spectra Database (version 3.1.5), http://physics.nist.gov/asd3. *Natiional Institute of Standards and Technology, Gaithersburg, MD.*

[RWvHH07] S. Rudolph, G. Wollny, K. von Haeften, and M. Havenith. Probing collective excitations in helium nanodroplets: Observation of phonon wings in the infrared spectrum of methane. *J. Chem. Phys.*, 126:124318–1–6, 2007.

[SBGI07] P. P. Semyannikov, T. V. Basova, V. M. Grankin, and I. K. Igumenov. Vapour pressure of some phthalocyanines. *J. Porphyrins and Phthalocyanines*, 4:271–277, 2007.

[SBH$^+$05] D. Schweke, H. Baumgarten, Y. Haas, Wolfgang Rettig, and Bernhard Dick. Charge-Transfer-Type Fluorescence of 4-(1H-Pyrrol-1-yl)benzonitrile (PBN) and N-Phenylpyrrole (PP) in Cryogenic Matrixes: Evidence for Direct Excitation of the CT Band. *J. Phys. Chem. A*, 109:576–585, 2005.

[ScD$^+$04] Roman Schmied, Çarcaçabal, Adriaan M. Dokter, Vincent P. A. Lonij, Kevin K. Lehmann, and Giacinto Scoles. UV spectra of benzene isotopomers and dimers in helium nanodroplets. *J. Chem. Phys.*, 121:2701–2710, 2004.

[Sch93] Bernhard Schilling. *Molekularstrahlexperimente mit Helium-Clustern.* PhD thesis, Bericht 14/1993, Max Planck Institut für Strömungsforschung, Göttingen, 1993.

[Sco88] Giacinto Scoles, editor. *Atomic and Molecular Beam Methods.* Oxford University Press, 1988.

[SDHT01] Alkwin Slenczka, Bernhard Dick, Matthias Hartmann, and J. Peter Toennies. Inhomogeneous broadening of the zero phonon line of phthalocyanine in superfluid helium droplets. *J. Chem. Phys.*, 115:10199–10205, 2001.

[SF09] Anja Stromeck-Faderl. *Hochauflösende Spektroskopie an isolierten Molekülen im Überschall-Düsenstrahl-Untersuchung von Pyrromethen-Farbstoffen.* PhD thesis, Universität Regensburg, 2009.

[SFS+85] J. A. Syage, P. M. Felker, D. H. Semmes, F. Al Adel, and A. H. Zewail. Picosecond excitation and selective intramolecular rates in supersonic molecular beams. IV. Alkylanthracenes. *J. Chem. Phys.*, 82:2896–2908, 1985.

[SGR+96] S. Schumm, M. Gerhards, W. Roth, H. Gier, and K. Kleinermanns. A CASSCF study of the S_0 and S_1 states of phenol. *Chem. Phys. Lett.*, 263(1-2):126–132, 1996.

[SH03a] Ken Sakata and Kimihiko Hara. Ab initio study of the torsional potential for 9-phenylanthracene in the ground and excited states. *Chem. Phys. Lett.*, 371:164–171, 2003.

[SH03b] Danielle Schweke and Yehuda Haas. The fluorescence of N-Phenylpyrrole in an Argon/Acetonitrile Matrix. *J. Chem. Phys. A*, 107:9554–9560, 2003.

[SHD05] D. Schweke, Y. Haas, and Bernhard Dick. Photophysics of Phenylpyrrole Derivatives and Their Acetonitrile Clusters in the Gas Phase and in Argon Matrices: Simulations of Structure and Reactivity. *J. Phys. Chem. A*, 109:3830, 2005.

[SHWJ09] Alexander Schmitt, Babette Hinkeldey, Mandy Wild, and Gregor Jung. Synthesis of the core compound of the bodipy dye class: 4,4´-difluoro-4-bora-(3a,4a)-diaza-s-indacene. *J. Fluoresc.*, 19:755–758, 2009.

[SKMV02] Mikhail N. Slipchenko, Susumu Kuma, Takamasa Momose, and Andrey F. Vilesov. Intense pulsed helium droplet beams. *Rev. Sci. Instrum.*, 73:3600–3605, 2002.

[SOK+09] Mohsen Sajadi, Thorsten Obernhuber, Sergey A. Kovalenko, Manuel Mosquera, Bernhard Dick, and Nikolaus P. Ernsting. Dynamic Polar Solvation is Reported by Fluorescing 4-Aminophthalimide Faithfully Despite H-Bonding. *J. Phys. Chem. A*, 113:44–55, 2009.

[SP96] Wayne E. Sinclair and David W. Pratt. Structure and vibrational dynamics of aniline and aniline-Ar from high-resolution electronic spectroscopy in the gas phase. *J. Chem. Phys.*, 105:7942–7956, 1996.

[Spa97] Lee H. Spangler. Structural information from methyl internal rotation spectroscopy. *Annu. Rev. Phys. Chem.*, 48:481–510, 1997.

[SRS+04] A. Staicu, G. Rouillé, O. Sukhorukov, Th. Henning, and F. Huisken. Cavity ring-down laser absorption spectroscopy of jet-cooled anthracene. *Mol. Phys.*, 102:1777–1783, 2004.

[ST08] A. Slenczka and J. P. Toennies. Chemical Dynamics Inside Superfluid Helium Nanodroplets at 0.37 K. In I. A. M. Smith, editor, *Low Temperatures and Cold Molecules*, page 345. World Scientific, Singapore, 2008.

[Str05] Anja Stromeck. Spektroskopie von Torsionsmoden isolierter Moleküle, Diplomarbeit, Universität Regensburg, 2005.

[STS+90] M. Shah, K. Thangaraj, M.-L. Soong, L. T. Wolford, J. H. Boyer, I. R. Politzer, and T. G. Pavlopoulos. Pyrromethene-bf$_2$ complexes as laser dyes: 1. *Heteroatom Chemistry*, 1(5):389–399, 1990.

[SV01] Frank Stienkemeier and Andrey F. Vilesov. Electronic spectroscopy in He droplets. *J. Chem. Phys.*, 115:10119–10137, 2001.

[TT90] R. D. Tilley and J. Tilley. *Superfluidity and Superconductivity.* Institute of Physics Publishing, Bristol, Philadelphia, 3rd edition, 1990.

[Tur78] Nicholas J. Turro. *Modern Molecular Photochemistry.* Benjamin/-Cummings Publishing Company, Inc., 1978.

[TV98] J. Peter Toennies and Andrei F. Vilesov. Spectroscopy of Atoms and Moelcules in Liquid Helium. *Annu. Rev. Phys. Chem.*, 49:1–41, 1998.

[TV04] J. Peter Toennies and Andrey F. Vilesov. Superfluid Helium Droplets: A Uniquely Cold Nanomatrix for Molecules and Molecular Complexes. *Angew. Chem. Int. Ed.*, 43:2622–22648, 2004.

[TYH+89] Fujio Tanaka, Shigeru Yamashita, Satoshi Hirayama, Akiho Adach, and Kosuke Shobatake. Fluorescence Decays of 9,10-Dichloroanthracene and its van der Waals Complexes with rare gas atoms in supersonic free jets. *Chem. Phys.*, 131:435–442, 1989.

[UZH08] Gilles Ulrich, Raymond Ziessel, and Anthony Harriman. The Chemistry of Fluorescent Bodipy Dyes: Versatility Unsurpassed. *Angew. Chem. Int. Ed.*, 47(7):1184–1201, 2008.

[VF82] Stephan P. Velsko and Graham R. Fleming. Photochemical isomerization in solution. Photophysics of diphenyl butadiene. *J. Chem. Phys.*, 76(7):3553–3562, 1982.

[WBGB87] David W. Werst, Ann M. Brearley, W. Ronald Gentry, and Paul F. Barbara. S_1 Torsional Potentials of Substituted Anthracenes. *J. Am. Chem. Soc.*, 109:32–40, 1987.

[WDW09] Heather D. Whitley, Jonathan L. DuBois, and K. Brigitta Whaley. Spectral shifts and helium configurations in ^4He_N-tetracene clusters. *J. Chem. Phys.*, 131:124514, 2009.

[Wed97] Gerd Wedler. *Lehrbuch der Physikalischen Chemie*. Wiley-VCH, 1997.

[WGB85] David W. Werst, W. Ronald Gentry, and Paul F. Barbara. The S_0 and S_1 Torsional Potentials of 9-Phenylanthracene. *J. Phys. Chem.*, 89:729–732, 1985.

[WHKW05] Heather D. Whitley, Patrick Hunag, Yongkyong Kwon, and K. Brigitta Whaley. Multiple solvation configurations around phthalocyanine in helium droplets. *J. Chem. Phys.*, 123:054307, 2005.

[WL96] R. W. Wagner and J. S. Lindsey. Boron-dipyrromethene dyes for incorporation in synthetic multi-pigment light-harvesting arrays. *Pure and Applied Chemistry*, 68(7):1373–1380, 1996.

[WLSB85] David W. Werst, William F. Londo, John L. Smith, and Paul F. Barbara. The Excited-State Torsional Potentials of Substituted 9-Phenylanthracenes. *Chem. Phys. Lett.*, 118, 1985.

[XCZ06] Xuefei Xu, Zexing Cao, and Qianer Zhang. Computational Characterization of Low-Lying States and Intramolecular Charge Transfers in N-Phenylpyrrole and the Planar-Rigidized Fluorazene. *J. Phys. Chem. A*, 110:1740–1748, 2006.

[YBE05] Shengfu Yang, Scott M. Brereton, and Andrew M. Ellis. Controlled growth of helium nanodroplets from a pulsed source. *Rev. Sci. Instrum.*, 76:104102–1–4, 2005.

[YBN$^+$07] Shengfu Yang, Scott M. Brereton, Satvinder Nandhra, Andrew M. Ellis, Bo Shang, Lan-Feng Yuan, and Jinlong Yang. Electron impact ionization of water-doped superfluid helium nanodroplets: Observation of $He(H_2O)_n^+$clusters. *J. Chem. Phys.*, 127:134303–1–6, 2007.

[YBWE05] Shengfu Yang, Scott M. Brereton, Martyn D. Wheeler, and Andrew M. Ellis. Soft or hard ionization of molecules in helium nanodroplets? An electron impact investigation of alcohols and ethers. *Phys. Chem. Chem. Phys.*, 7:4082–4088, 2005.

[YBWE06] Shengfu Yang, Scott M. Brereton, Martyn D. Wheeler, and Andrew M. Ellis. Electron Impact Ionization of Haloalkanes in Helium Nanodroplets. *J. Phys. Chem. A*, 110:1791–1797, 2006.

[YDZ04] Toshitada Yoshihara, Sergey I. Druzhinin, and Klaas A. Zachariasse. Fast Intramolecular Charge Transfer with a Planarized Rigidized Electron Donor/Acceptor Molecule. *J. Am. Chem. Soc.*, 126:8535–8539, 2004.

[YE08] Shengfu Yang and Andrew M. Ellis. Selecting the size helium nanodroplets using time-resolving probing of a pulsed helium droplet beam. *Rev. Sci. Instrum.*, 79:016106–1–2, 2008.

[YGD+03] Toshitada Yoshihara, Victor A. Galievsky, Sergey I. Druzhinin, Satyen Saha, and Klaas A. Zachariasse. Singlet excited state dipole moments of dual fluorescent N-phenylpyrroles and 4-(dimethylamino)benzonitrile from solvatochromic and thermochromic spectral shifts. *Photochem. Photobiol. Sci.*, 2:342–353, 2003.

[ZH02] Shmuel Zilberg and Yehuda Haas. The Nature of the Intramolecular Charge Transfer Excited State in p-Pyrrolocyanobenzene (PBN) and Other Derivatives of Benzene Substituted by Electron Donor and Acceptor Groups. *J. Phys. Chem. A*, 106:1–11, 2002.

[ZHS95] Shmuel Zilberg, Yehuda Haas, and Sason Shaik. Electronic Spectrum of Anthracene: An ab-Initio Molecular Orbital Calculation Combined with a Valence Bond Interpretation. *J. Phys. Chem.*, 99:16558–16565, 1995.

[ZLLB95] Ralf Zimmermann, Christoph Lermer, Dieter Lenoir, and Ulrich Boesl. Isomer Selective Ionization of Chlorinated PAHs: Detection of Impurities in Technical 9-Monochloroanthracene. In *AIP Conferenz Preceedings*, volume 329 (Resonance Ionization Spectroscopy 1994), pages 527–530, 1995.

[ZLS+95] R. Zimmermann, Ch. Lermer, K. W. Schramm, A. Kettrup, and U. Boesl. Three-dimensional trace analysis: combination of gas chromatography, supersonic beam UV spectroscopy and time-of-flight mass spectrometry. *Eur. Mass. Spectrom.*, 1:341–351, 1995.

[ZSFH94] S. Zilberg, U. Samuni, R. Fraenkel, and Y. Haas. The vibrational structure of the $S_0 \rightarrow S_1$ transition of anthracene. *Chem. Phys.*, 186:303–316, 1994.

[ZSGL04] Marina v. Zhigalko, Oleg V. Shishkin, Leonid Gorb, and Jerzy Leszczynski. Out-of-plane defromability of aromatic systems in naphthalene, anthracene and phenanthrene. *Journal of Molecular Structure*, 693:153–159, 2004.

[ZZ88] Francesco Zerbretto and Marek Z. Zgierski. Theoretical Analysis of Franck–Condon and Vibronic Activity of the a_g and b_{3g} Modes in the $S_0 \leftrightarrow S_1$ Transitions in Anthracene. *Chem. Phys.*, 127:17–29, 1988.

Acknowledgement

Thanks to ..

.. especially my supervisor Prof. Dr. Alkwin Slenczka for great scientific but also personal support and for granting the freedom to follow own ideas.

.. Prof. Dr. Bernhard Dick for the opportunity to work on this project and stimulating discussions.

.. Prof. Dr. Uzi Even for providing with an excellent experimental tool and the good cooperation.

.. Prof. jr. Dr. Gregor Jung for providing with the compounds BDP und 8-PhPM.

.. Dr. Anja Stromeck-Faderl and Christian Greil for the smooth cooperation, fruitful discussions and for providing with their gas phase spectra.

.. Dr. Uwe Kensy and Dr. Andreas Schmaunz for the measuring software and help with technical problems.

.. all current members of the helium droplet group Tobias Premke, Ricarda Riechers, and Eva-Maria Wirths and the former members Jonathan Gorodetsky, Jens Nielsen, and Dr. Alexander Vdovin for the friendly atmosphere in the lab and fruitful discussions.

.. all further members of the chair PD Dr. Stephan Bäuerle, Ulrike Berg, Dr. Udo Bogner, Dr. Rafal Czerwienicz, Tobias Fischer, Dr. Gerhard Herzog, Thomas Hofbeck, Birte Höing, Roger-Jan Kutta, Markus Leitl, Oliver Masur, Martina Müller, Emmanuel Peter, Manuel Schneider, Madlene v. Sanden-Flohe, Andreas Wenge, Prof. Dr. Hartmut Yersin, and Klaus Ziereis for the pleasant atmosphere and help whenever needed. I am especially grateful to Andreas Rausch for many discussions about science and his friendship.

.. the personal of the mechanical and electrical workshops for their valuable work.

.. in particular my family, friends, and my girlfriend Camille for their love and support and the great time outside the lab.